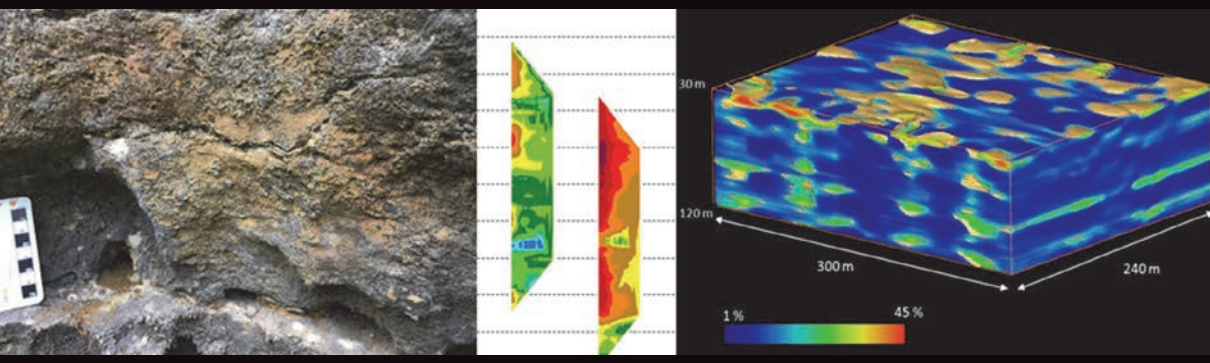

PROfile

A new concept of karst development based on hydrogeology and geophysics

The Poitou-threshold example

Thierry Gaillard and Jean-Luc Mari

edp sciences

agap QUALITÉ GÉOPHYSIQUE APPLIQUÉE

A new concept of karst development based on hydrogeology and geophysics

The Poitou-threshold example

Thierry Gaillard
and
Jean-Luc Mari

edp sciences

DOI: 10.1051/978-2-7598-3934-6
ISBN(print): 978-2-7598-3934-6 – ISBN(ebook): 978-2-7598-3935-3
This book is published under Open Access Creative Commons License CC-BY-NC-ND (https://creativecommons.org/licenses/by-nc-nd/4.0/en/) allowing non-commercial use, distribution, reproduction of the text, via any medium, provided the source is cited.
© EDP Sciences, 2026

Contents

Prefaces 9

Foreword 11
T. Gaillard and J.-L. Mari

The authors 13

Introduction 15
T. Gaillard and J.-L. Mari

Chapter 1 • The Poitou Threshold 19
T. Gaillard and P. Branger

Location and definition 19
Tectonic structure of the Poitou Threshold: a brief history of knowledge 21
Sedimentary coverage 28
Poitou threshold definition 31
References 32

Chapter 2 • The stratigraphy of the Middle Jurassic 37
P. Branger, T. Gaillard and H. Geairon

Paleontological division of the Middle Jurassic 37
Deposit sequences 38
Stratigraphy of the Middle Jurassic on the Poitou Threshold 40
Aalenian 40

D6 41
D7 – Lower Bajocian 41
D8 – Upper Bajocian 42
D9 – Lower Bathonian 43
D10 – Middle and upper Bathonian 43
Stratigraphy of the Bajocian south of Poitiers: the cliffs of Passelourdin 44
Conclusion 51
References 51

Chapter 3 • Hydrogeology of the Poitou Threshold 59
T. Gaillard and M. Moreau

Aquifers of the Poitou threshold 59
Two main aquifers 59
Piezometric map 60
The supra-Toarcian aquifer 64
Groundwater flow patterns in the supra-Toarcian aquifer 64
Comparison between lineaments and speleological networks 65
Typology of voids in Poitou threshold limestones 68
Pumping tests 71
Conclusion 77
Acknowledgements 78
References 78

Chapter 4 • The Hydrogeological Experimental Site of Poitiers University (France) 81
T. Gaillard

Origin of the hydrogeological experimental site (HES) 81
HES description 82
Scientific studies 84
References 85

Chapter 5 • Geophysical methods 87
J.-L. Mari

5.1 Seismic and acoustic methods 89
5.2 3D seismic imaging 92
5.3 Full waveform acoustic logging 98
5.4 Vertical seismic profiles versus full waveform acoustic logging 103
5.5 Electrical methods 107

5.6 Conclusions 111
Appendix: Static corrections
Acknowledgements 116
References 116

Chapter 6 • Borehole electrical panels: an experiment 119
M. Moreau, P. Brunel and J.-L. Mari
Material and method 120
Acquisition 123
Geological Interpretation 125
Summary 129
Conclusions 130
References 131

Chapter 7 • Hydrogeological flow logging and dye tracer tests on the Hydrogeological Experimental Site of Poitiers University (France) 133
A. Boulais, T. Gaillard and H. Geairon
Introduction 133
Borehole flow logging acquisition 135
Principle of flow logging 135
Downflow and upflow in the borehole 136
Dynamic flow logging 136
Flow logging with pumping in MP6 (crossed dynamics MP6) 141
Tracer tests 144
Tracer test protocol 144
Results 144
Conclusion and interpretation of pathways in karst horizons 148
References 149

Chapter 8 • Hydro-stratigraphic study of the Hydrogeological Experimental Site of Poitiers, France 151
T. Gaillard
Objectif and method 151
Aquifer stratigraphy of the HES 152
Stratigraphic context 152
Data available 153
Lithostratigraphy of the HES 154

Occurrence ok karst 161
Fracture inventory 161
Stratigraphy versus seismic and acoustic data 162
Stratigraphy versus borehole electrical methods 164
Stratigraphy and hydrogeological data 167
Conclusion 168
References 169

Chapter 9 • The Deffend hydrogeological model 173
T. Gaillard
Hydrogeological knowledge before Hydrogeological Experimental Site (HES) of Poitiers 173
Historical groundwater flow model of the Poitou Threshold 173
The Poitiers HES groundwater model 175
Karst dating 176
Syngenetic karstification hypothesis 178
Conclusion 182
References 182

Conclusion 187
J.-L. Mari and T. Gaillard

Acknowledgements 191
J.-L. Mari and T. Gaillard

Prefaces

In 1995, the DATAR (French Delegation for Regional Planning and Development) commissioned researchers from the University of Poitiers to design scientific activities related to the planned underground laboratory for radioactive waste storage, located in the southern part of the Vienne department. Drawing on the expertise I had acquired during my doctoral research at the Béthune study site—developed under the supervision of Professor Norbert Crampon—and on the data already collected in southern Vienne, I naturally proposed the creation of an ambitious hydrogeological study area. However, due to the high degree of fracturing in the granitic bedrock, the National Evaluation Commission issued an unfavorable opinion regarding the siting of the underground laboratory.

It was within this context that the Hydrogeological Experimental Site (HES) project was born. Submitted as part of the 2000–2006 State–Region planning contract to the Ministry of Research, the project was accepted and received funding of 13 million French francs. The first borehole was drilled in July 2002. By 2025, the HES comprised 45 boreholes spread over 32 hectares, traversing fractured and karstified limestone aquifers of the Lower and Middle Jurassic, with a thickness of 160 meters.

Today, the HES stands as a unique experimental platform in France, open to the entire scientific community. It supports research projects, both initial and ongoing education programs, and serves as a testing ground for various disciplines, including pedology, geology, geophysics, hydrogeology, hydrogeochemistry, and numerical modeling. For over twenty years, this infrastructure has enabled significant advances in the understanding of the structure, behavior, and dynamics of carbonate reservoirs.

I am particularly pleased by the fruitful collaboration between Thierry—a passionate geologist and Jurassic specialist—and Jean-Luc, a geophysicist involved with the HES from its inception. Together, they have produced a major work that skillfully combines their respective expertise to improve our understanding of the structural organization of the limestone reservoir. The detailed characterization of Middle

© EDP Sciences, 2026
DOI: https://doi.org/10.1051/978-2-7598-3934-6.c901

Jurassic lithology, combined with a diverse geophysical approach, made it possible to identify the karstic levels responsible for the rapid flows observed at the site.

Throughout the nine chapters, readers are guided toward a coherent and well-supported representation of the reservoir structure, where variations in carbonate chemistry (pure limestone vs dolomitized limestone) emerge as key drivers of karstification. Within the 100-meter-thick section under study, three horizontal productive levels have been clearly identified, representing priority targets for the sustainable extraction of groundwater resources.

Pr. Gilles POREL
Head of the hydrogeological experimental site
at the University of Poitiers

It is with genuine satisfaction that I have the privilege, less than a year after the publication of the AGAP notebook *"Geophysics in Geothermal Exploration: a review"*, to write the preface to this new work: *"A New Concept of Karst Development Based on Hydrogeology and Geophysics."*

Once again, the term *"notebook"* hardly does justice to the content, as this is far more than a simple collection of summaries. It is a work of undeniable scientific merit, enriched by clear and visually compelling figures of exceptional quality.

I would like to extend my sincere congratulations to the authors of the nine chapters and express my gratitude to Jean-Luc Mari and Thierry Gaillard. Their respective expertise in geophysics and in the geology of the Poitou-Charente Threshold has ensured a vital coherence in a work that demands true multidisciplinary mastery.

I am highly confident that this "notebook" will be well received by its readers—whether geologists, hydrogeologists, karstologists, geophysicists, or geoscientists in general.

Michel HAYET
President, AGAP Quality

Foreword

T. Gaillard and J.-L. Mari

Based on their experience in geophysics as applied to the oil and gas industry and in the geotechnical and hydrogeological fields, the authors have set out to explain how conventional seismic methods used in exploration or in reservoir geophysics for imaging can be applied to hydrogeological surveys and to site characterizations in the framework of karstified geological formations, using for example the Dogger limestone of the Poitou threshold. After reviewing the current state of geological knowledge of the Poitou threshold, the book aims to describe how 3D seismic surveying, implemented with light seismic spreads, combined with vertical seismic profiles and full waveform acoustic logging, can be used to obtain a very high-resolution 3D block in depth, which points out karstic levels.

The book highlights how seismic imaging, complemented with both a geological study at a regional biostratigraphic scale and sequential sections established from drilling data, can lead to a stratigraphic characterization of the Dogger limestone. The authors propose a coherent karstogenesis scheme, without involving tectonic constraints, of karstogenic horizons in a sequence of carbonate deposits.

In addition to the field study of the Dogger limestone of the Poitou threshold, the authors provide readers with guidelines to carry out a seismic and stratigraphic characterization methodology that can be applied to hydrogeological investigations and reservoir studies.

The authors thank the University of Poitiers for permission to use all the data sets available on the Hydrogeological Experimental Site (HES) of Poitiers, and more specifically Gilles Porel, who promoted their research project.

© EDP Sciences, 2026
DOI: https://doi.org/10.1051/978-2-7598-3934-6.c902

The authors

Thierry Gaillard

Thierry Gaillard is a hydrogeologist trained at the Universities of Bordeaux (ENSEGID) and Jussieu (Paris-Sorbonne). He has spent his career in consulting companies, and since 2017, he has been the CEO of CPGF-HORIZON. Alongside his professional activities, he is an active member of the French chapter of the International Association of Hydrogeologists (IAH) and of several other associations (Association des Géologues du Bassin Parisien, Aquassistance, Société géologique de France). He has worked in France and in several African countries as a consultant or with NGOs (Bénin, Togo, Ivory Coast, Senegal, Niger, Morocco). Email: tgaillard@cpgf-horizon.fr

Jean-Luc Mari

Jean-Luc Mari is a geophysicist with a distinguished career in applied geosciences. A graduate of the Institut de Physique du Globe de Strasbourg and IFP School (Petroleum Geosciences, major in Geophysics, 1978), he joined IFP Energies Nouvelles in 1979 as a research engineer in the Geophysics Department. He led and contributed to key research projects in high-resolution seismic imaging, reservoir monitoring, and borehole tool development, in collaboration with industrial partners such as GDF-Suez, CGG, Total, and ELF Aquitaine.

© EDP Sciences, 2026
DOI: https://doi.org/10.1051/978-2-7598-3934-6.c903

In 1986, he was seconded to ELF Aquitaine, where he focused on reservoir geophysics, before returning to IFPEN in 1987 to join the Reservoir Department. His work notably explored the application of geophysical methods in horizontal wells. In 1994, he became a professor at IFP School and earned his *Habilitation à Diriger des Recherches* (HDR) in Earth Sciences. He also served as a geophysics expert for IFPEN.

A member of the European Association of Geoscientists and Engineers (EAGE), Jean-Luc has been an associate editor for *Near Surface Geophysics*. Now retired from IFPEN, he works as an independent researcher and consultant. He sits on the board of the Association for Quality in Applied Geophysics (AGAP – Association pour la Qualité en Géophysique Appliquée). Jean-Luc Mari is the author and co-author of numerous scientific papers, patents, and educational resources, including textbooks and digital learning tools. In 2010, he was awarded the title of Chevalier in the *Ordre des Palmes Académiques* for his contributions to science and education. Email: jeanluc90.mari@gmail.com

Introduction

T. Gaillard and J.-L. Mari

Geophysical and hydrogeological investigations play a pivotal role in aquifer characterization. Here, we focus on a carbonate limestone aquifer in the Poitou region (France). We show how hydrogeology and geophysics have contributed to revising regional groundwater flow models and have provided significant new insights. The study highlights how a multidisciplinary geoscientific approach, integrating geophysical, hydrogeological, and stratigraphic analyses, can refine and strengthen a groundwater flow model.

The study area is located at a geological transition zone between the Aquitaine and Paris basins in France, known as the Poitou threshold. Chapter 1 of the book provides a geological overview of the threshold. Chapter 2 contains a detailed synthesis of the middle Jurassic limestone stratigraphy, which forms the basis for defining the regional geodynamic context. Particular attention is given to the Poitiers region, including newly developed geological cross-sections that delineate key stratigraphic features in the central part of the threshold. From a hydrogeological perspective, the Poitou threshold exhibits notable karst flows, despite its low hydraulic gradient, the relatively limited limestone thickness compared to the Périgord and Causses regions of the Aquitaine basin, and an altitude that does not exceed 150 m above sea level. Geologists of the 19th and 20th centuries unanimously attributed the origin of these karst systems to fissures formed under tectonic stress. The concepts underpinning the hydrogeology and karst morphology of the Poitou threshold are explored in detail in Chapter 3 entitled "Hydrogeology of the Poitou Threshold."

The traditional understanding has been challenged by recent research conducted on a hydrogeological platform established near Poitiers under the leadership of

© EDP Sciences, 2026
DOI: https://doi.org/10.1051/978-2-7598-3934-6.c904

Gilles Porel: *Le Deffend* Hydrogeological Experimental Site (HES). Spanning an area of 12 hectares and comprising approximately 35 systematically distributed boreholes, the site represents a significant research initiative. The platform and its associated research objectives are detailed in Chapter 4, dedicated to the description of the experimental hydrogeological site: *Le Deffend*.

Among the investigative techniques implemented at the HES, geophysics—particularly seismic methods—holds a central role, offering a renewed perspective on groundwater flow geometry. In exploration geophysics and reservoir studies, seismic methods are primarily used for constructing subsurface models. These techniques are increasingly significant in geotechnical, hydrogeological, and site characterization studies, particularly in the context of seismic hazard assessments. Surface seismic reflection provides a three-dimensional (3D) representation of subsurface acoustic impedance contrasts, either in terms of time or depth. The resulting 3D seismic blocks generate interpretable images that can be used to develop porosity and karst models.

When combined with borehole measurements such as vertical seismic profiles (VSP) in low-frequency ranges (5–200 Hz) and full-waveform acoustic logging in very high-frequency ranges (1–25 kHz), seismic data enable robust estimation of petrophysical parameters, such as seismic porosity. These methods also facilitate the characterization of specific geological attributes, including karstic features. More recently, electrical resistivity tomography (ERT), conducted both at the surface and in boreholes, has been deployed at the *Le Deffend* site, with findings that corroborate the seismic results.

The results of the geophysical investigations are presented across two chapters. Chapter 5 highlights the contributions of various geophysical techniques, including seismic, acoustic, and electrical methods. Chapter 6 is dedicated to a borehole experiment conducted using Electrical Resistivity Tomography (ERT). Based on the geophysical data, a revised geometry of the karstic horizons has been established. Notably, the karstic horizons within the Middle Jurassic limestones were found to be sub-horizontal rather than vertical, challenging hydrogeological interpretations from the 19th and 20th centuries regarding the karstification process.

To assess the implications for groundwater flow, logging and tracer tests were conducted alongside initial pumping tests. Pumping and hydraulic slug tests were used to evaluate the interference geometry between boreholes. These tests were initially aimed at identifying a preferential fracturing pattern shaped by the tectonic constraints of the Poitou threshold. However, the three-dimensional seismic block revealed the sub-horizontal geometry of the karst levels, leading to a re-evaluation of hydrogeological flow patterns and the development of a new conceptual model, referred to as the "Le Deffend model." Details of the logging and hydrogeological tests performed at the site are presented in Chapter 7 entitled "Hydrogeological flow logging and dye tracer tests.

The origin of the karstic horizons was also reexamined. While the distribution of karst horizons in limestone massifs is often considered random, a detailed stratigraphic

analysis was conducted at this site. The analysis included core sampling and optical televiewer (OPTV) imaging from open-hole drilling. These efforts, outlined in Chapter 8 entitled "Hydro-Stratigraphic study," made it possible to clarify the stratigraphic controls on the distribution of karstic horizons in the *Le Deffend* model.

The *Le Deffend* model was subsequently integrated into a geodynamic framework. The results suggest that the distribution of karstified strata is closely tied to low stand system tracts (LST) within a broader depositional sequence affected by sea-level fluctuations. This geophysical and stratigraphic reinterpretation has significant implications for groundwater resource exploration and preservation. These findings are detailed in Chapter 9, "Hydrogeological Model of the *Le Deffend* site (HES)."

The book aims to demonstrate that seismic attributes derived from 3D seismic blocks and other geophysical methods can effectively characterize karstic horizons within carbonate sequences through stratigraphic interpretation. Beyond advancing geophysical methods, the research conducted at the Le Deffend site over two decades provides actionable insights for preserving drinking water resources in the region. It underscores the necessity of controlling water well stratigraphy and borehole completion to optimize groundwater resource management. This collaborative effort between scientists and engineers serves as a model for how applied geophysics can support hydrogeologists, engineers, and policymakers in sustainably managing groundwater resources amidst challenges such as scarcity and pollution.

1

The Poitou Threshold

T. Gaillard and P. Branger

Location and definition

The Poitou region is a natural area located between the Paris and Aquitaine basins, and between the Massif Central and the southeastern terminus of the Armorican Massif (France). This unique geographical configuration has led Poitou to be alternatively conceptualized as a strait (Longuemar, 1870; Welsch, 1892; Fournier, 1888) or as a threshold (Welsch, 1892; Gabilly, 1962).

The term "strait" refers to the marine channel that once connected the Paris and Aquitaine basins, while the term "threshold" denotes a region of intermediate elevation located between higher and lower elevations. From a geological perspective, the Poitou region is characterized as a strait, whereas geographers consider it a threshold. Both terms describe the same physical reality. "Geologists refer to this region as the Poitou Strait to indicate its role in connecting the sedimentary formations of the Paris Basin with those of the Aquitaine Basin. This concept of a strait stems from the interpretation that the Jurassic deposits of the Poitou Threshold represent sediments from a marine channel or strait extending between the Paris and Aquitaine basins" (Welsch, 1903).

Welsch further elaborates: "Since the region around Poitiers is, in fact, a zone of lower elevation relative to the Limousin and Vendee areas that it separates, it is appropriate to designate it as the Poitou Threshold".

The threshold is thus defined by its intermediate elevation, its position between low-lying sedimentary basins and higher ancient massifs (Fig. 1). This geographical definition was adopted by Welsch, who described Poitou as "a vast plateau

© EDP Sciences, 2026
DOI: https://doi.org/10.1051/978-2-7598-3934-6.c001

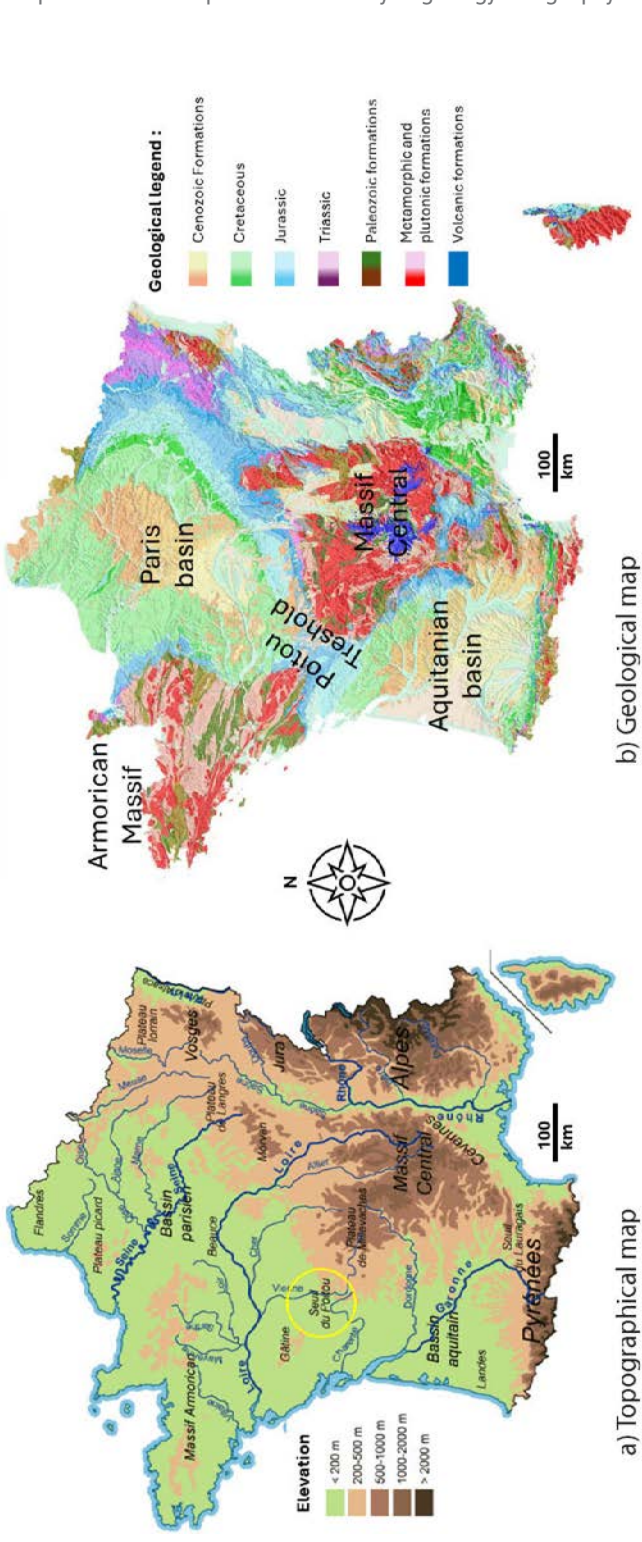

Figure 1 *Poitou threshold location.*

encompassing most of the Vienne department, the southern part of Deux-Sèvres, and the northern part of Charente. Its average elevation is 146 meters above sea level, with a gradual rise to the east and southeast toward Limousin, reaching 200 meters at Lathus and 225 meters beyond Isle-Jourdain. To the west, the elevation against the Vendée Massif reaches altitudes of 160 to 190 meters" (Welsch, 1892). The adoption of these concepts likely reflects the influence of geographical studies, particularly the maps produced by Vidal-Lablache, which were widely employed in educational settings during the French Third Republic. But the topographic approach suffers from the fact that no elevation was selected to define the threshold's limits/boundaries.

Tectonic structure of the Poitou Threshold: a brief history of knowledge

Welsch (1846, 1892) proposed the first tectonic structure of the Poitou Threshold, including two cross-sections: one cross-section that links the old Hercynian Mountain ranges and another that links the sedimentary basins (see Fig. 2 and 3).

In the first cross-section (Fig. 2), Welsch noted only one fault: the Montalembert Fault, located south of the Deux-Sèvres department. The bedrock includes two major anticlines that connect ancient massifs: the Champagné-Saint-Hilaire anticline and the Ligugé anticline. The Poitou area was described as a strait (isthme in French on Fig. 2).

The second cross-section (Fig. 3) links the Armorican and Limousin massifs, showing sub-horizontal sedimentary layers between Ménigoute (West) and Availles-Limouzine (East). The bedrock crops out at both ends. In this figure, the Poitou area was identified as a threshold (Seuil in French in Fig. 3).

Glangeaud's observations refined earlier interpretations by identifying faults that isolate the Champagné-Saint-Hilaire anticline from "collapsed layers" (Glangeaud, 1895). Fournier (1903) later produced a geologic map of the Poitou Threshold. After World War I, Mathieu (1937) conducted additional structural studies for his thesis on Paleozoic terrains in the Vendée region. He identified structural links between the Limousin and Gâtine Hills, revisiting the mapped features of Welsch. Mathieu described four major structural axes, listed from north to south (Fig. 4): A4 – the Ligugé Anticline; A3 – an anticline extending from Le Fouilloux, through Lusignan and Champagné-Saint-Hilaire to Availles-Limouzine; A2 – The Rouillé-Couhé-Civray Axis (also called the Saint-Sauvant Anticline), and A1 – a complex anticline connecting Mervent to the Montalembert Horst.

Axes A5 and A6 were not traced further east due to a lack of structural markers. The major axes were later integrated into the regional geological guide (Gabilly et al., 1978) under the names Essarts-Mervent-Melle-Montalembert Anticline (A1)

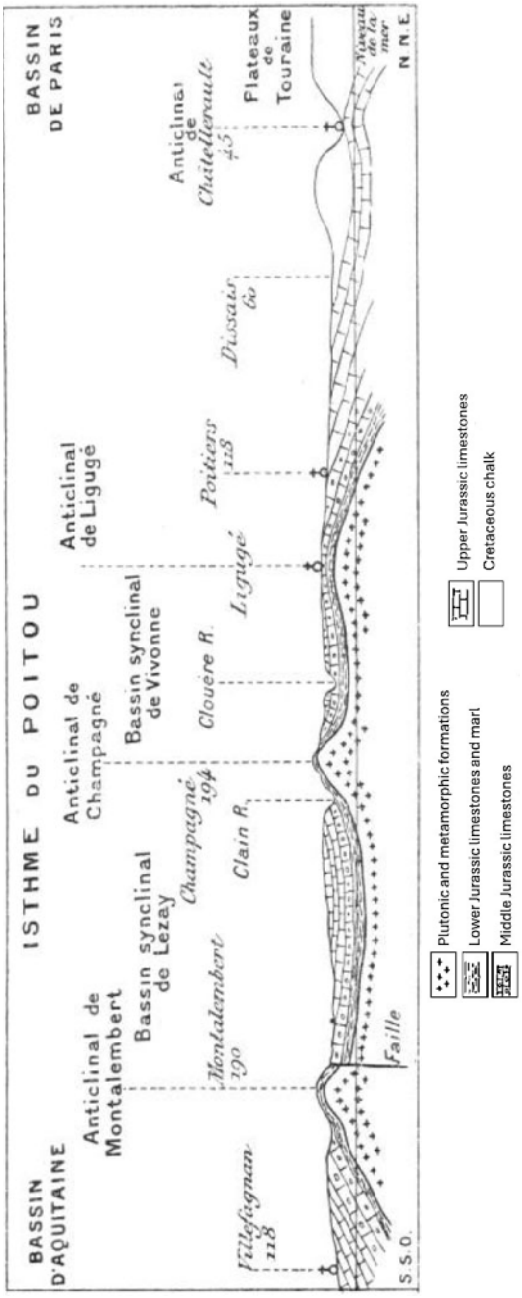

Figure 2 *SSW-NNE cross-section connecting the Aquitaine basin to the Paris basin (Welsch, 1892).*

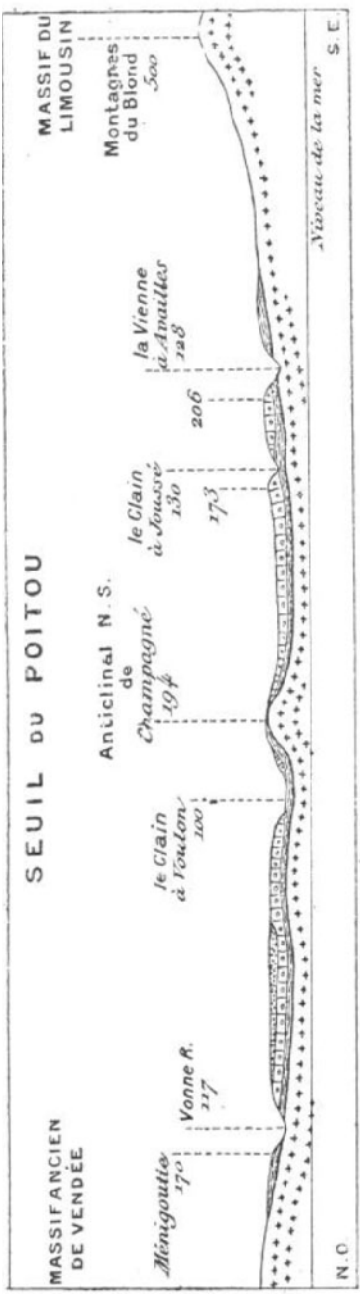

Figure 3 *NW-SE cross-section connecting the Armorican and Limousin massifs (Welsch, 1892).*

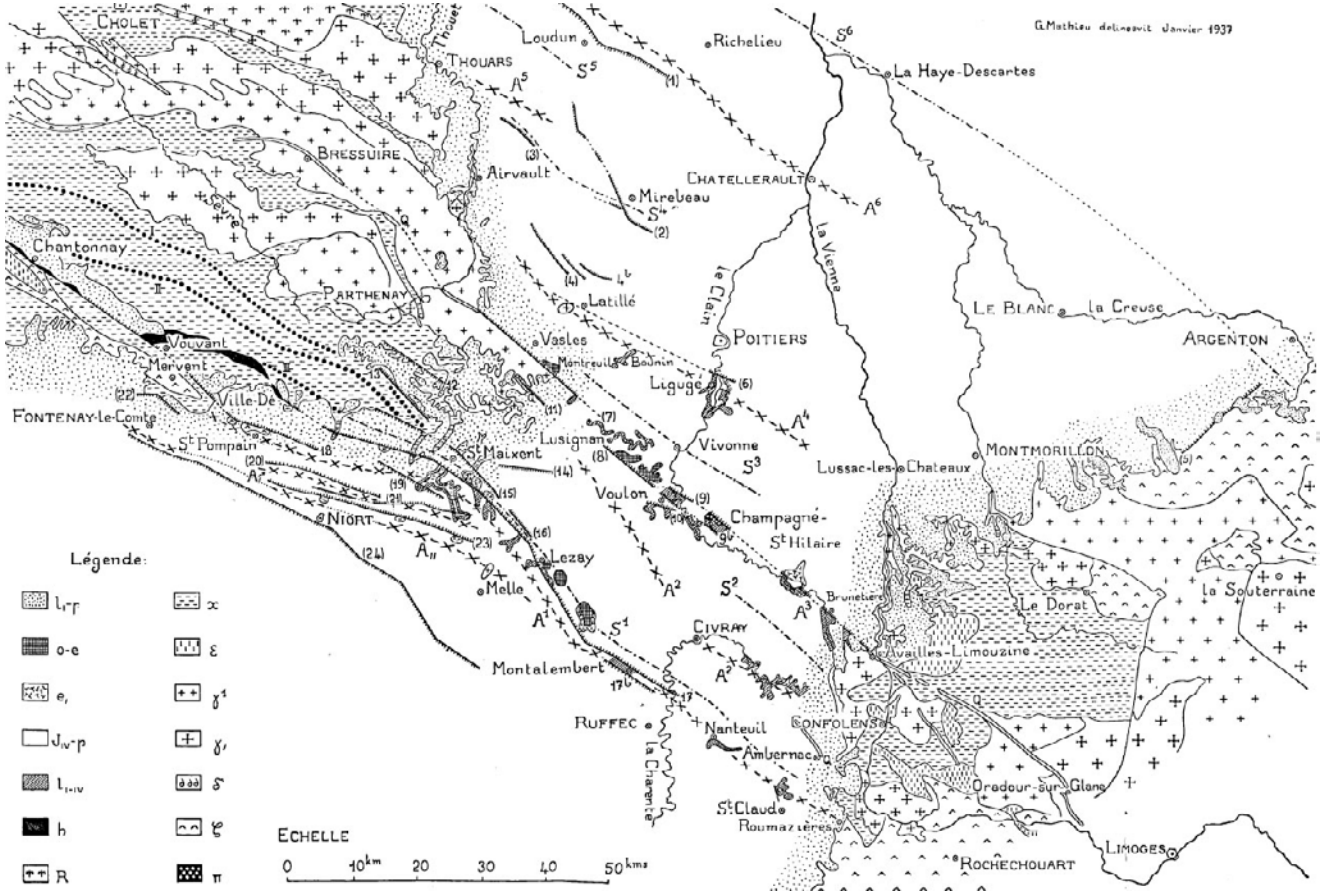

L1-p: Triassic formations; o-e: *"siderolic"* formation (clay with ferruginous pisolite), e = lacustrine marl (Eocene); JIV-p: Mesozoic limestones, L1-IV: lower Jurassic formations; h: "houiller" = coal formations; R: rhyolite of Cholet; x: shists; ε: amphibolite; γ1: granulite; γ2: granite; δ: diorite; ξ: gneiss; π porphyry; Q: quartz - A: anticline, S = syncline.

Figure 4 *Structural axes of the Poitou threshold by Mathieu (1937, p. 289).*

and Champagné-Saint-Hilaire Anticline (A3). This structural framework, based on a model of parallel fault alignments extending from the Limousin to the Vendée along a south-Armorican trend N120°E/N140°E (Fig. 5), prevailed until the early 1990s.

In the 1980s, this structural model was reinforced by the identification of the Limousin Tonalitic Line (LTL) linking the Parthenay Massif to Limousin granites and the Availles-Limouzine Fault (Dhoste, 1983; Peiffer, 1987; Cuney et al., 2001). North of the threshold, the Marche Fault line is well documented only in the southern Berry area. This fault system between the Massif Central and the Paris basin was long unknown westward beneath the Poitou Threshold. Early indications came from gravimetric anomalies (Goguel, 1954) and a magnetic anomaly map of the Paris Basin (Debeglia, 1980).

Figure 6 shows the correspondence between mapped faults and the gravity map of Martelet et al. (2009). The light gravimetric anomaly indicates the Eo-Variscan suture between Gondwana (or Central Armorica) and Laurussia and appears to cross the threshold without faulting in the sedimentary coverage. This contact is also highlighted by a negative Bouguer anomaly (Baptiste, 2017). The Nort-sur-Erdre Fault marks the Ligérienne Province boundary and coincides with the light Bouguer anomaly. This fault is interpreted as an Eo-Variscan suture (Dercourt, 1998) and extends towards the Loudun fault.

Goguel's (1954) heavy gravimetric anomaly north of Poitiers is aligned with the eastern extension of the Thouars fault (Weber, 1973). This anomaly corresponds to a contact of Jurassic and Upper Cretaceous sediments, suggesting that the Thouars fault is a heritage that gave rise to the Thouars granitic intrusion. The Mirebeau fault is aligned with the Thouars fault. However, no faults are mapped east of Mirebeau on the Vouneuil-sur-Vienne geological map (Bourgueil et al., 1976). Seismic activity in this area (e.g., a magnitude 3.2 earthquake in Saint-Léger-La-Pallu on June 14, 2019) reinforces the hypothesis of a fault that extends from the Armorican Massif and is masked by Eocene formations.

Further studies, including a study on the Parthenay Fault (Poncet, 1993) and ANDRA's recognition of the Charroux Granite in the late 1990s, revised the structural map of the bedrock of the Poitou Threshold. These studies revealed three main structures originating from the Armorican Massif (Fig. 7):

(i) the Vasles-Availles Fault Zone, passing through Champagné-Saint-Hilaire (formerly the Pouzauges-Oradour axis of Cariou et al., 1989);

(ii) the Parthenay Fault, trending N160°E, which connects to the Saint-Maixent and Lezay grabens rather than the Vasles Fault and Champagné-Saint-Hilaire Horst (Poncet, 1993; Cuney et al., 2001; Rolin and Colchen, 2001);

(iii) the Basse Marche Fault, south of Poitiers, is linked to the Ligugé Granite and extends to the Thouars Fault (Rolin and Colchen, 2001) via the Mirebeau fault.

Rolin et al. (2009) consider these fault systems to be shear zones. Figure 7 is a schematic map of Paleozoic faults and granites from Rolin and Colchen (2001) and

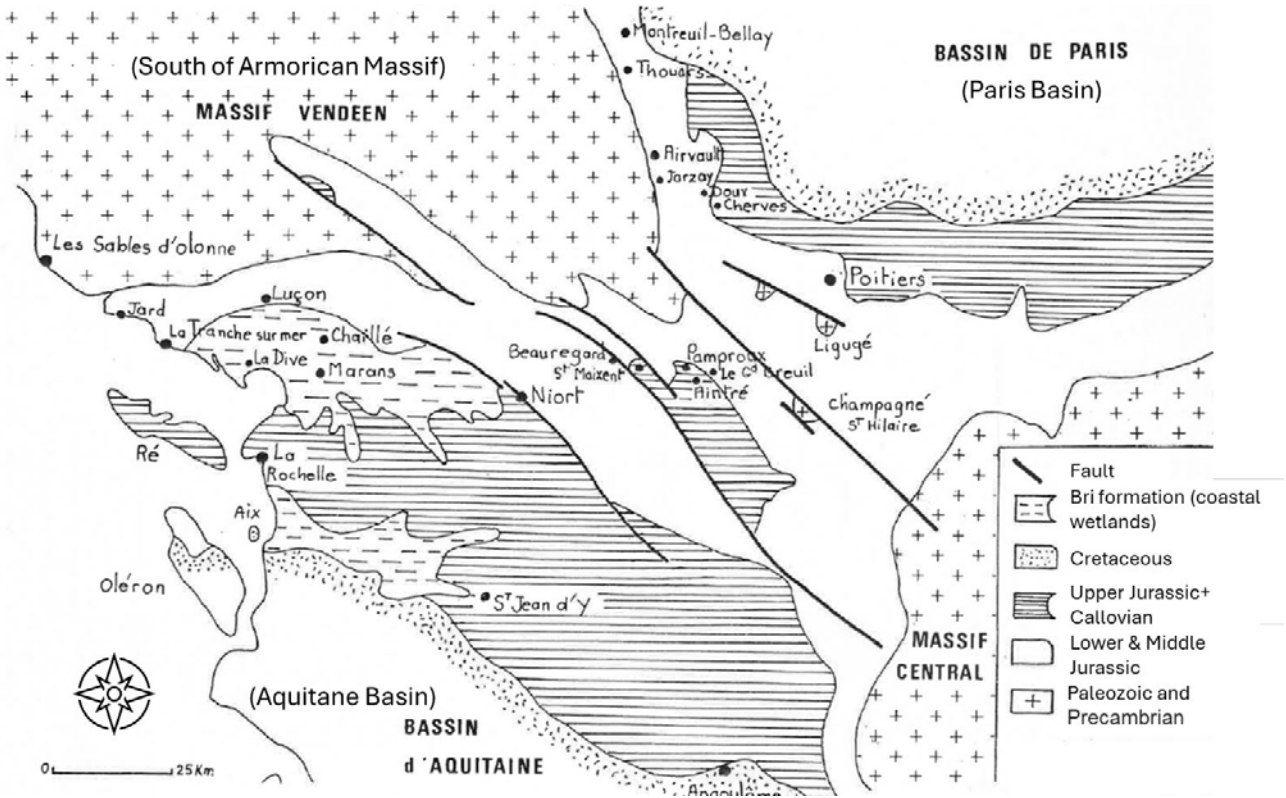

Figure 5 *Poitou threshold structure (from Gabilly and Cariou, 1974)*

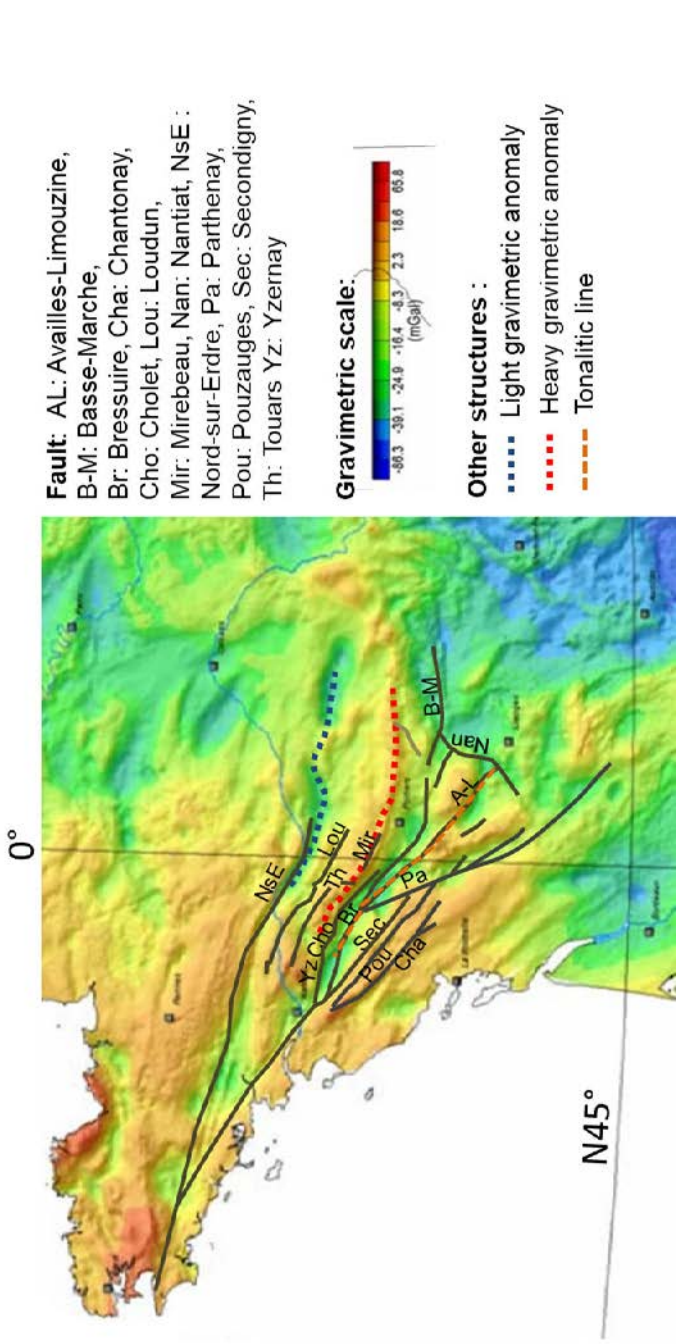

Figure 6 *Fault system and gravimetry map (from Martelet et al., 2009).*

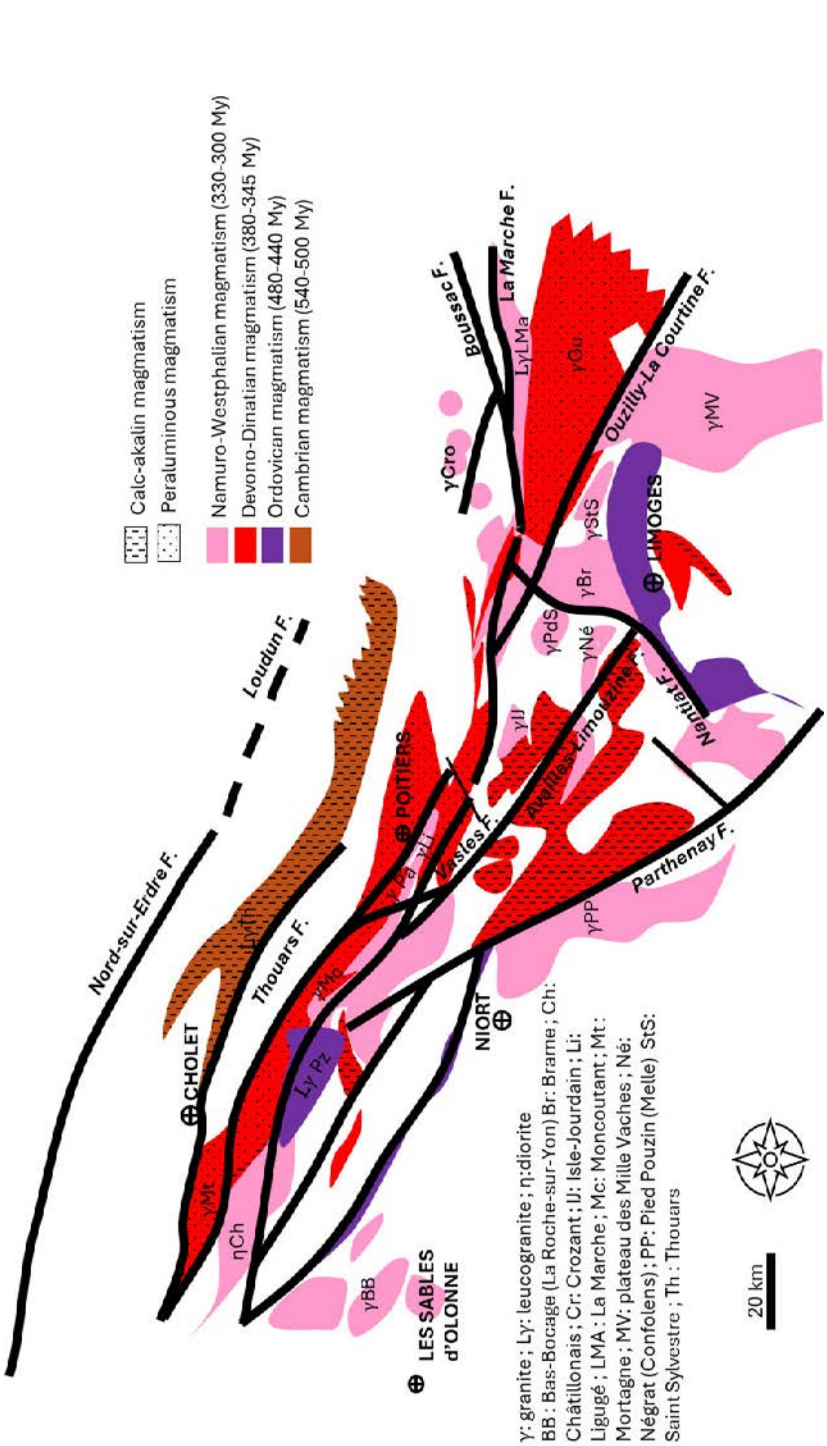

Figure 7 *Schematic map of Paleozoic faulting and calc-alkaline magmatism.*

Rolin (2001). Granites intruded the Paleozoic sediments during the Cambrian, Ordovician, Devonian-Visean, and Namurian-Westphalian (Carboniferous). The primary granitic intrusion activity occurred between the Devonian and the Westphalian (Moscovian). Calc-alkaline magmas may be the result of the fusion of a mantle layer intruded into the tectonics of the threshold between the Parthenay fault and the Vasles-Availles fault (Rolin et al., 1999).

Sedimentary coverage

Granites and Paleozoic metamorphic formations make up the bedrock that is covered by Jurassic formations. Triassic sediments are located only at the threshold border (Infra Lias clay in the Aquitanian basin and arkose in the Paris basin).

During the Early Jurassic (Sinemurian and Hettangian), shallow marine environments dominated the Poitou Threshold. The sediments consist primarily of shallow marine carbonates. During this period, three sedimentation areas were active: (i) the Atlantic area west of Fontenay-le-Comte, (ii) a Vendean area between Fontenay-le-Comte and Thouars, and (iii) the "Pictave" area around Poitiers (Gabilly and Cariou, 1974). The Toarcian is marked by the deposition of dark, organic-rich marls and shales, indicative of deeper, more anoxic conditions associated with the global Toarcian Oceanic Anoxic Event (TOAE).

Between the Aalenian and the Callovian, sedimentation transitioned to shallow marine carbonate platforms. These include micritic limestones, bioclastic limestones, oolitic limestones, and occasional reefal buildups. The Oxfordian is represented by limestones in the Pictave area. The sedimentary facies are marly from the Vendean to the Atlantic area. During the middle Jurassic, the sedimentation area was limited by the fault(s) inherited from Paleozoic tectonics (Mourier and Gabilly, 1985).

Fossils, particularly ammonites and brachiopods, are critical for establishing relative ages due to their stratigraphic distribution and global correlation. While ammonite dating is accurate towards the basins, the scarcity of pelagic fauna in the middle of the Poitou threshold makes dating a delicate matter. For this reason, Gabilly studied signs of exposure and erosion registered in limestones and the biozone gap (Gabilly, 1962). This evidence is used to make correlations between the Poitou threshold and the Aquitanian basin margin (Gabilly et al., 1985).

Gabilly et al. (1978) proposed a cross-section of the Poitou threshold, which is still valid (Fig. 8). The threshold affects sedimentation in several ways. The first is a thinning of the geological layers. The second is a facies variation, with carbonate facies on the threshold and marly facies towards the basins. The anticlines and synclines of the cross sections are associated with the fault system shown in Figure 8. No faults were identified as being related to the Paris Basin.

As a result of the new fault pattern shown in Figure 7, the facies distribution of the middle Jurassic deposits could be revised. For example, Figure 9 shows the facies distribution during the upper Bathonian, as mapped by Gabilly et al. (1978). With

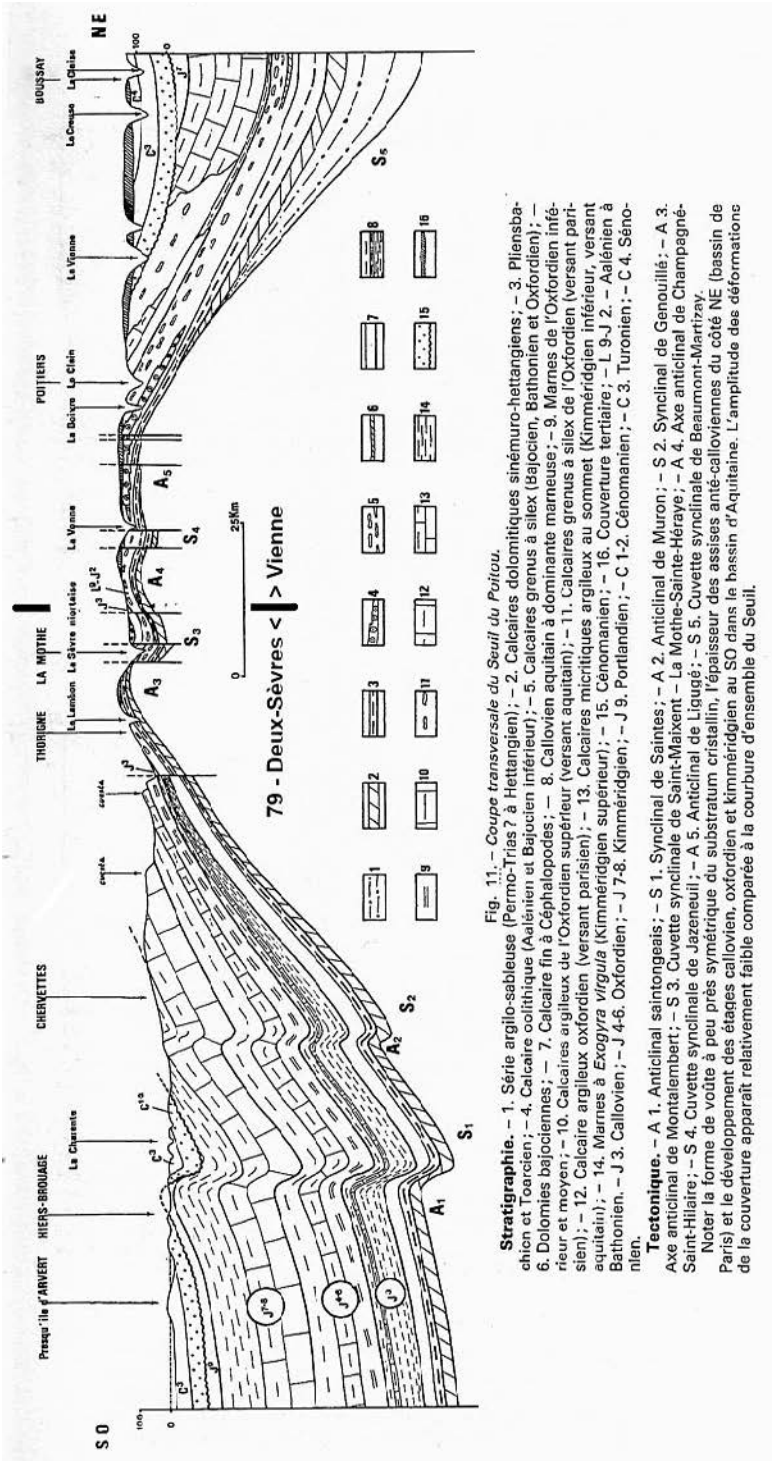

Fig. 11. – *Coupe transversale du Seuil du Poitou.*

Stratigraphie. – 1. Série argilo-sableuse (Permo-Trias ? à Hettangien) ; – 2. Calcaires dolomitiques sinémuro-hettangiens ; – 3. Pliensbachien et Toarcien ; – 4. Calcaire oolithique (Aalénien et Bajocien inférieur) ; – 5. Calcaires grenus à silex (Bajocien, Bathonien et Oxfordien) ; – 6. Dolomies bajociennes ; — 7. Calcaire fin à Céphalopodes ; — 8. Callovien aquitain à dominante marneuse ; – 9. Marnes de l'Oxfordien inférieur et moyen ; – 10. Calcaires argileux de l'Oxfordien supérieur (versant aquitain) ; – 11. Calcaires grenus à silex de l'Oxfordien (versant parisien) ; – 12. Calcaire argileux oxfordien (versant parisien) ; – 13. Calcaires micritiques argileux au sommet (Kimméridgien inférieur, versant aquitain) ; – 14. Marnes à *Exogyra virgula* (Kimméridgien supérieur) ; – 15. Cénomanien ; – 16. Couverture tertiaire ; – L 9-J 2. – Aalénien à Bathonien. – J 3. Callovien ; – J 4-6. Oxfordien ; – J 7-8. Kimméridgien ; – J 9. Portlandien ; – C 1-2. Cénomanien ; – C 3. Turonien ; – C 4. Sénonien.

Tectonique. – A 1. Anticlinal saintongeais ; – S 1. Synclinal de Saintes ; – A 2. Anticlinal de Muron ; – S 2. Synclinal de Genouillé ; – A 3. Axe anticlinal de Montalembert ; – S 3. Cuvette synclinale de Saint-Maixent – La Mothe-Sainte-Héraye ; – A 4. Axe anticlinal de Champagné-Saint-Hilaire ; – S 4. Cuvette synclinale de Jazeneuil ; – A 5. Anticlinal de Liguré ; – S 5. Cuvette synclinale de Beaumont-Martizay.

Noter la forme de voûte à peu près symétrique du substratum cristallin, l'épaisseur des assises anté-calloviennes du côté NE (bassin de Paris) et le développement des étages callovien, oxfordien et kimméridgien au SO dans le bassin d'Aquitaine. L'amplitude des déformations de la couverture apparaît relativement faible comparée à la courbure d'ensemble du Seuil.

Figure 8 *Cross-section of the Poitou threshold (Gabilly et al., 1978).*

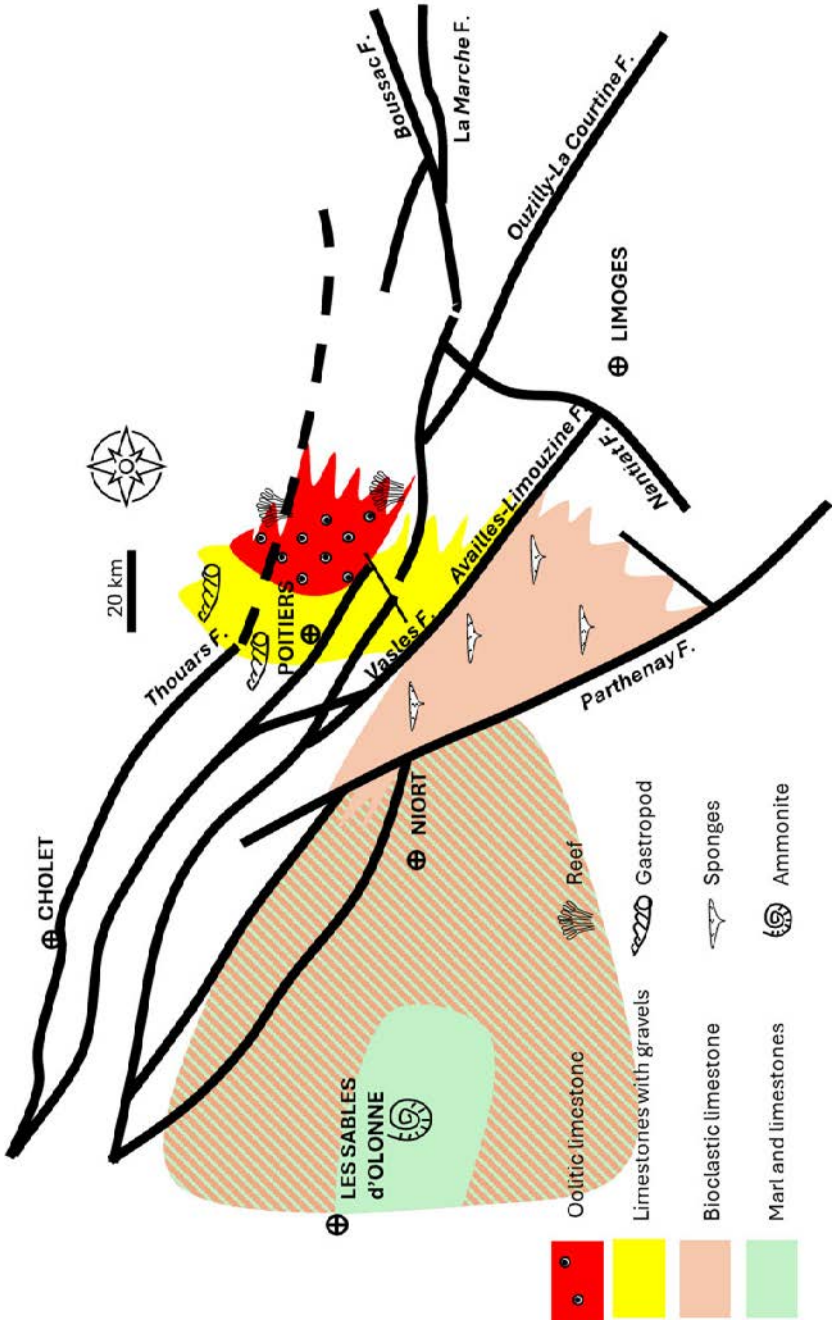

Figure 9 *Facies distribution during the upper Bathonian (from Gabilly et al., 1978).*

the proposed schematic fault map, the various areas of sedimentation are superposed onto tectonic blocks. High-energy facies (oolitic limestones) were placed between the faults that delimit the Pictave block. Gravelly limestones that extended to the west were pinched out against the Vasles-Availles fault. Bioclastic limestone with sponge beds was confined to the area between the Vasles-Availles fault and the Parthenay fault. To the west of the Parthenay fault, sedimentation was marly.

Poitou threshold definition

Gabilly et al. (1978) mapped the facies distribution for the Toarcian, lower Bajocian, and Callovian. Mourier and Gabilly (1985) mapped it in the Vienne and Charente valleys. The pattern of the fault system is similar to Figure 9.

The northern axis, which better limits the extension of high-energy facies, corresponds to the gravity anomaly parallel to the Thouars-Mirebeau fault. Sedimentation north of the Vasles-Availles-Limouzine axis is a carbonate platform environment, while to the south it becomes openly marine; this is the Vendean domain (Gabilly and Cariou, 1974; Mourier, 1983; Branger, 1989). The Vasles-Availles axis (roughly equivalent to the Pouzauges-Oradour axis of Gabilly, 1962; Mourier 1983; Branger, 1989) marks the end of the Poitevin Strait and the beginning of the Aquitaine Basin.

Defined in this way, the Poitou threshold appears to be a mid-Jurassic shoal, with the northern and southern limits of the platform aligned with the structuring axes inherited from the basement. The shorelines are controlled by these granitic horst sets from the Toarcian to the Bathonian. The platform continues into the Bajocian and Bathonian towards Berry. In the Callovian, however, the inherited higher elevations no longer seem to constrain sedimentation, and the gap in some Callovian ammonite zones extends over a vast plateau (Cariou, 1980). Although some authors have sometimes compared the Poitou threshold to a vast NW-SE anticline with a large radius of curvature (Gabilly, 1978), the geometry of the strata is sub-horizontal and is offset by normal faults. In fact, the geometry of the limestone strata on the Poitou platform conforms to cycles of sea-level variation and the creation of available space for proximal and distal depositional facies (Mourier, 1983; Branger, 1989; Gonnin et al., 1992). Based on structural maps, it is possible to give a purely geological definition to the Poitou Threshold as the region between the Thouars-Mirebeau fault to the north and the Vasles-Champagné-Saint-Hilaire-Availles-Limouzine axis to the south (Fig. 10). The advantage of this proposal is that it also represents the platform of the Pictave domain during the Jurassic (Gabilly and Cariou, 1974; Mourier and Gabilly, 1985).

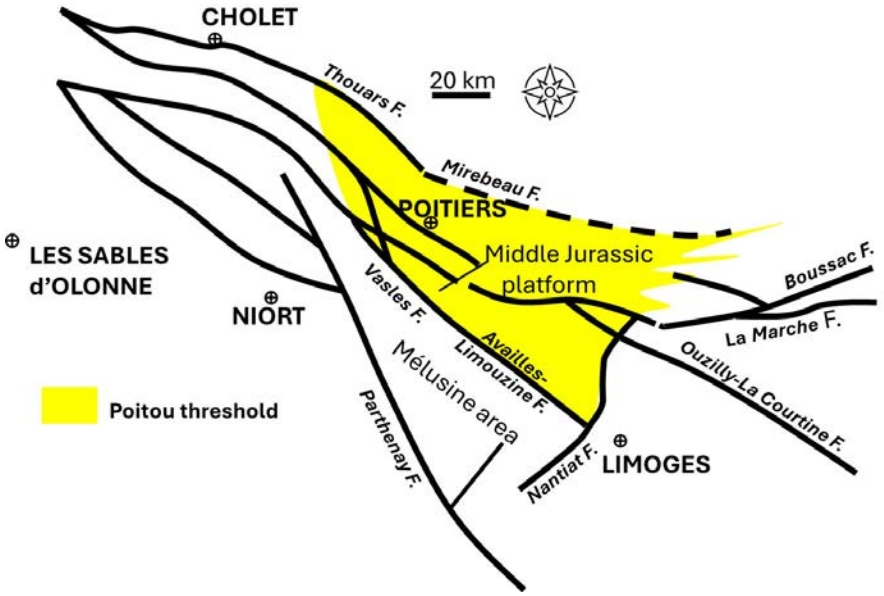

Figure 10 *The Poitou threshold defined by Dogger basement structure and platform facies.*

References

Baptiste J. (2017). Cartographie structurale et lithologique du substratum du Bassin parisien et sa place dans la chaîne varisque de l'Europe de l'ouest: approches combinées géophysiques, pétrophysiques, géochronologiques et modélisations 2D [Structural and lithological mapping of the bedrock of the Paris Basin and its place in the Variscan chain of Western Europe: combined geophysical, petrophysical, geochronological and 2D modelling approaches]. Ph.D. thesis, University of Orléans, France.

Bourgueil B., Cariou E., Moreau P., Ducloux J., Teissier J.-L. (1976). Carte géologique de la France au 1/50000: feuille de Vouneuil-sur-Vienne [1:50,000 geological map of France: Vouneuil-sur-Vienne sheet], BRGM, n° 567.

Branger P. (1989). La marge Nord-Aquitaine et le seuil du Poitou au Bajocien: stratigraphie séquentielle, évolution biosédimentaire et paléogéographie [The North Aquitaine margin and the Poitou Threshold in the Bajocian: sequence stratigraphy, biosedimentary evolution and palaeogeography]. Ph.D. thesis, University of Poitiers, France.

Cariou E. (1980). L'étage Callovien dans le centre-Ouest de la France, première partie: stratigraphie et paléogéographie [The Callovian stage in central-western France, part 1: stratigraphy and palaeogeography]. Ph.D. thesis, University of Poitiers, France.

Cariou E., Hantzpergue P., Jan Du Chene R., Vail P. (1989). Excursion in the Jurassic of the Charentes and Poitou area (France). University of Poitiers, France, STATOIL.

Cuney M., Brouand M., Stussi J.-M. (2001). Le magmatisme hercynien en Vendée. Corrélations avec le socle du Poitou et l'ouest du Massif Central français [Hercynian magmatism in the Vendée. Correlations with the Poitou basement and the west of the French Massif Central]. *Géologie de la France*, 1/2: 117-142.

Debeglia N. (1980). Carte du socle, écorché anté-triasique [Base map, Ante-Triassic crust], in Synthèse géologique du Bassin de Paris, sous la direction de C. Mégnien (Vol. III). Mémoire BRGM, n° 102.

Dhoste M. (1983). Prolongement en Poitou de la ligne tonalitique limousin [Extension of the Limousin tonalite line into Poitou]. *Compte Rendu de l'Académie des Sciences*, 2(296): 1659-1662.

Fournier A. (1888). Documents pour servir à l'étude géologique du détroit poitevin [Documents for the geological study of the Poitevin Strait]. *Bulletin de la Société Géologique de France*, 3e série (XVI): 113-182.

Fournier, A. (1903). Les maladies typhoïdes, L'hygiène et le sol en Poitou [Typhoid diseases, Hygiene and soil in Poitou]. Blais et Roy, Ed.

Gabilly, J. (1962). Les variations de sédimentations du Lias et du Jurassique en relation avec le seuil du Poitou [Variations in Lias and Jurassic sedimentation in relation to the Poitou Treshold]. 87e Congrès des Sociétés Savantes, colloques sur les seuils en géologie (Poitiers): 679-699.

Gabilly J., Cariou E. (1974). Groupe Français d'études du Jurassique: Journée d'études et excursion en Poitou 14-15-16 et 17 octobre 1974. Livret guide. University of Poitiers.

Gabilly J., Brillanceau A., Cariou E., Ducloux J., Dupuis J., Hantzpergue P., Moreau P., Santallier P., Ters M. (1978). *Guides géologiques régionaux: Poitou-Charentes-Vendée* (1re édition). Masson, Ed.

Glangeaud P. (1895). Le Lias et le Jurassique moyen en bordure à l'ouest du plateau central [The Lias and Middle Jurassic on the western edge of the central plateau]. *Bulletin de la Société Géologique de France*, 3e série (XXIII): 10-54.

Goguel J. (1954). Levé gravimétrique détaillé du Bassin parisien [Detailed gravity survey of the Paris Basin]. Mémoire BRGGM n° 12, BRGGM Ed.

Gonnin C., Cariou E., Branger P. (1992). Les facteurs de contrôle de la sédimentation au début du Jurassique moyen sur le seuil du Poitou et ses abords [Factors

controlling sedimentation at the beginning of the Middle Jurassic on the Poitou Treshold and its surroundings*]. Compte Rendu de l'Académie des Sciences*, 135(II): 853-859.

Longuemar (de) A. (Le Touzé) (1870). Études géologiques et agronomiques sur le département de la Vienne [Geological and agronomic studies on the Vienne department]. Conseil Général de la Vienne, Ed.

Martelet G., Pajot G., Debeglia N. (2009). Nouvelle carte gravimétrique de la France, RCGF09 [New gravity map of France, RCGF09]. Réseau et Carte Gravimétrique de la France. BRGM/RP-57908-FR.

Mathieu G. (1937). Recherches géologiques sur les terrains paléozoïques de la région vendéenne. 1er fascicule: stratigraphie et tectonique [Geological research on the Palaeozoic terrains of the Vendée region. 1st part: stratigraphy and tectonics]. Ph.D. thesis, University of Lille, France.

Mourier J.-P. (1983). Le versant Parisien du seuil du Poitou de l'Hettangien au Bathonien. Stratigraphie, sédimentologie, caractères paléontologiques, Paléogéographie [The Parisian slope of the Poitou Treshold from the Hettangian to the Bathonian. Stratigraphy, sedimentology, palaeontological features, palaeogeography]. Ph.D. thesis, University of Poitiers, France.

Mourier J.-P., Gabilly J. (1985). Le Lias et le Dogger au sud-est du seuil du Poitou: tectonique synsédimentaire, paléogéographie [The Lias and the Dogger southeast of the Poitou threshold: synsedimentary tectonics and palaeogeography]. *Géologie de la France*, 3: 293-310.

Peiffer M.T. (1987). La ligne tonalitique du Limousin, sa contribution à la connaissance de la géologie régionale [The Limousin tonalite line and its contribution to our knowledge of regional geology]. *Annales scientifiques du Limousin*, 3: 3-15.

Poncet D. (1993). Le Cisaillement sud-armoricain dans le Haut-Bocage vendéen: analyse pétrostructurale et étude de la déformation dans les granitoïdes et leur encaissant métamorphique [The South Armorican shear in the Vendean Haut-Bocage: petrostructural analysis and study of deformation in the granitoids and their metamorphic setting]. Ph.D. thesis, University of Poitiers, France.

Rolin P., Stussi J.M., Colchen M., Cuney M. (1999). Structuration et magmatisme hercyniens post-collisionnels dans le Confolentais (Ouest du Massif Central) [Post-collisional Hercynian structuring and magmatism in the Confolentais (western Massif Central)]. *Géologie de la France*, 3: 11-31.

Rolin P., Colchen M. (2001). Carte structurale du socle varisque Vendée-Seuil du Poitou-Limousin [Structural map of the Variscan basement Vendee-Poitou Threshold-Limousin]. *Géologie de la France*, 1-2: 3-6.

Rolin P., Marquer D., Colchen M., Cartannaz C., Cocherie A., Thiery V., Quenardel J.-M., Rossi P. (2009). Famenno-Carboniferous (370-320 Ma) strike

slip tectonics monitored by syn-kinematic plutons in the French Variscan belt (Massif Armoricain and French Massif Central). *Bulletin of the Société Géologique de France*, 80(3): 231-246. https://doi.org/10.2113/gssgfbull.180.3.231

Weber C. (1973). Le socle antétriasique sous la partie sud du bassin Parisien d'après les données de géophysique [The anteriassic basement beneath the southern part of the Paris Basin based on geophysical data]. *Bulletin du BRGM*, II(3): 293-343.

Welsch J. (1903). Étude des terrains du Poitou dans le détroit poitevin et sur les bordures du massif ancien de Gâtine [Study of the Poitou terrain in the Poitevin strait and on the edges of the ancient Gâtine massif]. *Bulletin de la société géologique de France*, 3(4): 798-881.

Welsch J. (1892). Essai sur la géographie physique du seuil du Poitou [Essay on the physical geography of the Poitou threshold]. *Annales de Géographie*, 2(5): 53-64.

2

The stratigraphy of the Middle Jurassic

P. Branger, T. Gaillard and H. Geairon

Paleontological division of the Middle Jurassic

Since the end of the Toarcian period, the Poitou threshold and its Parisian and Aquitaine slopes have corresponded to a carbonate platform that persisted throughout the Middle Jurassic (Aalenian, Bajocian, and Bathonian). At that time, Poitou was located at the edge of the Tethys, a vast ocean between Gondwana and Laurasia (Fig. 1).

The first sediments deposited on this platform date back to the Aalenian (174 Ma± in ICS, 2024). Two ammonite lineages are commonly used to date the sediments of this stage: Leioceratinae and Graphoceratinae. The Toarcian-Aalenian boundary is difficult to define paleontologically because the last *Pleydellia* have affinities with the first *Leioceras* (Cariou and Hantzpergue, 1997). In platform regions such as Poitou, the Toarcian-Aalenian boundary is linked to an ecological change with a drop in sea level. The first ammonite zone corresponds to the appearance of *L. opalinum*. This is followed by two species of ammonites that are widespread in Western Europe: *Ludwigia murchisonae* and *Brasilia bradfordensis*, whose horizons determine the Middle Aalenian and are separated by a discontinuity. In Poitou, the Middle Aalenian ends with the *Brasilia gigantea* horizon. The Upper Aalenian corresponds to the appearance of *Graphoceras concavum*.

© EDP Sciences, 2026
DOI: https://doi.org/10.1051/978-2-7598-3934-6.c002

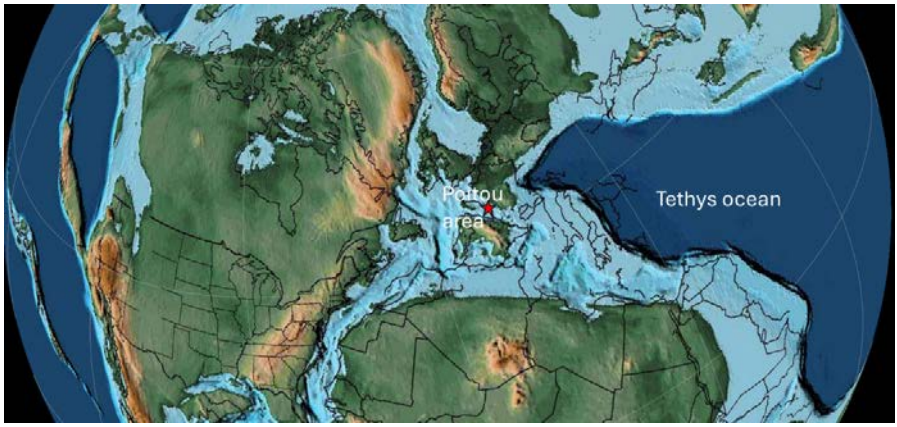

Figure 1 *175 My paleogeographic map of the western Tethys with the Poitou area (GPlates 2.5).*

A major renewal of marine fauna marks the first Bajocian transgression at the boundary between the *Concavum* and *Discites* zones. The carbonate platform is well dated by the Tethyan ammonite fauna in Western Europe, as the boreal fauna did not penetrate the epicontinental seas of the western Tethys. The ammonite zones of the Lower Bajocian are defined by *Hyperlioceras discites, Witchellia laeviuscula, Sonninia propinquans,* and *Stephanoceras humphresianum*.

The Upper Bajocian transgression lies between the *Humphriesianum* zone and the *Niortense* zone. The epicontinental seas underwent a reactivation of the basement faults and an oolitic barrier extending along the Massif Central to the Pyrenees, marking the sedimentation in the Aquitaine Basin (Cariou and Hantzpergue, 1997). The zonation of the Upper Bajocian is based on the ammonites *Strenoceras niortense, Garantiana garantiana,* and *Parkinsonia parkinsoni*.

The appearance of *Zigzagiceras zigzag* marks the base of the Bathonian stage. In Poitou, boreal ammonites (*Gonolkites convergens*) coexist with Mediterranean ammonites (*Morphoceras parvum*). This mixture of fauna is a distinctive feature of this stage. The Lower Bathonian ends with the Procerites aurigerus zone. The Middle Bathonian includes the *Procerites progracilis, Tulites subcontractus, Morrisiceras morrisi*, and *Cadomites bremeri* zones. The Upper Bathonian includes the *Prohecticoceras retrocostatum* zone and the *Clydoniceras discus* zone.

Deposit sequences

The dating of carbonate deposits using ammonite fauna has enabled a detailed reconstruction of the sequence of deposits in the Paris Basin (Rioult et al., 1991). On the Poitou threshold, dating using ammonites is hampered by the rarity of pelagic fauna. Furthermore, the study of Middle Jurassic terrains on the edge of the

Massif Central, particularly in Haut-Poitou, is difficult due to lateral variations in facies (Glangeaud, 1895). Under the impetus of Professor Gabilly, the stratigraphy of the Poitou threshold was revised in the 1970s with the definition of 107 ammonite biozones from the Sinemurian to the Oxfordian (Gabilly and Rioult, 1971; Gabilly and Cariou, 1974). This zoning was clarified using a lithological and sedimentological approach. Even before the advent of sequential stratigraphy, Gabilly understood the importance of taking into account major sedimentary discontinuities and deposit facies (Gabilly, 1962), which were often ignored by earlier authors (Welsch, 1895). The Poitou threshold series was thus revised and divided into 13 sequences separated by discontinuities and presented in 1974 during the excursion organized by Gabilly and Cariou on the Poitou threshold. The comparison of pelagic ammonite zones (Deux-Sèvres and Charente) with the discontinuities separating each sequence made it possible to define a sequential stratigraphy of the Jurassic platform on the threshold where ammonites are rare or even absent in the outcrops studied (Gonnin et al., 1993; Branger and Gonnin, 1994).

Table 1 shows the initial stratigraphic division by Gabilly and Cariou (1974), which was subsequently used in the work of the Faculty of Geology at Poitiers and in the notes on the 1:50,000 geological maps. The numbers of the discontinuities (D6 to D11) are borrowed from the scale used in the work of the University of Poitiers (Mourier, 1983; Gabilly et al., 1985) and follow the logic of the 1974 sequences.

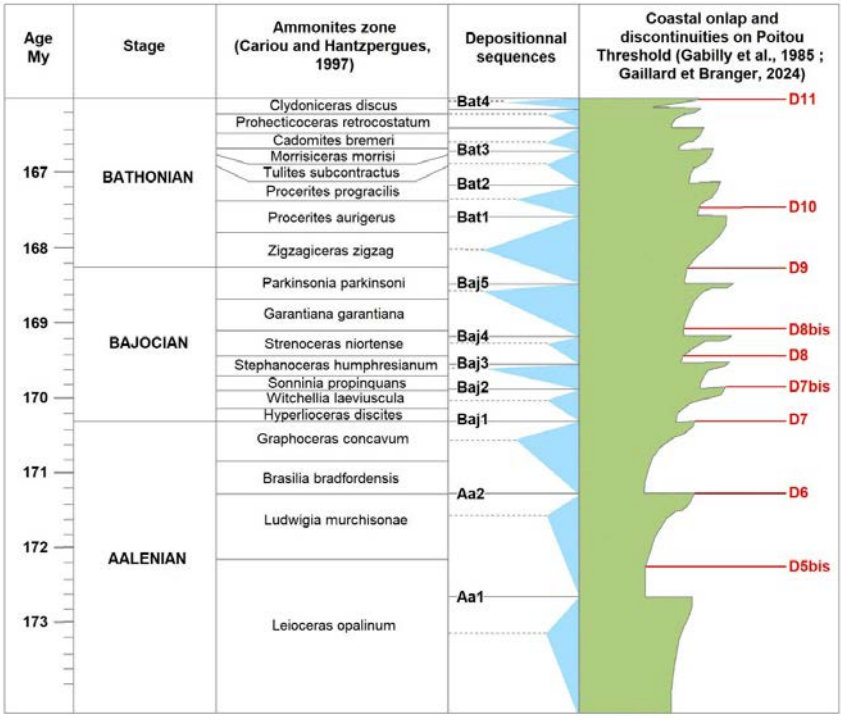

Table 1 *Sequence stratigraphy of the Poitou Threshold.*

With this sequential approach, the deposit sequences of the Poitou threshold can be precisely defined (Table 1). Discontinuities are associated with low sea levels on the eustatic curve. The sedimentary bodies correlate well with the discontinuities for the Aalenian and Bajocian. In the Bathonian, the deposit sequences follow a regressive trend. On the Poitou threshold, the determination of sequences with discontinuities is less precise.

Stratigraphy of the Middle Jurassic on the Poitou Threshold

Starting in the Early Jurassic period, the Poitou Threshold and its surroundings were gradually invaded by an epicontinental sea connected to the western Tethys Sea to the southeast. Throughout the Middle Jurassic, the region was a depositional area whose general physiography, inherited from the Permian-Triassic differential erosion of its Hercynian basement, allows several distinct areas to be identified. In simplified terms, an axis running from Pouzauges to Oradour-sur-Glane (Gabilly et al., 1978) separates, to the northeast, a shallow domain with abundant carbonate sedimentation and benthic fauna from a deeper domain to the southwest, where sedimentation was less abundant but often accompanied by a rich pelagic fauna of ammonites. This Pouzauges-Oradour-sur-Glane axis corresponds fairly closely to the Vasles fault line, which runs along the Nantes-Parthenay granite axis towards the Champagné Saint-Hilaire horst and the Availles-Limouzine fault (see southern limit in Gaillard and Branger, 2026). In detail, the shallowest deposits were formed on the northwestern edge of the Massif Central, which at that time formed a carbonate aureole bordering the central platform. The eastern edge of the Vendée Massif, also shallow, appears as a shoal backing onto the Armorican Landmass. These two areas are connected by the Pictavian domain. To the south of the paleogeographic axis lies the Melusine trough (see Gaillard and Branger, 2026), a depressed area linking the northern edge of the Aquitaine Basin, which can be traced as far as the Vendée coastline. The remarkable permanence of these sedimentary domains can be explained by low accumulation of deposits and the stability of the geological bedrock. Indeed, during this interval, the remobilization of the main Hercynian tectonic axes according to a tilted block model, which was paleogeographically decisive during the Callovian and Upper Jurassic periods, appears to have been very limited.

The deposit sequences are labeled D in reference to the discontinuities described by Gabilly et al. (1985).

Aalenian

Throughout the region, the sedimentary evolution that began in the Upper Toarcian with a reduction in clay inputs continued during the Aalenian (bodies labeled 1 and 2 in Fig. 2). The Lower Aalenian (*Opalinum* zone), which is very thin (2 to 3 m),

shows stratigraphic growth of fine clayey limestone beds. This is where the *Gryphaea beaumonti* lumachels are found, which constitute a regional stratigraphic marker.

D6

From the Middle Aalenian onwards (units 3-4-5-6), the paleogeography changes and two areas can be distinguished:

- a distal platform domain extending along the northern Aquitaine margin, characterized by highly condensed and lacunar sedimentation of calcareous biomicrites with ferruginous oolites, where nektonic fauna (ammonites, belemnites) and benthic fauna (mollusks) are equally abundant;
- a proximal carbonate platform edge domain, with much thicker sedimentation, consisting of fine dolomitic limestones with flints and predominantly benthic fauna, from a shallower environment with moderate energy.

In the basin area, from Niort to Saint-Maixent, the Middle Aalenian (*Murchisonae* zone) consists of thin marl beds and a more massive bank of clayey limestone. Above a marked discontinuity (D5bis?) is a level of reddish clayey limestone with ferruginous oolites and numerous fossils, gastropods, bivalves, belemnites, and ammonites characterizing the upper part of the zone. The whole is less than 1 m thick.

The Upper Aalenian, *Concavum* zone, is only represented from the Saint-Maixent graben and also at Vitré, north of Celles-sur-Belle, in the form of reddish, sometimes purplish, highly fossiliferous clayey limestones with ferruginous oolites and not exceeding 10 cm in thickness (unit 7).

In the Couhé-Vérac-Lusignan region, the Middle Aalenian thickens considerably (approximately 20 m) and occurs as dolomitic limestones with flints attributed to the *Murchisonae* subzone. The next 6 meters, *Bradfordensis* subzone, consist of often dolomitic limestones with flints alignments. The Upper Aalenian and the extreme base of the Bajocian (*Concavum* and *Discites* zones), nearly 5 m thick, correspond to pseudo-oncoides limestones. From Poitiers to Chauvigny, the Aalenian has the same facies with even greater thicknesses, from 19 to 27 m, for the whole. Islands dotted the platform with mangrove flora, giving rise to polyp limestones and driftwood. Continuing eastward into the Gartempe Valley, the Aalenian thins again as it approaches the northern edge of Limousin, with the return of ferruginous oolites in the *Bradfordensis* subzone and abundant pelagic fauna.

D7 – Lower Bajocian

Everywhere, the base of the Lower Bajocian is indicated by levels rich in ammonites, numerous Sonniniidae, and evidence of a major transgressive event (units 8 and 9). Along the entire northern Aquitaine border, there is a layer of gray limestone with ferruginous oolites, generally about 20 centimeters thick, rich in fossils, including

numerous benthic forms, bivalves, and gastropods, as well as cephalopods, ammonites, and belemnites. Above this, are thicker banks of very hard micritic limestone (paved limestone from the Niort region) dating from the *Laeviuscula* and *Propinquans* zones (units 10-11-12-13). In the Mellois region, these levels are very poorly developed and may still contain ferruginous oolites and phosphate nodules. The base of the *Humphriesianum* zone remains very fossiliferous (unit 14), particularly the *Umbilicum* horizon (*Humphriesianum* subzone). The rock contains large quantities of glauconite. Throughout the area, spongy bioherms developed during the *Subblagdeni* subzone. The top of the *Humphriesianum* zone is truncated by a major discontinuity, D8, as described by Gabilly et al. (1985).

In the Melusine gully and the Poitiers region, the Lower Bajocian reaches a thickness of around 20 meters, consisting of limestone with numerous pseudo-oncoides with nubeculars and flints levels. An oolitic bed marks the top of the zone at *Laeviuscula*, topped by calcarenites with crinoids containing very rare ammonites from the *Propinquans* and *Humphriesanum* zones (*Teloceras* cf. *subblagdeni* in the Vonne valley, Branger 1989). In the Boivre valley, polyp levels crown this series and probably constitute the lateral equivalent of the spongian bioherms developed in the distal domain. Towards the eastern part of the threshold, in the Gartempe valley, the Lower Bajocian ends with a flint-rich bank (silexite of Mourier, 1980, p. 35).

Further east, in the Civaux-Chauvigny region, it consists of granular limestone with tube worms, approximately 16 m thick, containing numerous flints and frequent dolomitic passages.

D8 – Upper Bajocian

A new transgressive episode marks the base of the Upper Bajocian (units 19-20-21). In Niort and Vendée, the *Niortense* and *Garantiana* zones, as well as the extreme base of the *Parkinsoni* zone, are recognized by a decimeter-thick layer of phosphate stromatolite nodules with reworked fossils (Branger, 1989). This bed becomes significantly more carbonated in the Mellois with multi-decimetric limestone banks rich in fossils. Moving towards the proximal platform, the transition from the Lower Bajocian to the Upper Bajocian is less distinct, but the fossiliferous beds of the *Garantiana* zone and the *Acris* subzone persist. Above, and throughout the sector, there are about ten meters more of massive beds of gravelly limestone, with abundant sponges and tuberoids (ferruginized intraclasts). These are the spotted limestones of the Saint-Maixent area (Cariou et al. 2006). Flints beds appear from the Saint-Maixent graben onwards.

On the Poitou platform, ammonites have also been collected at the base of the sub-stage. This is highlighted in the Poitiers cliffs by one or two burrow beds (units 20-21). Above, over about 20 meters, there are flint-dotted limestones (units 22 to 27). In the Vienne and Gartempe valleys, the facies indicate shallower environments. At a height of 25 to 40 meters, there are granular packstone limestones with isolated colonies of polyps (*Lochmaeosmilia*) interspersed with crinoid

grainstones (Lussac-les-Châteaux and Le Vigean sectors, Mourier and Gabilly, 1985). Exceptionally, in the terminal part of the stage, green clay lenses with ostracods can be observed (La Tour-au-Cognum).

D9 – Lower Bathonian

In northern Aquitaine, the base of the Bathonian stage corresponds to what former quarry workers called the "rotten bank." This is characterized by one or two multidecimeter limestone banks framed by greenish marl joints. In natural gamma-ray logs, this layer produces a marked peak that is easy to spot. It contains phosphate nodules and numerous fossils: bivalves, gastropods, sponges, and cephalopods typical of the *Zigzag* zone (units 28-29-30). As it approaches the Saint-Maixent graben, this level becomes much more carbonated but retains its paleontological characteristics (units 31 to 33). Above this, spotted limestones reappear over a thickness of about ten meters. Compared to those of the Upper Bajocian, there is an increase in the frequency of flints.

In Poitiers, at a height of about 3 meters, gravelly limestones with numerous *Ctenostreon* and, more rarely, a few ammonites from the *Zigzag* zone can be observed. Above this are thick beds of gravelly limestone with isolated flints (4 m). Moving eastward, this succession varies little, except for the upper part, which then consists of a marker level of oolitic limestone.

D10 – Middle and upper Bathonian

At the base of the Middle Bathonian, in the basin area, ammonites become frequent again (unit 36). The limestone facies with tuberoids and sponges remains predominant (approximately 3 meters), generally without flint, with a few greenish clay interbeds. Higher up, and only from la Crèche sector onwards, flints return temporarily. Sponges remain abundant and can locally form bioherm-type accumulations. At the top of the stage, much finer limestones (4 meters) are deposited, again rich in ammonites from the *Retrocostatum* zone. The virtual absence of *Clydoniceras* and the problems of correlation between the Tethyan and Boreal domains make it impossible to assess the extent of the gap in the late Bathonian. On the other hand, the erosion surface (D11) that truncates these beds and precedes the first Callovian deposits is well marked and, in most cases, easily identifiable thanks to the presence of glauconitic coatings.

As a result of their erosion, the Middle and Upper Bathonian deposits do not exist directly below the threshold. In Poitiers, this level consists of 5.50 m of gravelly and suboolithic limestone containing 4 to 5 continuous bars of flints, 0.15 to 0.30 meters thick. There are quite a few bivalves, polyps, and rare ammonites (*Cadomites orbignyi*). The stage ends with 7 m of gravelly to suboolithic limestone containing scattered flints. The whole is truncated by a weathering surface.

In the Chauvigny area, at a height of 21 meters, the Middle Bathonian consists of finely grained limestone with thin oolitic and oncolitic intercalations and a few beds rich in *Entolium* towards the top. Clayey intercalations of brackish origin persist at this level in the Creuse valley. The Upper Bathonian (25 to 30 meters) corresponds to the Chauvigny oolite. The lower part (10 to 12 meters) is formed of coarse limestone with colonies of polyps (*Lochmaeosmilia*), topped by fine oolite in massive banks. Here again, we find discontinuity D11 in the form of a flattened and threaded surface.

The various deposit sequences (systems tracts) are shown in Figure 2. Carbonate deposits are significantly thicker (gravelly and oolitic facies) on the threshold than on the Aquitaine slope (bioclastic facies). The discontinuities separating the deposit sequences extend from the basin to the platform. Correlations between the basin and the Poitevin platform with sedimentary discontinuities make it possible to define the geometry of the sedimentary bodies. An overall diagram of these deposit sequences is shown in Figure 2.

The ammonites indicating the biozones are shown in Plate 1.

Stratigraphy of the Bajocian south of Poitiers: the cliffs of Passelourdin

In Saint-Benoît, south of Poitiers, the Passelourdin cliffs in the Clain Valley provide an opportunity to observe the stratigraphy of the Lower and Upper Bajocian. The area has been briefly described by various authors (Gabilly, 1978; Benvel, 1978; Mourier et al., 1986). The cliff provides a detailed description of the Bajocian deposit sequences, thus providing a precise stratigraphic framework for this stage for the study of the results obtained at the Hydrogeological Experimental Site (HES) of the University of Poitiers.

The structural context is linked to the Ligugé horst (Fig. 3). The site is in fact at the center of a horst bounded to the south by the Mauroc fault and to the north by the Saint Benoit fault (Benvel, 1978). The Mauroc fault is parallel to the Ligugé horst faults and has a southward offset of approximately 10 to 12 m. It is not sufficient to bring the Bajocian and Pliensbachian into contact, as the Toarcian marls are approximately 22 m thick (see section of borehole 05894X0053/1030 on the horst). Together with the Saint Benoît fault, it thus delimits a small horst within which the equivalent of the Bajocian III of Benvel, 1978, in Figure 3 (Gaillard and Branger, 2024) outcrops.

A new survey was conducted in February 2025 with the help of a rope access technician. Due to very dense vegetation, the description is based on a synthetic survey of the entire height of the cliff ("survey with climbing"), illustrated by photographs (Plate 2).

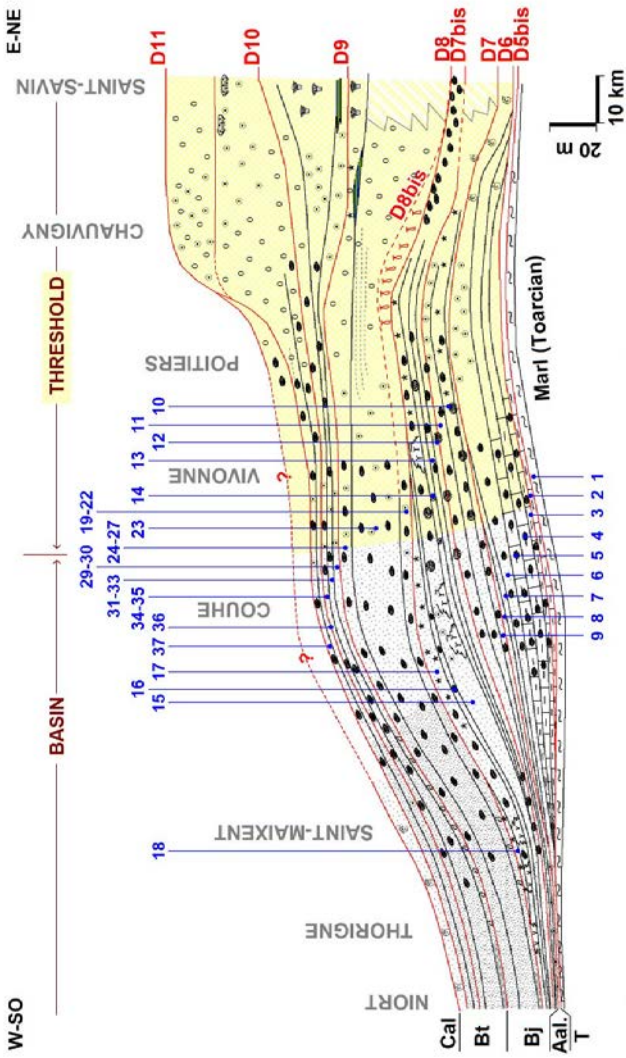

Figure 2 *Geometry of strata of the Middle Jurassic on the Poitou threshold.*

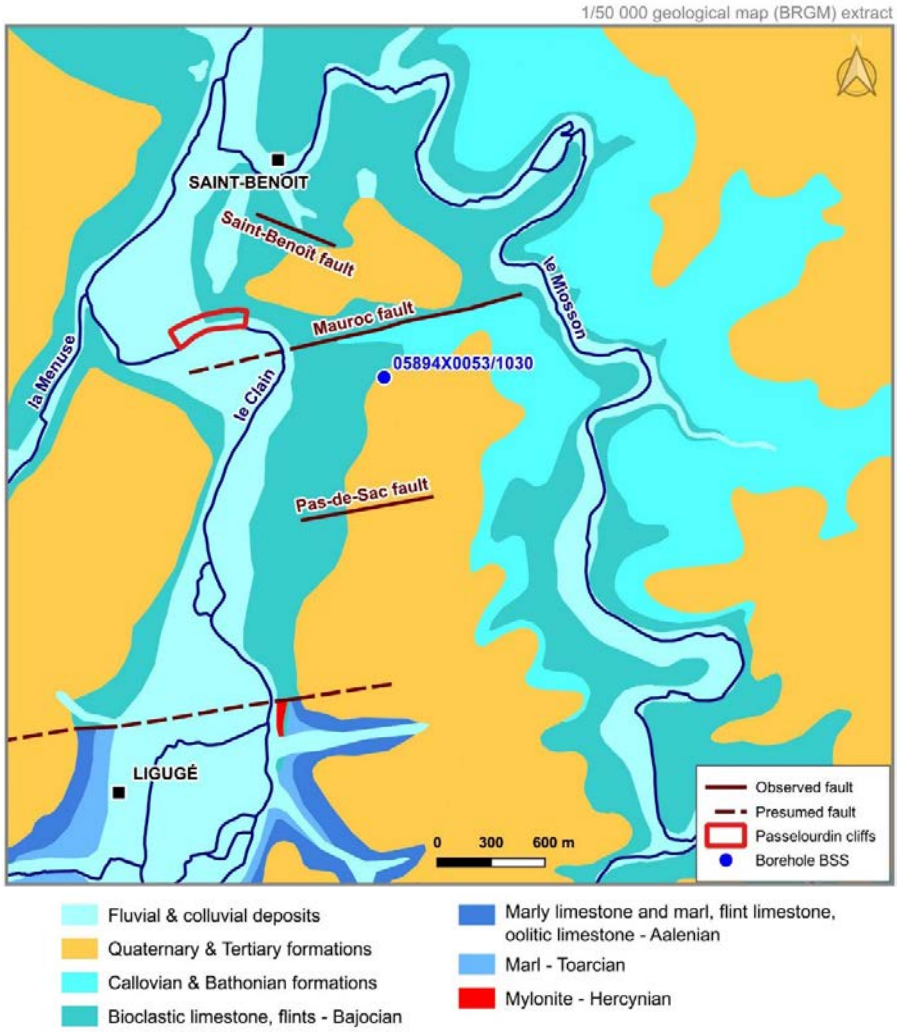

Figure 3 *Geological map of the site (after Mourier et al., 1986).*

Figure 4 shows the location of the different sections of cliff observed.

The oldest formations are observed at points known as "Yews n° 1 and n° 2." At point n° 1, the presence of *Graphoceras concavum* identifies the Upper Aalenian. This ammonite is located immediately below a bank of white oolites, which is itself topped by banks of bivalves (Fig. 5). These two banks are thought to represent the *Laeviuscula* zone (not observed), with the D7 discontinuity (leveled at an altitude of approximately 78 m) as a marker for the base of the Lower Bajocian. The "Yews n° 3" site is located at a higher altitude (the zone between "Yews 1 and 2" and "Yews 3" is not observable) and allows the identification of the white oolitic

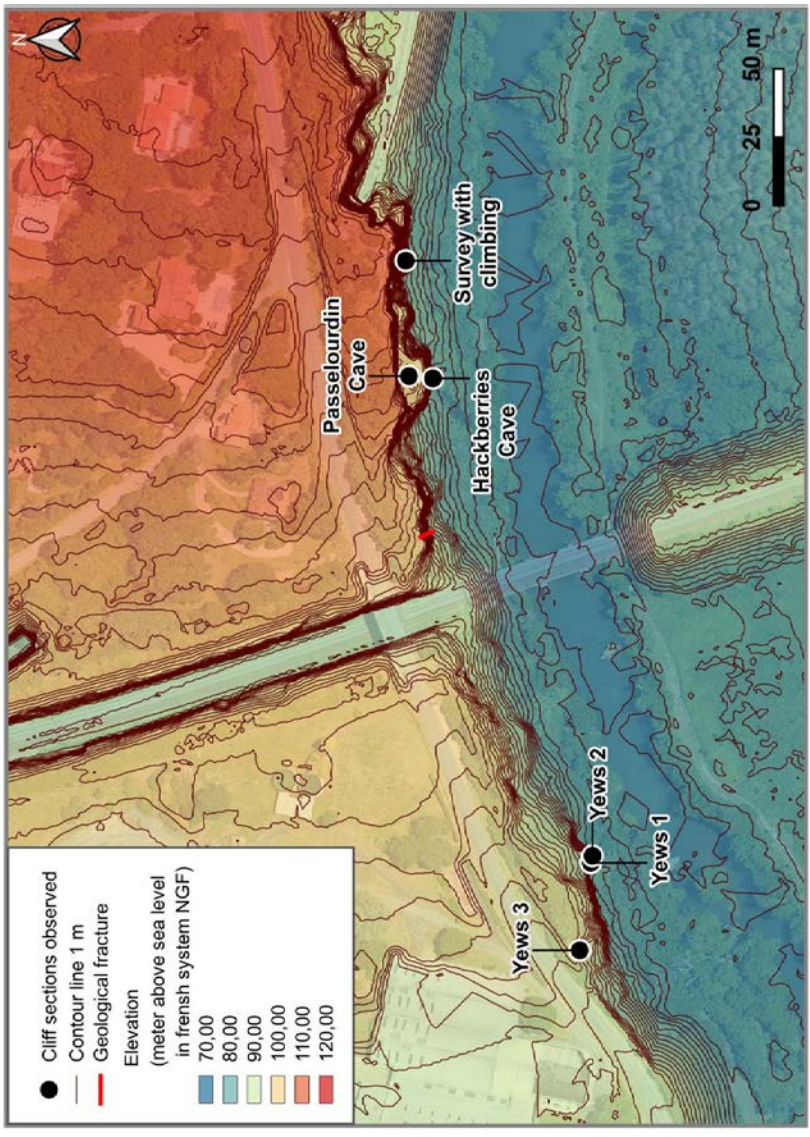

Figure 4 *Status of geological surveys in Passelourdin.*

limestone marking the end of the *Laeviuscula* zone, D7bis, located at an altitude of approximately 91.0 m. The thickness of the *Laeviuscula* and *Propinquans* formations is estimated to be at least 13 m.

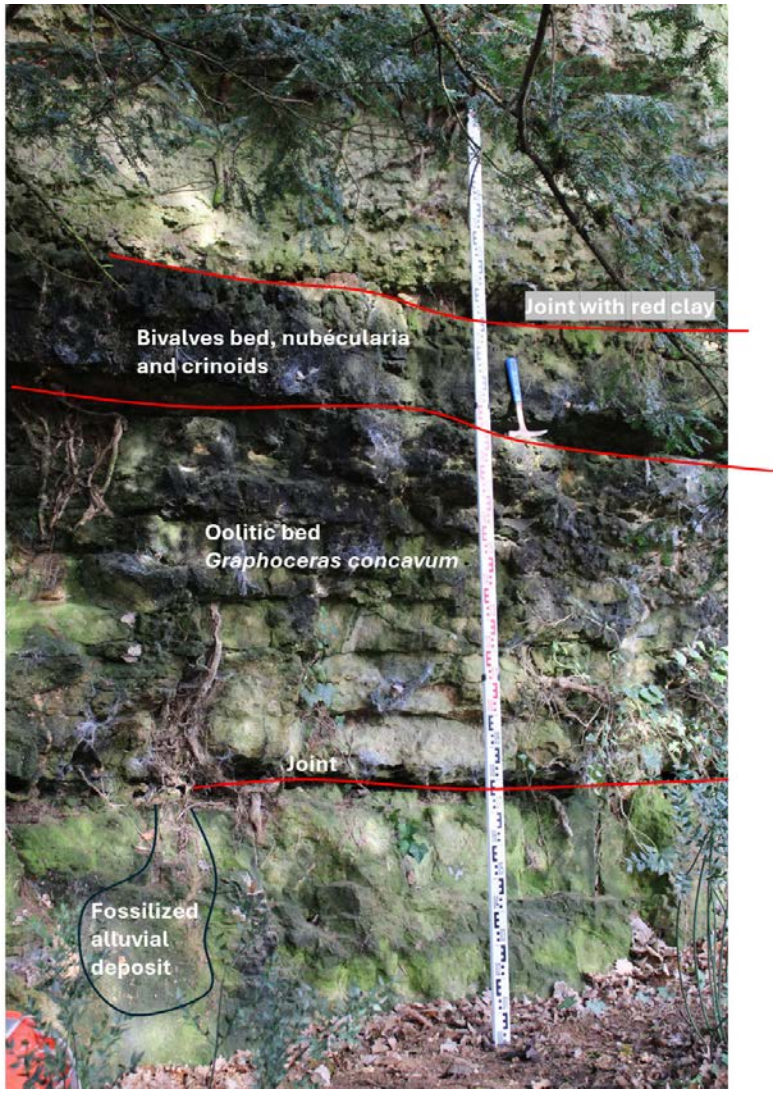

Figure 5 *Aalenian/Bajocian transition.*

In the east, the "survey with climbing" allows the entire height of the cliff to be recognized from the Lower Bajocian, with the continuity of a joint in the "ash cave," where dolomitized limestones with Trichites are observed in metric benches ending in a level of small decimeter-sized vacuoles.

The cavernous dolomite is topped by an oolite bed identified as the last term of the *Laeviuscula* zone, placing the D7 bis discontinuity at an altitude of 90.6 m at this point (Fig. 6).

Figure 6 *Oolitic facies from top of* Laeviuscula *biozone.*

The upper parts could not be observed directly by a geologist (and cannot be sampled). They are illustrated by plate n° 2. Above the D7bis, the *Humphresianum* zone has a lower vacuolar level. The upper vacuolar level is illustrated by photograph 5. Above a ledge, decimetric and ovoid cavernous forms have developed (photograph 4, plate 2).

Discontinuity D8 is observed at an elevation of approximately 101 m, in the form of a karst joint (photograph 3) located above a nodular bench approximately 0.55 m thick that continues into the cliff. At the same place, at the "Passelourdin cave," the cave floor rests on the pebble bench attributed by the authors to the reference level at the base of the *Niortense* zone, placing D8 at an altitude of approximately 99 m.

Above the D8, the burrowed zone (Gabilly, 1978) is illustrated by photographs 1 and 2. This formation corresponds to limestone with tubular structures several meters thick on the "survey with climbing" and at the "Passelourdin cave." This formation corresponds to the beginning of the Upper Bajocian and ends with the D8bis discontinuity, which marks the upper limit of the *Garantiana* zone. These vertical burrow banks are overlain by hard limestone belonging to the *Parkinsoni* zone above the D8bis discontinuity.

Figure 7 shows the correlations between the cliffs observed, the discontinuities and the location of the photographs (plate 2).

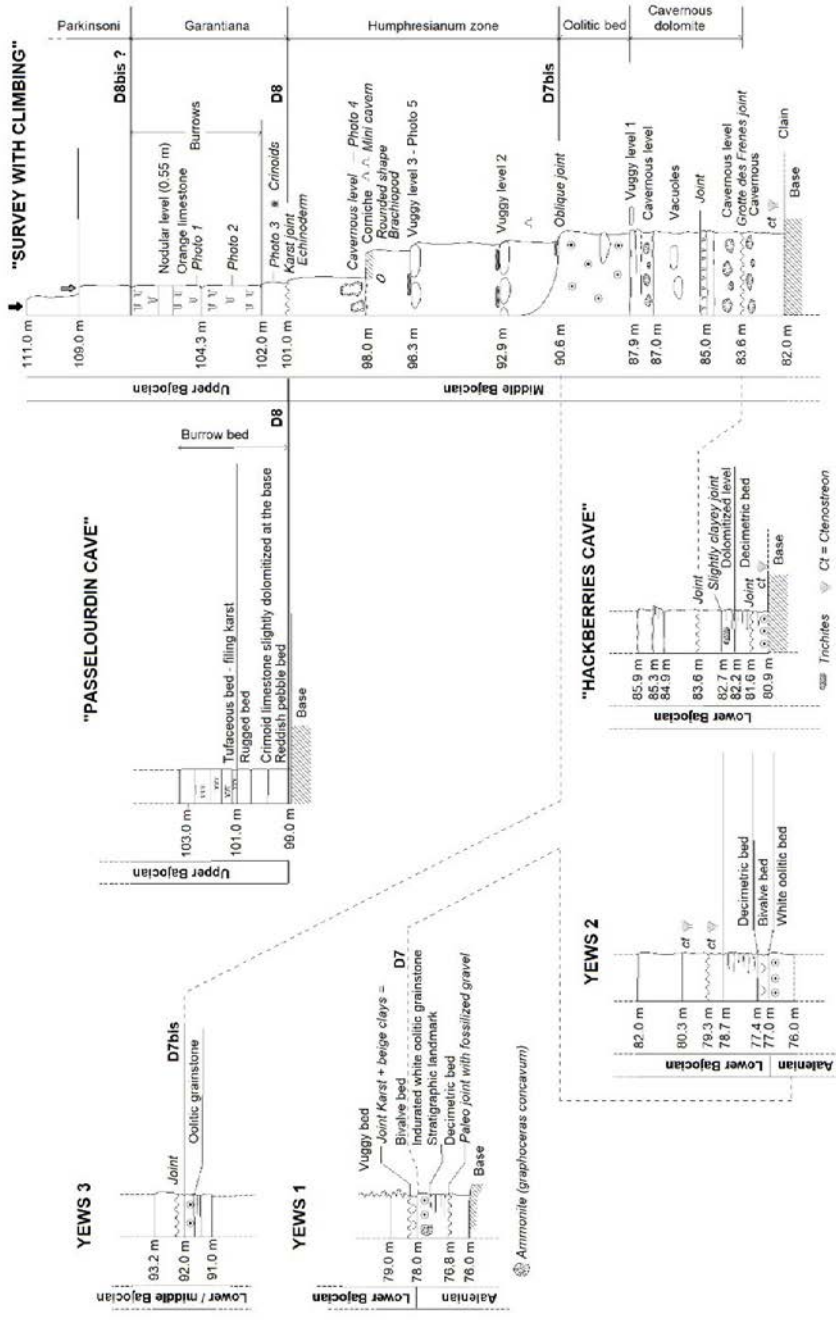

Figure 7 *Logs from survey with climbing at Passelourdin cliff.*

By comparing the different observation points on the Passelourdin cliffs, it is possible to see the very clear discontinuities along which the cavities are aligned. The dolomitized benches and vacuole zones are contained between the discontinuities previously identified by the authors:

- the Lower Bajocian (*Laeviuscula* zone) forms a locally dolomitized sequence constituting the karst at the base of the Bajocian, located between elevation 78 m (D7, top of the Aalenian) and below elevation 91 m (D7bis);
- above the *Laeviuscula* zone and D7bis, hollowed-out conduits line this surface, while overhanging benches feature aligned subhorizontal voids (vacuolar levels, Fig. 5). This complex ends with the pebble surface of the 'Passelourdin cave' (D8). This karst is therefore located between 91 and 99 to 101 m;
- above D8 and an altitude of 101 m, karst is initiated within the tubular limestones (burrowed zone). This so-called 'upper' karst has deepened to the pebble bench (D8), where the harground has limited its development.

Conclusion

The depositional sequences of the Poitou threshold end with discontinuities that appear to have planned the lower strata. These discontinuities allow correlations between, on the one hand, the distal facies in the Aquitaine basin and, on the other hand, the proximal facies in the center of the threshold defined by tectonics (Gaillard and Branger, 2026).

This precise stratigraphic framework allows to characterize the cliffs around Poitiers and highlight karst levels consisting either of cavernous levels in the *Laeviuscula* and *Humphriesianum* horizons or along discontinuities. These levels are developed and may have been filled with sediments (red clay or alluvial facies).

With this stratigraphic diagram, the position of the karstified levels can be more easily understood. The levels are not arranged randomly but are located at the edge of deposits or are concentrated within certain biozones in the form of vuggy levels.

References

Branger P. (1989). La marge nord-aquitaine et le Seuil du Poitou au Bajocien : stratigraphie séquentielle, évolution biosédimentaire et paléogéographique. Ph.D. thesis, University of Poitiers, France.

Branger P., Gonnin C. (1994). Distribution des ammonites et dynamique sédimentaire sur le seuil du Poitou de l'Aalénien au Bajocien. Proceedings 3rd International Meeting on Aalenian and Bajocian stratigraphy, Marrakech, 5: 293-295.

Cariou E., Joubert J.M. (1989). Notice explicative, Carte géol. France (1/50.000), feuille de Lusignan (612). Orléans : BRGM, 42 p.

Cariou E., Hantzpergue P. (1997). Biostratigraphie du Jurassique ouest-européen et méditerranéen : zonations parallèles et distribution des invertébrés et microfossiles (Vol. 17). Groupe Français d'Étude du Jurassique-Elf-Aquitaine.

Gabilly J. (1962). Les variations de sédimentation du Lias et du Jurassique en relation avec le seuil du Poitou. 87e Congrès des Sociétés Savantes : colloque sur les seuils en géologie, Poitiers : 679-699.

Gabilly J., Rioult M. (1971). Le Bajocien inférieur et le Toarcien supérieur sur les bordures du Massif armoricain. Dans Groupe Français d'étude du Jurassique, Deuxième colloque du Jurassique : 385-396.

Gabilly J., Cariou E. (1974). Journées d'étude et excursion en Poitou 14-15-16 et 17 octobres 1974. Groupe Français d'études du Jurassique : Livret guide. University of Poitiers, France.

Gabilly J., Cariou E., Hantzpergue P. (1985). Les grandes discontinuités stratigraphiques au Jurassique : témoins d'événements eustatiques, biologiques et sédimentaires. *Bull. Soc. Géol. France*, 8e sér., n° 3: 391-401.

Gaillard T., Branger P. (2024a). Le Jurassique moyen du Poitou (Middle Jurassic of Poitou). In Le karst du seuil du Poitou : Approche stratigraphique et rôle de la tectonique sous la direction de T. Gaillard, Comité Français d'Hydrogéologie, Livret Guide de l'excursion sur le seuil du Poitou, 29 au 31 mars 2024: 3-6.

Gaillard T., Branger P. (2024b). Le Bajocien de la vallée du Clain : Saint Benoit (Clain river valley Bajocian : Saint Benoit). In Le karst du seuil du Poitou : Approche stratigraphique et rôle de la tectonique sous la direction de T. Gaillard, Comité Français d'Hydrogéologie, Livret Guide de l'excursion sur le seuil du Poitou, 29 au 31 mars 2024: 52-58.

Gaillard T., Branger P. (2026). "The Poitou Threshold", Chapter 1 in *A new concept of karst development based on hydrogeology and geophysics*, EDP Sciences. https://doi.org/10.1051/978-2-7598-3934-6.c001.

Gonnin C., Cariou É., Branger P. (1992). Les facteurs de contrôle de la sédimentation au début du Jurassique moyen sur le Seuil du Poitou et ses abords. *C. R. Acad. Sci., Paris*, t. 315, sér. 2: 853-859.

Gonnin C., Cariou É, Branger P. (1993). Stratigraphie séquentielle des séries du Bajocien inférieur au Bathonien moyen du Seuil du Poitou et de son versant aquitain (France). *C. R. Acad. Sci., Paris*, t. 316, sér. 2: 209-215.

Glangeaud P. (1895). Le Lias et le Jurassique moyen à l'ouest du plateau central. *Bulletin de la Société Géologique de France*, 3e série (XXIII): 10-54.

Hardenbol J., Thierry J., Farley M.B., Jacquin T., de Graciansky P.C., Vail P. (1998). Mesozoic and Cenozoic Sequence Chronostratigraphic Framework

of European Basins. In: Graciansky, P.C., et al., Eds., Mesozoic and Cenozoic Sequence Stratigraphy of European Basins, SEPM Special Publication 60, Tulsa, Charts 1-8, 3-13.

Chronostratigraphic Framework of European Basins. SEPM Special Publication n° 60.

International Commission on Stratigraphy (2024). International chronostratigraphic chart v12, 2024. https://stratigraphy.org/chart#latest-version

Mourier J.-P. (1980). Étude stratigraphique des terrains jurassiques dans la vallée de la Gartempe entre Lathus et Saint-Savin (Vienne). D.E.P.S.U.P., University of Poitiers, France.

Mourier J.-P. (1983). Le versant parisien du seuil du Poitou de l'Hettangien au Bathonien. Stratigraphie, sédimentologie, caractères paléontologiques, paléogéographie. Ph.D. thesis, University of Poitiers, France.

Mourier J.P., Gabilly J. (1985). Le Lias et le Dogger au sud-est du seuil du Poitou : Tectonique synsédimentaire, paléogéographie. *Géologie de la France*, n° 3: 293-310.

Rioult M., Dugué O., Jan du Chêne R., Ponsot C., Fily G., Moron J.-M., Vail P. (1991). Outcrop sequence stratigraphy of the Anglo-Paris Basin, Middle to Upper Jurassic (Normandie, Maine, Dorset). Bulletin of the Elf-Aquitaine Research Center, 101-194.

Welsch J. (1895). Sur la succession des faunes du Lias et du Bajocien inférieur dans le détroit du Poitou. *Compte Rendu de l'Académie des Sciences*, 1 (CXX): 1291-1295.

Welsch J. (1903). Étude des terrains du Poitou dans le détroit poitevin et sur les bordures du massif ancien de Gâtine. *Bulletin de la société géologique de France*, 3(4): 798-881.

Plate 1 : Ammonites

Unless otherwise indicated, all ammonites come from the southern Deux-Sèvres region. Collection and photos P. Branger.

1 - *Leioceras opalinum* 28 cm (block length)

2 - *Ludwigia murchisonae* (Ø 20 cm)

3 - *Brasilia gigantea* (Ø 14.5 cm)

4 - *Graphoceras concavum* (Ø 13 cm)

5 - *Hyperlioceras discites* (Ø 12.5 cm) (Charente)

6 - *Sonninia adicra* (Ø 14 cm)

7 - *Witchellia romanoides* (Ø 10 cm)

8 - *Sonninia propinquans* (Ø 14 cm)

9 - *Stephanoceras scalare* (Ø 16.5 cm)

10 - *Strenoceras niortense* (Ø 5.3 cm)

11 - *Garantiana garantiana* (Ø 6 cm)

12 - *Parkinsonia parkinsoni* (Ø 19 cm)

13 - *Zigzagiceras zigzag* (Ø 5.5 cm)

14 - *Procerites progracilis* (Ø 12 cm)

15 - *Morrisiceras morrisi* (Ø 11 cm)

16 - *Cadomites bremeri* (Ø 7.6 cm)

17 - *Prohecticoceras retrocostatum* (Ø 5 cm) (Sud Deux-Sèvres)

18 - *Clydoniceras discus* (Ø 9 cm) (Sud Deux-Sèvres)

Plate 2 : Passelourdin

Photographs M. Chollet.

Photo 1

Photo 2

Photo 3

Photo 5

Photo 4

3

Hydrogeology of the Poitou Threshold

T. Gaillard and M. Moreau

Aquifers of the Poitou threshold

Two main aquifers

The sedimentary cover of the Poitou Threshold (Branger et al., 2026) consists of Lower and Middle Jurassic deposits. Consequently, only two aquifers were historically defined by the first geologists who studied the region's hydrogeology (Welsch, 1912). These are referred to as the Supra-Toarcian Aquifer and the Infra-Toarcian Aquifer, named after the intervening Toarcian marls that separate them (Welsch, 1912). Continuous coring from boreholes drilled at the Hydrogeological Experimental Site of Poitiers University (HES) has provided a detailed lithostratigraphic and hydrogeological description of the Jurassic sequence (Fig. 1).

Beneath the site, the granitic basement occurs at a depth of 158 m. The Infra-Toarcian Aquifer overlies this basement and is approximately 21 m thick. Its basal section comprises clays and dolomites of Hettangian–Sinemurian age (150–158 m), overlain by bioclastic marly limestones of Pliensbachian age (135–150 m). This aquifer is overlain by the Toarcian marls, which are about 15 m thick (120–135 m).

© EDP Sciences, 2026
DOI: https://doi.org/10.1051/978-2-7598-3934-6.c003

Above the Toarcian marls lies the Supra-Toarcian Aquifer. Its base consists of marly limestones passing upward into more carbonate-rich and oolitic facies of Aalenian age (101–120 m). The overlying Bajocian limestones (46–101 m) display a range of facies, from bioclastic to gravelly textures, and include a distinct interval of white oolites between 80 and 83 m. This unit is followed by fine-gravelly limestones interbedded with flint of Bathonian age (21–46 m) and capped by "chalky" white limestones of Callovian age (6–21 m). Near the surface, these limestones are weathered to form a red clay horizon (0–6 m).

The Infra-Toarcian Aquifer is confined, whereas the Supra-Toarcian Aquifer is unconfined. The substantial thickness of the Toarcian marls ensures effective hydraulic separation between the two, except in faulted zones where vertical displacements exceed 20 m.

Piezometric map

At the HES, groundwater levels in the Infra-Toarcian Aquifer range from 95 to 100 m NGF (meters above sea level, French elevation datum), while those in the Supra-Toarcian Aquifer range from 100 to 105 m NGF. The piezometry of the Supra-Toarcian Aquifer is relatively well documented as a result of several monitoring campaigns carried out between the Vienne River (east of Poitiers) and the Clain River (Coirier et al., 1968).

In 2004, two additional piezometric surveys were conducted on the Supra-Toarcian Aquifer. Each survey covered approximately 800 measurement points (Marchais and Bichot, 2005). The piezometric map derived from the October 2004 survey is considered representative of low-water conditions (Fig. 2).

The main drainage axis in the Clain River basin trends south–north from Vivonne to Poitiers. The downcutting by the Clain began during interglacial stages of the Mindel and Riss glaciations. Secondary drainage axes, oriented perpendicular to the main one, correspond to younger valleys incised during the Weichselian: the Clouère River (Gencay–Vivonne axis), the Vonne River west of Vivonne, the Auxance River north of Poitiers, and the Boivre River. In these valleys, Supra-Toarcian limestones are deeply eroded, and riverbeds may locally cut down to the Infra-Toarcian Aquifer. Piezometric gradients in the area range between 0.5% and 1%.

The piezometric watershed of the Clain differs markedly from its topographic watershed (Fig. 3). To the east, a north–south-oriented groundwater divide separates the Vienne and Clain basins. This divide is near the axis of the Miosson River, which is perched and hydraulically disconnected from the Supra-Toarcian Aquifer in its upstream reaches. The piezometric divide defines the hydrogeological catchments of the Vienne and Clain, which do not coincide with their surface watershed boundaries. The piezometric catchment of the Clain is smaller than its topographic watershed due to a westward offset of the divide. As early as 1968, Coirier et al. attributed this offset to the lower base level of the Vienne

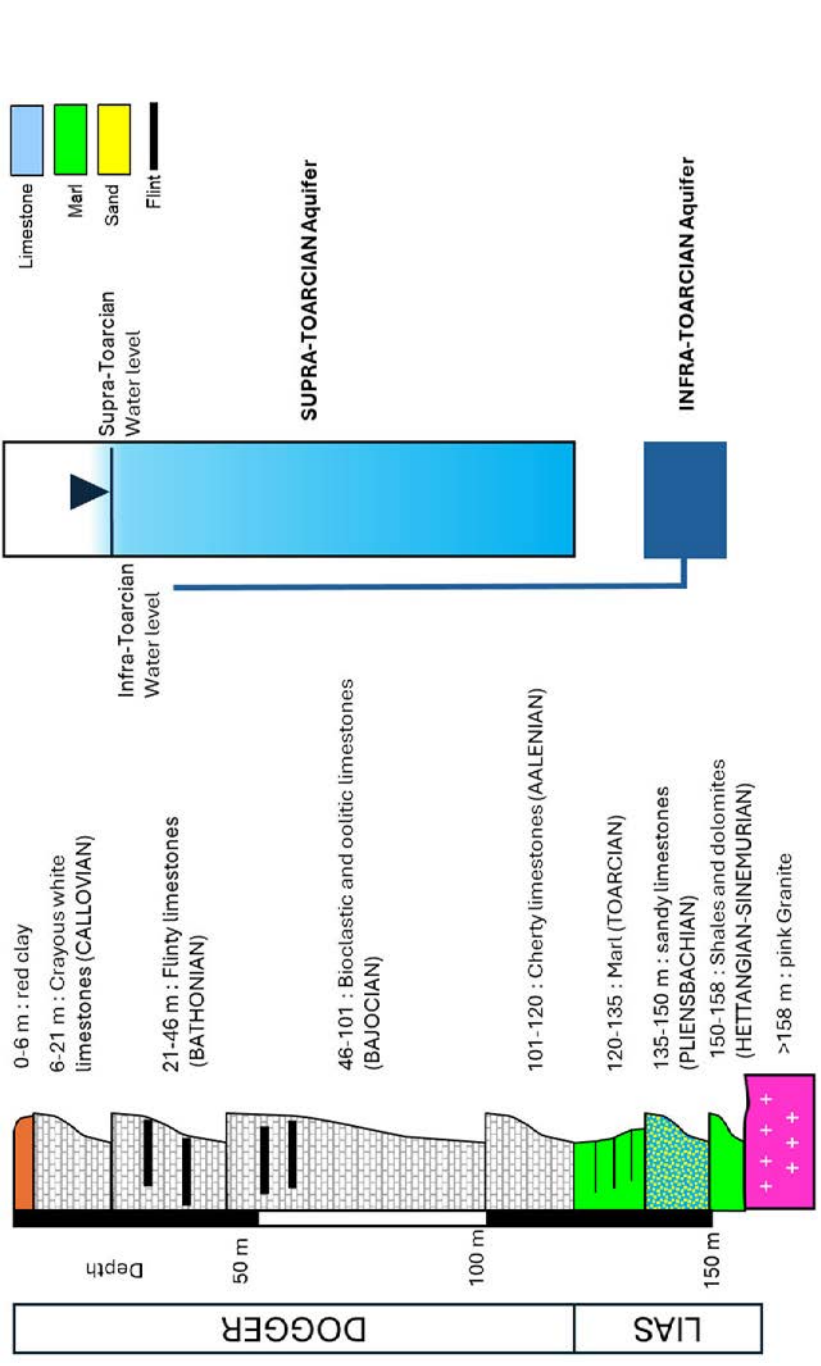

Figure 1 *Schematic cross-section of the Infra and Supra-Toarcian aquifers at the HES, Poitiers, France.*

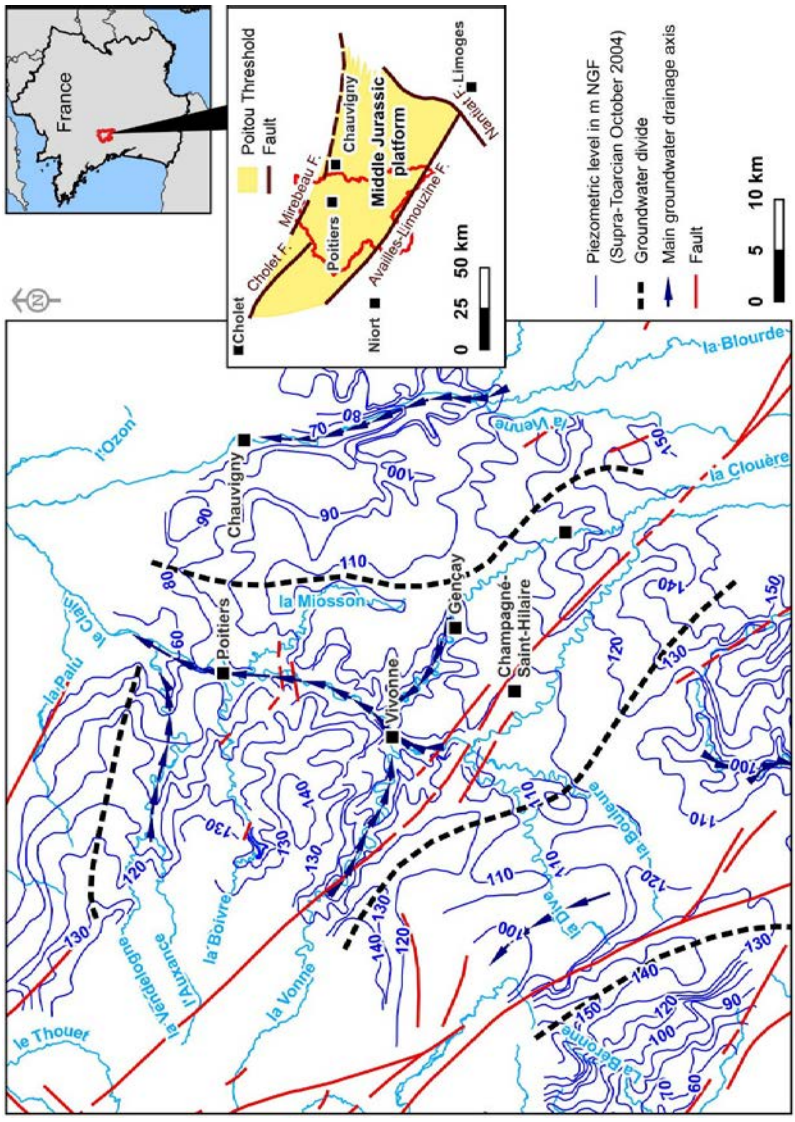

Figure 2 *Piezometric map of the supra-Toarcian aquifer (Marchais and Bichot, 2005, modified). mNGF: French elevation system above sea level in meters.*

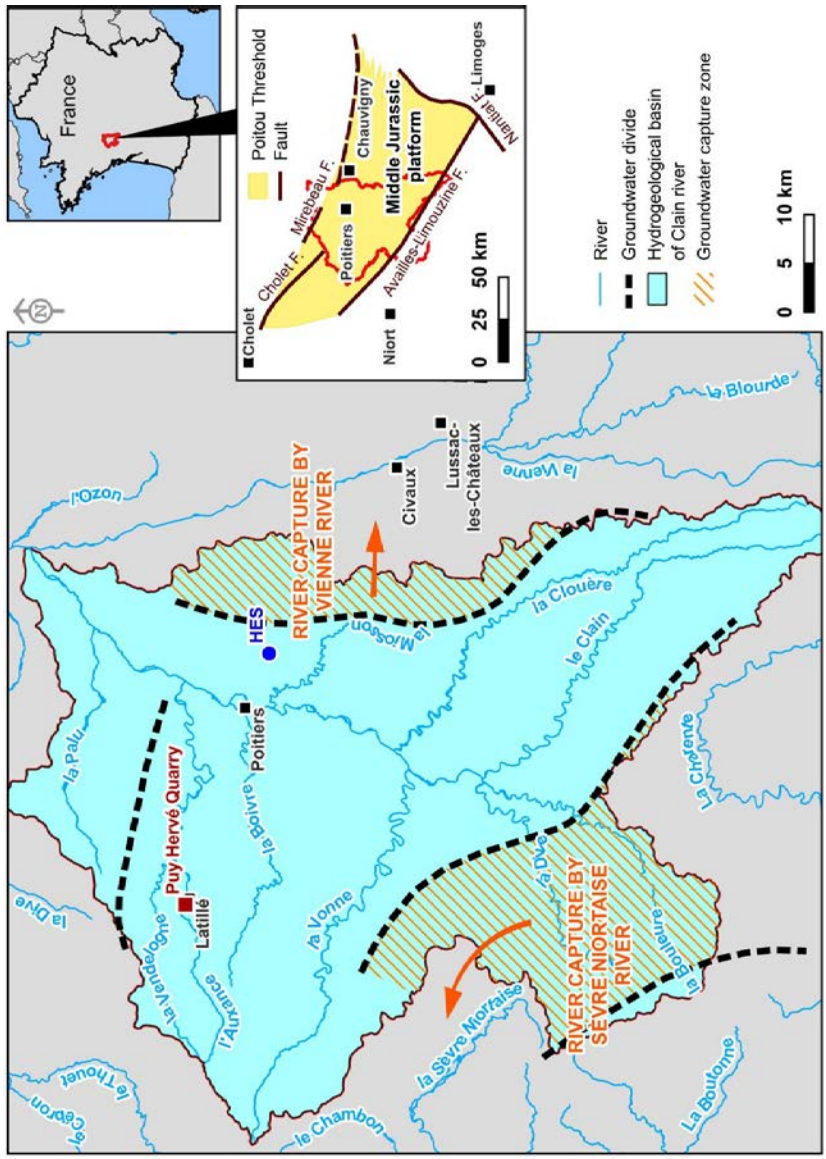

Figure 3 *Hydrogeological basin of Clain river.*

valley. Indeed, downcutting of the Vienne valley during the Mindel and Riss periods extended well beyond the paleovalleys of the Clain, which do not extend northward beyond Vivonne (46.42°N). The deeper incision of the Vienne valley into Supra-Toarcian formations south of Chauvigny enhances groundwater drainage toward the Vienne at the expense of the Clain basin. More recent, localized piezometric investigations have shown that this groundwater divide fluctuates spatially and temporally over several kilometers (Gaillard and Moreau, 2024). The piezometric map in Figure 3 depicts the easternmost position of the divide recorded to date. In the upstream part of the Clain watershed, another piezometric divide occurs south of the Availles-Limouzine Fault (Champagné-Saint-Hilaire Horst; see Gaillard, 2026). This divide separates the Clain from the Charente Basin, which drains westward to the Atlantic Ocean. Finally, to the southwestern part of the Clain Basin, a portion of groundwater is captured by the springs of the Sèvre Niortaise river via several karstic sinkholes located in the Dive-du-Sud valley. This karstic capture has been demonstrated by dye tracing experiments (Coirier, 1964).

The supra-Toarcian aquifer

Groundwater flow patterns in the supra-Toarcian aquifer

Groundwater flow in the Supra-Toarcian Aquifer exhibits characteristics of both a porous aquifer system—evidenced by piezometric mapping—and a karstic system, as demonstrated by numerous dye tracing tests and the exploration of karst networks by speleologists (Déribéré, 1937; SCP, 1990; Sibert et al., 2008).

The speleological networks explored within the Vienne département can be classified into two main types: introduction karsts and restitution karsts. Introduction karsts (also referred to as sinkholes or "gouffres") are circular depressions, sometimes reaching diameters of up to 100 m (e.g., the Gouffre du Grand Soubis in the Moulière Forest; Gouffre de la Troussaye at Marnay). Their depths generally do not exceed 50 m (e.g., 48 m at the Gouffre du Charreau de Boussec, Chauvigny). These features are predominantly vertical shafts, occasionally interrupted by ledges corresponding to bedding plane discontinuities. Restitution karsts are most commonly accessed through caves, and less frequently by cave diving. These systems include *laminoirs* (passages developed along bedding planes) and *trémies* (collapse zones connected to the surface). The galleries are typically sub-horizontal (Bigot, 2004, p. 105) and often display parallel orientations (SCP, 1990, p. 58).

As early as the 19th century, Longuemar (1856) highlighted the role of vertical fractures in controlling spring emergence at the contact with Toarcian marls. This model implicitly assumes that karst conduits develop preferentially along such fractures, supplied by concentrated recharge via sinkholes. Similarly, Welsch (1912) proposed a conceptual model in which dry valleys act as preferential drainage pathways toward springs. In this interpretation, decompression of the limestone massif within the dry valleys facilitates the karst conduit development. Official reports by hydrogeologists accredited by public health authorities consistently describe groundwater flow in these Jurassic limestones as occurring through fissure and conduit porosity, which locally generates preferential flow zones with high transmissivities (Mourrier et al., 1986).

Comparison between lineaments and speleological networks

The dominant structural orientations in the study area include faults trending N115–125°, representing the main tectonic axis, and faults oriented N40–50°, corresponding to conjugate extension directions (Burbaud-Vergneaud, 1987). Additional orientations are also present, including N20–30°, N90°, N150°, and N180°.

To evaluate the influence of tectonics on the spatial organization of karst networks (restitution karst), a comparative analysis was carried out between lineament orientations and Speleological geometries in two study areas. The first area is centred on the largest known karst system of the Poitou Threshold (the Cuchon Cave system). The second encompasses the Hydrogeological Experimental Site (HES) of Poitiers University (Fig. 4). Lineaments were mapped by extracting elevation data from a 5 m resolution digital terrain model. Their orientations and lengths were used to construct stereo-net plots depicting the local tectonic framework. Karst void orientations for the Cuchon area were derived from a detailed speleological survey of the cave system (approximately 4 km of mapped passages). At the HES, fracture networks were characterized using the OPtical TeleViewer (OPTV) method, which produces high-resolution, magnetically oriented colour images of the borehole wall.

The results are shown in Figures 5 and 6. In the Cuchon area, the dominant lineament orientation is N45–55°E, whereas the surveyed karst conduits predominantly trend N130–140°E. This suggests that local fracturing does not exert primary control on the orientation of the Cuchon network galleries. At the HES, two regional fracture sets were identified, trending N50–65°E and N120–130°E. However, discontinuities observed in boreholes are mainly oriented between N80–100°E. These two examples indicate that restitution-type karst systems are only weakly influenced by regional fracturing patterns.

Figure 4 *Location of lineament analysis east of Poitiers (HES) and Chauvigny (Cuchon caves)*

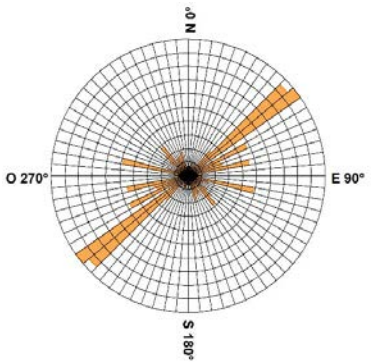

a) Lineaments

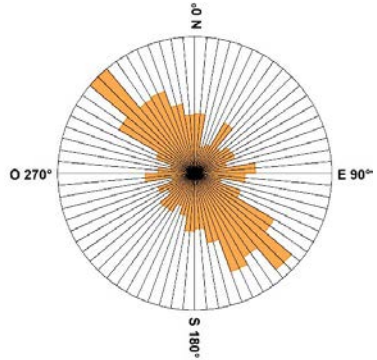

b) Cuchon network

Figure 5 *Comparison between lineament directions and the galleries direction of the Cuchon network caves*

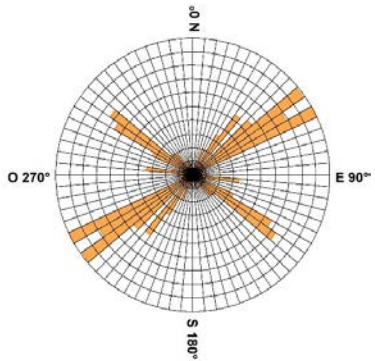

a) Lineaments

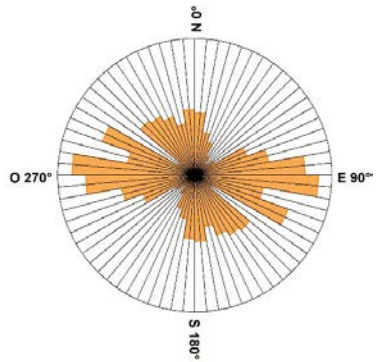

b) OPTV

Figure 6 *Comparison between lineament directions and OPTV direction in boreholes of HES.*

Typology of voids in Poitou threshold limestones

For both study sites (HES and Cuchon Cave), the observed tectonic patterns do not coincide with the karst networks' orientations. This prompted an investigation into the potential role of stratigraphy in controlling karst development, based on analyses of primary cliff outcrops described in several doctoral dissertations on the Poitou Threshold (Benvel, 1978; Beaulieu, 1978; Balusseau, 1980; Mourrier, 1983). This work was presented during a field excursion of the French Chapter of the International Association of Hydrogeologists (www.cfh-aih.fr/colloques-et-visites/excursion-seuil-du-poitou-ag-12-au-15-03-2020.html and "Le karst du seuil du Poitou : Approche stratigraphique et rôle de la tectonique" on researchgate).

The methodology consisted of identifying macroporosity features in stratigraphically well-constrained outcrop sections. An illustrative example is shown in Figure 7, taken from the former Puy-Hervé quarry in Latillé, approximately 27 km west of Poitiers (see Fig. 3). Stratigraphic correlation was established through the collection of two index ammonite specimens: *Brasilia* sp. (Aalenian) and *Sonninia ovalis* (Early Bajocian). A distinct discontinuity separates the oolitic Aalenian formation from the gravelly limestones of the Bajocian. This surface, infilled with red clay, corresponds to Discontinuity D7 as defined by Gabilly et al. (1985). Locally, this discontinuity has been subject to dissolution, resulting in the development of macroporous zones within the limestone massif.

Using this method, two types of voids were identified, both in the examined outcrops and in the cores from the HES boreholes:

- type 1: scattered vacuoles within massive limestone beds, variably interconnected. These vacuolar levels are predominantly concentrated in the Lower Bajocian, specifically within the *Laeviuscula* and *Humphriesianum* ammonite zones;
- type 2: conduits aligned along stratigraphic discontinuities between two depositional sequences. These discontinuities are often filled with red clay, possibly corresponding to paleosol horizons. Their numbering follows the classification of Gabilly et al. (1985).

These void types are illustrated in Figure 8. They are not associated with vertical fractures. The dolomitization observed in certain formations was not considered in this analysis, as stratigraphic correlation was not possible due to the absence of paleontological markers in those units.

Type 1 voids are observed within the Bajocian limestones. In the area surrounding Poitiers (Boivre Valley, Clain Valley), these vacuoles are concentrated near the top of strata within the *Humphriesianum* zone and form distinct vuggy levels. Figure 9 shows an example from the Passelourdin cliff, located six kilometers south of Poitiers (Branger et al., 2026). In certain outcrops of Aalenian age (Gartempe Valley, east of Poitiers), calcite geodes of similar shape and size have been observed by the authors.

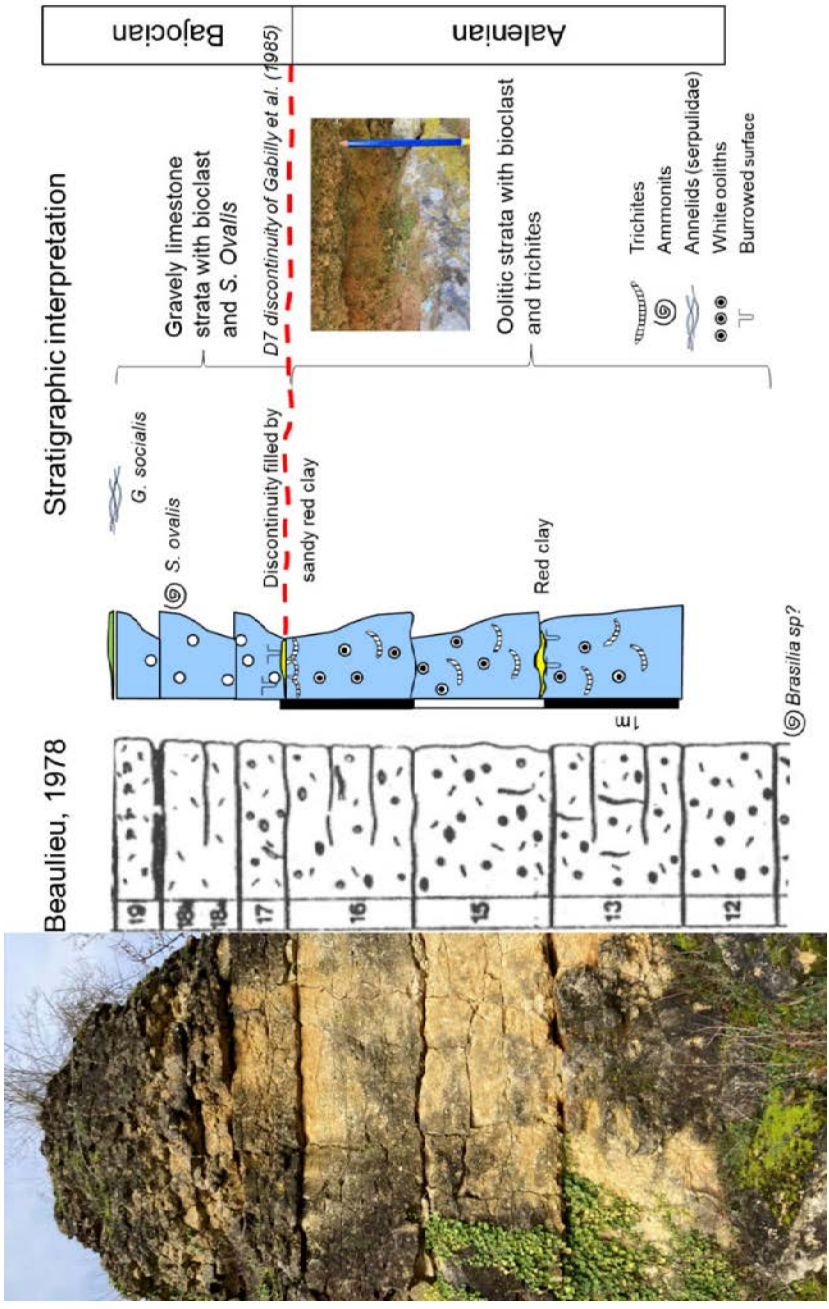

Figure 7 *Example of stratigraphical calibration of discontinuity in the supra-Toarcian aquifer (Latillé, Puy-Hervé quarry).*

a) Type 1 in Boivre Valley (Bajocian, *Humphriesianum* biozone)
Scale bar: 3 m

b) Type 1 in Clain valley (Bajocian, *Humphriesianum* biozone)

c) Type 2 at the bottom of Upper Bajocian (D8 discontinuity) at Poitiers

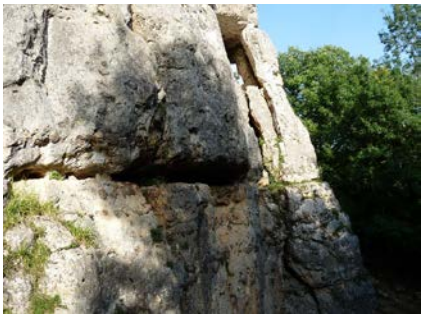

c) Type 2 at the top of the *Garantiana* biozone in the Bajocian (D8bis discontinuity)

Figure 8 *Typology of macroporosity in middle Jurassic limestones on Poitou Threshold.*

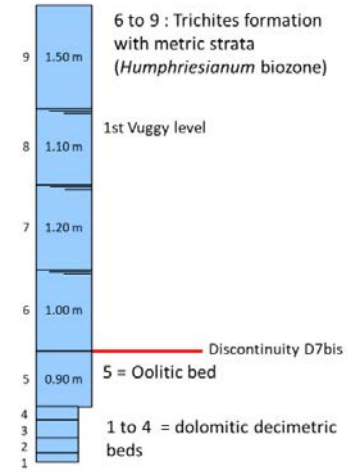

Figure 9 *Vuggy level in* Humphriesianum *zone of upper Bajocian (Saint Benoit - Passelourdin cliff).*

The spatial extent of Type 2 voids forms a sub-horizontal, interconnected macroporous system, due to the low dip of the strata. Locally, these voids form aligned conduits only a few centimeters in diameter, which may evolve into cave networks, such as those observed in Lussac-les-Châteaux, in the Vienne Valley (Fig. 10).

Figure 10 *Macroporosity on D8 discontinuity (Lussac-les-Châteaux cliff).*

Pumping tests

On the Poitou Threshold, the Aalenian and Bajocian limestones are located within the saturated zone. These two geological formations are exploited for drinking water supply (19 million m^3/year according to SAGE Clain, 2011) and for agricultural irrigation (23 million m^3/year). Transmissivity values, estimated using the Cooper-Jacob method (1946), range from 10^{-2} to 10^{-3} m^2/s. The storage coefficient ranges between 10^{-2} and 10^{-4} depending on the borehole. These orders of magnitude were confirmed at the HES (Bernard, 2005). Two series of pumping tests were conducted in 2004 and 2005 after borehole drilling. Transmissivity values interpreted using the Cooper-Jacob method range from $2.2.10^{-3}$ to $4.4.10^{-3}$ m^2/s. Storage coefficients exhibit substantial variability over three orders of magnitude, ranging from $3.6.10^{-4}$ to $2.8.10^{-1}$. However, drawdown data cannot be consistently interpreted using a single straight line on a Cooper-Jacob semi-log plot, rendering the method ultimately inconclusive (Bernard, 2005, p. 125).

Three families of drawdown curves have been identified (Bernard, 2005): 1) The first exhibits a drawdown that doesn't follow a linear trend in the semi-log time domain; 2) The second displays two distinct linear segments in semi-log time, and 3) the third is characterized by a plateau or transition zone between two linear segments.

To improve curve fitting, a solution for interpreting interference pumping tests in a fractally fractured medium of Euclidean dimension two was developed using the

Cooper-Jacob equation (Delay et al., 2004). Bernard et al. (2008) demonstrated that permeability tends to homogenize rapidly over distances of 100–200 m, despite the drawdown data exhibiting significant variability and fractal characteristics. However, this fractal approach applied to fractures does not allow for calibration of the third family of curves. A different modelling approach has recently been applied to interpret pumping tests at the Civaux Nuclear Power Plant[1], located approximately 22 km southeast of Poitiers (see location on Fig. 3). This approach aims to account not only for fractures, but also for the influence of the porosity and permeability of the limestone blocks separating the horizontal discontinuities. The aquifer is conceptualized as containing regularly spaced horizontal discontinuities, which delimit rectangular limestone blocks of uniform thickness b (Fig. 11). For such an aquifer system, Streltsova (1976) proposed two drawdown equations: one for flow through fractures and another for flow through a porous matrix toward a pumping well operating at a constant discharge rate Q. The discontinuities are characterized by a hydraulic conductivity K_f and specific storage Ssf, while the matrix possesses a hydraulic conductivity K_m and specific storage Ssm.

To incorporate the flow dimensionality of Delay et al. (2004), the general Radial Flow equation of Barker was employed (Barker, 1988). This model generalized radial flow in an unsteady, n-dimensional, dual-porosity fractured aquifer. The flow dimension n governs the transition in flow behavior from linear to radial flow regimes. Exchange between the matrix and the fractures is controlled by a skin factor defined as $Sf = K_m b_s / (K_s b)$, where b_s and K_s denote respectively the thickness and hydraulic conductivity of the skin (the wall zone of the limestone block). Figure 11 illustrates pumping in a confined dual-porosity aquifer. The observed

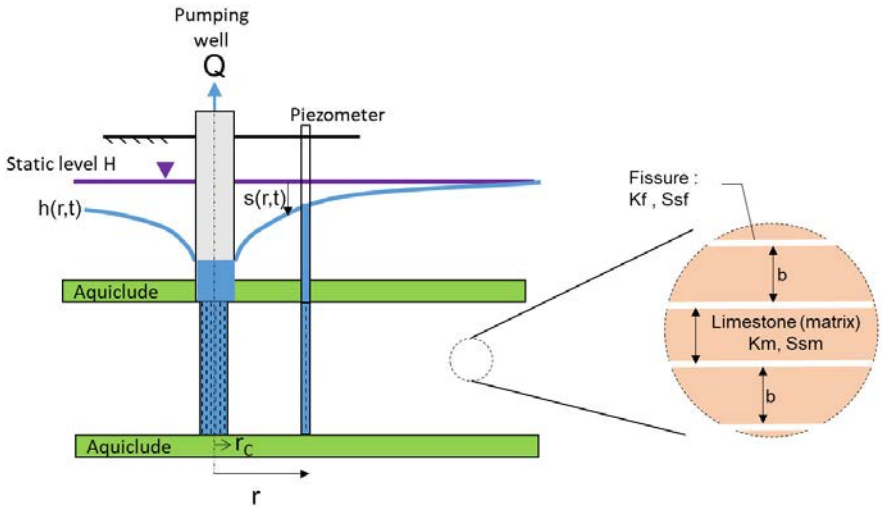

Figure 11 *Diagram illustrating cylindrical flow system (n=2) in a double porosity aquifer.*

1. © EDF 2024: these data are the property of EDF; any use is subject to EDF's prior agreement.

drawdown during a pumping test, at a distance r and time t, is denoted s(r,t) and reflects the total pressure change within the aquifer at the observation point, that is, the pressure variations in the fracture network.

Two examples of pumping tests are presented in Figure 12. On the left, graph (a) shows the results of a pumping test conducted at the HES. The drawdown was measured in observation well M2 during pumping at well M21 at a discharge rate of 62 m^3/h. Well M2 is located 103.7 meters from the pumping well. The drawdown derivative (ds) is shown in red and the drawdown curve in blue (HES) or green (Civaux). Initially, the derivative follows the trend of the drawdown, then decreases until approximately 10^4 seconds. Thereafter, the derivative increases steadily until the end of the test. No wellbore storage disturbs the start of the drawdown curves. On the right, graph (b) presents the results of a pumping test conducted at Civaux[2]. The drawdown was measured at piezometer P1, located 37.2 meters from the pumping well P2. The discharge rate for this test was 51 m^3/h. The drawdown does not exhibit a linear relationship with the logarithm of time. The derivative appears to stabilize around 10^4 seconds, then begins to increase again around 8.10^4 seconds.

To compare the two pumping tests, graph (c) shows the drawdown derivatives of both tests using the dimensionless parameters defined by Streltsova (1976), namely $tD = Tt/(r^2S)$ and $sD = (2\pi s(r, t))/Q$, where t is the pumping time, r is the distance to the pumping well, T is the transmissivity, S is the storage coefficient, s(r,t) is the measured drawdown, and Q is the pumping rate. The transmissivity and storage coefficient values used were those obtained from fitting the early-time data to the Cooper-Jacob straight line. The two presented pumping tests also exhibit a similar dimensionless radius around $rD = 0.01$, allowing them to be compared on the same plot ($rD = r\sqrt{Km / K /b}$). Both pumping tests are plotted in graph (c) of Figure 12. The derivatives of both tests show very similar behaviour, structured in three distinct sequences[3]:

- early-time behavior: The derivative slope ranges between 0.4 and 0.7. This initial stage is interpreted as representing the flow contribution from the horizontal fracture network;
- intermediate-time behavior: The drawdown rate decreases, and the derivative stabilizes. This sequence is interpreted as the contribution from the rock matrix;
- late-time behavior: This phase reflects the combined influence of both fractures and matrix, where the pumping rate exceeds the crossflow from the matrix. As a result, drawdown does not stabilize but instead continues to increase over time.

This method was used to estimate aquifer parameters by interpreting eight pumping tests conducted at the HES and three tests at the Civaux site[4]. At the HES, for each test interpretation, two piezometers aligned with the pumping well were selected to analyse the drawdown curves. For both sites, the thickness of the matrix

2. © EDF 2024: these data are the property of EDF; any use is subject to EDF's prior agreement.
3. © EDF 2024: these data are the property of EDF; any use is subject to EDF's prior agreement
4. © EDF 2024: these data are the property of EDF; any use is subject to EDF's prior agreement

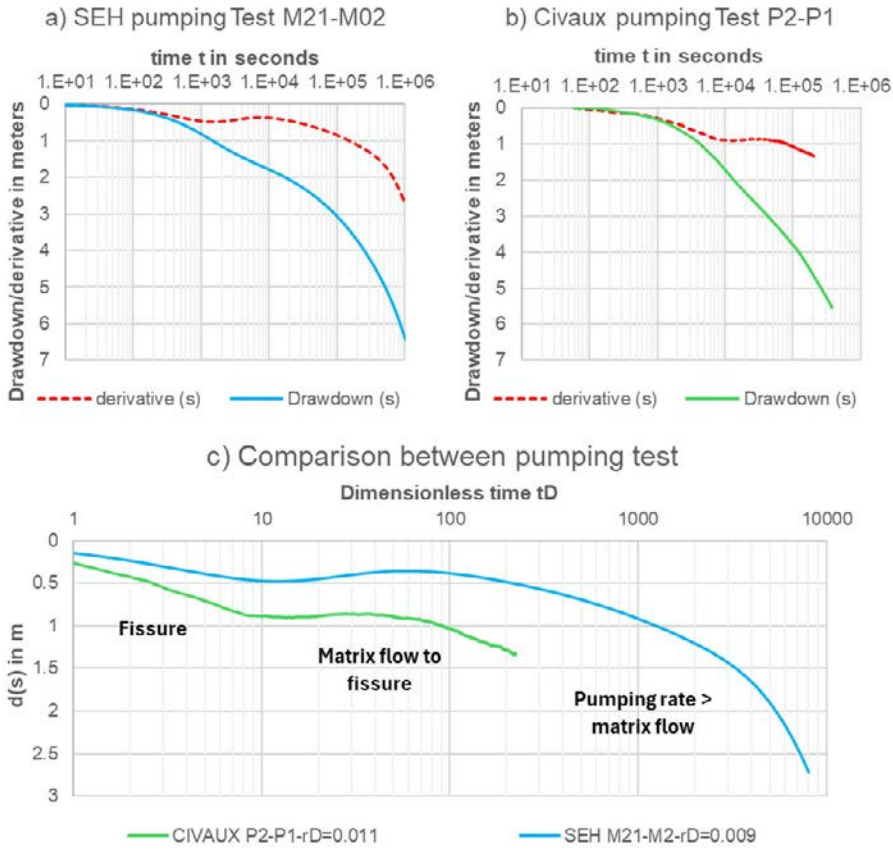

Figure 12 *Pumping test at constant rate. © EDF 2024: these data are the property of EDF; any use is subject to EDF's prior agreement.*

blocks was defined based on the stratigraphic interpretation of each borehole and on the identification of discontinuities between depositional sequences (Gaillard, 2026).

Figure 13 presents the results obtained from the pumping tests conducted at the HES site with AQTESOLV software. In the fracture medium, the hydraulic conductivity (K) appears to be homogeneous, with values ranging between 10^{-4} and 10^{-5} m/s. The specific storage (Ss) of the fractures varies between 10^{-6} and 10^{-3} m^{-1}. This parameter depends on fracture aperture and infilling material, which is consistent with field observations (Fig. 9 and 10) and borehole data. In contrast, data for the matrix are more scattered. The matrix hydraulic conductivity is several orders of magnitude lower than that of the fractures, with values ranging from 10^{-6} to 10^{-9} m/s. The specific storage of the matrix blocks appears to lie between 10^{-5} and 10^{-4} m^{-1}, with the highest value reaching 4.10^{-4} m^{-1}. The fracture skin factor (Sf) varies from 0 to 3, while the flow dimension (n) ranges between 1.5 and 2.

At Civaux (Fig. 14), the parameter values are less dispersed[5]. For the fracture network, hydraulic conductivity remains in the same order of magnitude (10^{-4} to 10^{-5} m/s), and specific storage ranges from 10^{-5} to 10^{-4} m^{-1}. The results for the matrix are also within a narrow range: matrix hydraulic conductivity varies between 10^{-9} and 2.10^{-8} m/s, and the specific storage of the matrix blocks ranges from 10^{-5} to 10^{-4} m^{-1}.

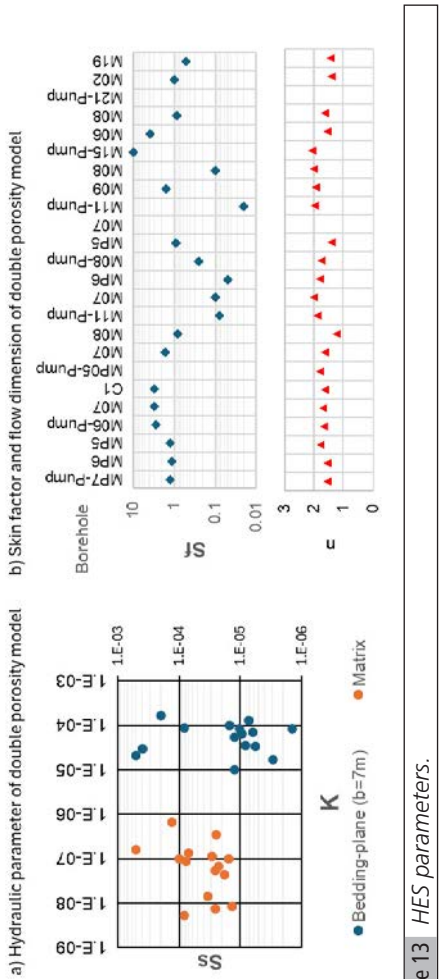

Figure 13 *HES parameters.*

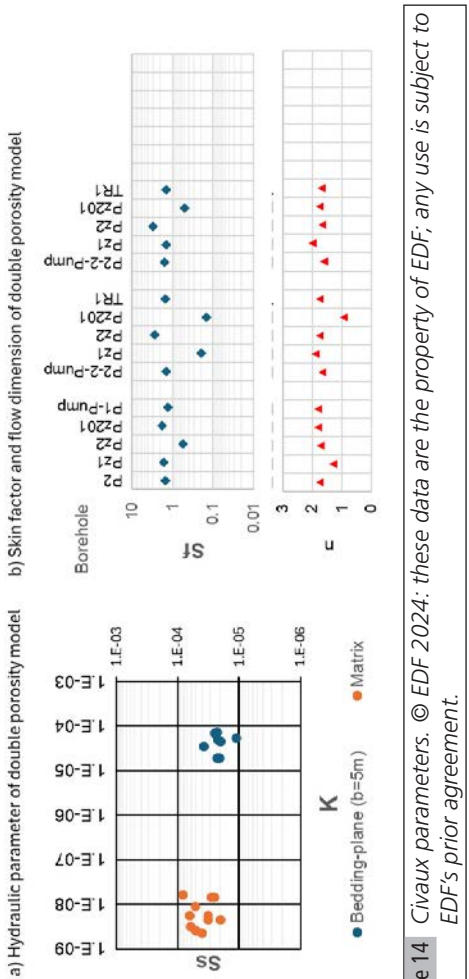

Figure 14 *Civaux parameters. © EDF 2024: these data are the property of EDF; any use is subject to EDF's prior agreement.*

5. © EDF 2024: these data are the property of EDF; any use is subject to EDF's prior agreement.

The dual-porosity model incorporating the flow dimension approach enables the calibration of all observed drawdown curves with a standard error less than 0.02. The matrix/discontinuity skin factor explains the various shapes observed in both the drawdown curves and their corresponding derivatives. An illustrative example is presented in Figure 15. The calibration was performed on both the drawdown curve and its derivative from a pumping test conducted at the HES. Graphs (a) show the drawdowns measured at observation well M19 during pumping at M21 (Q = 62.3 m^3/h). The test was calibrated using a skin factor value of Sf = 0. When the skin factor increases (Sf = 0.5 to 5), a plateau begins to appear on the drawdown

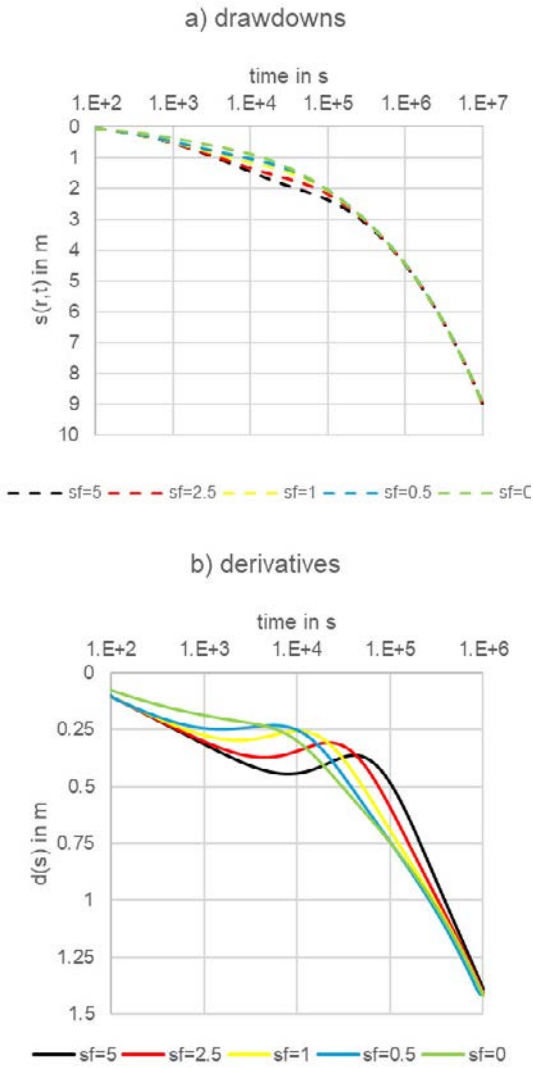

Figure 15 *Drawdown and derivative curves with and without Skin.*

curve. This phenomenon is even more evident in the drawdown derivatives shown in graph (b), where a wave-like shape forms in the derivative curve before dropping off.

Pumping test results from both the HES and the Civaux site[6] demonstrate that the heterogeneity of the supra-Toarcian aquifer can be effectively described using a dual-porosity conceptual model. This modelling approach is consistent with field data and highlights the role of sedimentary discontinuities in controlling groundwater flow.

Conclusion

The Aalenian, Bajocian, and Bathonian limestones constitute microporous aquifers affected by various forms of karstic dissolution. Tectonic structures do not account for the location or geometry of speleological networks, the most extensive of which—the Cuchon Cave—reaches 4,000 m in mapped extent.

To explain the position of karstic outflow systems, a stratigraphic approach is required. Centimeter to decimeter-scale dissolution features have been correlated with the outcrop's stratigraphy. In non-dolomitized limestones, ovoid dissolution features are found within Lower Aalenian strata (*Opalinum* Zone) and Lower Bajocian strata (*Humphriesianum* Zone). Additional voids are associated with stratigraphic discontinuities separating sedimentary sequences. The regional extent of these discontinuities accounts for the recurrence of similar dissolution features in all valleys intersecting the Poitou Threshold.

Pumping tests conducted at two sites[7] on the threshold indicate that the Supra-Toarcian Aquifer behaves as a dual-porosity medium, with horizontal flow paths corresponding to bedding planes and discontinuities.

The role of stratigraphy is often underestimated in karst studies. Nevertheless, several works have demonstrated its importance in the development of horizontal karst systems (Esteban and Klappa, 1983) and in explaining intrinsic permeability variations in carbonate oil reservoirs (Reynolds, 1993). More recently, stratigraphic controls have been invoked to explain the distribution of macroporous levels in Upper Cretaceous Chalk formations in both Normandy (Gaillard et al., 2022) and England (Farrant et al., 2022). The stratigraphic correlation of karst features has revealed basin-scale trends in the Anglo-Norman Basin, enabling the prediction of karstic horizons. This approach is also applicable to the limestones of the supra-Toarcian aquifer of the Poitou Threshold.

6. © EDF 2024: these data are the property of EDF; any use is subject to EDF's prior agreement.
7. © EDF 2024: these data are the property of EDF; any use is subject to EDF's prior agreement

Acknowledgements

The authors are grateful to thank Frédéric Lalbat (Electricité de France) for agreeing to use pumping tests at the Civaux site.

References

Balusseau B. (1980). Le Jurassique inférieur et moyen sur la bordure nord-ouest du Limousin (région de Gouex à L'Isle-Jourdain, Vienne) [The Lower and Middle Jurassic on the north-western of the Limousin area (from Gouex to L'Isle-Jourdain, Vienne)]. Ph.D. thesis, University of Poitiers, France.

Barker J.A. (1988). A generalized radial flow model for hydraulic tests in fractured rock. *Water Resources Research*, 24(10): 1796-1804. https://doi.org/10.1029/WR024i010p01796

Beaulieu, G. (1978). Étude géologique des terrains jurassiques dans la région de Lusignan, Montreuil-Bonnin et Latillé: stratigraphie, cartographie et structure [Geological study of the Jurassic in the Lusignan, Montreuil-Bonnin and Latillé area : stratigraphy, cartography and structure]. Ph.D. thesis; University of Poitiers, France.

Bernard S. (2005). Caractérisation hydrodynamique des réservoirs carbonatés fracturés. Application au site expérimental hydrogéologique (SEH) de l'université de Poitiers [Hydrodynamic Characterization of Fractured Carbonate Reservoirs: Application to the Hydrogeological Experimental Site (HES) of the University of Poitiers]. Ph.D. thesis; University of Poitiers, France.

Bernard S., Delay F., Porel G. (2008). A new method of data inversion for the identification of fractal characteristics and homogenization scale from hydraulic pumping tests in fractured aquifers. *Journal of Hydrology*, 328(3-4): 647-658. https://doi.org/10.1016/j.jhydrol.2006.01.008

Benvel B. (1978). Étude stratigraphique, sédimentologique et structurale du Jurassique dans les vallées du Clain et de la Boivre en amont de Poitiers [Stratigraphic, sedimentological and structural study of the Jurassic in the Clain and Boivre valleys upstream of Poitiers]. Ph.D. thesis, University of Poitiers, France.

Bigot J.-Y. (2004). Spéléométrie de la France : Cavités classées par département, par dénivellation et développement, Situation au 31 décembre 2000 [Caving in France: Caves classified by department, by vertical drop and by development, Situation at December 31, 2000]. *Mémoire Spelunca* 27. https://speluncamemoires.ffspeleo.fr/200407_Spelunca_memoires_27.pdf

Burbaud-Vergneaud M. 1987. Fracturation et interactions socle-couverture : le Seuil du Poitou [Fracturing and Basement-Cover Interaction: The Poitou Threshold]. Ph.D. thesis, University of Poitiers, France.

Branger P., Gailard T., Geairon H. (2026). "The stratigraphy of the Middle Jurassic of the Poitou threshold", Chapter 2 in *A new concept of karst development based on hydrogeology and geophysics*, EDP Sciences. https://doi.org/10.1051/978-2-7598-3934-6.c002

Coirier B. (1964). Essai de coloration à la fluorescéine des eaux de la Dive de Lezay, disparaissant au gouffre de « Jument blanche » près Bonneuil, commune de Sainte-Soline (Deux-Sèvres). Le problème de la source de la Sèvre Niortaise [Fluorescein dye tracer test of the Dive de Lezay, disappearing at the "Jument blanche" sinkhole near Bonneuil, commune of Sainte-Soline (Deux-Sèvres). The problem of the Sèvre Niortaise spring]. *Bulletin de l'Institut de Géologie et d'Anthropologie Préhistorique de la Faculté des Sciences de Poitiers*, V: 25-33.

Coirier B., Moreau P., Bourgueil B., Gabilly J. (1968). Hydrogéologie du plateau jurassique de Poitiers à Chauvigny [Hydrogeology of the Jurassic plateau from Poitiers to Chauvigny]. Bulletin de l'institut de Géologie et d'Anthropologie préhistorique, Université de Poitiers: 12-24.

Cooper H.H., Jacob C.E. (1946). A generalized graphical method for evaluating formation constants and summarizing well field history. *American Geophysical Union Transaction*, 27: 526-534. https://doi.org/10.1029/TR027i004p00526

Delay F., Porel G., Bernard S. (2004). Analytical 2D model to invert hydraulic pumping tests in fractured rocks with fractal behavior. Geophysical Research letters, Hydrology and Land Surface studies, 31(16). https://doi.org/10.1029/2004GL020500

Déribéré M. (1937). Les grottes de La Norée [La Norée caves]. *Spélunca*, 8: 19-23.

Esteban M., Klappa C. (1983). Subaerial exposure environments. In: P.A. Scholle, D.G. Bebout & C.H. Moore (Eds.): Carbonate depositional environments. American Association of Petroleum Geologists, Tulsa, 1-54.

Farrant A.R., Maurice L., Ballesteros D., Nehme C. (2022). The genesis and evolution of karstic conduit systems in the Chalk. Geological Society, London, Special Publications, 517. https://doi.org/10.1144/SP517-2020-126

Gaillard T., Branger P. (2026). "The Poitou Threshold", Chapter 1 in *A new concept of karst development based on hydrogeology and geophysics*, EDP Sciences. https://doi.org/10.1051/978-2-7598-3934-6.c001

Gaillard T. (2026). "Hydrostratigraphic study of the Hydrogeological Experimental Site of Poitiers, France", Chapter 8 in *A new concept of karst development based on hydrogeology and geophysics*, EDP Sciences. https://doi.org/10.1051/978-2-7598-3934-6.c008

Gabilly J., Cariou E., Hantzpergue P. (1985). Les grandes discontinuités du Jurassique : témoins d'évènements eustatiques, biologiques et sédimentaires [Major Jurassic discontinuities: evidence of eustatic, biological and sedimentary events]. *Bulletin de la Société Géologique de France*, I(3): 391-401. https://doi.org/10.2113/gssgfbull.I.3.391

Gaillard T., Hoyez B., Hauchard E. (2022). Contribution of stratigraphy to groundwater motion understanding in chalk: examples of karstogenic horizons of the Pointe de Caux, France. Geological Society of London, Special Publications, 517. https://doi.org/10.1144/SP517-2020-157

Gaillard T., Moreau M. (2024). Le Bajocien de la vallée du Miosson : Nouaillé-Maupertuis [Bajocian of Miosson valley : Nouaillé-Maupertuis]. In Le karst du seuil du Poitou : Approche stratigraphique et rôle de la tectonique, Livret Guide de l'excursion du CFH sur le seuil du Poitou, 29 au 31 mars 2024: 46-49.

Longuemar (Le Touzé de) A. (1856). Études sur la circulation naturelle des eaux superficielles et souterraines dans le département de la Vienne [Studies on the natural circulation of surface and ground water in the Vienne department]. Journal de la Vienne. Poitiers.

Marchais E., Bichot G. (2005). Référentiels piézométriques Phase 3 : Piézométries de l'aquifère du Dogger [Piezometric maps of the Dogger aquifer]. BRGM/RP-55847-FR.

Mourrier J.-P. (1983). Le versant parisien du seuil du Poitou de l'Hettangien au Bathonien. Stratigraphie, sédimentologie, caractères paléontologiques, Paleogéographie [The Parisian slope of the Poitou sill from the Hettangian to the Bathonian. Stratigraphy, sedimentology, paleontological features, paleogeography]. Ph.D. thesis, University of Poitiers, France.

Mourier J.-P., Gabilly J., Platel J.-P. (1986). Carte géologique de la France : Notice explicative de la feuille Poitiers à 1/50000 [Geological map of France: note for the Poitiers 1:50,000 sheet]. BRGM.

Reynolds A.D. (1993). Sedimentology and sequence stratigraphy of the Thistle field, northern North Sea, In Sequence Stratigraphy on the Northwest European Margin by Steel R.J., Felt V.L., Johannesson E.P., Mathieu C. (Editors). *Norwegian Petroleum Society Special Publications*, 5: 257-271.

Schéma d'Aménagement et de Gestion des Eaux du Clain "SAGE" (2011). État Initial (water development and management scheme for the river Clain (SAGE), 2011. initial status).

Sibert E., Loiseau C., Rouy J.-L. (2008). La grotte de la Vallée Cuchon (Chauvigny, Vienne) [Cuchon valley cave, Chauvigny, Vienne]. *Spelunca*, 10: 21-26.

SCP/ Spéléo-Club Poitevin (1990). Bilan d'activités.

Streltsova T.D. (1976). Hydrodynamics of groundwater flow in a fractured formation. Water Resources Research, 12(3): 405-414. https://doi.org/10.1029/WR012i003p00405

Welsch J. (1912). Hydrologie souterraine du Poitou calcaire [Underground hydrology of the Poitou limestone area]. Spelunca, IX (69).

4

The Hydrogeological Experimental Site of Poitiers University (France)

T. Gaillard

Origin of the hydrogeological experimental site (HES)

In 1991, the French government decided to create a storage site for long-lived nuclear waste. After studying some thirty sites, three of them were selected for an underground laboratory: Bures (Meuse and Haute-Marne), Chasclan (Nord), and La Chapelle Bâton (Vienne). In the end, the Chapelle-Bâton site was not selected due to severe fracturing of the granite. However, the abandonment of this site enabled part of the Jurassic research program to be transferred to the *Le Deffend* site near Poitiers (Commune of Mignaloux Beauvoir) as part of the XIIth "Etat-Region" plan (CPER 2000-2006). The research objective, led by Gilles Porel and his team at the University of Poitiers, was initiated to experimentally test theories on fractured media in terms of flow, pollutant transport, and identification of hydrodynamic parameters (Bernard, 2005).

The Poitiers Hydrogeological Experimental Site (HES) was then developed next to a botanical garden of Poitiers University (Le Deffend). The site covers 33 hectares,

© EDP Sciences, 2026
DOI: https://doi.org/10.1051/978-2-7598-3934-6.c004

and a large meadow was used for drilling (Fig. 1). The HES is animated by the IC2MP/Hydrasa team (UMR CNRS 7285) as part of the National Network of Hydrogeological Sites (SNO H+) and the 'EAUX' programs of the former Poitou-Charentes region (CPER 2002-2006 and 2007-2013).

Figure 1 *Aerian view of the HES.*

HES description

The HES is situated in the middle of the Poitou threshold, in the watershed of the Clain river (Fig. 2). The plateau is above 125 m above sea level, and a little talweg crosses the site.

The first drilling campaign (2002) resulted in the completion of eight wells distributed over a wide area, intending to establish a protocol for positioning future boreholes. However, the heterogeneous nature of the formations encountered and the discharge rates observed by air-lift testing did not allow for the development of a drilling strategy based on lithology or fracturing. Consequently, a "five-spot" design was adopted for subsequent boreholes.

Widely used in the oil and gas industry to maximize reservoir recovery, the five-spot scheme enhances fluid circulation and reservoir drainage by positioning one central well surrounded by four additional wells located at the corners of a square. At the beginning of summer 2003, a second drilling campaign was initiated to install the experimental system, which was completed at the end of 2004. Following these three phases, the system now provides four distinct mesh sizes: i) 13 meshes with 70-m sides, ii) 5 meshes with 100-m sides, iii) 5 meshes with 140-m sides, and iv) 1 mesh with 210-m sides (Fig. 3).

At present, the experimental platform comprises 45 boreholes, including two vertical and two oblique cored holes. The vertical cores (C1 and C2) were drilled to investigate sedimentary heterogeneity and fracturing in the limestones, while the two oblique cores (C4 and C5) targeted potential fault zones (see location on Fig. 2).

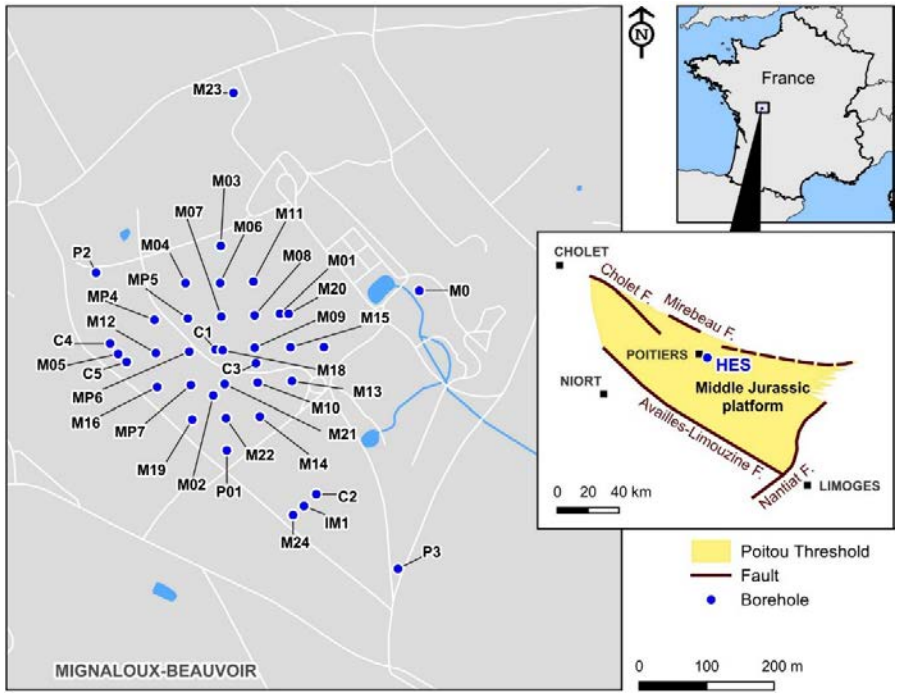

Figure 2 *Location of HES boreholes.*

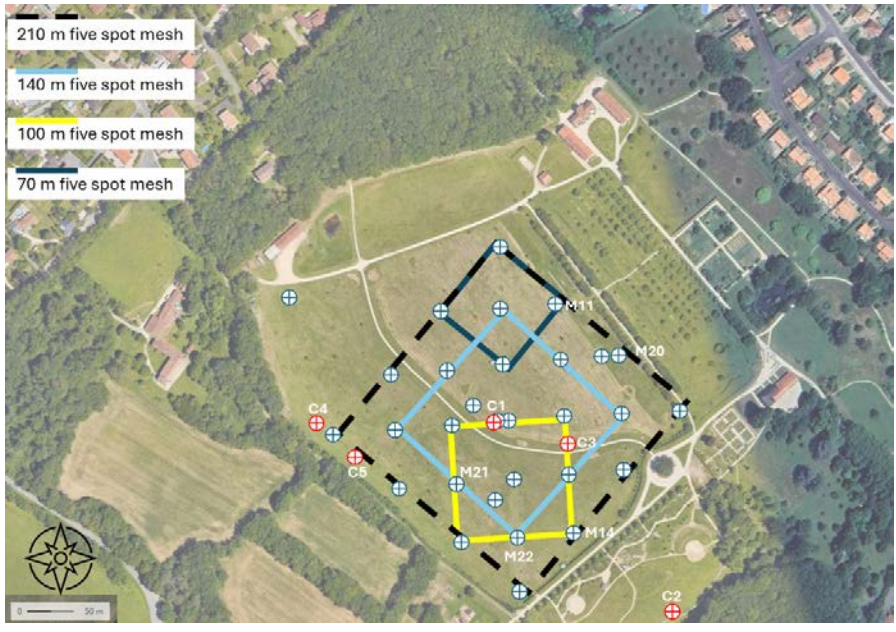

Figure 3 *Mesh size distribution of the defend HES.*

The HES boreholes are either left uncased or fitted with casings screened across the full thickness of the Supra-Toarcian aquifer. As a result, the piezometric level recorded in the boreholes reflects an average hydraulic head over the aquifer's thickness. Under natural conditions, piezometric levels range between 20 and 25 m below the ground surface. Drilling consistently revealed dry clayey limestones down to about 30 m, confirming that the Dogger aquifer is confined beneath this low-permeability formation. Two additional boreholes (C2 and IM1, each ~160 m deep) were drilled into the crystalline basement to monitor hydraulic heads in the Infra Toarcian aquifer during hydraulic testing in the other wells. No pressure disturbances were ever detected in the Infra-Toarcian aquifer, demonstrating that they are effectively isolated from the Supra-Toarcian aquifer by the Toarcian marls (Porel, 2024).

Scientific studies

Since 2002, investigations carried out on the HES have resulted in the collection of a large amount of data concerning the Supra-Toarcian aquifer (Mari and Porel, 2024). These data, now archived in the H+ database (http://hplus.ore.fr/poitiers/donnees-poitiers), concern:

- the geological structure of the reservoir: stratigraphy/lithology on two core drillings, 3D seismic imaging of the reservoir, Vertical seismic profiles (VSP), Full waveform acoustic logging, Gamma ray logs, acoustic imaging, high-resolution camera, and optical televiewers acquisition (OPTV);
- petrophysical properties of carbonate rocks: laboratory porosity and permeability measurements on core samples;
- flow structure in boreholes: heat-pulse flowmetry, cross-flow logs; temperature-conductivity logs;
- groundwater dynamics under "natural" and/or forced flow conditions: pumping tests and slug tests;
- transport dynamics (non-reactive) in forced flow: Radially convergent tracer tests (RCT).

HES is currently used for the training in hydrogeology and geophysics of young professionals and students coming from universities and high schools. HES is used to study the vadose zone, and data collected since 2002 could be useful to study the impact of climate change on groundwater.

The site gives universities and private companies the opportunity to conduct in situ tests and research projects, for example, the "Karst'ogène" project of CPGF HORIZON.

References

Bernard S. (2005). Caractérisation hydrodynamique des réservoirs carbonatés fracturés [Hydrodynamic characterization of fractured carbonate reservoirs], Ph.D. thesis, University of Poitiers, France.

Porel G. (2024). Le site expérimental hydrogéologique du Deffend in Le karst du seuil du Poitou : Approche stratigraphique et rôle de la tectonique, Livret Guide de l'excursion du CFH sur le seuil du Poitou, 29 au 31 mars 2024: 64-73 [The Deffend hydrogeological experimental site in the Poitou Threshold karst: Stratigraphic approach and role of tectonics, CFH excursion guidebook on the Poitou threshold, 29 to 31 March 2024].

Mari J.-L., Porel G. (2024). The Hydrogeological Experimental Site of Poitiers: Hydrogeological versus Geophysical investigations, *E3S Web of Conferences* 504, 05003, Journées Scientifiques AGAP Qualité 2024. https://doi.org/10.1051/e3sconf/202450405003

5

Geophysical methods

J.-L. Mari

Studies conducted at the Hydrogeological Experimental Site (HES) focus mainly on the Dogger Aquifer. Conventional hydrogeological surveys have investigated the site, which was also subjected to geophysical investigations both from the surface and in wells. These studies include conventional hydrological surveys and geophysical investigations, both from the surface and in wells. On the site, 35 boreholes have been drilled (Fig. 1).

In 2004, 3D seismic data were recorded to obtain a 3D velocity model in depth. A vertical seismic profile (VSP) was recorded in borehole C1 to perform the time-to-depth conversion of the seismic block. An acoustic tool was run in boreholes C1, MP5, MP6, M08, and M09 to record full waveform acoustic data and compute velocity logs used as constraints for converting seismic amplitudes in pseudo-velocities during the inversion process. The resulting 3D seismic pseudo-velocity block revealed three main high-porosity, presumably water-producing layers, at depths of 35-40, 85-87, and 110-115 m that were identified as karstic levels.

Multi-borehole logging investigations were carried out at the HES site (Audouin et al., 2008). To confirm the presence of karstic layers, both acoustic and seismic borehole data were collected from several boreholes. In the low-frequency range (10–150 Hz), Vertical Seismic Profile (VSP) data were acquired using a hydrophone sensor, which is particularly sensitive to Stoneley waves — commonly used to detect subsurface discontinuities such as fractures or faults. In the high-frequency range (1–20 kHz), full waveform acoustic logs were recorded to provide a detailed characterization of the formations.

© EDP Sciences, 2026
DOI: https://doi.org/10.1051/978-2-7598-3934-6.c005

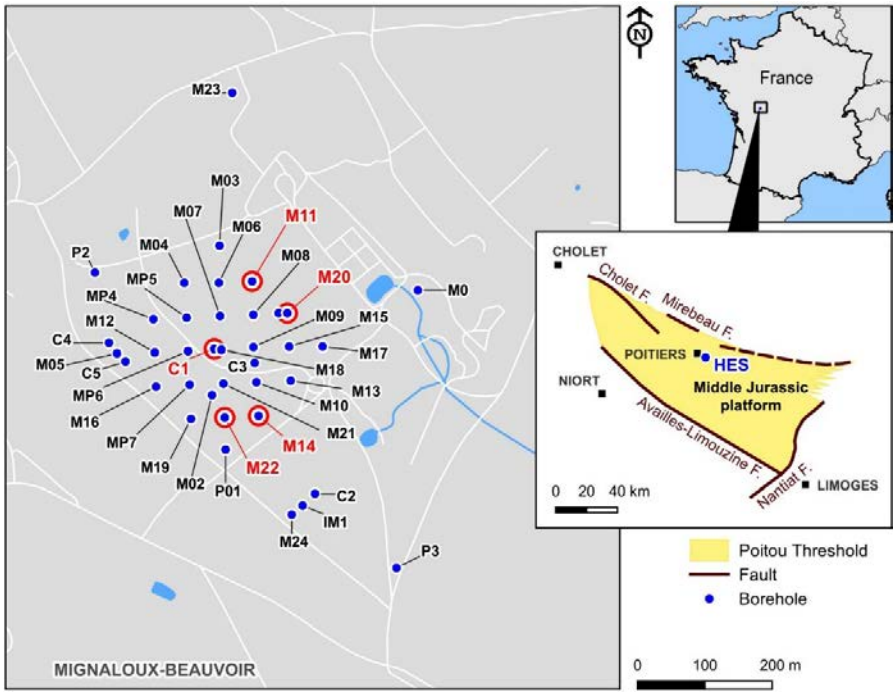

Figure 1 *The hydrological experimental site and borehole locations. Boreholes C1, M11, M14, M20, and M22 (indicated by red circles) were selected for seismic and stratigraphic characterization of karstogenic horizons.*

In 2014, the acoustic tool was rerun in boreholes C1, MP5, MP6, MP7, M03, M05, M11, M13, M14, M20, and M22. In 2015, VSP with hydrophones was recorded in boreholes C1, M03, M04, M07, M11, M20, MP6, and MP7. In each borehole, in addition to VSP recording, ambient noise measurements were done.

Boreholes M11, M14, M20, and M22 were selected for seismic and stratigraphic characterization of karstogenic horizons (Gaillard et al., 2024).

The chapter presents an overview of the field experiments conducted using mainly seismic and acoustic methods and shows their relative contribution to the understanding of the experimental site. Boreholes C1 and M20 are selected to illustrate the VSP method. Boreholes C1, M11, M14, M20, and M22 are selected to illustrate the acoustic method.

5.1 Seismic and acoustic methods

The 3D survey was designed to obtain a 3D block based on records of low amounts of data [1, 2, 3]. The complete survey is composed of 20 receiver lines (the in-line direction) with a 15 m lag distance between adjacent lines (Fig. 2a), each line being composed of 48 single geophones with 5 m spacing between adjacent geophones. For each receiver line investigated, direct and reverse shots (source in line with the receiver line) were recorded (Fig. 2b top), as well as cross-line shots fired at distances of 40, 50, and 60 m perpendicular to the receiver line (Fig. 2b bottom). Processing the data from in-line direct and reverse shots gathers the results in a vertical section of 240 m in-line extension (the blue arrow, in

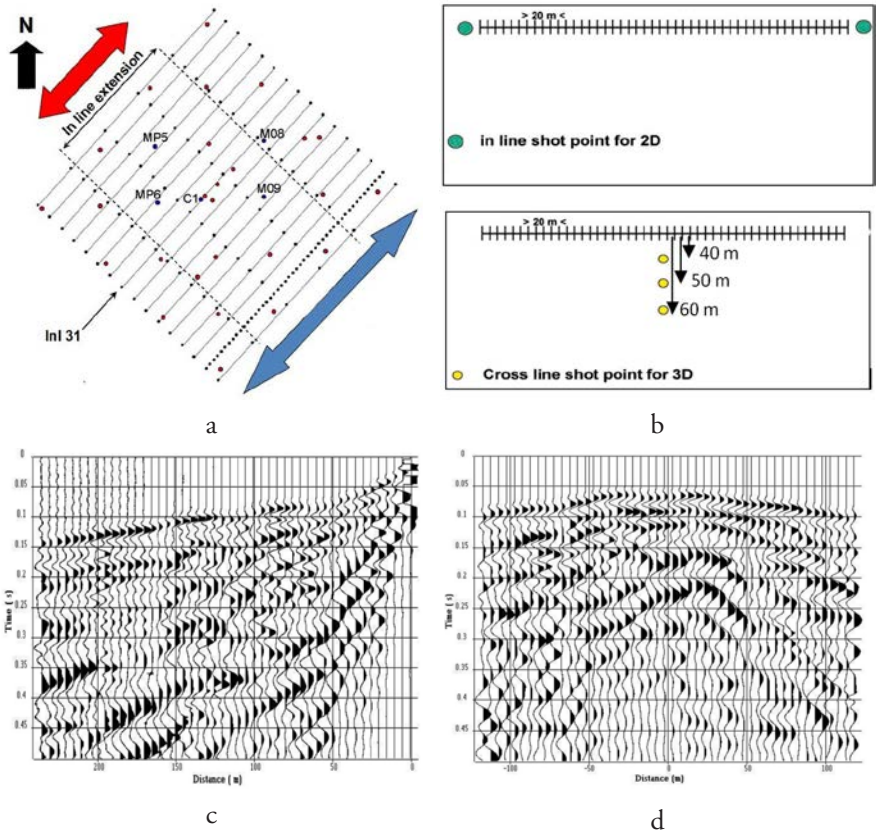

Figure 2 *Seismic spreads and field implementation of seismic lines. Modified after Mari et al. 2008 and 2011. (a) Seismic line implementation: the distance between two adjacent lines is 15 m; red points indicate well locations. (b) Seismic spreads: A direct shot and a reverse shot are fired in line to obtain 2D seismic images (top). Several shots are fired cross-line to obtain 3D seismic images (bottom). (c) Example of in-line shot gather, d) Example of cross-line shot gather with 60 m of lateral offset.*

Fig. 2a) with an in-line extension of 240 m, while a cross-line shot gathers results in a vertical section of only 120 m extension along the in-line direction (the red arrow on the location map of seismic lines, in Fig. 2a). Figures 2c and 2d show examples of an in-line shot (Fig. 2c) and a cross-line shot with a lateral offset of 60 m, respectively (Fig. 2d).

The range of offsets was selected to optimize the quality of the seismic image over the reservoir depth interval, i.e., between 40 m and 130 m. A 40 m minimum offset distance was chosen to reduce the influence of the surface waves. The time-sampling interval was 0.25 ms, and the recording length was 0.5 s.

To perform the time-to-depth conversion of the seismic block, a vertical seismic profile (VSP) was recorded in borehole C1, using a vertical geophone as a borehole sensor. The source is a light seismic source (weight dropper). The sensor was clamped in the borehole, in the 25–120 m depth interval, with a depth sampling interval of 2.5 m. The time-sampling interval was 0.25 ms, and the recording length was 0.5 s. The VSP record is shown in Figure 3a. The vertical axis represents the recording time, and the horizontal axis represents the depth locations of the borehole sensor. The first arrival wave is the down-going P-wave. The picking of its arrival times at the different sensor locations is used to compute both the time vs depth law and the Rms-velocity log (Fig. 3b).

Acoustic data were recorded in borehole C1. The acoustic probe (Gaudiani, 1979) is a flexible monopole tool holding a source as a magnetostrictive transducer and a pair of far receivers (3 and 3.25 m offsets beneath the source). The acoustic data were recorded in the 1–20 kHz frequency band. The sampling intervals are 5 µs in time and 5 cm in depth. In a vertical well, monopole tools can enable the recording of five propagation modes including: refracted compression waves (P), refracted shear waves (S, only in fast formations VS > VP fluid, P-wave velocity of the borehole fluid), fluid waves (F), and two dispersive guided modes as pseudo-Rayleigh waves (in fast formations), and Stoneley waves (ST). The acoustic logs associated with the different waves are very high-resolution logs and can be compared with core measurements. The acoustic logs currently obtained for each type of wave are velocity or slowness logs, frequency, and attenuation logs. Full waveform acoustic measurements can be represented as constant-offset sections. A constant-offset section is a set of acoustic records represented as a function of depth and obtained with a fixed source-to-receiver distance. Figure 3c shows the 3m constant-offset acoustic section, with the identification of the refracted P-wave (P), the converted refracted S-wave (S), and the Stoneley wave. One can notice a strong attenuation of the different waves (P, S, Stoneley) in the 50–53 m depth interval, which corresponds to a karstic level (Mari & Porel, 2015).

Figure 3d shows the velocity logs computed from the picked arrival times of the refracted P-wave at the two receivers of the acoustic probe. The acoustic velocity log (Fig. 3d left) has been filtered (Fig. 3d right) to have a vertical resolution compatible with the seismic resolution to invert the seismic data to recover seismic velocities from seismic amplitudes.

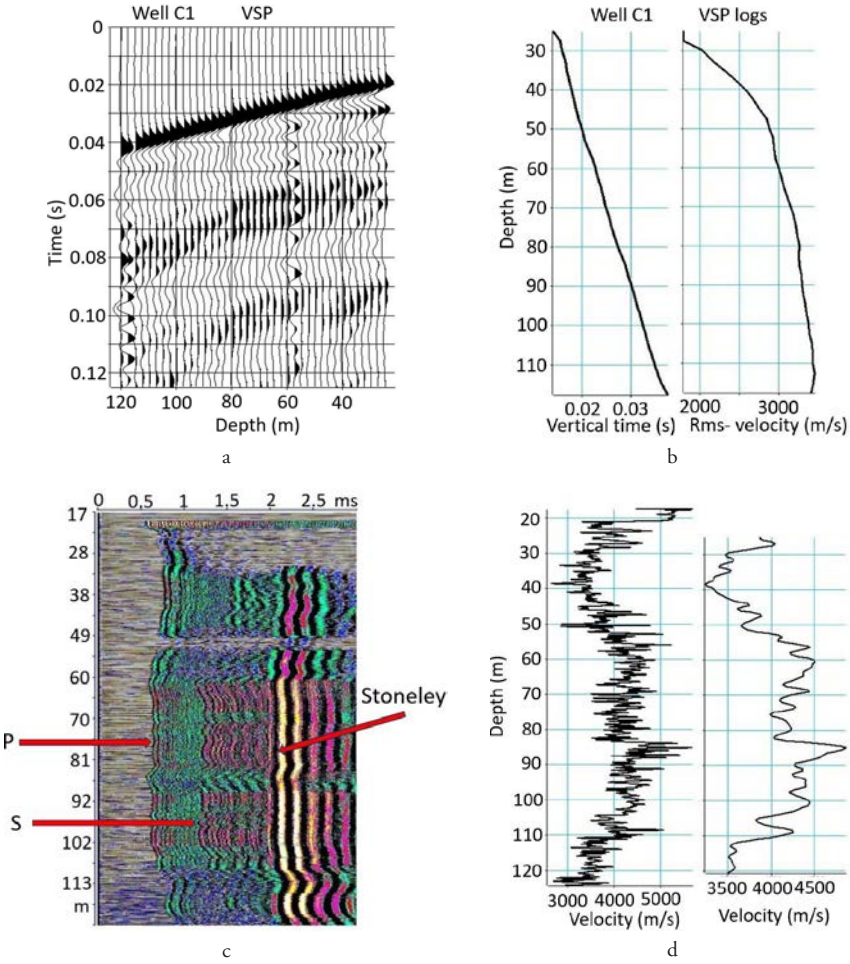

Figure 3 *Vertical Seismic Profile (VSP) and acoustic logging at well C1. Modified after Mari et al. 2009, Delay et al., 2022. (a) VSP section. (b) Time vs depth law and Rms-velocity log. (c) Acoustic section; vertical axis: depth in m, horizontal axis: time in ms. (d) acoustic velocity logs.*

Combined analyses of geophysical and hydrogeological data can be conducted locally at wells or at a larger scale using 3D seismic data. These studies are done for the purpose of detecting water-producing levels at wells and establishing a probable network of karst conduits. An integrated approach based on tracer tests and geophysical data has been developed for identifying effective three-dimensional (3D) discrete karst conduit networks (3D velocity block, Fig. 5) (Bodin, Porel et al., 2022).

5.2 3D seismic imaging

The processing sequence has been described in detail in several publications (Mari & Porel 2008, 2018, and Mari & Delay, 2011), so it is only briefly explained here. Each shot point was processed independently (both in the cross-line direction and in the in-line direction) to obtain a single-fold section with a sampling interval of 2.5 m (half the distance between two adjacent geophones) in the in-line direction. The processing of an in-line direct and reverse shot gather has made it possible to obtain a single-fold section with an in-line extension of 240 m (indicated by a blue arrow on the seismic line map, Fig. 2a) while a cross-line shot gather has provided a single-fold section with an in-line extension of 120 m (indicated by a red arrow on the seismic lines map, Fig. 2a).

A 3D refraction seismic tomography (Mari & Mendes, 2012) was done to map the irregular shape of the top of the karstic reservoir and to obtain static corrections (obtained by inversion tomography after geostatistical analysis, see appendix) and a velocity model of the overburden. To add information to the inversion procedure, we used in-line and cross-line cross shots simultaneously, with an offset of 60 m. The shots were selected to ensure that the refracted wave was the first arrival wave, regardless of the source-receiver distance. The picked times of the first seismic arrivals for all shots (in-line and cross-line shots), and both the depth map of the top of the reservoir and the velocity model obtained by the Plus–Minus (Mari & Mendes, 2019) method were used as input data for the tomographic inversion procedure.

The processing sequence (Mari & Porel, 2008, 2018) includes amplitude recovery, deconvolution, wave separation, static corrections (obtained by inversion tomography) and normal move-out (NMO) corrections, using the Vrms velocity log obtained from VSP recorded in borehole C1 (Fig. 3a and 3b). The VSP time versus depth law (Fig. 3b) was also used to convert the time sections into depth sections with a 0.5 m depth sampling interval. The single-fold depth sections were merged to create the 3D block. The width of the block in the in-line direction is 240 m, and 300 m in the cross-line direction. In the in-line direction, the abscissa zero indicates the location of the source line. The abscissa of the reflecting points ranges between -120 m and 120 m in the in-line direction. The distance between the two reflecting points is 2.5 m. In the cross-line direction, the distance between two reflecting points is 5 m. The depth sections were deconvolved to increase the vertical resolution. They were then integrated to transform a 3D amplitude block into a pseudo-velocity block, using velocity functions (filtered sonic logs obtained by full waveform acoustic logging at boreholes C1 (Fig. 3d), MP5, MP6, M08, and M09 as constraints. The pseudo-velocity sections of the 3D block thus obtained were merged with those obtained by refraction tomography to create a 3D extended velocity model from the surface. Figure 4 shows the in-line 31 pseudo-velocity section. The upper part of the figure shows the velocity distribution obtained by refraction tomography. The seismic section clearly shows nearly horizontal stratifications with strong lateral variations of seismic velocities. Figure 5 shows both the 3D seismic velocity model from 35 to 130 m below the ground surface and the

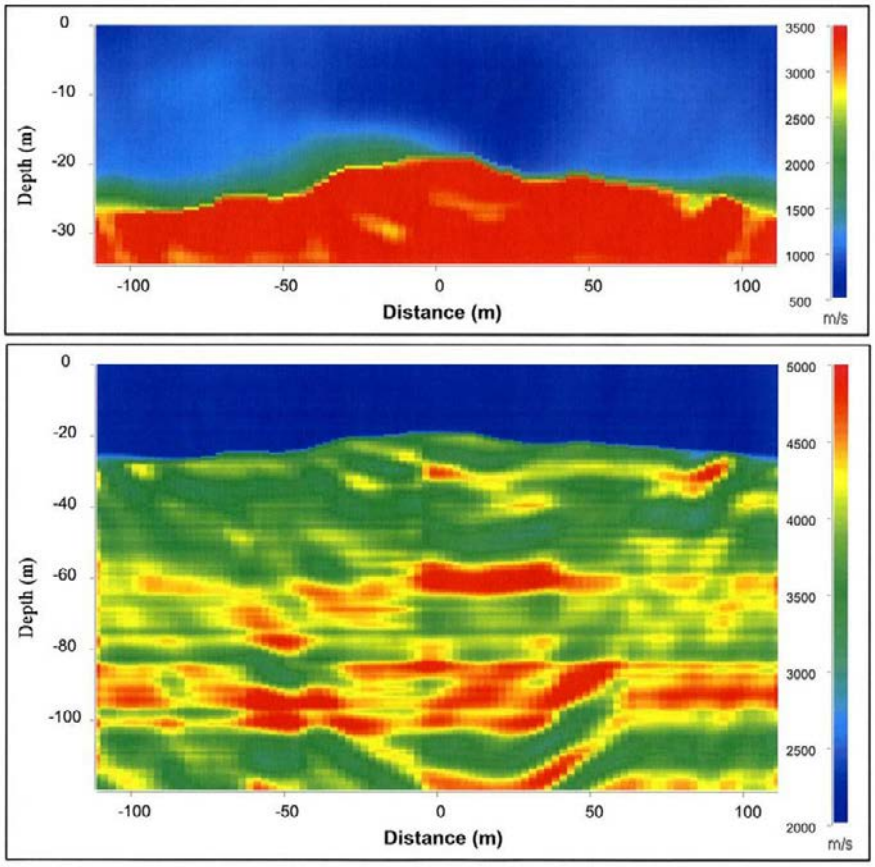

Figure 4 *3D seismic imaging: in-line 31 pseudo-velocity section (upper part: zoom of 0 to 35 m depth interval). Modified after Mari et al., 2018.*

seismic velocity logs extracted from the 3D block at borehole locations M11, M14, M20, and M22. We notice a strong velocity decrease in the 80–90 m depth interval.

To quantify porosity variations within this aquifer, the seismic interval velocities were first converted into resistivity values. For this purpose, the empirical relationship between seismic velocity and resistivity proposed by Faust [1953] was used (Mari, Porel & Bourbiaux, 2009). At each well where a long normal log Rt (Chapellier, 2001b) has been recorded, an interval velocity log V was extracted from the 3D block. The two sets of data (resistivity Rt and seismic velocity V) were combined to compute empirical Faust's laws which were used to transform the 3D pseudo-velocity block into a 3D pseudo resistivity block, using resistivity functions (resistivity logs Rt recorded at 12 wells MP4, MP5, MP6, M11, M13, M14, M18, M21, M04, M07, M08 and M09) as constraints. Figure 6a shows comparisons between resistivity logs Rt from logging and resistivity logs Rt-seis from seismic velocity at boreholes M11 and M14. Figure 6b shows the resistivity logs Rt-seis at

boreholes M11, M14, M20, and M22, which highlight a strong resistivity decrease in the 80–90 m depth interval. Resistivity values were then converted into porosity values, using Archie's law (1942). The resulting 3D seismic pseudo-porosity block (Fig. 7a) revealed three high-porosity layers, at depths of 35 to 55 m, 85 to 87 m,

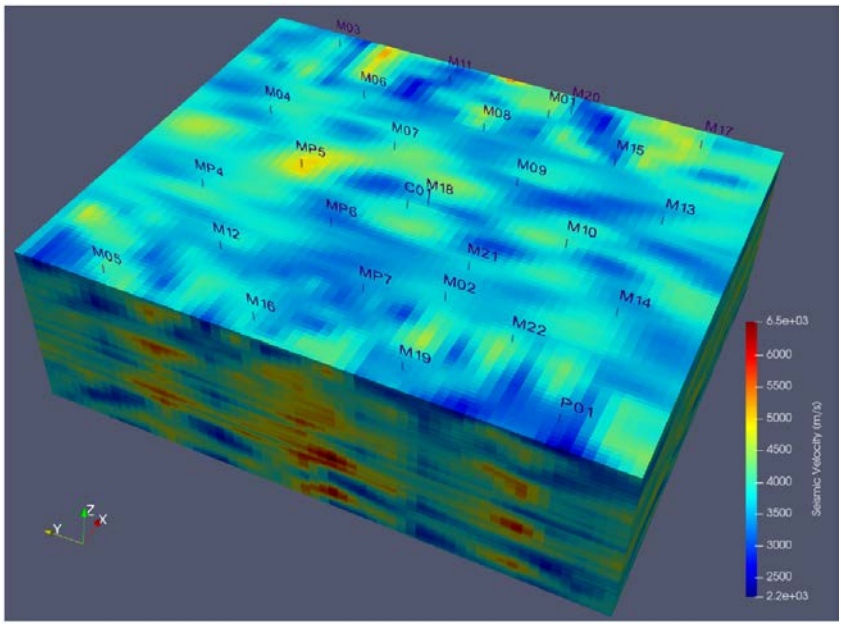

(a)

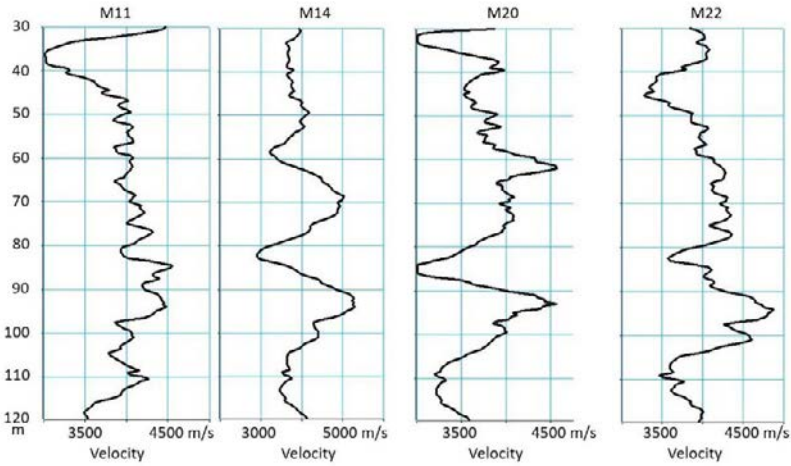

(b)

Figure 5 *3D seismic imaging. (a) 3D seismic velocity model from 35 to 130 m below the ground surface. Modified after Bodin et al. 2022. (b) Velocity log extracted from the 3D block at borehole locations: M11, M14, M20, and M22.*

and 110 to 115 m. The 85 to 87 m layer is the most porous, with porosities higher than 30 %, which represents the karstic part of the reservoir. Figure 7b shows the seismic pseudo-porosity logs extracted from the 3D block at boreholes M11, M14, M20, and M22.

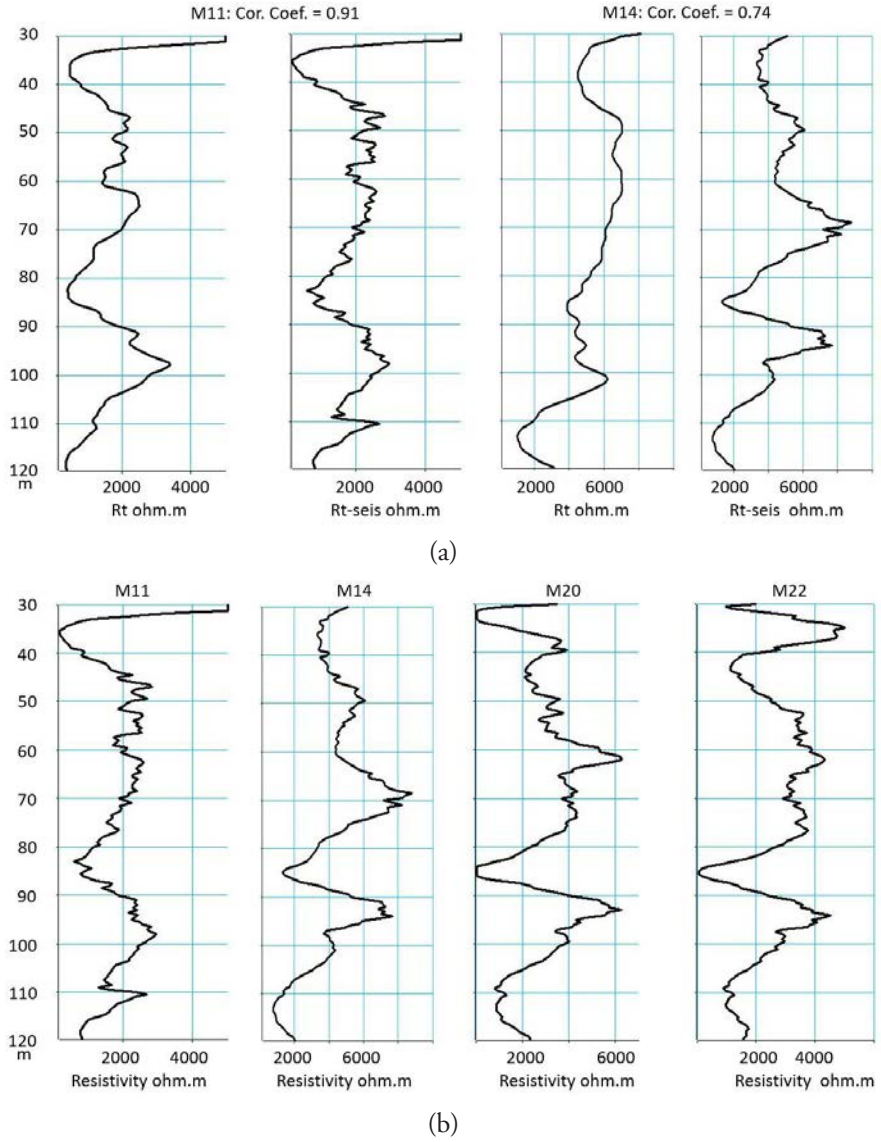

Figure 6 *Resistivity log from the 3D velocity block. (a) Comparison between the resistivity log from logging and resistivity log from seismic velocity at boreholes M11 and M14. (b) Resistivity log from seismic velocity at boreholes M11, M14, M20, and M22.*

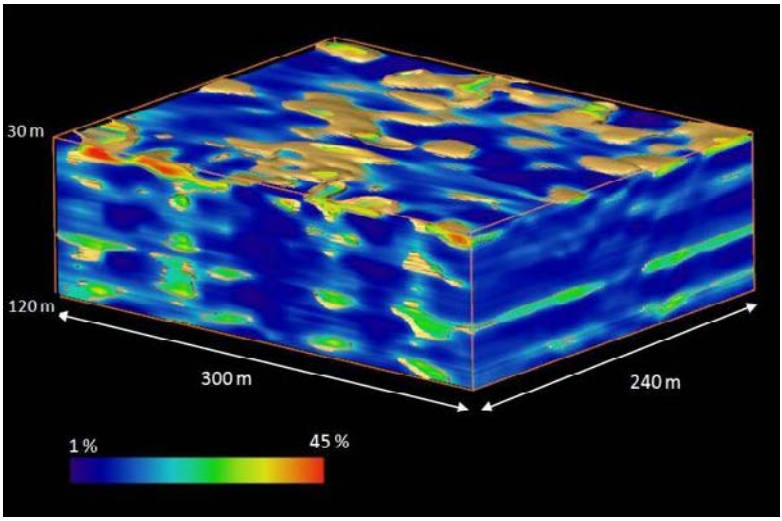

(a)

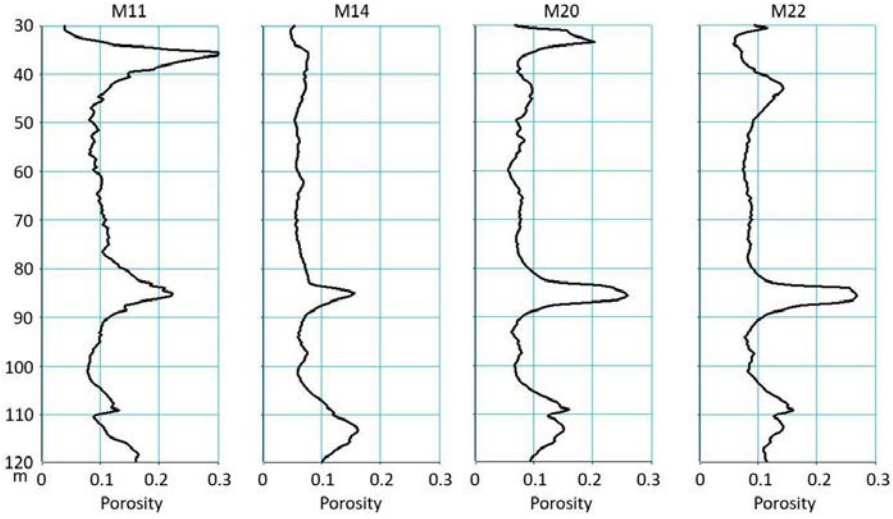

(b)

Figure 7 *3D porosity block. (a) 3D Seismic porosity block in the 30–120 m depth interval. Modified after Mari et al. 2009, Delay et al., 2022. (b) Seismic porosity logs extracted from the 3D porosity block at boreholes M11, M14, M20, and M22.*

Figure 8a shows the distribution of porous bodies in the 80 to 120 m depth intervals. Figure 8b shows the porosity distribution (A) and karstic body extension (B) in the central part of the 3D block.

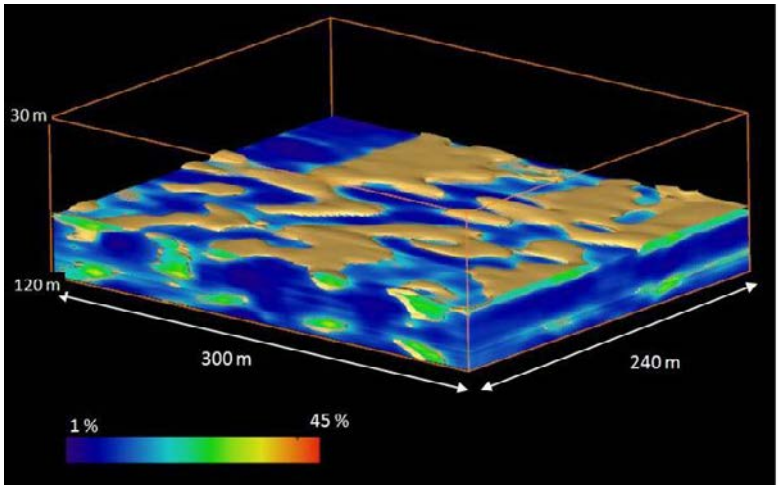

(a)

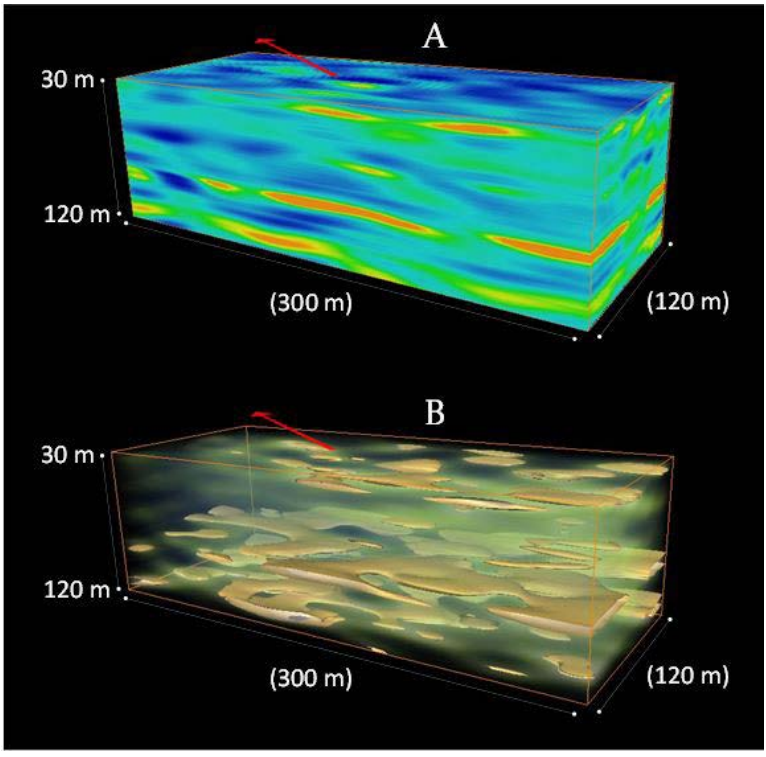

(b)

Figure 8 *3D Seismic porosity block. (a) Porosity distribution in the 80–120 m depth interval. Modified after Mari et al. 2009, Delay et al., 2022. (b) b: Porosity distribution (A) and karstic body extension (B) in the central part of the 3D block. Poitiers University document.*

5.3 Full waveform acoustic logging

Processing based on Singular Value Decomposition (Mari & Porel, 2018) was conducted independently on the two offset sections (3 m and 3.25 m) recorded with the acoustic tool. The processing is done to extract the wavelets associated with the different waves (refracted P-wave, converted refracted S-wave, and Stoneley wave) on the two sections. For a wave type (for example, the refracted P-wave), the correlation of the two wavelets observed at offsets 3 m and 3.25 m enables the simultaneous computation of the formation velocity V, the correlation coefficient between the wavelets, and the amplitude of each wavelet. The amplitude measurements can be used to compute amplitude ratio and attenuation logs, which can be expressed in dB and dB/m. Figure 9 shows the velocity, correlation, and attenuation logs computed from acoustic sections (Fig. 2c) recorded in borehole C1. In the 50–53 m depth interval, which corresponds to a karstic level, we notice a significant decrease in velocity, a very low correlation coefficient, and strong attenuation. The same observations can be made in the 85–90 m depth interval on the correlation and attenuation logs.

SVD processing leads to the calculation of a specific attribute used to detect karstic levels. The attribute, called Karstic Index, is the product of three normalized terms:

- a velocity term: $CV = 1 - (V/V_{max})$. The lower the velocity, the higher the velocity term. In karstic zones, a high CV coefficient is observed;
- an amplitude ratio term: $CAR = 1 - (AR/AR_{max})$, where AR is amplitude ratio. In karstic zones, a high CAR coefficient is observed;

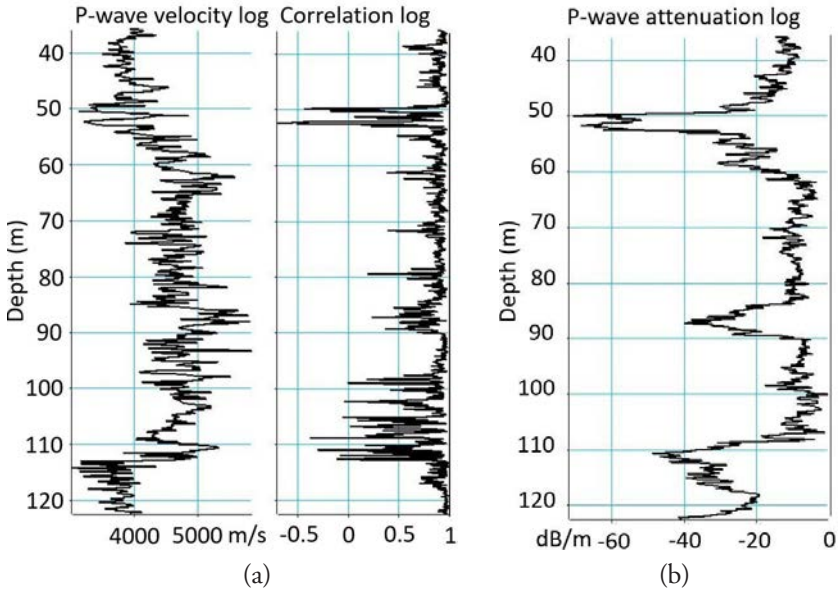

Figure 9 *FWAL at well C1: Refracted P-waves. (**a**) Velocity log and its associated correlation coefficient log. (**b**) Attenuation log. Modified after Delay et al., 2022.*

- a correlation term: CCor = 1 – (Cor/Cor_{max}), with Cor being the correlation coefficient between two normalized wavelets. In karstic zones, a high CCor coefficient is observed.

Figure 10a shows the 3m constant offset sections recorded in boreholes M11, M14, M20, and M22. On the acoustic sections, refracted P-waves appear in the 0.5–1.2 ms time interval, converted refracted S-waves and pseudo-Rayleigh waves

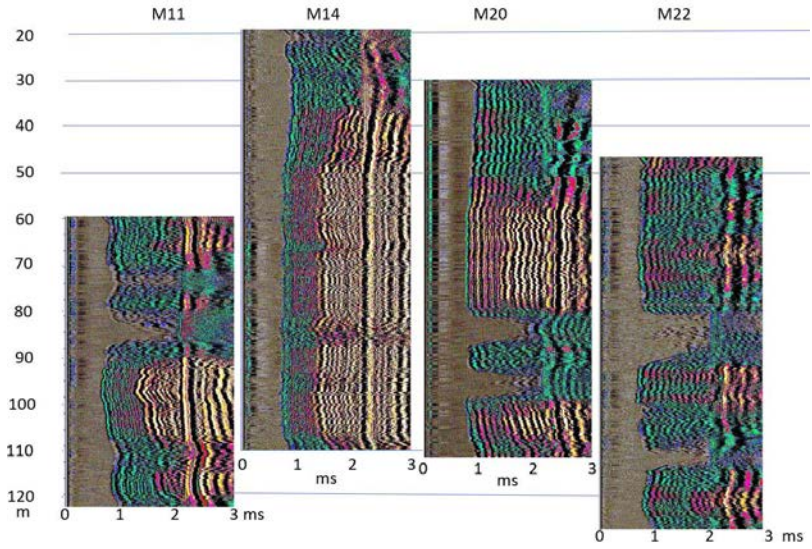

(a)

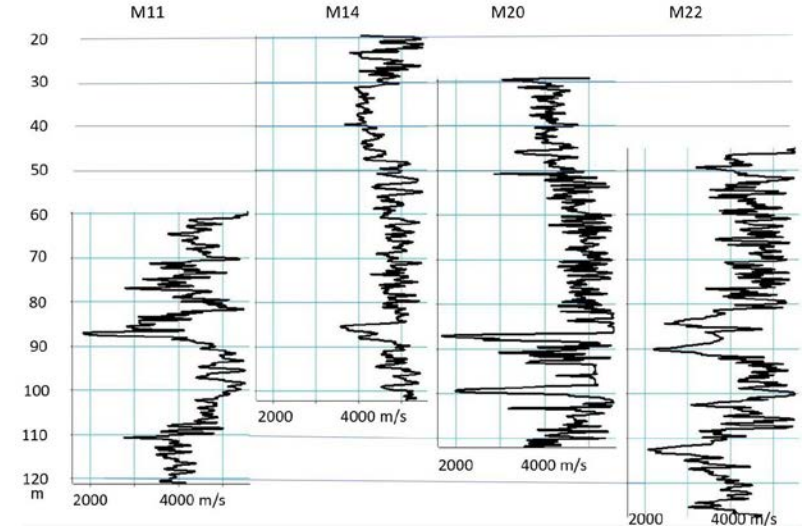

(b)

Figure 10 *FWAL at boreholes M11, M14, M20, and M22: (a) acoustic sections, (b) P-wave velocity logs.*

in the 1.2- 2 ms time interval, and Stoneley waves in the 2–3 ms time interval. Velocity, amplitude ratio, and karstic index logs are shown in Figures 10b, 11a, 11b, respectively.

The acoustic section recorded in borehole M11 shows:

- the 60–72 m depth interval, all acoustic waves (refracted P-wave, converted refracted S-wave, and Stoneley wave) are visible with high amplitude, indicating a compact formation;
- the 72–75 m depth interval, the refracted P-wave has low amplitude, the S-wave cannot be observed. Stoneley waves are strongly attenuated, and fluid waves appear;
- the 75–80 m depth interval is a homogenous formation;
- the 80–90 m depth interval, body waves (P and S) and Stoneley waves are not present. Only fluid waves are present, indicating a karstic level;
- the 90–120 m depth interval corresponds to a homogeneous formation, all acoustic waves (refracted P-wave, converted refracted S-wave, and Stoneley wave) are visible and of high amplitude, indicating a compact formation. However, in the 110–115 m depth interval, we notice a slight attenuation of the different waves (Fig.11a) and the presence of a fluid wave.

The acoustic section recorded in borehole M14 shows:

- the 22–38 m depth interval, where only refracted P-waves and Stoneley waves are recorded, indicating a slow formation. We note the presence of fluid waves;
- the 38–110 m depth interval of homogeneous profile with a high signal-to-noise ratio; all acoustic waves (refracted P-wave, converted refracted S-wave, and Stoneley wave) are visible and of high amplitude, indicating a compact formation. No fluid waves are visible. However, in the 85–88 m depth interval, we note a very weak attenuation of the various waves, which is confirmed by small decreases of both the P-wave velocity log and the amplitude log (Fig. 10b and 11a).

Analysis of the acoustic data (Fig. 11b) shows a small but significant increase of karstic body indicators in the 85–90 m depth interval, suggesting the presence of a karstic feature filled with sediments such as shale. However, no flow is present.

The acoustic section recorded in borehole M20 shows:

- in the 30–58 m depth interval, an acoustically slow formation where only refracted P-waves and Stoneley waves propagate;
- in the 58–80 m depth interval, an acoustically fast formation where refracted P-waves, converted refracted S-waves and Stoneley waves propagate, indicating a compact geological formation;
- A karstic unit in the 80–100 m depth interval, characterized by strong attenuation of refracted P-waves (Fig. 11a) and Stoneley waves. In the interval, we can infer the presence of fluid waves, indicating the presence of flow;
- in the 100–110 m depth interval, an acoustically fast formation where refracted P-waves, converted refracted S-waves and Stoneley waves propagate, indicating a compact geological formation.

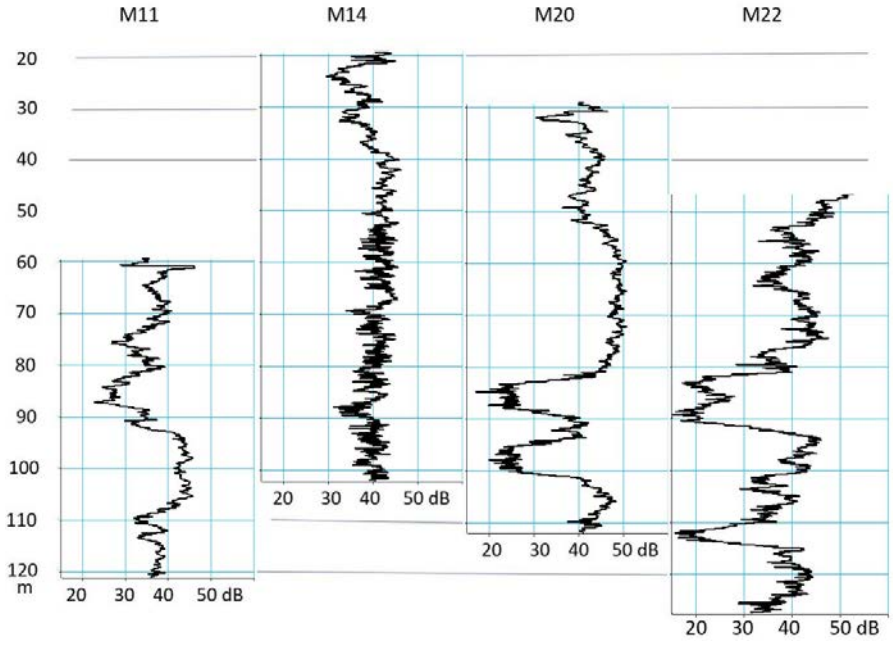

(a)

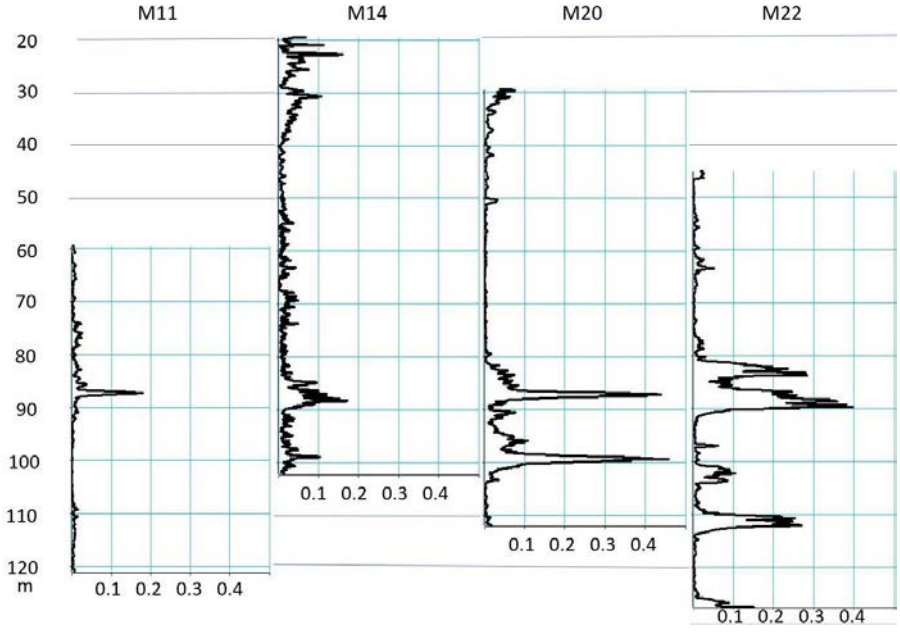

(b)

Figure 11 *Acoustic logs in boreholes M11, M14, M20, and M22: (a) amplitude ratio logs, (b) karstic Index logs.*

The acoustic logs (Fig. 10b, 11a and 11b) clearly show that the karstic unit is composed of two karstic levels at depths of 82–87 m and 93–100 m.

The acoustic section recorded in borehole M22 shows:

- in the 45–80 m depth interval, an acoustically homogeneous formation. Refracted P-waves and Stoneley waves are clearly visible. It is more difficult to identify the converted refracted S-wave;
- a karstic unit in the 80–90 m depth interval, characterized by strong attenuation of refracted P-waves (Fig. 11a) and Stoneley waves. In the interval, we can infer the presence of fluid waves, indicating the presence of flow;
- in the 90–110 m depth interval, an acoustically homogeneous formation;
- a second karstic unit in the 110–115 m depth interval, characterized by strong attenuation of refracted P-waves (Fig. 11a) and Stoneley waves. In the interval, we can infer the presence of fluid waves, indicating the presence of flow;
- in the 115–125 m depth interval, an acoustically homogeneous formation.

The amplitude ratio and karstic index logs (Fig. 11a and 11b) clearly show two karstic levels at depth intervals of 80–90 m and 110–115 m.

In addition to the analysis of the acoustic sections, acoustic logs are used to identify the karstic levels. A high karstic index value (Fig. 11b) provides an accurate location of a karstic layer. Integration in depth of the karstic index from the bottom to the top of the borehole is computed to mimic a flowmeter (Mari & Porel, 2015). Acoustic flowmeters are shown in Figure 12.

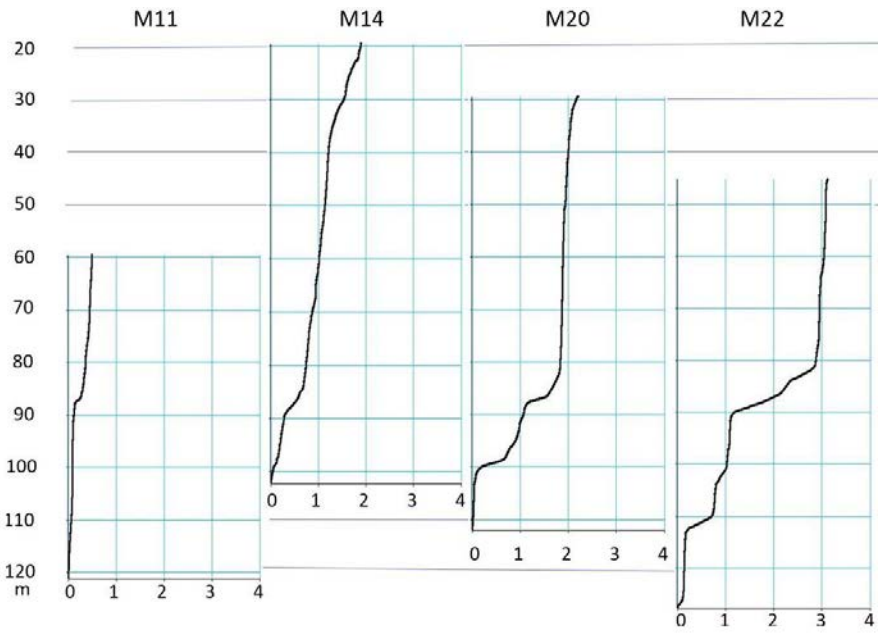

Figure 12 *Acoustic logs in boreholes M11, M14, M20, and M22: acoustic flow logs.*

5.4 Vertical seismic profiles versus full waveform acoustic logging

VSP acquisition was also done using a hydrophone as a borehole sensor and a light-weight dropper as a source. The depth sampling interval is 2.5 m. Figure 13 shows the VSPs recorded in boreholes C1 and M20. The VSPs were highly corrupted by Stoneley waves. The conversion of down-going P-waves (blue arrow in VSP

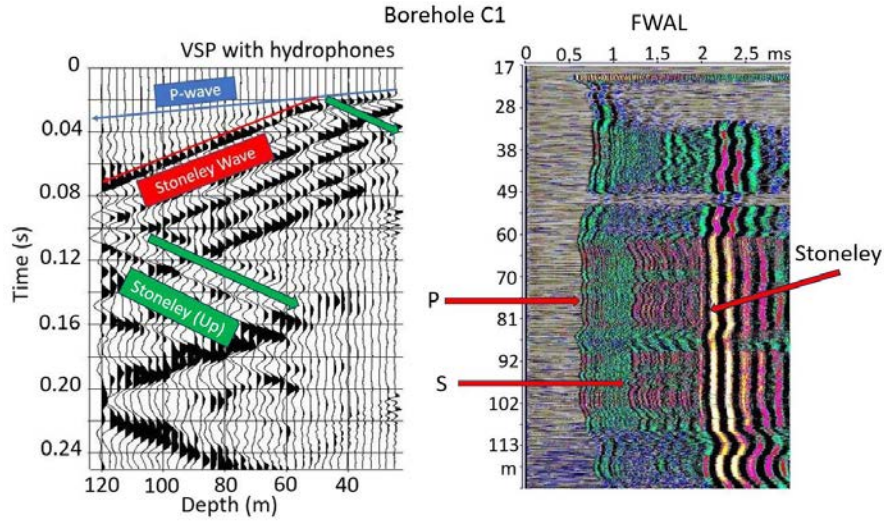

(a)

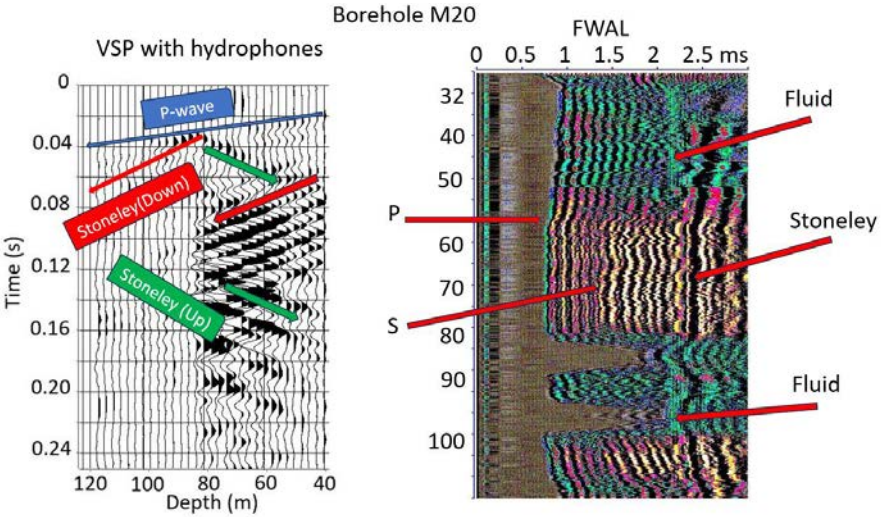

(b)

Figure 13 *Comparison between VSP and acoustic data at boreholes C1 (a) and M20 (b).*

sections) into down-going and up-going Stoneley waves was observed at the level of the karstic bodies. This phenomenon occurs in highly permeable formations. On the VSP sections, the down-going P-wave is identified by a blue arrow, the down-going Stoneley waves by red arrows, and the up-going Stoneley waves by green arrows.

On VSP recorded at borehole C1, the phenomenon of conversion of a down-going P-wave into a down-going Stoneley wave can be observed at a depth of 50 m (Fig. 13a, left). It is more difficult to identify the converted upgoing Stoneley wave. Indeed, it can be noted that the down-going P-wave is highly attenuated at the same depth. The acoustic section (Fig. 13a, right) clearly shows the karstic level where the conversion phenomenon occurs.

On VSP recorded at borehole M20, the conversion of the down-going P-wave into down-going and up-going Stoneley waves is clearly visible at a depth of 80 m (Fig. 13b, left), which corresponds to the top of karstic layers identified on the acoustic section (Fig. 13b, right).

On the VSP section below 60 ms, in the 40–80 m depth interval, a low-frequency – strong-amplitude down-going Stoneley wave can be seen. The Stoneley wave, generated in the borehole at the air-borehole fluid contact, is reflected at the top of karstic layers and strongly attenuated below.

The VSP was processed to separate the different wave fields. Figure 14 shows the extraction of the down-going Stoneley waves (Fig. 14a) and the up-going Stoneley waves (Fig. 14b).

The VSP sections clearly show the converted down-going and up-going Stoneley waves. The VSP sections are converted into instantaneous amplitude sections (Fig. 14a and b, central part). In each instantaneous amplitude VSP section, the instantaneous amplitudes of the Stoneley waves are stacked in a small corridor located after the arrival time of the down-going P-wave, to obtain body-wave to Stoneley-wave conversion factors (Fig. 14a and b, right part) used to detect the depth at which the conversion occurs (80–90 m depth interval).

During VSP acquisition, at each sensor (hydrophone) position, several records of ambient noise were registered. Figure 15a left, is an example of an ambient noise VSP section. The seismic noise was analyzed to detect the presence of flows (Mari & Porel, 2016). For this purpose, an ambient noise factor is calculated, which is defined as the average-to-standard deviation ratio of the amplitude spectrum of each noise trace. We noted a significant increase in the ambient noise factor at the level of karstic bodies. Ambient noise analysis therefore, shows that variations of the ambient noise factor correlate with the conversion level of P-waves into Stoneley waves (Fig.15a right).

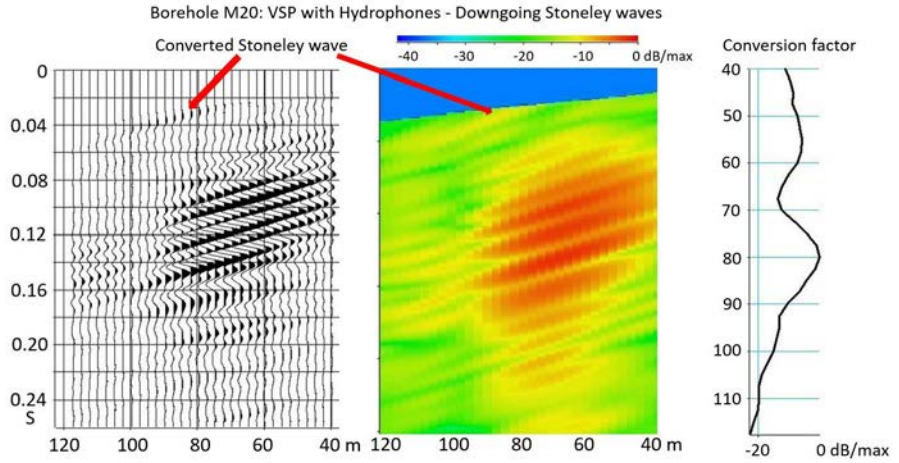

(a)

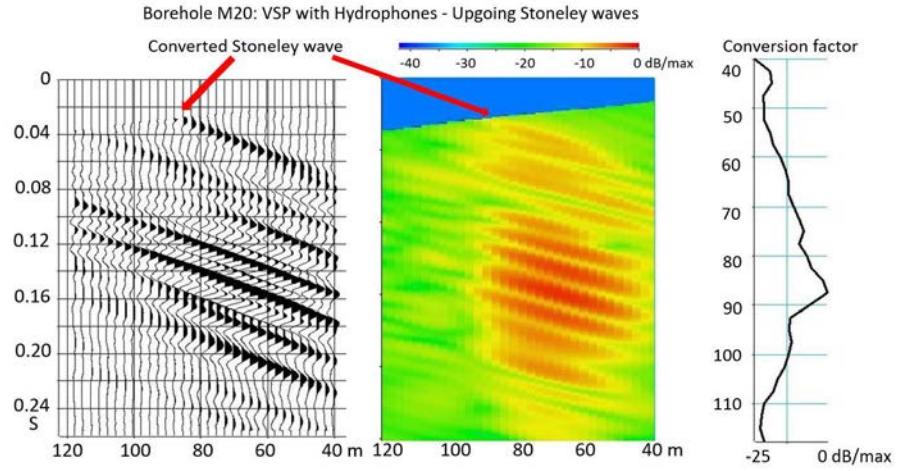

(b)

Figure 14 *Borehole M20: VSP with Hydrophones – Stoneley wave separations and conversion factor estimate. (a) Down-going Stoneley waves, (b) Up-going Stoneley waves.*

The attribute, called the VSP flow index, which is defined as the product of the ambient noise factor by the body-wave to Stoneley-wave conversion factor, was used to detect both karstic bodies and flow (Fig. 15b). In the same way as for the calculation of the acoustic flow log, a VSP flow rate is calculated from the VSP flow index.

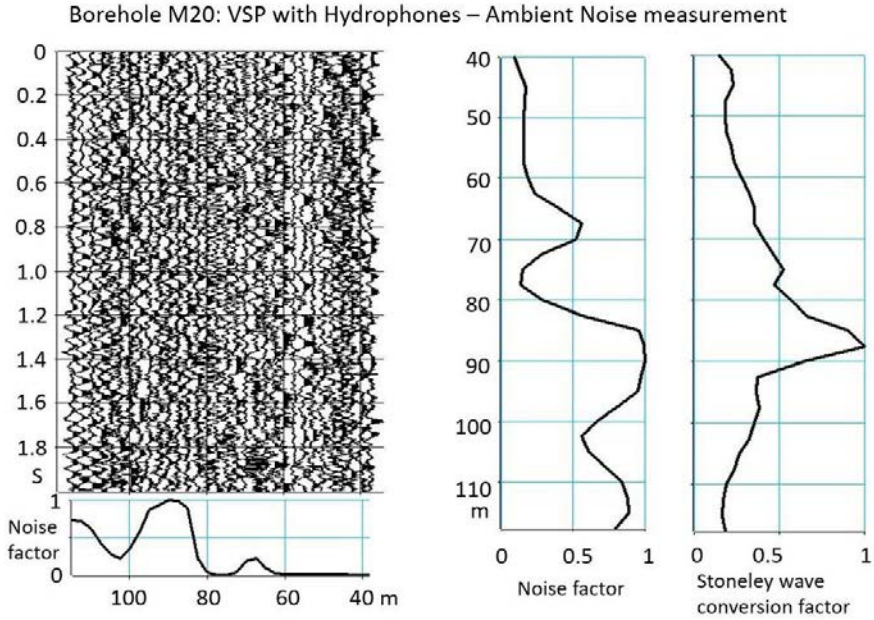

(a)

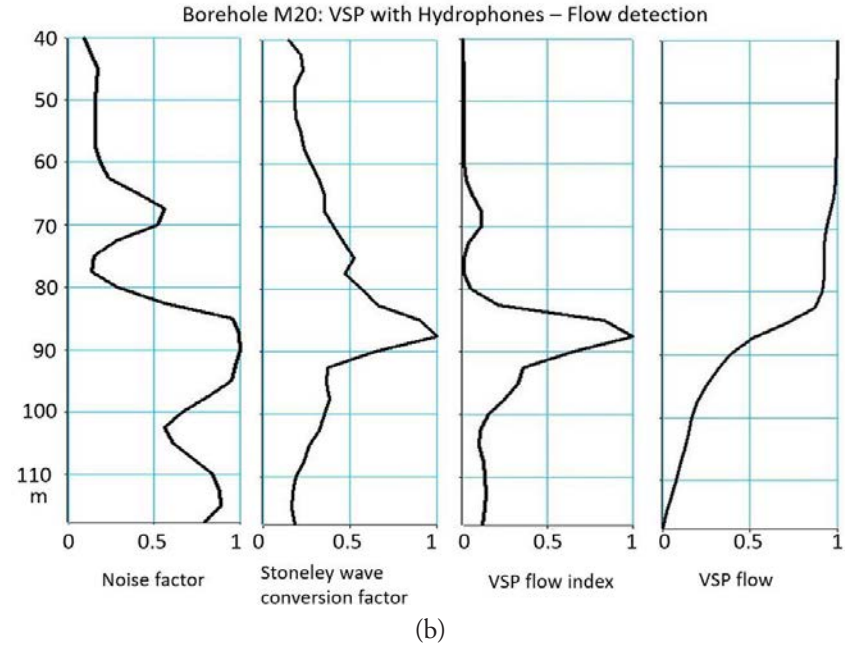

(b)

Figure 15 *Borehole M20: VSP with Hydrophones – ambient noise and flow detection estimate. (a) ambient noise, noise factor versus Stoneley wave conversion factor, (b) VSP logs and flow detection.*

5.5 Electrical methods

Electrical methods (Chapellier, 2001a) are extensively employed in near-surface geophysical investigations due to their sensitivity to subsurface resistivity contrasts. Surface-based techniques primarily include vertical electrical soundings (VES) and electrical profiling, implemented with various electrode configurations such as Wenner, Schlumberger, dipole-dipole, and pole-pole arrays. These configurations enable the investigation of both lateral and vertical resistivity variations (Loke & Barker, 1996a; Chapellier, 2001a).

Advanced 2D and 3D electrical resistivity imaging techniques have been developed to obtain spatially distributed resistivity models of the subsurface. These methods rely on the deployment of dense arrays of electrodes (often 48 to 256), connected via multicore cables, and positioned along linear or areal profiles. A computer-controlled multichannel resistivity meter sequentially selects electrode pairs for current injection and for measuring the resulting potential differences (ΔV), allowing for a large number of independent measurements in a single acquisition sequence.

Apparent resistivity values are computed for each measurement based on the known electrode geometry and are spatially referenced in terms of pseudo-depth (Z) and lateral position (X, Y). The resulting dataset is then processed using non-linear, iterative inversion algorithms that solve the governing equations of electrical conduction, typically using finite-element or finite-difference approaches (Loke & Barker, 1996b). The inversion reconstructs the true resistivity distribution within a 2D or 3D volume, subject to regularization constraints and starting from an initial a priori model.

This methodology, commonly referred to as Electrical Resistivity Tomography (ERT), is particularly effective for imaging complex geological structures, such as stratigraphic interfaces, fault zones, and karst features (Daily et al., 2004; Dahlin & Zhou, 2004; Torrese, 2020).

In addition to the 3D seismic survey, the HES was also analyzed using pseudo three-dimensional (3-D) Electrical Resistivity Tomography (ERT, https://doi.org/10.1016/j.jhydrol.2019.124257), where a 3-D model was constructed through the joint inversion of resistivity data acquired along parallel profiles (Torrese, 2020). The inverse resistivity model successfully identified the primary hydrogeological units, albeit with lower resolution compared to the 3D seismic survey. Modeling of synthetic datasets demonstrated the detectability of karst features through the pseudo 3-D ERT method. Furthermore, synthetic dataset modeling enabled the estimation of the experimental and inversion setup responses to varying levels of aquifer heterogeneity, utilizing well-log data and the 3D seismic block as geological prior information (Torrese, 2020).

In the context of borehole geophysics, conventional electric logging tools (Chapellier, 2001b) include laterolog and induction probes, which measure formation resistivity and conductivity over lateral investigation depths ranging from decimetric to

several meters. These tools offer vertical resolutions of approximately 10–50 cm and are commonly used for lithological interpretation, fluid identification, and fracture detection (Ellis & Singer, 2007).

Electric logging tools — including single-point, short normal, and long normal logs (used to determine the resistivity Rt of the virgin zone) — were run in 12 wells: MP4, MP5, MP6, M11, M13, M14, M18, M21, M04, M07, M08, and M09. The Rt logs were used to estimate the formation porosity using Archie's law (Fig. 6 and 7). Figure 16 presents a comparison between the Rt logs and optical televiewer (OPTV) images for wells M04, M07, M08, and M11. The OPTV imagery confirms that zones of low resistivity correspond to open, water-filled karst conduits in the 85–90 m depth interval at boreholes M07, M08, and M11. A conductive horizon is identified on borehole M04, between 50.05 and 53.15 m depth, where a sequence of vertically stacked cavities up to 1 m in height is observed both on the OPTV log and on the long normal resistivity log (Fig. 16). This karstified interval corresponds to a bioturbated interval.

Figure 17 presents a comparison between the short normal (Rxo), caliper, and optical televiewer (OPTV) logs in borehole M07. The karst conduit in the 87–90 m depth interval is detected with a vertical resolution higher than that of the long normal resistivity (Rt) log. The caliper log provides very high vertical resolution and is particularly effective for detecting cavities and karst conduits. Unfortunately, at the SEH site, the caliper tool was run in only a limited number of boreholes.

The Electric Cylinder Method (ECM, Lantier and Frappin, 2000) represents an advanced borehole-based resistivity imaging technique. It involves the deployment of a flexible multi-conductor cable equipped with evenly spaced electrodes (spacing typically ranging from 0.3 m to 2 m) over a length of 9 to 60 meters. The cable is inserted into a borehole, and a programmable acquisition unit controls the selection of electrodes for current injections and potential measurements. A potential difference is established between a designated remote electrode (often outside the borehole) and an active current-injecting electrode along the cable. Multiple ΔV measurements are recorded between electrode pairs during each injection cycle, and the procedure is iterated for multiple injection positions along the cable. This configuration enables a quasi-volumetric acquisition within a cylindrical domain centered on the borehole axis. 3D inversion of the acquired dataset yields a high-resolution resistivity model within a radius of 2 to 20 meters around the borehole, depending on formation resistivity, electrode spacing, and inversion parameters (e.g., mesh density, regularization strength).

The ECM is particularly suited for the detection and characterization of subsurface heterogeneities (Frappin, 2011a) such as lithological discontinuities, fracture networks, altered or weathered zones, fault planes, karstic cavities, or anthropogenic voids (e.g., tunnels or buried structures). Its ability to provide continuous 3D imaging makes it a powerful complement to conventional borehole logging tools, especially in heterogeneous or anisotropic geological settings. The ECM is commonly used in geotechnical applications to measure the diameter of jet grouting columns (Frappin, 2011b).

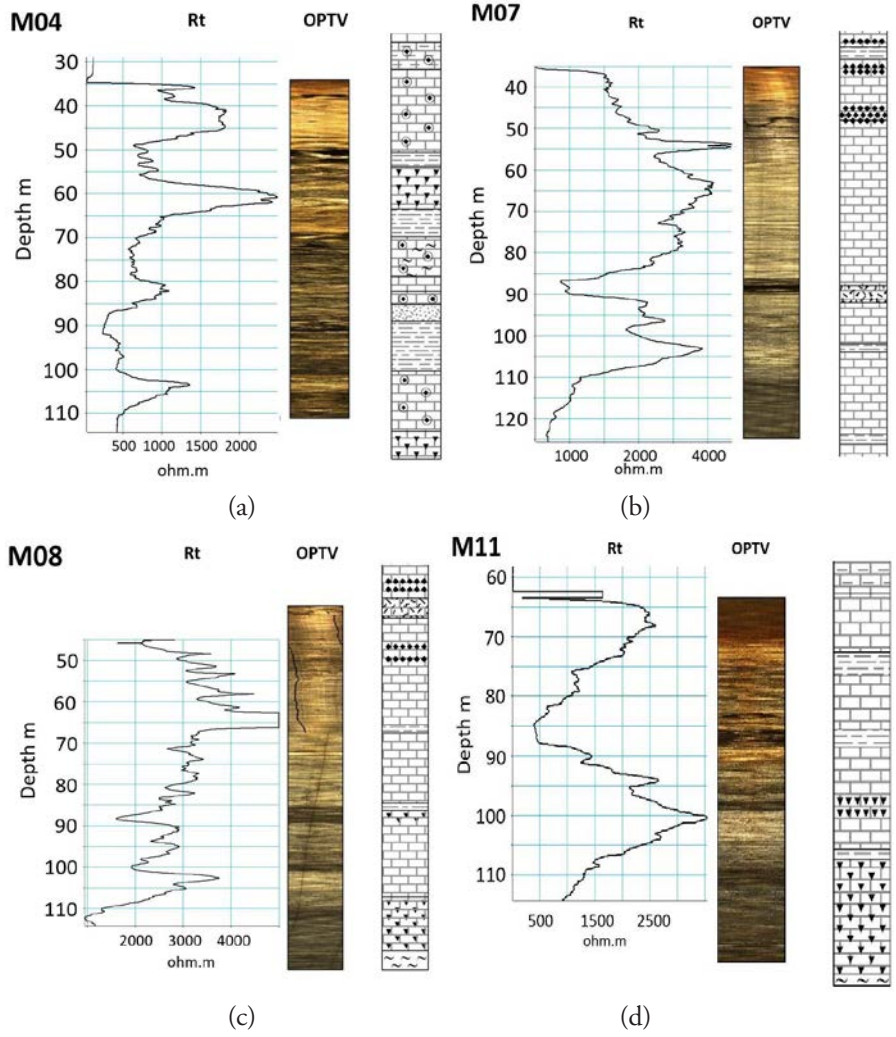

Figure 16 *Comparison of resistivity (Rt) logs and optical televiewer (OPTV) images in boreholes M04, M07, M08, and M11. On the OPTV images, dark zones — corresponding to low Rt values — indicate open, water-filled karst conduits in the 85–90 m depth interval in boreholes M07, M08, and M11.*

In addition to the 3D ERT method, the HES was also investigated using borehole electrical methods of the ERT type. The results are presented and discussed in Chapter 6, entitled *Borehole Electrical Panels: an experiment* (Moreau et al., 2026).

For example, the borehole electrical panels also detect the karst level identified through acoustic methods (Fig. 10 and 11) at a depth of 100 m in borehole M20 (Fig. 18). A comparison between the resistivity panels and optical wall imagery confirms that low-apparent resistivity anomalies correspond to open, water-filled karst conduits.

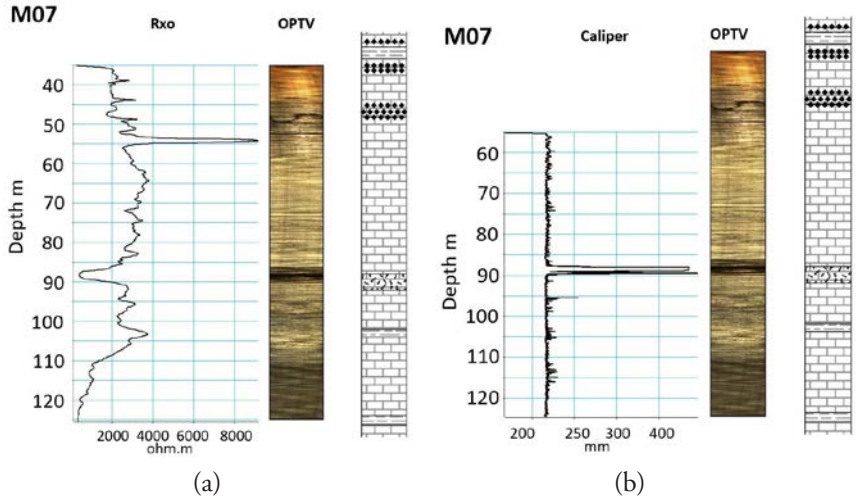

Figure 17 *Comparison of the short normal resistivity (Rxo) log and borehole caliper with the optical televiewer (OPTV) image in borehole M07. The karst conduit is clearly identified in the 87–90 m depth interval.*

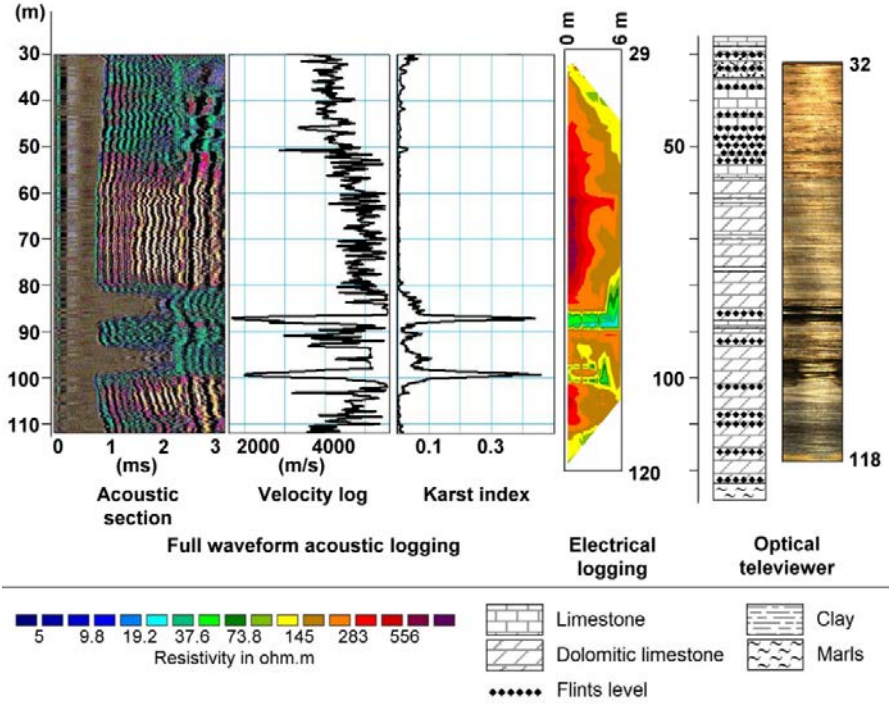

Figure 18 *Comparison of acoustic, electrical, and optical wall imaging methods in borehole M20. From left to right: acoustic section, velocity log, karst index log, electrical resistivity panel, geological log, and optical wall imagery (OPTV).*

5.6 Conclusions

The Hydrogeological Experimental Site (HES) of Poitiers, which was developed to conduct long-term monitoring and experiments on water and mass transfer processes, has been the site of hydrogeological and geophysical surveys as part of this study.

The chapter provides an overview of various field experiments based on seismic and acoustic methods and shows their relative contribution to knowledge of the experimental site.

A 3D seismic reflection and refraction survey was carried out. The 3D seismic data was processed to obtain both a structural model in depth (VSP data being used to define a time to depth conversion law), and the distribution of seismic velocities in the reservoir, using an inversion process with acoustic velocity logs as constraints. The result was a high-resolution 3D seismic block, with nearly horizontal stratification and strong lateral variations of velocity. This made it possible to identify three high-porosity, presumably water-producing layers, at depths of 35 to 40 m, 85 to 87 m, and 110 to 115 m. The 85 to 87 m deep layer is the most porous, with porosities of over 30%, which represents the karstic part of the reservoir.

To confirm the presence of karstic levels, borehole data were recorded in several boreholes in different frequency bandwidths. A methodology was developed to detect flow using both ambient noise measurement and VSP data. In low frequency band (10–150 Hz), VSP data were recorded with a hydrophone sensor, known to be sensitive to Stoneley waves that are currently used to detect discontinuities such as fractures or faults. Conversion of the down-going P-waves into Stoneley waves was observed at the level of the karstic bodies. This phenomenon occurs in highly permeable formations. Analysis of the ambient noise shows that variations of its characteristics (spectral variance) are correlated with the conversion level of P-waves into Stoneley waves. A VSP attribute, called VSP flow index, was calculated to detect both karstic levels and flows.

In high frequency bandwidth (1–20 kHz), full waveform acoustic data were recorded, both to locally validate the results obtained by the seismic methods (3D and VSP) and to evaluate the potential of the acoustic method to detect karstic bodies with a very high resolution. An acoustic attribute, called Karstic Index, was calculated to detect karstic levels.

Hydrogeological sites are currently investigated primarily by hydrogeological methods. In this study, we have shown how electrical logging (long normal logs), seismic and acoustic methods (3D seismic, full waveform acoustic logging, and VSP) can contribute to the understanding and description of karstic formations at different scales.

Both hydrogeological and geophysical investigations contribute to hydrogeological model building and site description. Figure 19 shows the benefit of combining the two types of investigation. The figure is a synthesis of the methods developed to detect karstic bodies and to quantify flows. The synthesis gathers data from acoustic

logging (Karstic index), ambient seismic noise and VSP (VSP flow index), borehole wall imaging (OPTV optical televiewer) and flow measurement in dynamic conditions.

Combined analyses of geophysical and hydrogeological data can be done locally at wells or on a larger scale using 3D seismic data. These studies are done to detect water-producing levels in wells and to establish probable karst conduit networks. An integrated approach for the identification of effective three-dimensional (3D) discrete karst conduit networks conditioned on tracer tests and geophysical data (3D velocity block, Fig. 5a) has been developed (Bodin et al., 2022).

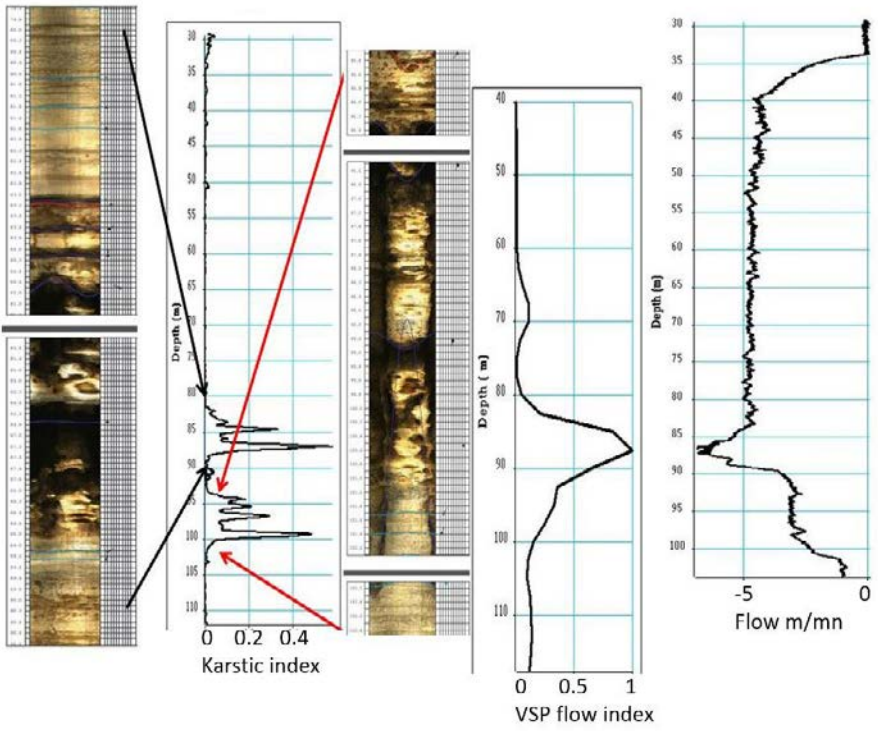

Figure 19 *Borehole M20: Detection of karstic levels and flows by acoustic logging (karstic index), VSP (VSP flow index), borehole wall imaging (OPTV) and flow measurement under dynamic conditions.*

Appendix: Static corrections

Refraction imaging of the subsurface is based on the analysis of refraction time-distance curves. The arrival time t(x) of the refracted wave is given by the following relationship:

$$t(x) = x.\cos(\alpha)/ VR + \delta(0) + \delta(x)$$

- x: the source – receiver distance,
- α: the dip of refractor over the spread length,
- VR: the velocity of the refractor,
- $\delta(0)$: the delay time at the source point,
- $\delta(x)$: the delay time at the receiver point.

To accurately determine the true velocity, dip, and thickness of each subsurface marker, it is essential to obtain time-distance curves in both directions — i.e., up-dip and down-dip shooting. This requires seismic recordings where geophones are aligned with the shot points. The most widely known techniques for this are Hagedoorn's Plus-Minus method (1959) and the Generalized Reciprocal Method (GRM) introduced by Palmer (1986). The GRM is essentially an extension of the Plus-Minus method, and both rely on the concept of delay time. The Plus-Minus method is extensively used in seismic refraction surveying. Picked travel times are used to construct the t+ and t– curves. The t– curve provides the velocity of the refractor, while the t+ curve offers a time-based image of the refractor's depth (via delay times). If the velocity of the overlying medium is known, this delay curve can be converted into depth. This velocity is determined from the slope of the direct arrival. The overlying medium is referred to as the weathering zone (WZ). In the HES study area, the refractor velocity has been estimated at 3350 m/s based on t– curve interpretation, while the velocity of the weathering zone is approximately 850 m/s.

The arrival times of both direct and refracted waves were picked for all shots. These picked times serve as input data for applying Hagedoorn's Plus-Minus method. Cross-spread shots with a 60 m offset were also used to compute delay-time curves. These particular shots (Fig. 2d) were selected to ensure that the refracted wave is always the first arrival, regardless of the source–receiver distance.

For all shots — whether in-line or cross-line — the picked arrival times were carefully verified. This verification involved flattening the first arrival by applying the picked times as static corrections. Perfect flattening confirms accurate picking.

Picked times from in-line shots (Fig. 2b and 2c) and from 60 m cross-spread shots (Fig. 2b and 2d) were used to generate two delay-time maps.

The geostatistical processing applied to each delay-time map (Bourges et al., 2012) involved two main steps:

- detection of anomalous delay-time lines responsible for high spatial variability;
- kriging and extraction of long-wavelength structures, to reveal underlying geological features.

An initial variographic analysis was performed on both delay-time maps. The variograms were modeled using the following nested structures:

- in-line shot delay-time map: A cubic structure with a range of 50 m, consistent with the size of geological heterogeneities, and a spherical structure with a range of 140 m. The cross-line variogram revealed an additional source of variability attributed to acquisition artifacts, modeled by a spherical structure with a range of 10 m;
- cross-line shot delay-time map: A cubic structure with a range of 60 m, and an anisotropic spherical structure with ranges of 120 m in the in-line direction and 110 m in the cross-line direction.
  As with the in-line data, an additional variability source — attributed to acquisition artifacts — was modeled by a spherical structure with a range of 15 m.

Using the previously defined variogram models, both delay-time maps were interpolated. During this process, small-scale variability — associated with acquisition artifacts in the cross-line direction — was filtered out using factorial kriging. The interpolated maps were then compared to the original delay-time profiles. For the in-line shot survey, one anomalous acquisition line responsible for additional variability was identified, while two such lines were highlighted in the cross-line shot survey.

After removing the anomalous delay-time lines, omnidirectional variograms were computed, focusing on mid-scale variability (up to 50–70 m). For both delay-time maps, the updated variograms consist of:

- a cubic structure with a range of 49 m (in-line shots) and 60 m (cross-line shots), and
- a large-scale structure with a range of 120 m.

Finally, the two large-scale delay-time maps — representing long-wavelength geological features — were interpolated using factorial kriging. Given the high correlation between the two resulting maps (correlation coefficient ≈ 0.8), an average long-wavelength structure was computed.

The picked first-arrival times from all shots (both in-line and cross-line), the weathering zone (WZ) depth map derived from the averaged delay-time map (long-wavelength structure), and the velocity model obtained using the Plus–Minus method serve as input data for the inversion procedure — tomography — which is suitable for determining the subsurface velocity distribution (Mari and Mendes, 2012).

The velocity distribution obtained through the joint Plus-Minus tomographic inversion can be effectively used to compute 3D static corrections. For this purpose:

- the thickness H of the weathering zone is defined by the 2500 m/s iso-velocity depth map;
- the average velocity V_1 within the weathering zone is calculated from the velocity model in the 0 to H depth interval;
- the velocity V_2 of the refractor is derived from the velocity model within a narrow depth window (approximately 3 m) just below the interface at depth H.

The application of this methodology to the 3D dataset is illustrated in Figure A.1.

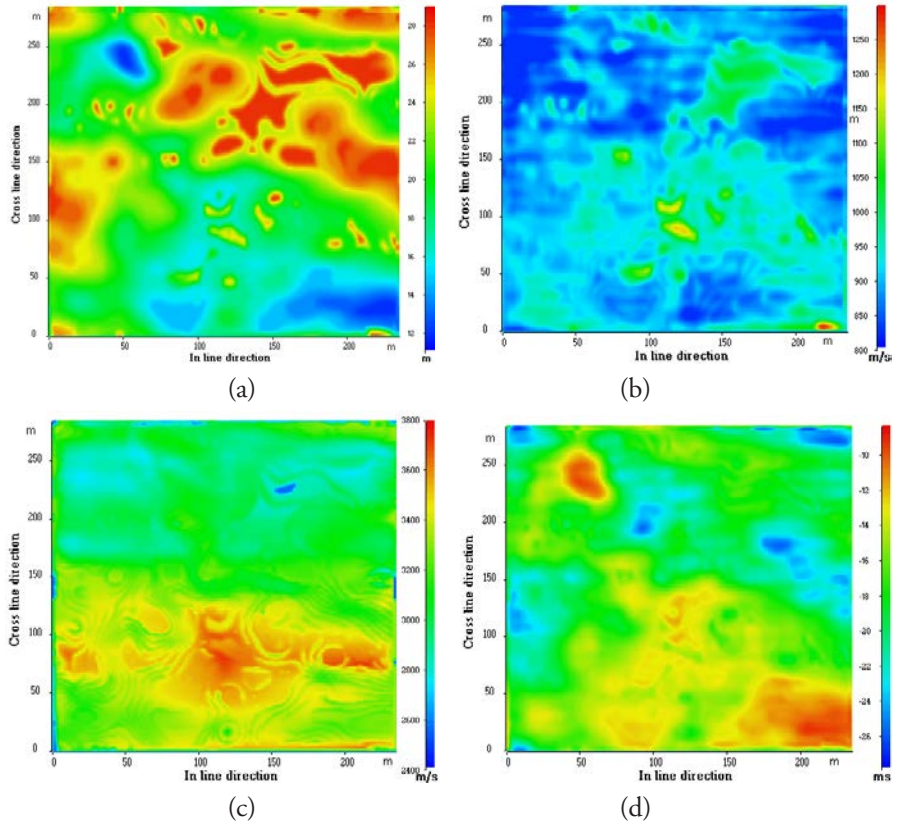

Figure A.1. *3D static corrections from 3D tomographic inversion after geostatistical processing. (a) Thickness H of the weathering zone. (b) Average velocity V1 in the weathering zone. (c) Velocity V2 below the weathering zone. (d) 3D static correction map (–H/V1 + H/V2).*

Acknowledgements

Special thanks to Matthieu Bourges for his help and expert advice in the geostatistical processing involved in computing 3D static corrections

References

Archie G.E. (1942). The electrical resistivity logs as an aid in determining some reservoir characteristics, *Petroleum Technology*, 146: 54-62.

Audouin O., Bodin J., Porel G., Bourbiaux B. (2008). Flowpath structure in a limestone aquifer: multi-borehole logging investigations at the hydrogeological experimental site of Poitiers, France, *Hydrogeology Journal*, 16(5): 939-950. https://doi.org/10.1007/s10040-008-0275-4

Binley A., Kemna A. (2005). DC resistivity and induced polarization methods. In Rubin, Y., & Hubbard, S. S. (Eds.), *Hydrogeophysics* (pp. 129-156). Springer.

Bodin J., Porel G., Nauleau B., Paquet D. (2022). Delineation of discrete conduit networks in karst aquifers via combined analysis of tracer tests and geophysical data, *Hydrol. Earth Syst. Sci*., 26: 1713-1726, https://doi.org/10.5194/hess-26-1713-2022

Bourges M., Mari J.-L., Jeannee N. (2012). A practical review of geostatistical processing applied to geophysical data: methods and applications, *Geophysical prospecting,* 60: 400-412.

Chapellier D. (2001a). Electrical methods, from On-line course of geophysics (http://www-ig.unil.ch/)

Chapellier D. (2001b). Aquifer logging course, from On-line course of geophysics (http://www-ig.unil.ch/)

Dahlin T., Zhou B. (2004). A numerical comparison of 2D resistivity imaging with 10 electrode arrays. *Geophysical Prospecting*, 52(5): 379-398.

Daily W., Ramirez A., Binley A., La Brecque D. (2004). Electrical resistance tomography. *The Leading Edge*, 23(5): 438–442. https://doi.org/10.1190/1.1729225

Delay F., Mari J.-L., Porel G., Chabaux F., Ackerer P. (2022). Is subsurface geophysics as seismic and acoustic investigations a rescue to groundwater flow inversion? *Comptes Rendus Geoscience*, Part of Special Issue: Geo-hydrological data & models, https://doi.org/10.5802/crgeos.157

Ellis D.V., Singer J.M. (2007). *Well Logging for Earth Scientists* (2nd ed.). Springer.

Faust L.Y. (1953). A velocity function including lithologic variation, *Geophysics*, 18: 271-288.

Frappin P. (2011a). The electric cylinder. paper EG9, EAGE Conference & Exhibition, First International conference on Engineering Geophysics, 11-14 December 2011, AI Ain, United Arab Emirates.

Frappin P. (2011b). CYLJET: an innovative method for jet grouting column diameter measurement. paper EG44, EAGE Conference & Exhibition, First International conference on Engineering Geophysics, 11-14 December 2011, AI Ain, United Arab Emirates.

Gaudiani P. (1979). Système améliorant les procédés de mesures acoustiques, Brevet (Patent). 1979; 79 27528. Service des Brevets, 20 bis rue de Leningrad, 75800 Paris cedex 08.

Gaillard T., Moreau M., Mari J.-L. (2024). Seismic and stratigraphic characterization of karstogenic horizons in a sequence of carbonate deposits: Example of the Dogger limestones of the Poitou threshold, Journees Scientifiques AGAP Qualité 2024, *E3S Web of Conferences* 504, 05005, https://doi.org/10.1051/e3sconf/202450405005

Hagedoorn G.J. (1959). The Plus–Minus method of interpreting seismic refraction sections. *Geophysical Prospecting* 7: 158-182.

Lantier F., Frappin P. (2000). Method and apparatus for probing and inspecting an underground volume, patent EP 0 786 673 B1, deposit number: 97106066.0, European Patent office.

Loke M.H., Barker R.D. (1996a). Rapid least-squares inversion of apparent resistivity pseudo sections using a quasi-Newton method. *Geophysical Prospecting*, 44(1): 131–152. http://dx.doi.org/10.1111/j.1365-2478.1996.tb00142.x

Loke M.H., Barker R.D. (1996b). Practical techniques for 3D resistivity surveys and data inversion. *Geophysical Prospecting*, 44(3): 499–523. https://doi.org/10.1111/j.1365-2478.1996.tb00162.x

Mari J.-L., Porel G. (2008). 3D seismic imaging of a near – surface heterogeneous aquifer: a case study, *Oil and Gas Science and Technology*, *Rev. IFP*, 63: 179-201. https://doi.org/10.2516/ogst:2007077

Mari J.-L., Porel G., Bourbiaux B. (2009). From 3D seismic to 3D reservoir deterministic model thanks to logging data: the case study of a near – surface heterogeneous aquifer, *Oil and Gas Science and Technology, Rev. IFP,* 64: 119-131. https://doi.org/10.2516/ogst/2008049

Mari J.-L., Delay F. (2011). Contribution of Seismic and acoustic methods to reservoir model building, in "Hydraulic Conductivity / Book 1", *In Tech, Open Access Publisher*, ISBN 978-953-307-288-3, https://doi.org/10.5772/22051

Mari J.-L., Mendes M. (2012). High resolution near surface imaging of fracture corridors and cavities by combining Plus Minus method and refraction tomography. *Near Surface Geophysics*, 10: 185-195. https://doi.org/10.3997/1873-0604.2011052

Mari J.-L., Porel G. (2015). Automated karstic reservoir analysis utilizing attributes, We N117 02, 77th EAGE Conference & Exhibition, Madrid IFEMA, Spain.

Mari J.-L., Porel, G. (2016). Flow detection using well seismic data, Tu P2 02, 78th EAGE Conference & Exhibition, Vienna, Austria, 30 May-2 June.

Mari J.-L., Porel G. (2018). "Contribution of seismic and acoustic methods to the characterisation of karstic formations", Chapter 5 in *Well seismic surveying and acoustic logging*, EDP Sciences. https://doi.org/10.1051/978-2-7598-2263-8

Mari J.-L., Mendes M. (2019). *Seismic imaging: a practical approach*, EDP Sciences. https://doi.org/10.1051/978-2-7598-2351-2

Mari J.-L., Porel G., Delay F. (2020). Contribution of Full Wave Acoustic Logging to the Detection and Prediction of Karstic Bodies. *Water,* 12(4): 948. https://doi.org/10.3390/w12040948

Mari J.-L., Porel G. (2024). The hydrogeological experimental site of Poitiers: Hydrogeological versus geophysical investigations, Journees Scientifiques AGAP Qualité 2024, *E3S Web of Conferences* 504: 05003. https://doi.org/10.1051/e3sconf/202450405003

Moreau M., Brunel P., Mari J.-L. (2026). "Borehole electrical panels: an experiment", Chapter 6 in *A new concept of karst development based on hydrogeology and geophysics*, EDP Sciences. https://doi.org/10.1051/978-2-7598-3934-6.c006

Palmer D. (1986). Refraction seismic, *Geophysical Press*, 13.

Torrese P. (2020). Investigating karst aquifers: using pseudo 3-D electrical resistivity tomography to identify major karsts features, *Journal of Hydrology*, 580(2): 124257. https://doi.org/10.1016/j.jhydrol.2019.124257

6

Borehole electrical panels: an experiment

M. Moreau, P. Brunel and J.-L. Mari

The Hydrogeological Experimental Site (HES) has been the subject of several studies over the past 20 years (Gaillard, 2026a). Multi-borehole logging investigations were carried out at the HES site (Audouin et al., 2008).

In this chapter, we focus on the potential of vertical electrical panels installed in five open boreholes (recorded by *CPGF Horizon* in 2021), combined with optical wall imaging (carried out by *SOLEO Mesures et Développements* in 2005 and *SEMM Logging* in 2006), to detect karst networks.

In 2021, as part of the KARST'OGENE project, *CPGF Horizon* carried out measurement campaigns on the HES. These investigations included hydrogeological tracer studies (see Chapter 7, Boulais et al. 2026) and vertical electrical panels. The objectives of the KARST'OGENE project were as follows:

1. to test and validate measurement methods and equipment on a well-documented hydrogeological site, with a view to applying them to applied hydrogeology projects;
2. to verify mass transfer between the various horizontal karst levels intersected by the HES boreholes, using convergent radial tracers.

Following the 3D seismic survey, Mari and Porel (2008) identified 3 main porous layers at depths of 35-40, 85-87, and 110-115 m that turned out to be karstic levels.

© EDP Sciences, 2026
DOI: https://doi.org/10.1051/978-2-7598-3934-6.c006

The primary objective of the electrical resistivity panels was to investigate the electrical signature of these layers.

Vertical resistivity panels were implemented in five boreholes: M20, M04, M08, M07, and M11 (Fig. 1).

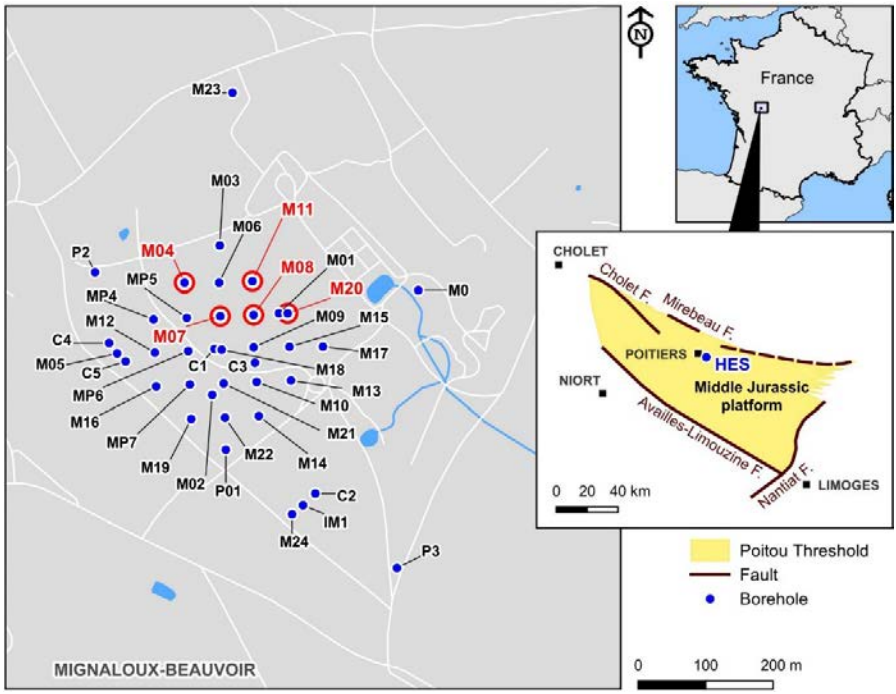

Figure 1 *Location of boreholes at the Poitiers HES site, France. Red circles indicate the boreholes selected for electrical measurements.*

Material and method

Electrical prospecting (Chapellier, 2001a) is a non-destructive geophysical method used to determine the structure and quality of the terrain. This method is based on the ability to represent the nature of the terrain in terms of one of its physical parameters: electrical resistivity.

The resistivity of geological formations primarily depends on the following factors:

- water and clay content;
- composition of electrically conductive minerals, such as sulfides (pyrite, galena), iron oxides, graphite, gold, and silver.

In boreholes, the Electrical Cylinder Method (Lantier & Frappin, 2000), developed by Soldata Geophysic (now known as Sixense Geophysics), is a technique

that enables radial investigation around boreholes (Habert et al., 2006). Today, this method has been adapted and is commonly used in geotechnical applications to measure the diameter of jet grouting columns (Frappin et al., 2001; Frappin, 2011).

At the HES site, a similar method was used, involving transmitting and receiving electrodes placed within the borehole to measure variations in electrical potential. Data processing focused exclusively on apparent resistivity values. As part of the KARST'OGENE project, vertical electrical panels were incorporated to assess the detectability of karst horizons by comparing the results with existing data.

The vertical electrical panels were performed using the following equipment:

- a 132-meter cable lowered to the desired depth in the boreholes, holding 32 electrodes spaced at 1-meter intervals.
- an ABEM Terrameter LS2 resistivity meter.

(a)

(b)

Figure 2 *View of measurement equipment. (a) Electrode on measuring cable, (b) ABEM Terrameter LS2 resistivity meter.*

A Wenner-Schlumberger measurement protocol was used from the bottom to the top of the open-hole sections of the boreholes, with offsets of 15 m for each roll-along measurement performed.

For each measurement, one set of 4 electrodes out of the 32 is used. Two electrodes are used for current injections (A and B), and two for measuring the electrical

potential (M and N). The greater the spacing between the quadruplet of electrodes (A and B, M and N), the thicker the slice of ground surveyed around the borehole.

Using this quadrupole configuration for surface measurements, the apparent resistivity ρ_a (in Ohm·m) of the ground through which the current flows is calculated using the following formula:

$$\rho_a = K \Delta V / I$$

With I the current intensity, ΔV the potential difference between electrodes M and N, K a geometric factor depending on the electrode arrangement:

$$K = 2\pi \times (1/AM - 1/AN - 1/BM + 1/BN)^{-1}$$

The factor 2π is used for surface measurements, as it represents the half-sphere of current displacement around the injection electrodes. This half-sphere is the result of the electrode positioning at the interface between two media:

- the ground, through which the current propagates.
- the infinitely resistant air, where the current does not propagate.

In a vertical borehole, the acquisition device is placed inside the well. The contact between the electrodes and the formation is indirect, occurring through the borehole fluid, which is typically either a water-based drilling mud or fresh water. The resistivity of fresh water generally ranges from 10 to 1000 ohm·m, depending on factors such as ionic concentration, temperature, and the presence of dissolved solids. For water-based drilling muds, resistivity typically ranges from a few ohm·m to around ten ohm·m, depending on salinity and temperature.

The apparent resistivity equation for a borehole configuration is similar to that used in surface measurements but must take into account the cylindrical geometry of the medium. In certain idealized cases—such as a narrow borehole within a homogeneous formation—apparent resistivity can be approximated using a formula analogous to that of surface configurations, with an adapted geometric factor K. This factor depends on electrode spacing, the relative position of the electrodes in the well, borehole diameter, borehole fluid properties, and the geological model.

The borehole resistivity profile is then obtained by successively combining different quadrupoles along the measurement cable, with each electrode alternately playing the role of current injection or measurement (Fig. 3).

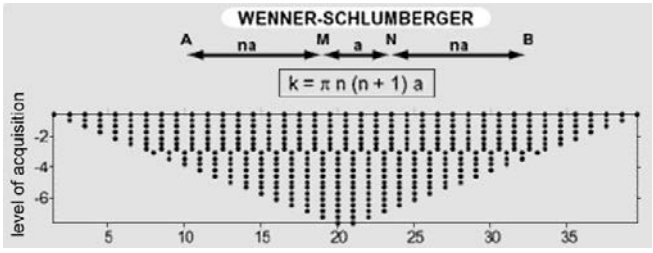

Figure 3 *Electrical resistivity measuring devices based on a Wenner-Schlumberger scheme, with a = MN (m) separation and n = acquisition data level (after D. Chapellier, 2001a).*

Acquisition

The five electrical resistivity panels produced are shown as apparent resistivities in Figure 4.

According to the porous levels identified by Mari and Porel (2008):

- the 30-meter depth level could not be studied, as electrical measurements in the boreholes only started at best at 35 meters for panels M04 and M20;
- the 50-meter depth level was studied for panels M04 and M20;
- the 85-meter depth level is covered by all five vertical panels;
- finally, the 115-meter depth level is covered by all panels except M04, which ends at 105 meters.

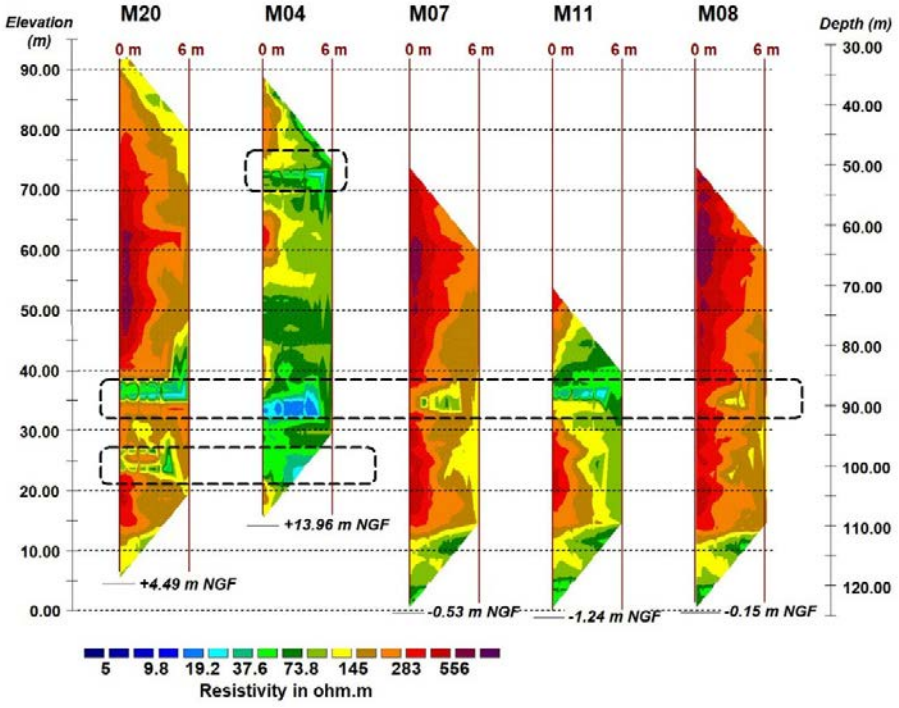

Figure 4 *Vertical resistivity panels measured from boreholes M20, M04, M07, M11, and M08. Dotted boxes indicate the location of karstic levels.*

Figure 5 presents a comparison between electrical resistivity measurements obtained from long normal logs (Chapellier, 2001b) and those from the electrical panels.

In the electrical panels, the apparent resistivity of the limestones is generally above 180 ohm·m down to approximately 110 meters. An exception is observed in panel

M04, where apparent resistivities remain lower throughout the entire depth range. Below 110 meters, apparent resistivities in boreholes M20, M07, M08, and M011 drop below 100 ohm·m.

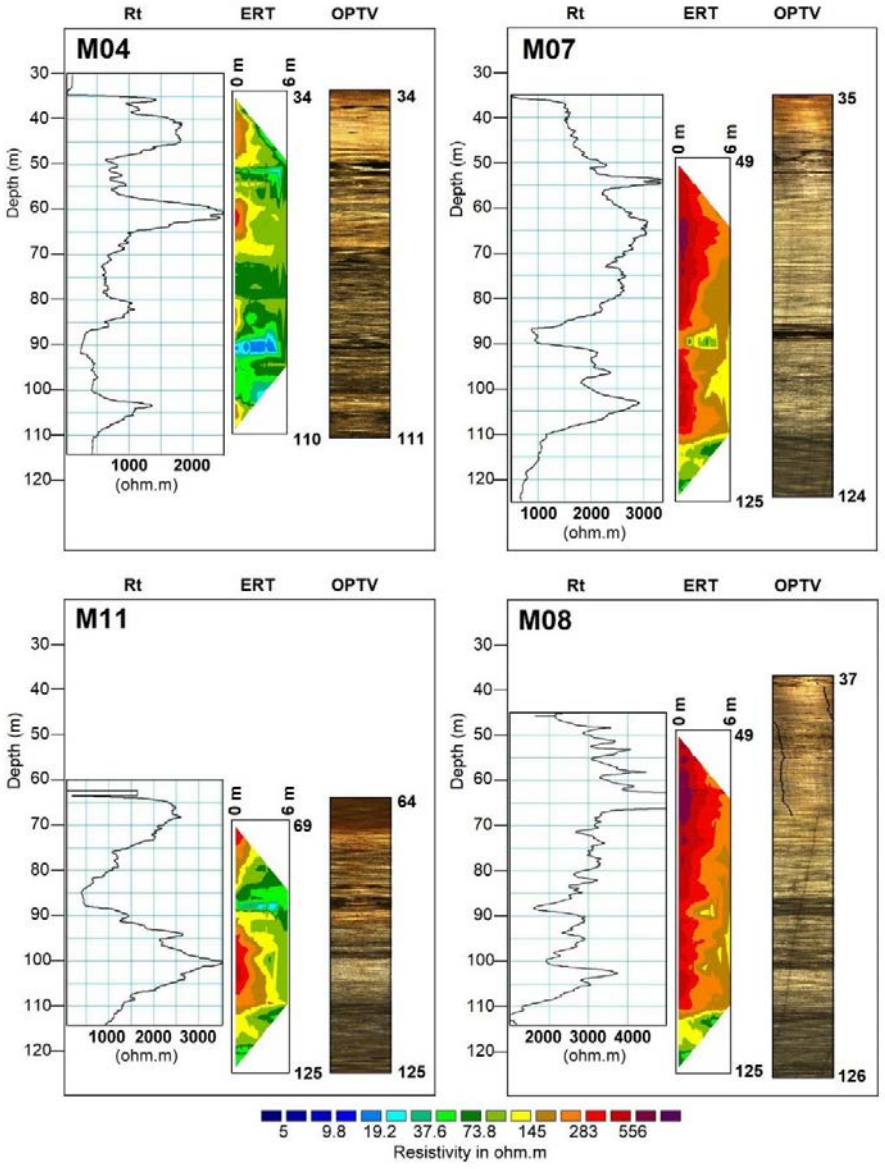

Figure 5 *Comparison of measured resistivities (long normal logs vs. ERT resistivity panels) with OPTV images for boreholes M04, M07, M08, and M11. For each borehole, from left to right: long normal resistivity log (Rt), ERT resistivity panel, and optical televiewer image (OPTV).*

The lower resistivity values observed in the electrical panels, compared to those obtained from longnormal Rt logs, arise both from the choice of the geometric factor K and, more importantly, from the effect of the borehole fluid (its conductivity), which conducts current and substantially influences the measurements. However, if the borehole geometry remains constant (i.e., the diameter does not vary) and the borehole fluid properties are unchanged, then for a given electrode configuration, the influence of the borehole fluid remains consistent at all depths. Under these conditions, relative variations in apparent resistivity still offer valuable insights for geological interpretation.

A GFTC tool, which simultaneously records Gamma Ray, Flow, Temperature, and Water Conductivity logs, was run in boreholes M08, M11, and M20. The measured water conductivity averaged 500 µS/cm, corresponding to a water resistivity of approximately 20 ohm·m.

Figure 5 also illustrates the correlation between electrical resistivity measurements and Optical Televiewer (OPTV) imagery (Mari, 2026).

The optical televiewer is a downhole probe that provides a continuous, high-resolution, 360° digital unwrapped image of the borehole wall, oriented to magnetic north, using an integrated light source. It functions effectively in air or clear water and typically achieves an average resolution of approximately 2 mm, depending on borehole conditions and logging speed. In boreholes containing mud or turbid fluids, the optical televiewer must be replaced with alternative imaging tools, such as the acoustic televiewer or microresistivity imaging tools. These alternatives also generate continuous unwrapped images of the borehole wall and are extensively used for in situ mapping of natural fracture orientations, as well as for determining the orientation of the principal horizontal stress field—based on the identification of drilling-induced tensile fractures or borehole breakouts (Genter et al., 2025). In this study, the optical televiewer was deployed in boreholes with minimal karstification and long open-hole sections (M01, M09, M10, M14, M15, M17), to enable a very high-resolution hydro-stratigraphic analysis of the HES (Gaillard, 2026b).

In boreholes M07, M08, and M11, low resistivity values identified by resistivity logs (Rt and ERT) are correlated with dark zones on the OPTV images between 85- and 90-meters depth. In borehole M04, a conductive horizon is observed between 50.05 and 53.15 meters, where a sequence of vertically stacked cavities—up to 1 meter in height—is clearly visible on both the OPTV and Rt resistivity logs.

Geological Interpretation

Each borehole is presented in a summary figure that, from left to right, compiles four pieces of information (Fig. 6, 7, and 8):

- vertical electrical resistivity panel (ERT),
- optical Televiewer image (OPTV),

- geological description derived from cuttings analysis during drilling (Bernard, 2005),
- associated geological layers (general stratigraphy).

All electrical resistivity measurements were taken in the open hole section of the boreholes.

In borehole M20 (Fig. 6), the open-hole section begins with partially altered oolitic limestone extending down to 56 m. Below this depth, the formation transitions into dolomitized limestone containing several flint layers. The boundary between the oolitic and dolomitic limestones is clearly distinguishable on the OPTV images due to a change in coloration. The OPTV also reveals two dark zones, between 85–89 m and 96–102 m, which correspond to voids that were not identified in the cuttings log.

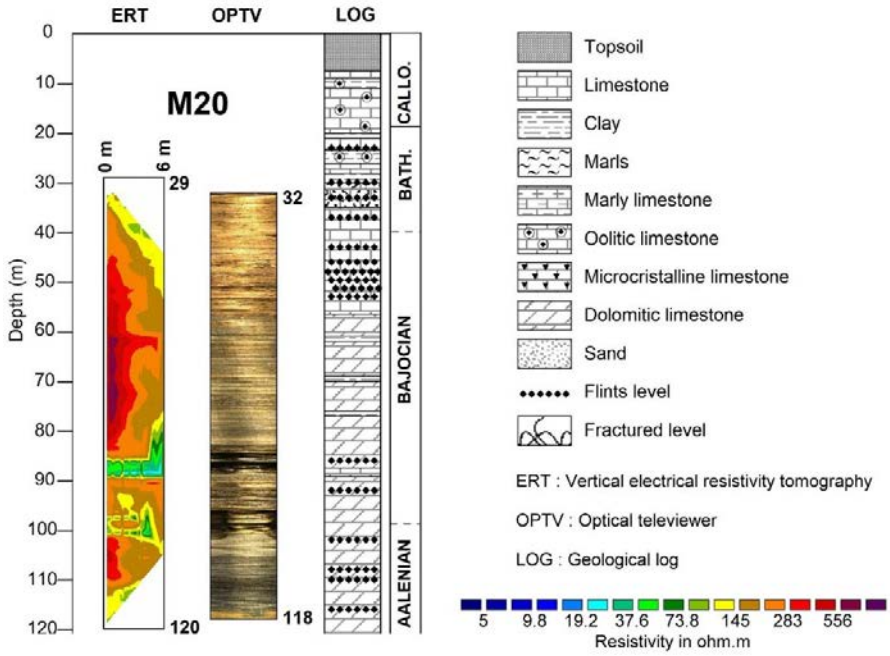

Figure 6 *Comparison of measured resistivities with available geological data for borehole M20. From left to right: vertical electrical resistivity tomography (ERT), optical televiewer (OPTV), geological log (LOG).*

The vertical resistivity profile indicates that the Dogger limestones are generally resistive (ρ_a >150 ohm·m). However, three lower resistivity anomalies are present. Two of these coincide precisely with the voids observed on the OPTV, while the third is located near the base of the borehole, at a depth of less than 110 m.

In borehole M04 (Fig. 7), the open-hole section begins with oolitic limestone down to a depth of 49 m. Below this, the cuttings log describes a succession of clayey and marly layers within the Bajocian formation. Compared to M20, the OPTV data from M04 reveal generally darker intervals, reflecting the clayey-marly nature of the limestone. The first clayey interval, described between 49 and 53 m in the cuttings log, corresponds to a karstic void observed on the OPTV. Two additional karstic zones are identified on the OPTV at depths of 70 m and 91 m.

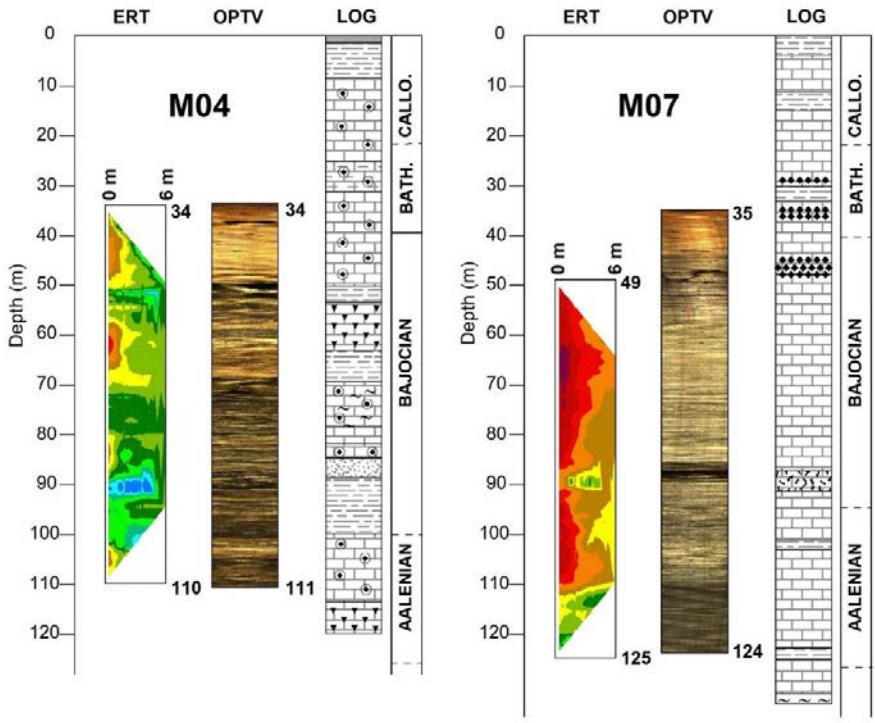

Figure 7 *Comparison of measured resistivities with available geological data for borehole M04 and M07. Refer to Figure 6 for the ERT resistivity color scale. From left to right: vertical electrical resistivity tomography (ERT), optical televiewer (OPTV), geological log (LOG).*

Electrical resistivity tomography (ERT) indicates that the limestone in this section has relatively low resistivity values, often below 100 ohm·m, which aligns with the clayey-marly composition described in both the cuttings log and the OPTV imagery. Two horizontal zones of very low resistivity are detected at the karstic levels observed on the OPTV at 49–53 m and 91 m.

In borehole M07, the cuttings log indicates limestone throughout the open-hole section, with a fractured zone around 90 m and clay-rich intervals at depths of 104 m and 124 m. The OPTV imagery reveals well-indurated limestone over most

of the open-hole section. A darker interval is observed between 86 and 90 m, corresponding to a karstic zone. From a depth of 110 m onward, the OPTV shows a general darkening, suggesting increased clay content or alteration.

The electrical resistivity tomography (ERT) data show high resistivity values (ρ_a >150 ohm·m) down to approximately 110 m, consistent with compact limestone. Below this depth, resistivity decreases (ρ_a <150 ohm·m), reflecting the presence of clay or increased porosity. A single horizontal low-resistivity anomaly is detected at 90 m, matching the karstic level observed on the OPTV between 86 and 90 m.

In borehole M11, the cuttings log indicates limestone interbedded with clayey layers within the Bathonian and Bajocian formations. This is reflected in the OPTV imagery, which generally appears dark, except for a lighter interval between 100 and 110 m. A very dark zone is visible on OPTV between 86 and 89 m, corresponding to an open and highly fractured level. Interestingly, this interval is described as a clay layer in the cuttings log.

The ERT profile shows relatively low resistivity starting from a depth of 110 m. Between 90 and 110 m, the resistivity is slightly higher but remains lower than in

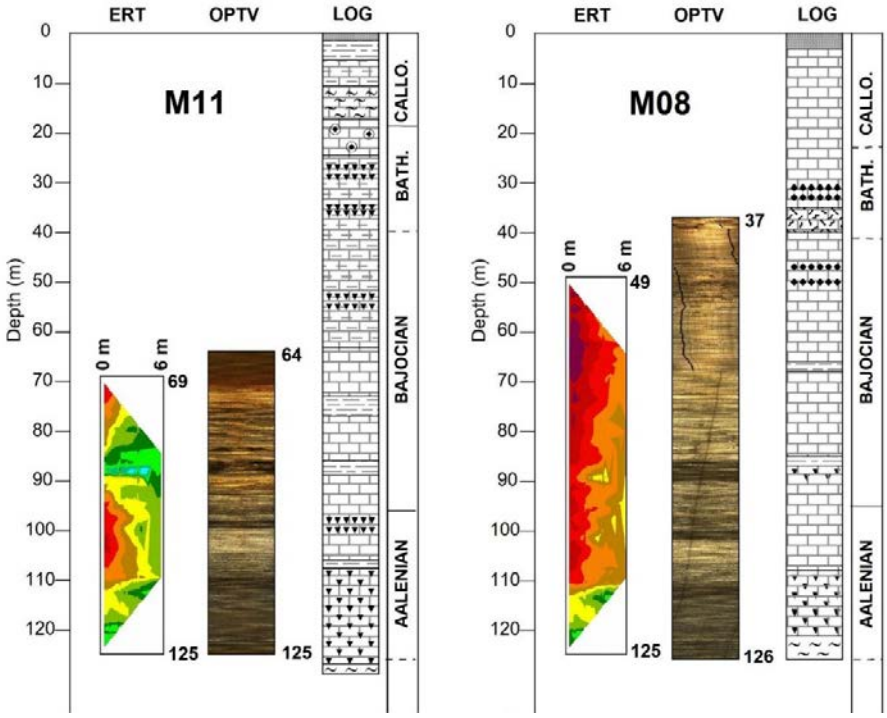

Figure 8 *Comparison of measured resistivities with available geological data for boreholes M11 and M08. Refer to Figure 6 for the ERT resistivity color scale. From left to right: vertical electrical resistivity tomography (ERT), optical televiewer (OPTV), geological log (LOG).*

boreholes M07, M20, and M08, suggesting a higher clay content in the limestone consistent with the cuttings log and OPTV observations. A distinct low-resistivity anomaly is observed between 86 and 89 m, corresponding precisely to the fractured zone identified on the OPTV.

In borehole M08, the cuttings log describes Bathonian and Bajocian limestone with occasional clay layers at depths of 67 m and 86 m. The OPTV imagery reveals darker zones at approximately 90 m, 100 m, and below 110 m. However, no karstic features are observed on the OPTV.

The ERT profile indicates that the limestone is generally resistive (ρ_a >150 ohm·m), except below 110 m where resistivity decreases, likely due to increased clay content or porosity. No distinct low-resistivity anomalies are detected, which is consistent with the absence of karstic cavities intersected by this borehole.

Summary

The apparent resistivities of the limestone formations are generally greater than 150 ohm·m down to a depth of approximately 110 meters. The only exception is observed in panel M04, where apparent resistivities remain lower throughout the entire section. Below 110 meters, the apparent resistivities measured in boreholes M20, M07, M08, and M11 decrease to values below 100 ohm·m.

Lithological data obtained from OPTV imaging and cuttings logs allow for correlating the geological nature of the formations encountered in the boreholes with the ranges of apparent resistivities recorded. Apparent resistivities exceeding 150 ohm·m correspond to carbonate formations of the Upper Aalenian, Bajocian, and, to a lesser extent, Bathonian stages. The exception in borehole M04, where lower resistivities are observed in these formations, can be attributed to the more clayey-marly composition of the limestones described in the cuttings logs and evidenced by generally darker intervals on the OPTV images. The low resistivities measured at the base of the panels likely correspond to marly-limestone facies characteristic of the Aalenian.

The three main depth intervals identified by the 3D seismic block (35–40 m, 85–87 m, and 110–115 m) were clearly detected by the electrical measurements (Fig. 5). These conductive anomalies are often confirmed by OPTV images. The level located between 85 and 87 m based on seismic data is detected between 85 and 90 m by electrical methods. Comparison of resistivity panels and optical wall imagery confirms that low-resistivity point anomalies correspond to open, water-filled karst conduits.

Additionally, the karstic level identified through acoustic methods (Mari and Porel, 2018; Mari, Porel, and Delay, 2020; see also Chapter 5, Mari 2026) at approximately 100 m depth in borehole M20 is also detected by electrical panels (Fig. 6 and 9). This level exhibits a double conductive anomaly and is particularly well defined on

the OPTV images, which reveal two distinct dark corridors. The convergence of detection through acoustic, electrical, and optical wall imaging methods is noteworthy (Fig. 9).

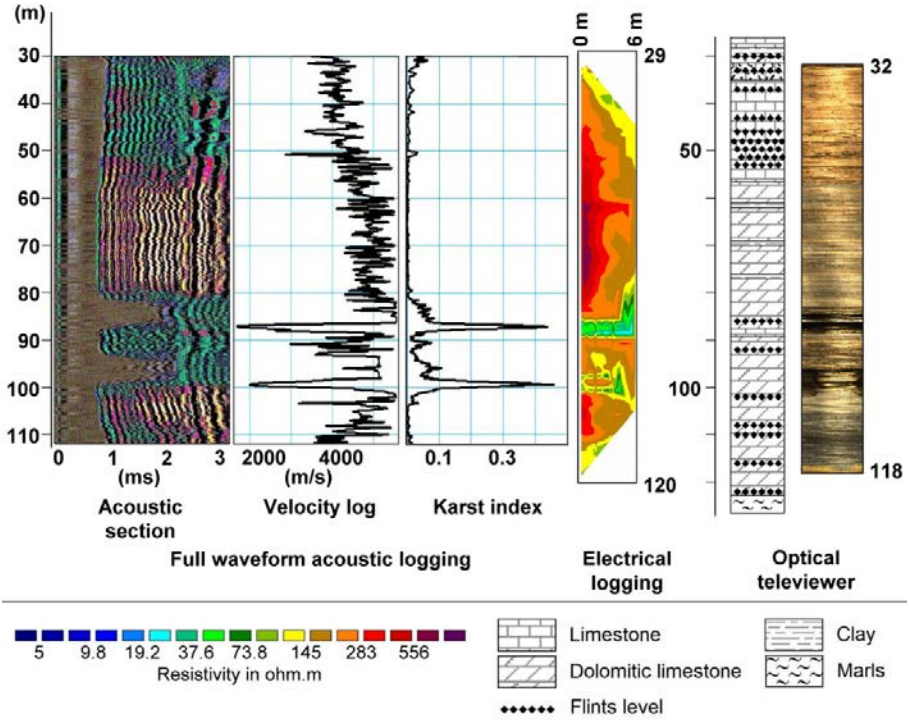

Figure 9 *Comparison of acoustic, electrical, and optical wall imaging methods in borehole M20. From left to right: the acoustic section, the velocity log, the karstic index log, the electrical resistivity panel, the geological log, the optical wall imagery*

Conclusions

The 3D seismic block acquired over the HES revealed three main high-porosity layers—presumably water-bearing—located at depths of 35–40 m, 85–87 m, and 110–115 m. These layers were identified as karstic zones. The presence of these karstic levels was clearly confirmed by both electrical resistivity measurements (Fig. 5) and Optical Televiewer (OPTV) imagery.

A comparison between the resistivity panels, long normal resistivity logs, and optical borehole images confirms that the low apparent resistivity anomalies observed in the electrical panels correspond to open, water-filled karst conduits. This correlation is particularly evident in boreholes M07 and M11.

The vertical electrical resistivity panels have demonstrated the ability to detect individual karst conduits in the Dogger limestone. When these voids are filled with water, they appear as point anomalies with low apparent resistivity. However, interpretation should always be supported by long normal resistivity logs (when available) and OPTV imagery.

References

Audouin O., Bodin J., Porel G., Bourbiaux B. (2008). Flowpath structure in a limestone aquifer: multi- borehole investigation at the hydrogeological experimental site of Poitiers, France. *Hydrogeology journal*, 16(5): 939–950. https://doi.org/10.1007/s10040-008-0275-4

Bernard S. (2005). Caractérisation hydrodynamique des réservoirs carbonatés fracturés. Application au site expérimental hydrogéologique (SEH) de l'Université de Poitiers – Ph.D. thesis, University of Poitiers, 24 November 2005.

Boulais A., Geairon H. Gaillard T. (2026). "Hydrogeological flow logging and dry tracer tests", Chapter 7 in *A new concept of karst development based on hydrogeology and geophysics*, EDP Sciences. https://doi.org/10.1051/978-2-7598-3934-6.c007.

Chapellier D. (2001a). Electrical methods, from Online course of geophysics (http://www-ig.unil.ch/)

Chapellier D. (2001b). Aquifer logging course, from Online course of geophysics (http://www-ig.unil.ch/)

Frappin P., Morey J. (2001). Jet grouting column diameter measurement using the electric cylinder method, Travaux n° 775.

Frappin P. (2011). CYLJET: an innovative method for jet grouting column diameter measurement. paper EG44, EAGE Conference & Exhibition, First International conference on Engineering Geophysics, 11–14 December 2011, AI Ain, United Arab Emirates.

Gaillard T. (2026a). "Hydrogeological Experimental Site (HES)", Chapter 4 in *A new concept of karst development based on hydrogeology and geophysics*, EDP Sciences. https://doi.org/10.1051/978-2-7598-3934-6.c004

Gaillard T. (2026b). "Hydro-stratigraphic study of hydrogeological Experimental Site", Chapter 8 in *A new concept of karst development based on hydrogeology and geophysics*, EDP Sciences. https://doi.org/10.1051/978-2-7598-3934-6.c008

Genter A., Baujard C., Glaas C., Maurer V. (2025). "Towards a revisited geothermal conceptual model in the Upper Rhine Graben", Chapter 4 in *Geophysics in geothermal exploration: a review*, EDP Sciences, https://doi.org/10.1051/978-2-7598-3752-6.c004

Habert J., Bievre G., Zumbo V. (2006). Optimization of geophysical methods for the old mining galleries, in National Geotechnical and Engineering Geology Day – JNGG' 2006 Lyon (France): 17-24.

Lantier F., Frappin P. (2000). Method and apparatus for probing and inspecting an underground volume, patent EP 0 786 673 B1, deposit number: 97106066.0, European Patent Office.

Mari J.-L., Porel, G. (2008). 3D seismic imaging of a near–surface heterogeneous aquifer: a case study, *Oil and Gas Science and Technology*, Rev IFP63: 179-201. https://doi.org/10.2516/ogst:2007077

Mari J.-L., Porel G. (2018). "Contribution of seismic and acoustic methods to the characterisation of karstic formations", Chapter 5 in *Well seismic surveying and acoustic logging*, EDP Sciences, https://doi.org/10.1051/978-2-7598-2263-8.c007

Mari J.-L., Porel G., Delay F. (2020). Contribution of Full Wave Acoustic Logging to the Detection and Prediction of Karstic Bodies, *Water,* 12(4): 948. https://doi.org/10.3390/w12040948

Mari J.-L. (2026). "Geophysical methods", Chapter 5 in *A new concept of karst development based on hydrogeology and geophysics*, EDP Sciences, https://doi.org/10.1051/978-2-7598-3934-6.c005

7

Hydrogeological flow logging and dye tracer tests on the Hydrogeological Experimental Site of Poitiers University (France)

A. Boulais, T. Gaillard and H. Geairon

Introduction

Karst may be defined as a network of conduits that enable groundwater transfer. Conduit dimensions range from centimetres to meters. Karst systems are organized around the connectivity of different types of voids: the primary porosity of the host rock, fissure porosity, and dissolution voids produced by karstification of carbonates.

At the regional scale, karst voids are typically smaller in volume than fissures and pores. Mangin (1975), based on drainage analyses of systems studied at the Moulis laboratory (France), concluded that karst voids account for only a very small fraction of the limestone massif—on the order of 0.2%. This estimate has been supported by data from various karst systems compiled by Worthington (2003).

© EDP Sciences, 2026
DOI: https://doi.org/10.1051/978-2-7598-3934-6.c007

The spatial distribution of karst conduits is only partially known, generally at locations where they intersect the land surface (e.g., sinkholes and springs) or are intercepted by boreholes. Even when accessible portions of a karst system can be mapped by speleologists, the explored conduits represent only a small fraction of the full drainage network.

Research at the Hydrogeological Experimental Site (HES) of Poitiers University (France), focuses on a limestone aquifer located at depths of approximately 35–130 m (supra-Toarcian aquifer). The site comprises 45 boreholes over an area of 15 ha, including 28 boreholes concentrated within a 210 × 210 m square (Fig. 1).

Karst features at the site occur preferentially within four lithostratigraphic units, each sub-horizontal, 2–5 m thick, and located at depths of ~30, 50, 85, and 115 m below ground surface (Mari and Porel, 2008; Mari et al., 2009; Mari and Porel, 2024).

A 3D seismic survey was conducted at the HES in 2004. Complementary to the surface seismic data, full acoustic logs were acquired in 6 boreholes: C1, MP5, MP6, M08, and M09. Cross-analysis of the 3D seismic model and borehole logs revealed a strong relationship between low-velocity seismic zones and inflow/outflow horizons associated with high hydraulic conductivity (Mari and Porel, 2008).

Finally, using tracer-test data from 50 inter-well tests performed within the seismic survey area, together with borehole flowmeter logs, Bodin et al. (2022) demonstrated the feasibility of delineating discrete karst conduit networks.

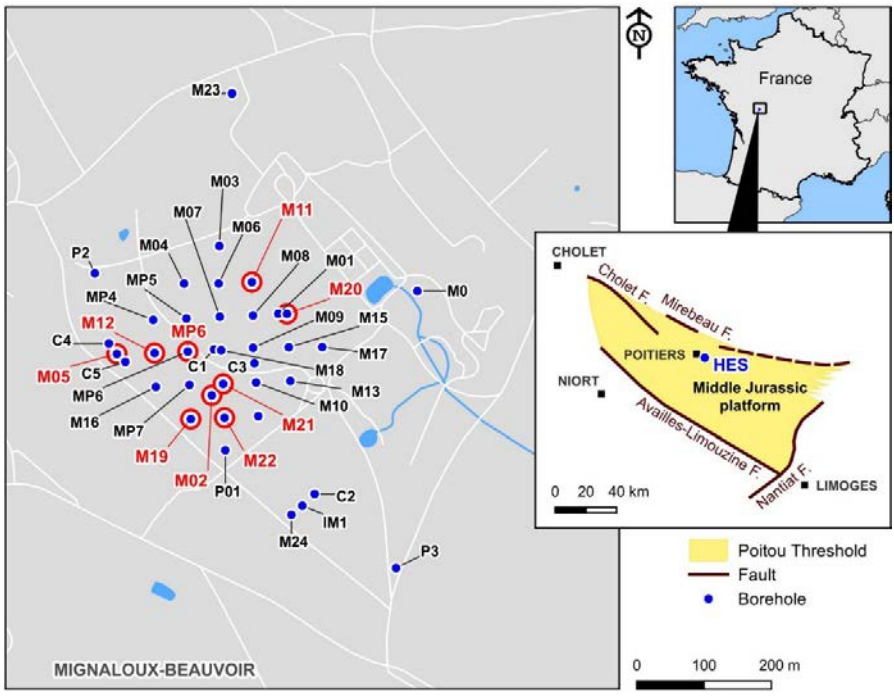

Figure 1 *Location of the boreholes at the HES in Poitiers, France.*

The value of borehole logging for aquifer characterization has been demonstrated by several authors (Keys, 1990; Paillet, 1993; US National Research Council, 1996; Paillet and Reese, 2000; Muldoon et al., 2001; Schürch and Buckley, 2002; Williams et al., 2002; Audouin et al., 2008). At the HES, geophysical borehole investigations have included caliper, natural gamma, electrical logs, flow logs, borehole imaging (Optical Televiewer - OPTV), and heat-pulse flowmeter surveys. All resulting data are publicly available via the "H+" database, developed within the framework of the Environmental Research Observatory (ERO) program.

Two categories of information have been derived from borehole logging: (1) the geological structure of the aquifer, and (2) the structure of the flow paths. Electrical, natural gamma-ray, and borehole imaging logs have been applied both to identify lithologic variations and to correlate stratigraphic units between boreholes (Gaillard et al., 2024).

Remote pumping logs revealed both upward and downward flows within the same boreholes during pumping tests. In 2021, tracer tests were performed to confirm these flow patterns in several wells, specifically M02, M05, MP6, M12, M19, and M21.

This paper presents the results of experiments conducted in collaboration with the University of Poitiers team in 2021. It builds upon the findings previously obtained at the site, which were used to define the operational methodology for the 2021 investigations.

Borehole flow logging acquisition

Principle of flow logging

The principle of borehole logging consists of lowering probes or measuring devices into the borehole, connected by a cable that ensures both electrical and mechanical linkage to surface instruments (Fig. 2). These tools continuously record physical or chemical parameters as a function of depth. In flow logging, the instruments measure the velocity and/or quality of moving fluids (e.g., water temperature and electrical conductivity).

At the HES, logging was conducted using a GFTC probe to measure natural Gamma-ray, Flow, Temperature, and electrical Conductivity. The micro-mill tool, equipped with an impeller, records the vertical velocity of water movement within the borehole. This allows identification and quantification of water inflows by detecting variations in fluid velocity along the borehole depth.

Flow logging can be performed under three conditions: (i) without pumping (ambient regime), (ii) with pumping in the borehole being logged (dynamic regime), and (iii) with pumping in an adjacent borehole (cross-dynamic regime), enabling detection of both upward and downward flows.

However, logging results may be disturbed by borehole casings or changes in borehole diameter, which can mask certain inflows. For instance, water moving through a reduced-diameter casing produces artificially elevated flow velocities that are not always associated with natural inflows.

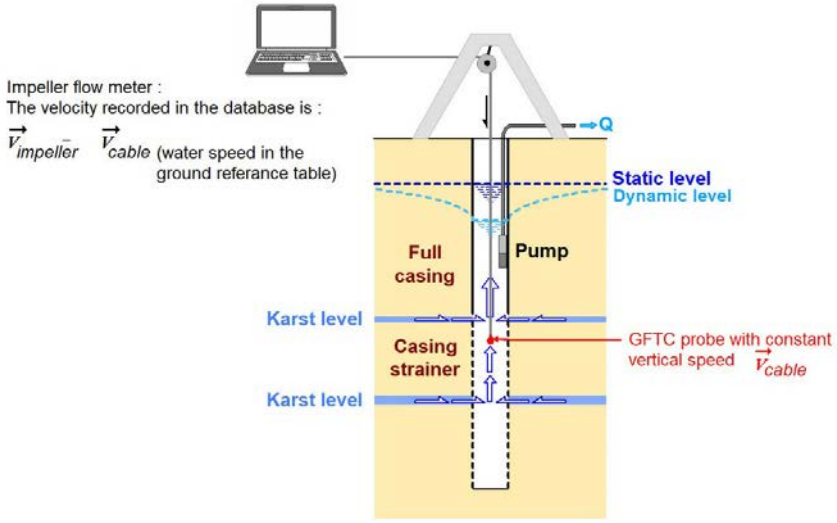

Figure 2 *Schematic diagram of flow logging.*

Downflow and upflow in the borehole

To obtain a complete picture of borehole flow, two recording passes are typically performed:

– downhole pass: The tool is lowered into the borehole, recording data continuously;
– uphole pass: Once at the bottom, the tool is raised while recording data.

When the tool moves with the flow, its velocity is added to that of the fluid. Conversely, when the tool moves against the flow, its velocity is subtracted from that of the fluid (or, if the flow is stronger than the tool's movement, the fluid velocity is subtracted from the tool's velocity). By knowing the downhole and uphole velocities of the tool (measured in a logger linked with a computer), it is possible to correct the micro-current meter readings to obtain the true fluid velocity and its direction of movement in the borehole.

Following the recommendations of Keys (1990), logging was performed during downward passes at a low speed (6 m/min) to minimize disturbance of the water column.

The data under study concern the velocities (in m/mn) and the temperatures (in degrees Celsius).

Dynamic flow logging

The flow logs presented in Figures 3 to 10 allow the identification of water inlets corresponding to productive karst levels. Since the pump is positioned above the probe, only upward flows are measured. The GFTC probe is positioned at the bottom of the borehole and recording is performed by lifting the tool. Water entering the borehole thus causes an increase in velocity measured in rounds per second (rps).

Borehole M05 (Fig. 3) is cased with PVC slotted screens oriented horizontally. The temperature log indicates that groundwater is cooler at 120 m depth (12.70 °C) than at 30 m depth near the surface (12.87 °C). Consequently, the geothermal gradient cannot account for this observation, and the presence of a cooler inflow around 120 m depth is confirmed by the flow log between 110 and 120 m. The velocity derivative shows that no additional flow disturbs the measurement down to 72–76 m, where the signal is perturbed on the derivative (variation in well radius?). Between 32-34 m a typical inflow is detected on the derivative curve.

Borehole MP6B is uncased, and therefore the measurement is not affected by the presence of a screen (Fig. 4). On the temperature log, a pronounced inflection at a depth of 84 m indicates an inflow of water, which is confirmed by the flow log, showing two signal variations clearly highlighted by the derivative at depths of 77 m and 83 m. At the bottom of the borehole, the signal becomes more complex, with a decrease in flow velocity associated with vacuoles clearly visible on the OPTV borehole wall imaging. A variation in the diameter of the open hole may account for the velocity decrease observed between 92 and 100 m.

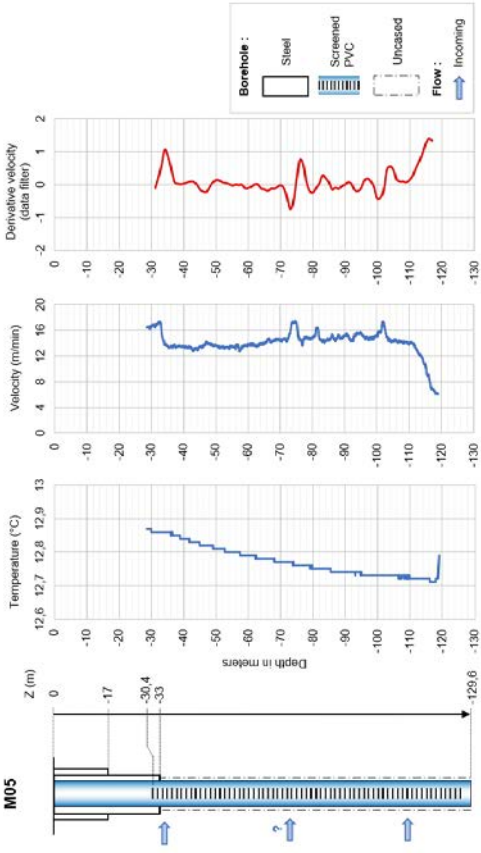

Figure 3 *M05 Flowmeters log with pumping in M05.*

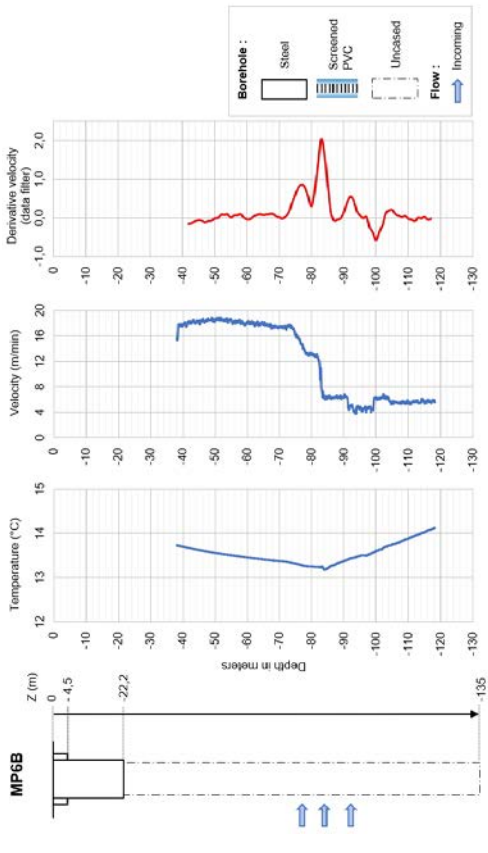

Figure 4 *MP6 Flowmeters log with pumping in MP6.*

The logs from borehole M11 (Fig. 5) are of particular interest because a large cavity encountered between 86.3 and 88.4 m depth results in a significant enlargement of the borehole diameter. In the open-hole section, the temperature log shows two variations at 74 m and 95 m, corresponding to cooler water inflows, but no anomaly is observed within the cavity between 86.3 and 88.4 m. In contrast, the flow log is disturbed between 86 and 88 m due to the enlarged borehole diameter. Water inflows therefore appear to occur around 90–92 m, within a dolomitized and vuggy level, and also between 72 and 74 m, within another dolomitized interval located below a discontinuity.

In borehole M12 (Fig. 6), the logs are affected by the presence of the screen (from 69.9 to 105 m) and by changes in borehole diameter. The temperature log indicates cooler water between 90 and 104 m (13.4 °C). On the flow log, velocity increases at 104 m near the bottom of the screen, an effect attributed to the change in borehole diameter. At the top of the screen, the diameter change also causes a decrease in

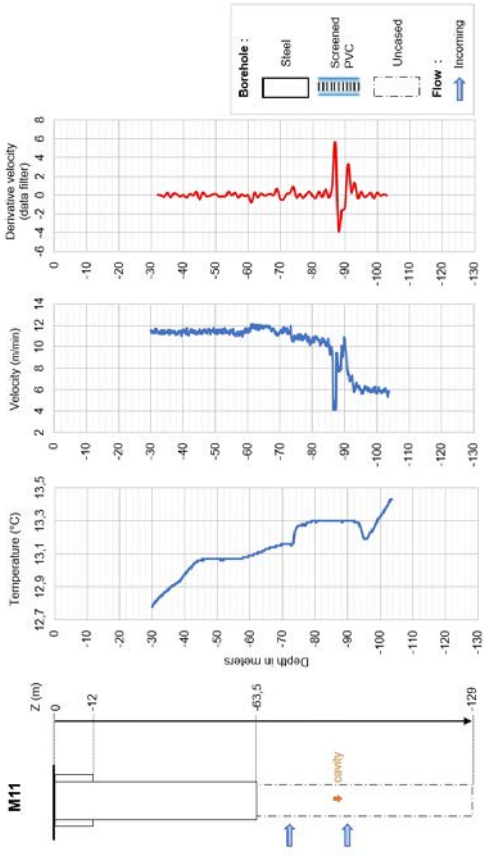

Figure 5 *M11 Flowmeters log with pumping in M11.*

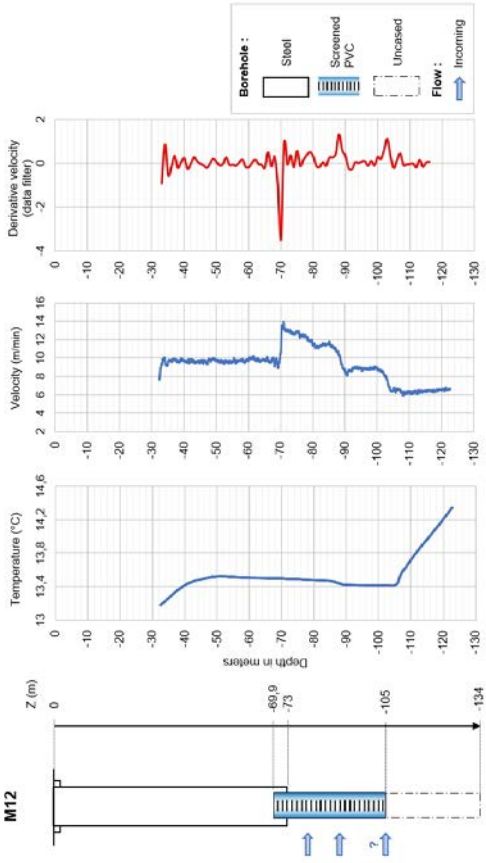

Figure 6 *M12 Flowmeters log with pumping in M12.*

flow velocity. However, between 88 and 90 m depth, a clear water inflow is detected within the screen, confirmed by the flow log. This inflow is also associated with a temperature increase between 86 and 90 m. A second inflow within the screen is identified between 78 and 80 m.

Borehole M19 is fully screened from 75.5 to 133 m depth (Fig. 7). The temperature log provides little information. On the flow log, a water inflow is identified between 116 and 118 m. At 82 m, another inflow causes the velocity to increase (>12 rps), although the transition from PVC screen to steel screen disturbs the measurement.

The logs from borehole M20 (Fig. 8) record a main water inflow, clearly identified on both the temperature log and the flow log, between 86 and 88 m. The velocity derivative is typical of a localized inflow. The geological formation at this depth corresponds to a dolomitized limestone.

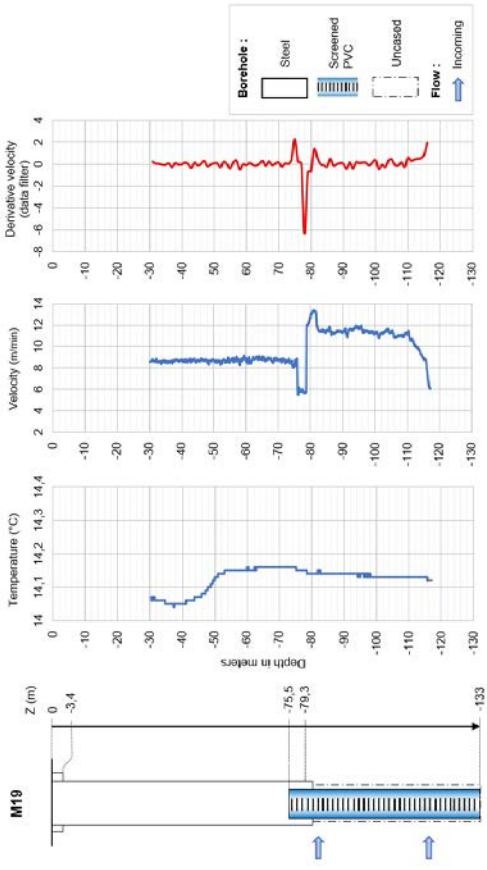

Figure 7 *M19 Flowmeters log with pumping in M19.*

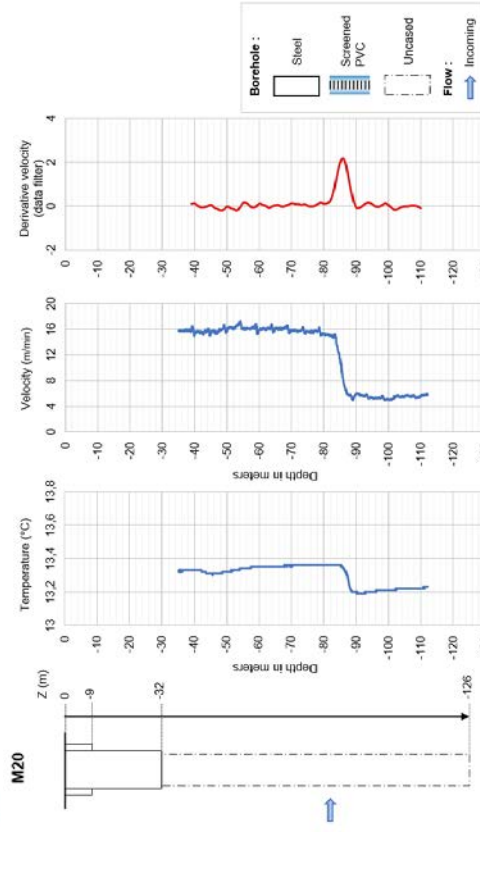

Figure 8 *M20 Flowmeters log with pumping in M20.*

In borehole M21 (Fig. 9), the main water inflow in the open-hole section is located between 91 and 94 m, within a highly dolomitized black limestone. The inflowing water at this depth is cooler (13.6 °C). A minor inflow at 55 m provides an additional contribution to discharge. At the bottom of the screen (68–70 m), the measurement is disturbed.

Finally, Figure 10 presents the measurements from borehole M22. Four successive water inflows are identified, from bottom to top, at approximately 114–116 m, 98–100 m, 84–86 m, and 64–66 m. Unlike the logs from M21 and MP6 (Fig. 4 and 9, respectively), the temperature log shows no distinct anomaly.

In summary, several productive levels (numbered 1 to 10 in Tab. 1) are identified when the flow log is performed under pumping conditions. Comparison of these results with the karst index of Mari and Porel (2024) for boreholes M11, M20, and M21 shows good agreement for levels 3 (64–66 m), 4 (72–74 m),

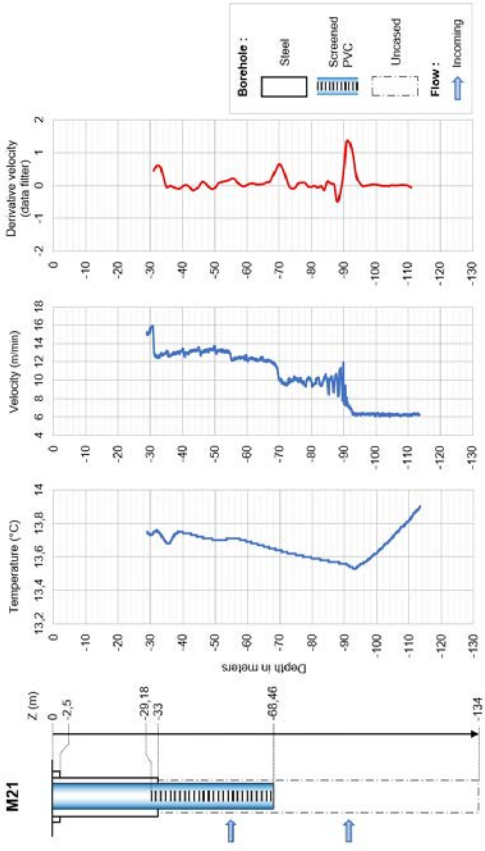

Figure 9 *M21 Flowmeters log with pumping in M21.*

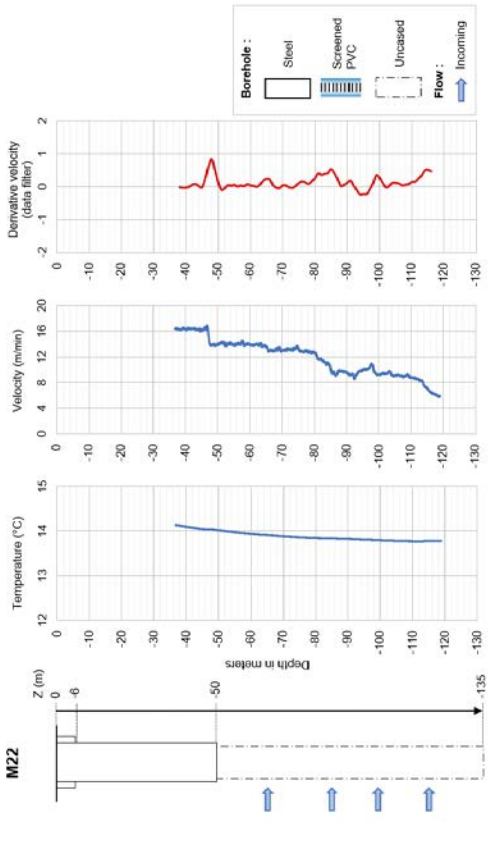

Figure 10 *M22 Flowmeters log with pumping in M22.*

7 (84–88 m), and 10 (114–116 m). They are marked with an asterisk (*) in Table 1. The level that is both the most karstified and the most productive is level 7 (86–88 m). The lithology of this interval corresponds to a dolomitized limestone. The comparison between M21 and M22 provides additional insights. For instance, the karst levels identified by Mari and Porel (2008; 2024) at 100 m (M20) and at 90 m and 110 m (M22) yield only limited water inflows. The lithology of these intervals consists of limestone containing numerous type 1 vacuoles (Gaillard and Moreau, 2026), which appear to be poorly interconnected. Moreover, in M22, the level at 90 m seems to result from the collapse of a dolomitized horizon during drilling.

Table 1 *Locating water inflows into the Supra Toarcian aquifer using temperature and flow logs (in m depth)*

inflow	M05	MP06B	M11	M12	M19	M20	M21	M22
1	32-34							
2							55	
3								**64-66***
4	72-76	77-78	**72-74***					
5		82-84		78-80	80-82			
6								
7			**86-88***	88-90		**86-88***		**84-86***
8		92	**90-92***				91-94	
9								98-100
10	110-120				116-118			114-116
Flow in m3/h	10.6	10.0	10.8	9.8	10.0	10.4	10.1	10.2

Flow logging with pumping in MP6 (crossed dynamics MP6)

Flow logs were carried out on boreholes M02, M05, M12, M19, and M21 with pumping in borehole MP6 at 60 m^3/h. The borehole logs were carried out upwards, at a speed of 6 m/min. Vertical flow velocities are measured, and the velocity derivative is calculated to identify the incoming and outgoing flows from the different karst levels. When velocities decrease, flows in the borehole are downward. Conversely, when velocities increase, flows are upward.

According to the flow log results, upward flows are identified on M02 (Fig. 11) and M12 (Fig. 12), and downward flows are observed on M05 (Fig. 13) and M21 (Fig. 15). Flow directions are uncertain regarding M19 (Fig. 14).

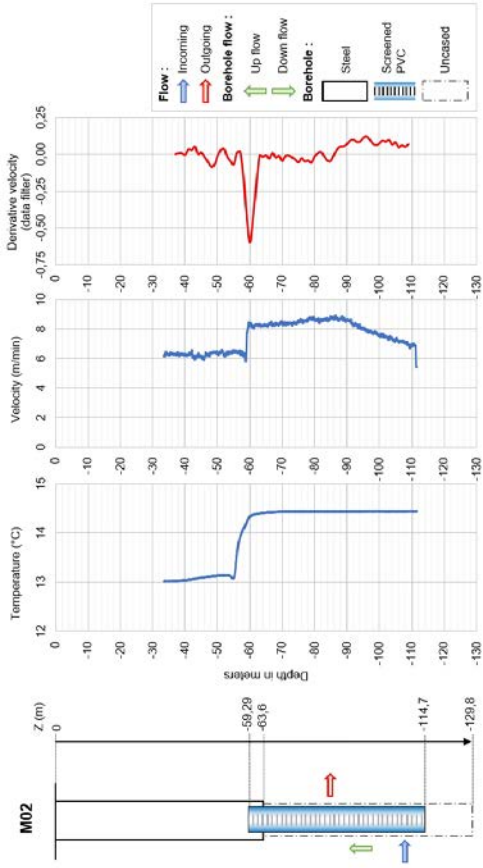

Figure 11 *M02 Flowmeters log - crossed dynamics MP6.*

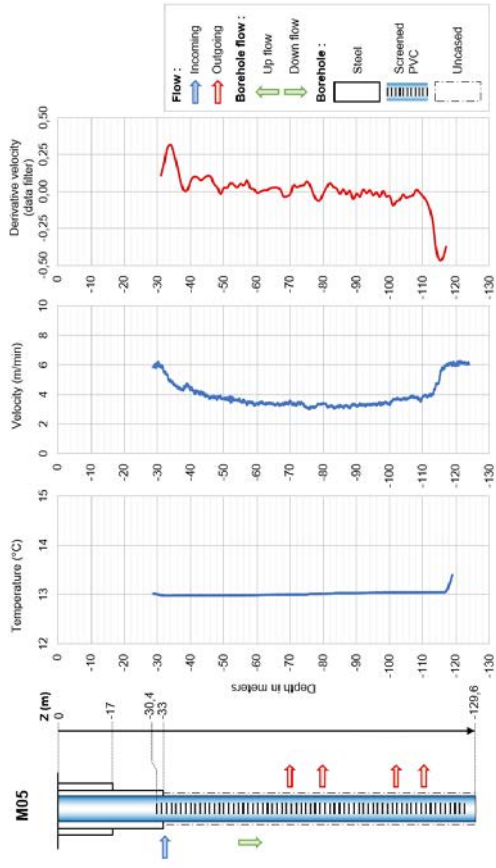

Figure 12 *M05 Flowmeters log - crossed dynamics MP6.*

The productive levels in borehole MP6 are located at depths of 77 m, 83 m, and 92 m (Fig. 4). Considering the spatial distribution of the boreholes (Fig. 1), groundwater flow along the cross-section M05–M12–MP6 follows a complex trajectory. In M05, the productive level at ~35 m is activated and feeds, *per descensum*, the pumped levels in MP6 at 77 m, and in the interval 88 to 92 m, as well as the deeper level at 114 m. In M12, flows converge toward the productive intervals at 78 m and between 80 and 90 m, with part of the discharge also originating from the base of the borehole (104–106 m). Thus, the boreholes alter the natural flow regime by hydraulically connecting multiple porous and/or karstified horizons.

Around boreholes M19, M02, and M21, the flow logs are less contrasted. In M02, the 85–90 m interval is partly supplied by upward flow originating from the 90–110 m level. In M21, the intervals at 70 m and 80–90 m are instead partly fed by flow coming from the 35–60 m level. Once again, the boreholes likely promote mixing between porous and karstified horizons.

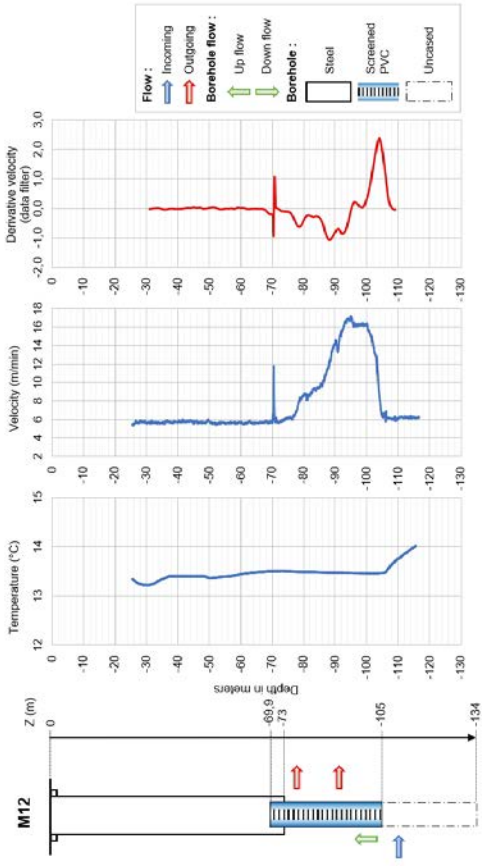

Figure 13 *M12 flowmeters log - crossed dynamics MP6.*

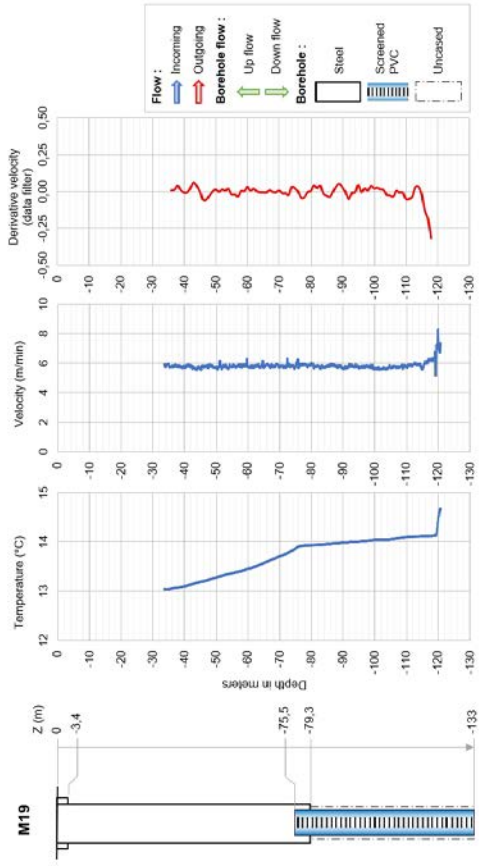

Figure 14 *M19 flowmeters log - crossed dynamics MP6.*

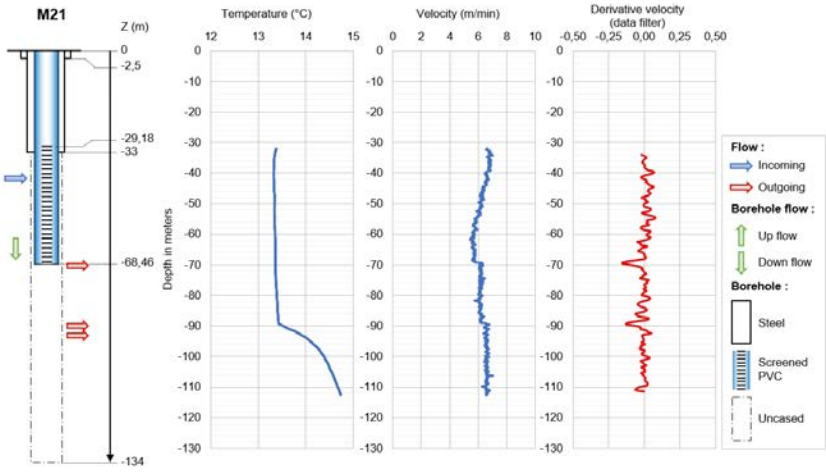

Figure 15 *M21 flowmeters log - crossed dynamics MP6.*

Tracer tests

Tracer test protocol

Tracer tests were conducted to verify mass transfers between the different karst horizons developed in the Supra-Toarcian aquifer. Artificial hydrogeological tracing is an "experimental procedure aimed at making apparent and observable the actual movement of groundwater in an aquifer along one or more defined trajectories between a point of origin and one or more detection points, using an artificial tracer marking the water" (Castany and Margat, 1977, p. 180).

These tests complement those carried out by researchers from the University of Poitiers on other boreholes (see Bodin et al., 2022). The protocol applied in these tests can be summarized as follows (Tab. 2):

1. a pumping operation is launched at a constant flow rate on MP6 until a pseudo-steady flow regime is obtained;
2. the wellbore and tracer injection depth are selected from the results of GFTC logs. The targeted injection depth is generally a few tens of cm upstream of a flow horizon (from the well to the aquifer). The injection boreholes are (Fig. 16):
   - M19 at a depth of 111 m: injection No. 1 on 29/06/2021 at 9:25 a.m. UTC,
   - M19 at a depth of 85 m: injection No. 2 on 01/07/2021 at 1:50 p.m. UTC,
   - M05 at a depth of 111 m: injection No. 3 on 05/07/2021 at 3:40 p.m. UTC;
3. the tracer solution (5 g of uranine diluted in 2 L of water) is injected, followed by rinsing with a volume of 40 L of water. Pipes 2.5 m in length and 1.5 cm in internal diameter are connected down to the targeted injection depth. The total injection time, including rinsing, is less than 3 minutes;
4. tracer migration was monitored at the MP6 pumping borehole outlet pumped at 60 m3/h, using a fluorometer. The fluorometers were positioned at different depths in the observation boreholes M02, M12 and M21 in order to verify the nature of the flows (ascending or descending) between the different karst levels (Tab. 1);
5. the fluorometers used were Valeport Hyperion probes (3) and Albillia GGUN probes (4). The 7 fluorometers were previously calibrated with standard solutions whose concentrations were between 0 µg/L and 999 µg/L.

Results

The Breakthrough Curves (BTC) obtained following the 2 injections carried out on M19 are reported in Figures 17 and 18. The arrival times of the first concentration and the concentration peaks made it possible to better identify an upward flow in the M02 observation borehole and a downward flow in the M21 borehole. The tracer transfer times are longer in the case of the second injection at 85 m depth, which highlights a longer travel distance.

Table 2 *Dye tracer test design.*

Injection borehole	Observation borehole	Fluorometer	
		Depth/ground (m)	Reference fluorometer
M19	M02	62	HYPERION 74041
		85	HYPERION 74039
		100	FL22-243
	M21	65	FL22-241
		85	FL22-242
	MP6	0 (at the outlet of the pumped well)	HYPERION 74040 et FL22-240
M05	M12	76	FL22-242
		85	HYPERION 74041
		100	HYPERION 74039
		105	FL22-241
	MP6	0 (at the outlet of the pumped well)	FL22-239

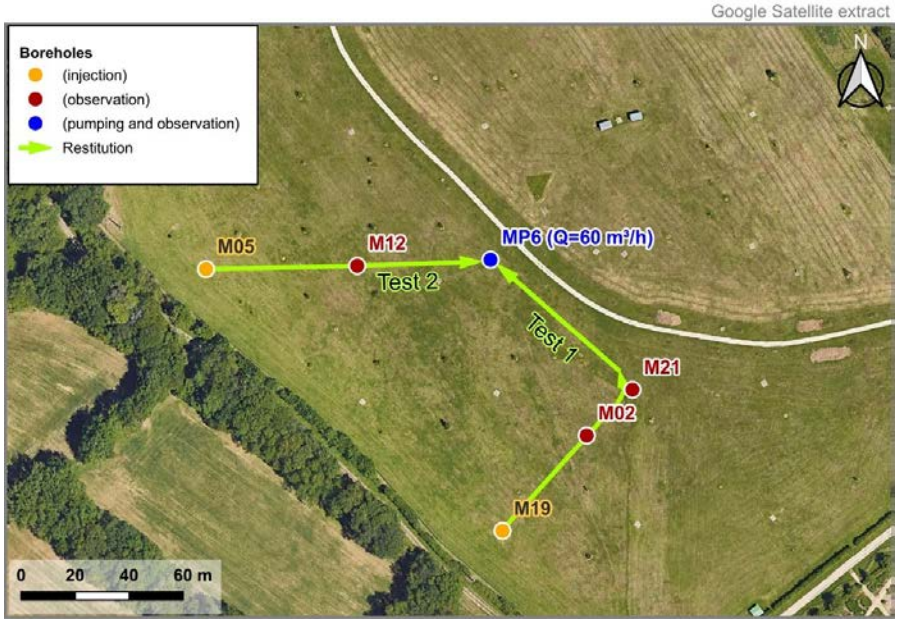

Figure 16 *Location of the boreholes MP6 (pumping and observation) M05 (injection) M19 (injection) and observation wells (M02, M12, M21).*

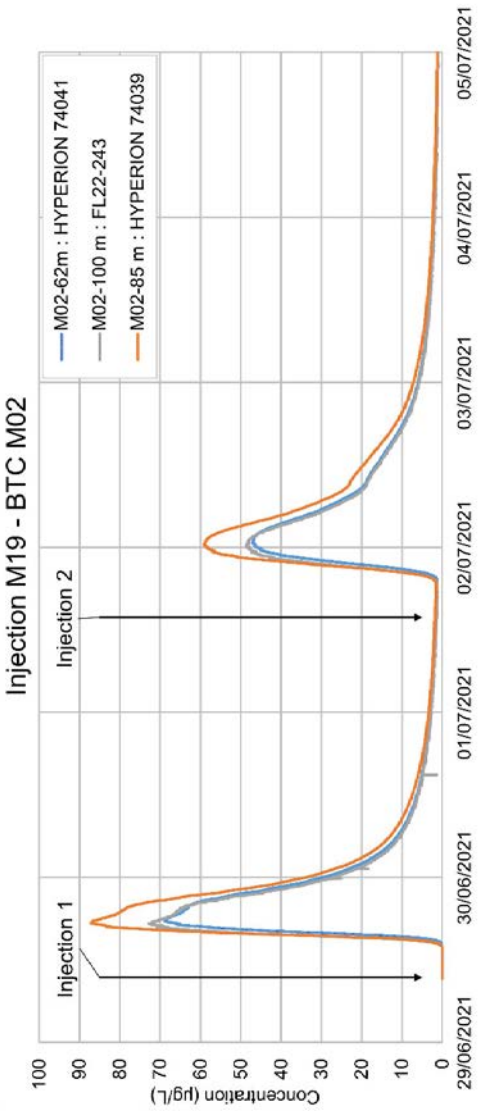

Figure 17 *Experimental BTC M02 after injections into M19.*

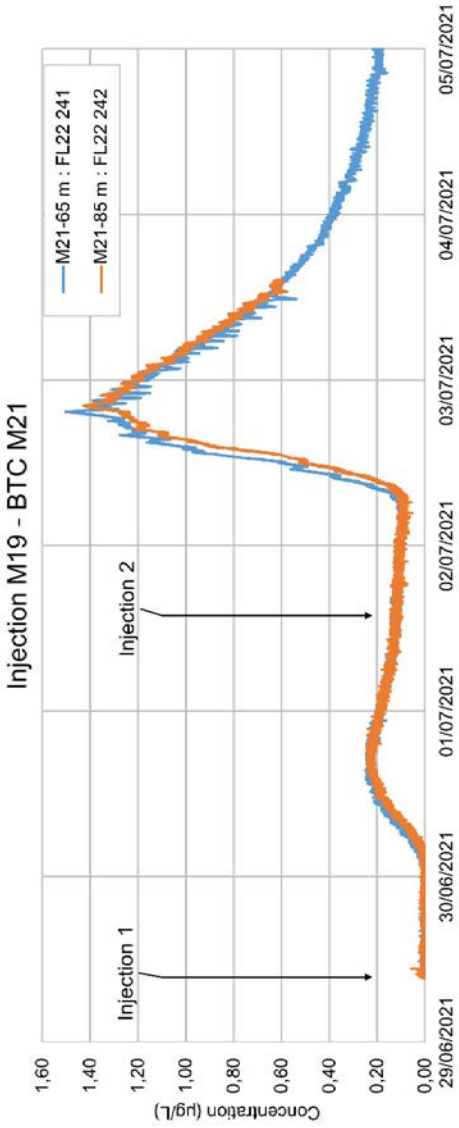

Figure 18 *Experimental BTC M21 after injections into M19.*

The BTC obtained following the injection carried out on M05 at 111 m depth is reported in Figure 19. The arrival times of the first concentration and the concentration peaks made it possible to confirm an upward flow in the M12 observation borehole.

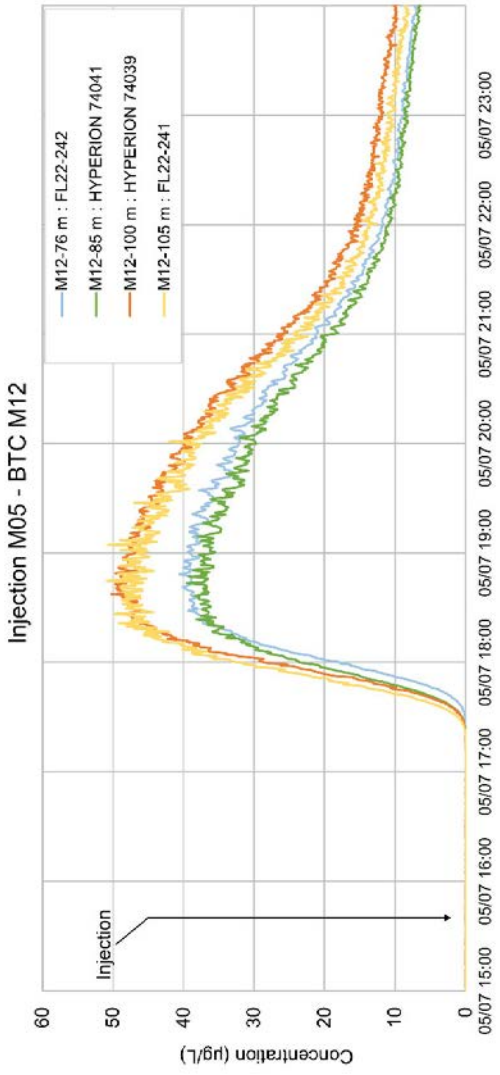

Figure 19 *BTC experimental M12 after injection in M05.*

Conclusion and interpretation of pathways in karst horizons

In addition to the flow log results, the tracer tests provide further clarification of mass transfers within the boreholes, in relation to the porous and karstic levels intersected between 35 m and 115 m, as defined by geophysical and GFTC logs (Tab. 1). The results are presented in Figures 20 and 21.

The tracer responses indicate ascending flows in M02 and M12, and descending flows in M21 (Fig. 20). The boreholes drilled on the experimental site thus act as conduits connecting the karst levels and appear to be solely responsible for the

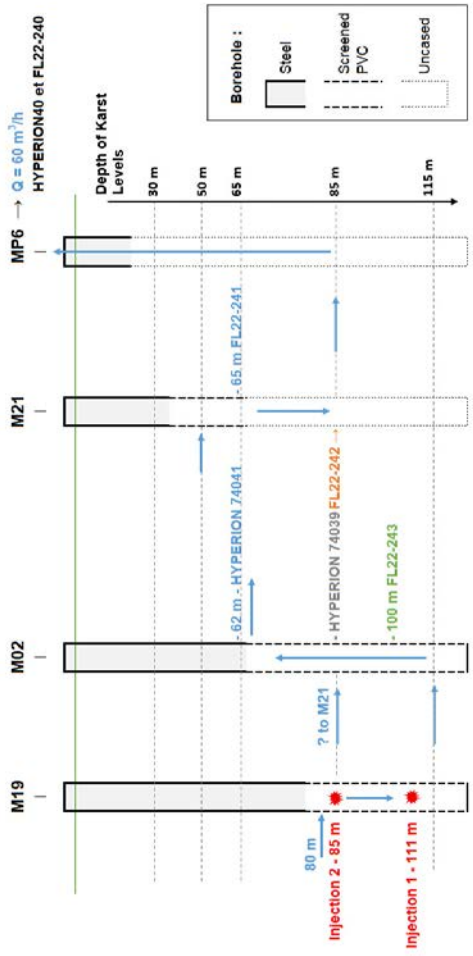

Figure 20 *Hydrogeological cross-section from M19 to MP6.*

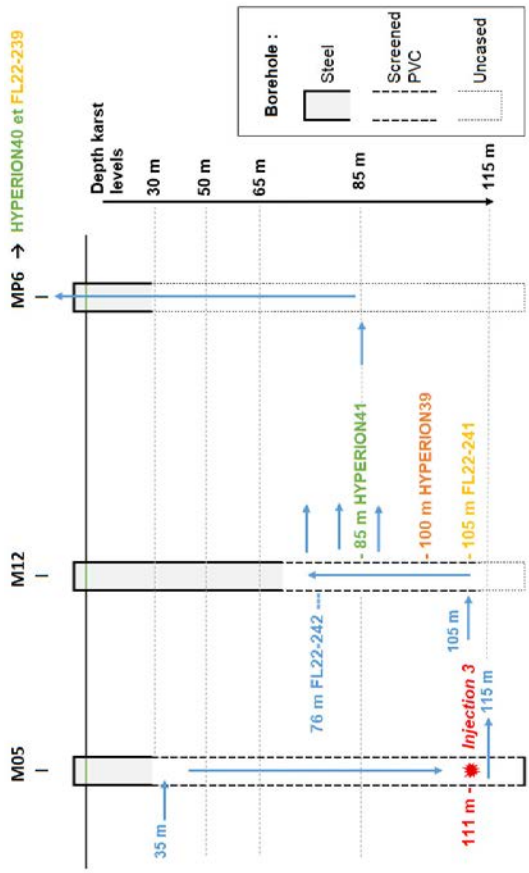

Figure 21 *Hydrogeological cross-section from M05 to MP6.*

observed mass transfers. These transfer fluxes are consistent with the borehole flow results obtained during pumping tests on MP6 (Fig. 4).

Furthermore, the stratified organization of karst conduits is corroborated by field observations of rock outcrops located a few kilometres from the HES, within the same lithostratigraphic horizons (Gaillard et al., 2024).

References

Audouin O., Bodin J., Porel G., Bourbiaux B. (2008). Flowpath structure in a limestone aquifer: multi-borehole logging investigations at the hydrogeological experimental site of Poitiers, France, *Hydrogeology Journal*, 16: 939-950. https://doi.org/10.1007/s10040-008-0275-4

Bodin J., Porel G., Nauleau B., Paquet D. (2022). Delineation of discrete conduit networks in karst aquifers via combined analysis of tracer tests and geophysical data, *Hydrology and Earth System Sciences*, 26 (6): 1713-1726. https://doi.org/10.5194/hess-26-1713-2022

Castany J., Margat J. (1977). Dictionnaire français d'hydrogéologie (French dictionary of hydrogeology). BRGM Ed.

Gaillard T., Moreau M., Mari J.-L. (2024). Seismic and stratigraphic characterization of karstogenic horizons in a sequence of carbonate deposits: Example of the Dogger limestones of the Poitou threshold. In E3S Web of Conferences, Volume 504 (2024) Journées Scientifiques AGAP Qualité 2024, Poitiers, France, 26 au 28 mars 2024, Published online: 26 March 2024, Published online: 26 March 2024. https://doi.org/10.1051/e3sconf/202450405005

Gaillard T., Moreau M. (2026). "Hydrogeology of the Poitou Threshold", Chapter 3 in *A new concept of karst development based on hydrogeology and geophysics*, EDP Science, https://doi.org/10.1051/978-2-7598-3934-6.c003

Keys W.S. (1990) Borehole geophysics applied to ground-water investigations. Techniques of Water Resources Investigations, book 2, chapt. E-2, US Geological Survey, Reston, VA.

Mangin A. (1975). Contribution à l'étude hydrodynamique des aquifères karstiques, troisième partie: constitution et fonctionnement des aquifères karstiques [Contribution to the hydrodynamic study of karst aquifers, part three: constitution and functioning of karst aquifers]. *Annales de spéléologie*, 30(1): 21-124.

Mari J.-L., Porel G. (2008). 3D Seismic Imaging of a Near-Surface Heterogeneous Aquifer: A Case Study. *Oil & Gas Science and Technology (IFP)*, 63(2): 179-201. https://doi.org/10.2516/ogst:2007077

Mari J.-L., Porel G., Bourbiaux B. (2009). From 3D Seismic to 3D Reservoir Deterministic Model Thanks to Logging Data: the Case Study of a Near Surface Heterogeneous Aquifer. *Oil & Gas Science and Technology (IFP)*, 64(2): 119-131. https://doi.org/10.2516/ogst/2008049

Mari J.-L., Porel G. (2024). "The Hydrogeological Experimental Site of Poitiers: Hydrogeological versus geophysical investigations", In *E3S Web of Conferences* 504, Journées Scientifiques AGAP Qualité 2024, Poitiers, France, 26 au 28 mars 2024, Published online: 26 March 2024. https://doi.org/10.1051/e3sconf/202450405003

Muldoon M.A., Simo J.A.T., Bradbury K.R. (2001) Correlation of hydraulic conductivity with stratigraphy in a fractured-dolomite aquifer, northeastern Wisconsin, USA. *Hydrogeol J.*, 9: 570-583. https://doi.org/10.1007/s10040-001-0165-5

Nauleau B., Porel G., Paquet D., Battais A., Bodin, J. (2022). Technical specifications of the boreholes at the Hydrogeological Experimental Site (HES) of Poitiers, France, French National Observatory HC, https://doi.org/10.26169/hplus.poitiers_technical_logs

Paillet F.L. (1993). Using borehole geophysics and cross-borehole flow testing to define hydraulic connections between fracture zones in bedrock aquifers. *J. Appl. Geophys.*, 30: 261-279.

Paillet F.L., Reese R.S. (2000) Integrating borehole logs and aquifer tests in aquifer characterization. *Ground Water*, 38: 713-725.

Schürch M., Buckley D. (2002) Integrating geophysical and hydrochemical borehole log measurements to characterize the Chalk aquifer, Berkshire, United Kingdom. *Hydrogeol. J.*, 10: 610-627.

Williams J.H., Lane J.W., Singha K., Haeni F.P. (2002) Application of advanced geophysical logging methods in the characterization of a fractured-sedimentary bedrock aquifer, Ventura County, California. US Geol Surv. Water Resour Invest Rep 00-4083.

Worthington S.R.H. (2003). A comprehensive strategy for understanding flow in carbonate aquifers. Speleogenesis and Evolution of Karst Aquifers 1 (1), www.speleogenesis.info, re-published from: Palmer, A.N., Palmer, M.V., and Sasowsky, I.D. (eds.), 1999. Karst Modeling: Special Publication 5, The Karst Waters Institute, Charles Town, West Virginia (USA): 30-37.

8

Hydro-stratigraphic study of the Hydrogeological Experimental Site of Poitiers, France

T. Gaillard

Objectif and method

The Hydrogeological Experimental Site (HES), located near Poitiers (France), was originally established to investigate the role of fracturing in Middle Jurassic limestones. The supra-Toarcian aquifer has been extensively characterized through surface geophysics (Mari et al., 2009), borehole geophysical logging (Mari et al., 2020; Moreau et al., 2026), and numerous downhole investigations conducted by the University of Poitiers (Delay et al., 2004).

Early studies demonstrated the absence of major vertical structures such as faults or open vertical fractures. However, the presence of discontinuous sub-horizontal porous horizons has been clearly documented (Bourbiaux et al., 2007; Audouin et al., 2008; Mari et al., 2009; Bodin et al., 2022; Mari et al., 2024). In this paper, these planar features are reinterpreted within the framework of the regional stratigraphic context (Gabilly, 1978; Mourier et al., 1986; Gaillard et al., 2024) and by

© EDP Sciences, 2026
DOI: https://doi.org/10.1051/978-2-7598-3934-6.c008

comparison with geological outcrops in the Clain Valley (Branger et al., 2026). Dating of sedimentation across the Poitou Threshold (Fig. 1) remains difficult, as ammonite occurrences are rare and largely restricted to the base of the depositional sequence (Gabilly, 1978, p. 150). Consequently, stratigraphic interpretation relies primarily on the identification of erosional surfaces (Gabilly et al., 1985), bed thickness, fossil assemblages, and established regional reference sections (Gabilly, 1978; Mourier et al., 1986).

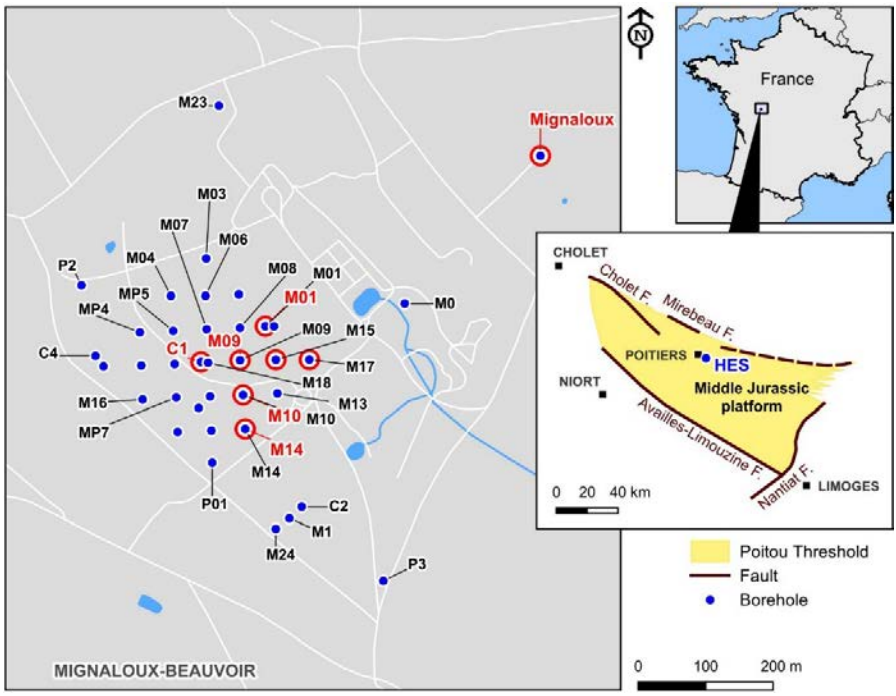

Figure 1 *The hydrological experimental site and borehole locations (Poitiers University document).*

This study is based on the analysis of two continuous cores (C1 and C2) and high-resolution borehole optical imagery (OPtical TeleView - OPTV). Figure 1 shows the location of the HES, the core drillings, and the Mignaloux borehole described by Mourier (1983).

Aquifer stratigraphy of the HES

Stratigraphic context

The reference stratigraphy for the supra-Toarcian aquifer is derived from the works of Gabilly (1978), Benvel (1978), and Mourier (1986). For further details about

the Bajocian, refer to Branger et al. (2026). The discontinuities (D) are numbered according to Gabilly et al (1985).

The Aalenian stage is subdivided into three main terms with reference to ammonite zones (base to top):

a) laminated marly limestones (*Opalinum* Biozone, 4–5 m),
b) siliceous (cherty) formation (*Murchisonae* Biozone, 8–10 m),
c) bioclastic and oolitic limestones (*Bradfordensis* and *Concavum* Biozones, 9–14 m), often partially dolomitized and locally displaying cavernous textures (c′ unit).

A regional discontinuity (D5bis) separates the *Opalinum* and *Murchisonae* Biozones, while discontinuities D6 and D7 mark the base and top of the *Concavum* interval.

The Bajocian comprises:

d) decimetric limestone beds with Serpulid fossils (*Ovalis* Biozone, 1–2 m),
e) bioclastic and pelletal limestones (*Laeviuscula* Biozone, 7–8 m),
f) white oolitic limestones (top of *Laeviuscula*, 2–4 m),
g) limestone beds of the *Propinquans* and *Humphriesianum* Biozones (9–10 m), topped by h) a crinoid-rich horizon,
h) bioturbated limestones referred to as the burrowed limestones "Assise à terriers" (*Garantiana* Biozone, 5–6 m), and
i) fine-grained gravelly limestones with flint nodules (*Parkinsoni* Biozone, 23–25 m).

Discontinuities are identified at the top of the *Laeviuscula* zone (D7bis) and at the base and top of the *Garantiana* interval (D8 and D8bis, respectively).

The Bathonian is more difficult to interpret due to gaps in biostratigraphic markers. Bathonian limestones lie above discontinuity D9. Gabilly (1978) subdivided this interval into:

k) ctenostreon beds (possibly *Zigzag* Biozone?, 2–3 m),
l) siliceous, bioclastic and pelletal limestones (15–16 m),
m) bioturbated limestones (7 m).

The overlying Callovian is easily recognizable due to its micropackstone texture and chalky appearance.

Data available

The borehole drilled during Mourier's thesis (1983), near the HES, identified key marker horizons (notably the oolitic limestone of the *Concavum* Biozone and the crinoidal bed atop the *Humphriesianum* interval). Stratigraphic details for the supra-Toarcian aquifer were further refined using two cored boreholes (C1 and C2) described by the French Petroleum Institute (Gaumet et al., 2004). These cores made it possible to characterize the depositional facies (mudstone, packstone,

grainstone) and provided a preliminary sequence stratigraphy. However, erosional surfaces were poorly sampled and often absent in the cores.

To address this shortcoming, borehole optical imagery was analysed for the first time and presented at the "Journées Scientifiques de l'AGAP-Qualité" at the University of Poitiers (Gaillard et al., 2024). OPTV logs offer high-resolution imaging of bedding surfaces and discontinuities, enhancing the identification of sequence boundaries described on the Poitou Threshold (Gabilly, 1978; Gabilly et al., 1985; Gaillard et al., 2024; Branger et al., 2026).

Initial OPTV analyses were focused on boreholes with minimal karstification and long open-hole sections (M01, M09, M10, M14, M15, M17). Subsequent analyses targeted boreholes extensively studied through geophysics and hydrogeological testing. Additional data include resistivity and natural gamma-ray logs.

Table 1 *List of open holes and drilling cores studied.*

Borehole	X_RGF93	Y_RGF93	Z NGF	Depth of top OH in m	Depth of bottom OH	OH length in m
C1	501299.97	6609513.918	125.36	23.8	129.7	129.70
C2	501449.316	6609299.466	123.12	/	/	
C3	501359.815	6609493.411	125.65	/	/	
M01	501395.377	6609566.963	124.95	20.4	125.7	105.3
M09	501357.926	6609516.374	125.48	33.0	121.0	88.0
M10	501362.346	6609464.802	125.98	20.0	117.0	97.0
M14	501308.442	6609562.542	124.71	23.4	120.0	96.6
M15(b)	501357.803	6609564.507	124.89	23.5	124.5	101.0
M17	501460.577	6609517.356	124.05	23.0	128.0	105.0

RGF93: French geodesic system in meters; NGF: meter above sea level (masl) in the French elevation system; OH: open hole section.

A summary of the results is proposed to properly constrain the HES stratigraphy with reference to the regional geological context. Figure 1 shows the locations of boreholes and core drilling.

Lithostratigraphy of the HES

The Callovian/Bathonian boundary can be observed in core logs. The Callovian limestone is a chalky, porous micropackstone to packstone containing peloids. On the OPTV log, discontinuity D11 is clearly visible in borehole M01 at a depth of 23.15 m and 23.02 m in M10, appearing as a sharp planar erosion surface (Fig. 2). A comparable surface is identified at 23.17 m depth in the PZ6 located between MP7 and M21.

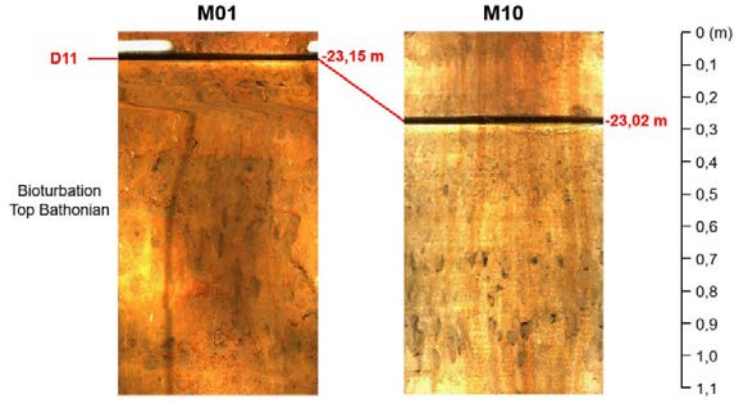

Figure 2 *Bathonian / Callovian transition with D11 discontinuity.*

The Middle Bathonian is characterized by bioturbated limestone with basal chert layers. The formation thickness exceeds 2.20 m in M01 and 3.30 m in M10. At the Poitiers cliff outcrop, a comparable unit was described as gravelly and oolitic limestone containing *Procerites sp*. (Gabilly, 1978, p. 150).

The Bathonian flinty limestone corresponds to a micrograinstone facies, previously described as sub-oolitic limestone by Gabilly (1978). Two distinct chert bands are observed at the top of this formation, clearly identifiable in boreholes M15 and M10. This double chert band is characteristic of the "Assise à silextite" (flint band) described by Mourier (1986) and Gabilly (1978).

A significant change in sedimentation occurs above the 42 m depth, where very fine-grained limestones overlie a bioturbated interval between 42 and 45 m depth (noted in M10, M14, and M15). This lithological transition is interpreted as marking the Bajocian–Bathonian boundary (Fig. 3). A *Ctenostreon* fossil was recovered from the inclined borehole C4 at a depth of 66.25 m. Considering the borehole's

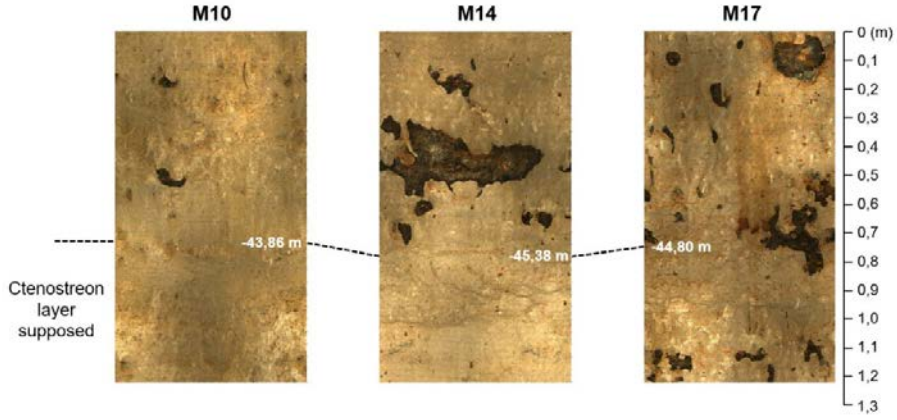

Figure 3 *Bajocian – Bathonian transition (D9 discontinuity).*

inclination (26°), the true vertical depth of the fossil is calculated at approximately 42 m. This finding supports the identification of the Bajocian–Bathonian boundary at 42 m, previously inferred from OPTV data based on the presence of two strongly bioturbated layers in boreholes M10, M14, and M15 (Fig. 3).

The D9 discontinuity, which defines the base of the Bathonian, appears subtly on OPTV images at depths of 45.60 m in M14, 45.10 m in M15 (visible at a bedding joint), and 45.02 m in M17.

A flinty limestone unit is consistently observed below the planar erosion surface identified as D9. This unit is characterized by intense bioturbation around a depth of 50 m and the presence of distinctive chert (flint) bands that can be correlated between boreholes using OPTV data. A wavy erosional surface, highlighted by a concentration of bivalve shells, marks the top of the first depositional sequence of the *Parkinsoni* Biozone. This surface is observed at the following depths: M01 (61.77 m), M10 (62.49 m), M14 (62.35 m), M15 (63.60 m), and M17 (59.12 m) (Fig. 4).

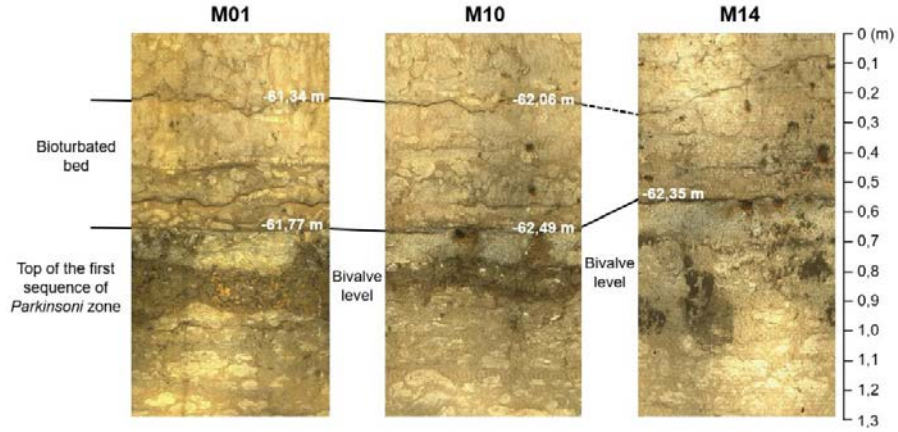

Figure 4 *Top of the first "Parkinsoni" sequence.*

A major planar erosional surface, underlain by a clay-rich horizon, defines the top of the bioturbated formation traditionally referred to as the "Assise à terriers" (Fig. 5). This key stratigraphic surface is clearly identified in several boreholes: M01 (64.81 m), M02 (65.48 m), M10 (65.48 m), M14 (65.31 m), M15 (63.60m) and M17 (62.25 m). It is interpreted as corresponding to the regional D8bis discontinuity.

A bioclastic horizon, associated with the base of this formation, is recorded at 67.00 m in the C1 core and identified at 66.42 m in M01 and 67.05 m in M10. The base of this unit is marked by a wavy erosional surface overlying a 15 cm thick bed rich in *Trichites* sections (Mollusca). This surface is well expressed across several HES boreholes: M01 (72.15 m depth), M10 (71.99 m), M14 (71.13 m), M15 (72.00 m), and inferred at 70.63 m in M17. This erosional boundary is interpreted as the D8 discontinuity (Fig. 6).

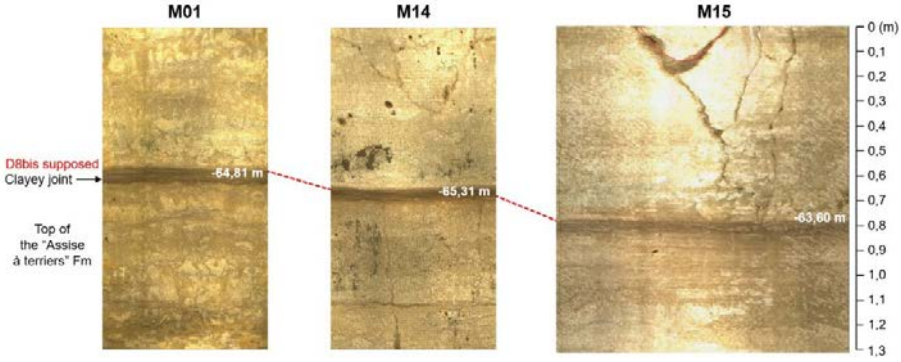

Figure 5 *Clayey joint at the top of the "Assise à terriers" Formation (D8bis discontinuity).*

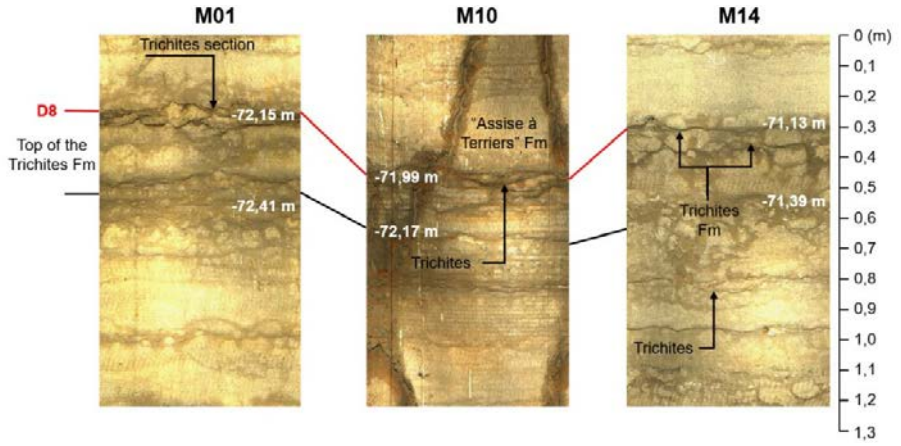

Figure 6 *Transition between* Trichites *formation and the "Assise à terriers" formation.*

The *Trichites* Limestone Formation is composed of pluricentimetric beds of packstone, each capped by a bioturbated horizon rich in Trichites sections. Based on the C1 core description, the formation begins with grain-supported lamination, producing a distinctive "snake-skin" facies on OPTV imagery (Gaillard et al., 2024). The initial stratum of the Trichites Formation is approximately 30 cm thick and is consistently bounded at the top by a clayey joint visible on all OPTV logs.

The *Trichites* Formation directly overlies the Oolitic limestone Unit corresponding to the upper *Laeviuscula* Biozone. This oolitic interval is readily identifiable in core material. On OPTV logs, the Oolitic limestone appears as a white level composed of 3 grainstone strata that are about 1 m thick each. The base of this unit is marked by a discontinuous black clay observed at the following depths: M01 (84.35 m), M09 (84.45 m), M10 (85.37 m), M14 (84.97 m), and M17 (81.87 m). The upper sequence boundary corresponds to the contact with a 50 cm-thick bed identified on all OPTV logs. The contact between the 50 cm thick bed and the Trichites Formation is equivalent to the D7bis discontinuity.

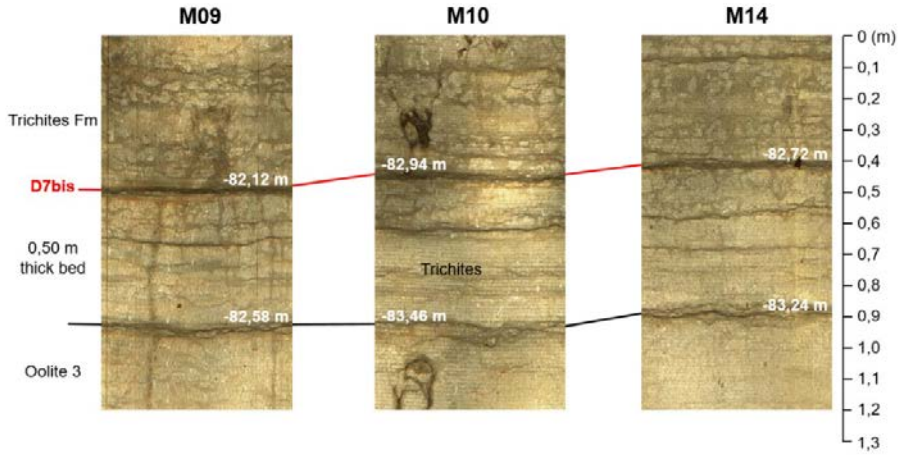

(a) D7bis discontinuity

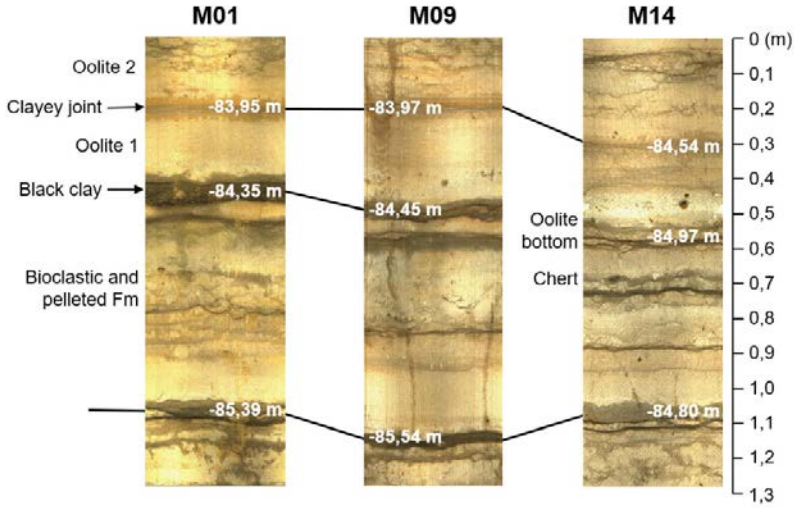

(b) Lower sequence boundary (Oolitic unit/Formation)

Figure 7 *Sequence boundaries of the Oolite unit.*

Beneath the Oolitic Formation, the limestone is a bioclastic and peloidal facies characteristic of the *Laeviuscula* Biozone. A vuggy interval of black dolomite, likely related to pyrite oxidation contained in black clay, is clearly visible within the upper dolomitized section of the oolitic facies. Similar vuggy textures are observed at the Passelourdin cliff, located approximately 2 km south of the HES (Branger et al., 2026).

At the base of this unit, two distinctive beds are consistently identified across all OPTV logs. The upper bed, approximately 0.60 m thick, is bounded by two pronounced joints and is rich in crinoids and bivalves. The lower bed, ranging

from 0.60 to 0.80 m thick, underlies a hardground surface associated with a bivalve-rich horizon. The upper bed is correlated with the *Galeolaria socialis* (serpulidae) bed described by Gabilly (1978) and is interpreted as marking the base of the *Laeviuscula* Biozone (Fig. 8). Based on this interpretation, the *Laeviuscula* Zone begins at 95.59 m (M01), 95,92 m (M09), 96.61 m (M10), and 96.26 m (M14). The bioclastic horizon beneath the hardground forms part of a 0.80 m thick fossiliferous bed, whose basal contact is a planar to undulating erosional surface. This surface is interpreted as the Aalenian–Bajocian unconformity (D7) and is observed at 96.41 m (M01), 97.52 m (M10), and 97.20 m (M14). The lower stratum is tentatively assigned to the *Ovalis* Biozone (Gabilly, 1978, p. 148) with the identification of a *Sonninidae* in the Saint Benoit cliff by Patrick Branger, 4 kilometers south of the HES. D7 discontinuity delimits a vacuolated texture interval with a dark hue, referred to as the Middle Dolomitized Zone.

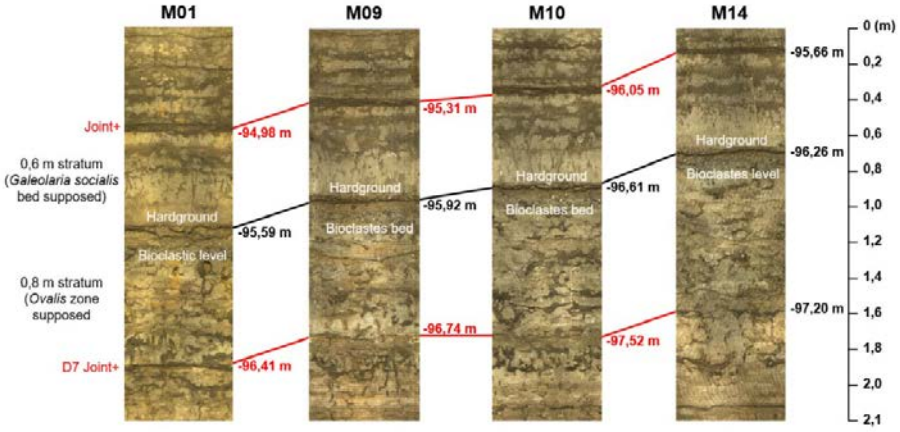

Figure 8 *Bajocian lower boundary.*

Below the D7 discontinuity, a packstone unit can be correlated with the oolitic and oncolitic facies of the *Concavum* Biozone (Mourier, 1986, p. 13). At its base, chert nodules and bands following bedding planes are present, particularly at 98.56 m (M14). These cherts, typically 20–30 cm thick, are attributed to the *Murchisonae* Biozone of the Aalenian, though their stratigraphic value is limited due to their occurrence across multiple Biozones (Benvel, 1978; Mourier, 1986).

Two hardgrounds are recognized at the base of this formation, at 105.86 m (M10) and 105.21 m (M14), and are cautiously correlated—due to dolomitization effects—with the D6bis discontinuity. Another hardground, observed at 110.15 m (M10) and 110.85 m (M14), marks the top of a decimetric-bedded limestone unit. The base of this unit is poorly defined on OPTV logs because of intense dolomitization (Lower dolomitized zone). This hardground is correlated with the D6 discontinuity.

A change in sedimentation is observed at 119.10 m (M14) and likely corresponds to the top of the Toarcian marls. In another OPTV borehole (M09), this boundary

occurs at 119.92 m, supporting the correlation. Above this surface, a bivalve-rich level—interpreted as the *Gryphaea beaumonti* bed—is recognized and considered to mark the base of the Aalenian.

Figure 9 presents a stratigraphic synthesis of the supra-Toarcian aquifer at the HES.

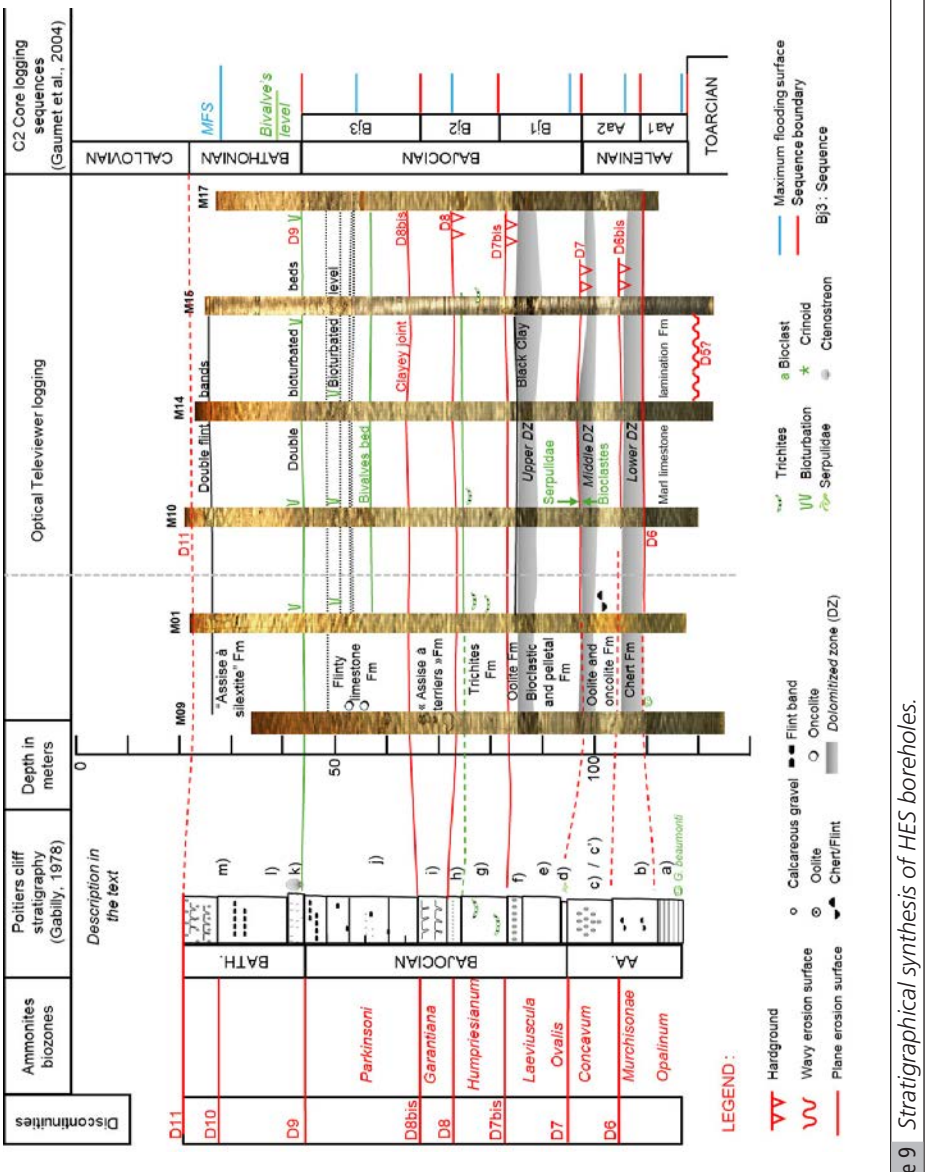

Figure 9 *Stratigraphical synthesis of HES boreholes.*

Occurrence ok karst

Fracture inventory

Audouin et al. (2008) identified a set of potentially productive fractures through the integration of heat-pulse flowmeter measurements and OPTV borehole imaging. While some of these features reveal the morphology of inclined fractures—as observed in borehole M07—most are interpreted as the result of collapse within karstified horizons and are more accurately described as sedimentary joints. Based on their analysis, the authors concluded that fewer than 3% of the identified fractures appear to be hydraulically conductive.

To verify and expand upon these conclusions, a comprehensive review of all OPTV logs of this study was conducted, focusing specifically on the identification of inclined and vertical fractures. These were systematically mapped across the boreholes to assess their spatial distribution and relationship to karstic voids. The results are compiled in Table 2, which lists the depths and apparent apertures of each feature. Only non-horizontal fractures (i.e., vertical and inclined) are included in this dataset; horizontal features, interpreted as bedding planes or sedimentary joints, were excluded from this classification.

Table 2 *Depth of fractures reported on OPTV logs.*

Boreholes	Fracture typology		
	Open	Filled by clay	Recrystallised
M01	0	1 38.67-39.80	0
M09			6 (36.71-37.70; 60.00-60.84; 66.53-70.13; 71.31-72.25; 72.52-73.73; 84.58-85.49)
M10	0	0	0
M14	1 73.25-73.60;	0	1 85.49-85.75
M15(b)	1 47.8-48.8	1 61.4-63.0	0
M17	0	0	1 (43.02-44.19)

The total length of all boreholes equals 593 m. Within these 593 meters, only 12 fractures are well identified, which gives a density of 0,02 fractures per meter. This ratio is largely due to M09, with 6 fractures identified. In general, reported fractures are located above the Oolite Formation of the *Laeviuscula* Biozone and are not present in Aalenian limestones. Only two of them are open and could provide water flow.

Stratigraphy versus seismic and acoustic data

Following earlier studies (Bourbiaux et al., 2007; Audouin et al., 2008), a 3D seismic survey was carried out (Mari & Porel, 2008; Mari, 2026) to obtain a volumetric image with extensive horizontal coverage. Structural interpretation revealed a nearly horizontal stratigraphy with a gentle westward dip of about one degree, confirming the absence of significant vertical tectonic displacements.

The 3D seismic volume was subsequently converted into a pseudo-velocity model, calibrated using acoustic velocity logs, and then into a pseudo-porosity model (Fig. 10; Mari et al., 2009; Delay et al., 2022). This seismic-derived porosity model highlighted three high-porosity—and presumably water-bearing—layers at depths of 35–40 m, 85–87 m, and 110–115 m, which were interpreted as karstic horizons. These porous levels are subhorizontal but laterally discontinuous across the HES study area.

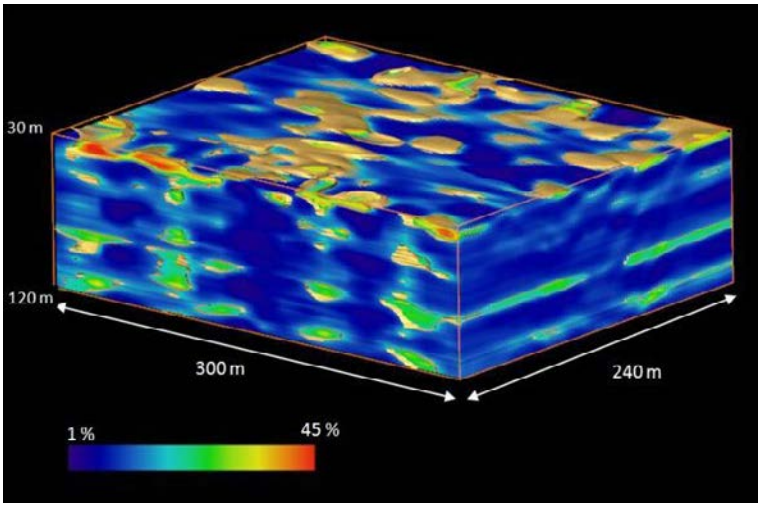

Figure 10 *3D Seismic porosity block in the 30–120 m depth interval. Modified after Mari et al. 2009, Delay et al., 2022.*

An integrated approach has since been developed to identify effective three-dimensional (3D) discrete karst conduit networks, constrained by tracer tests and geophysical data (3D seismic velocity block) (Bodin et al., 2022). The karstic horizons were independently confirmed through acoustic logging and borehole wall imaging with an Optical Televiewer (OPTV). In addition, a specific acoustic attribute, the Karstic Index, was introduced to identify karstic bodies (Fig. 11). However, owing to the relatively low vertical resolution of seismic data (meter scale) compared with borehole logs (centimeter to decimeter scale), some karstic features were detected only through borehole investigations.

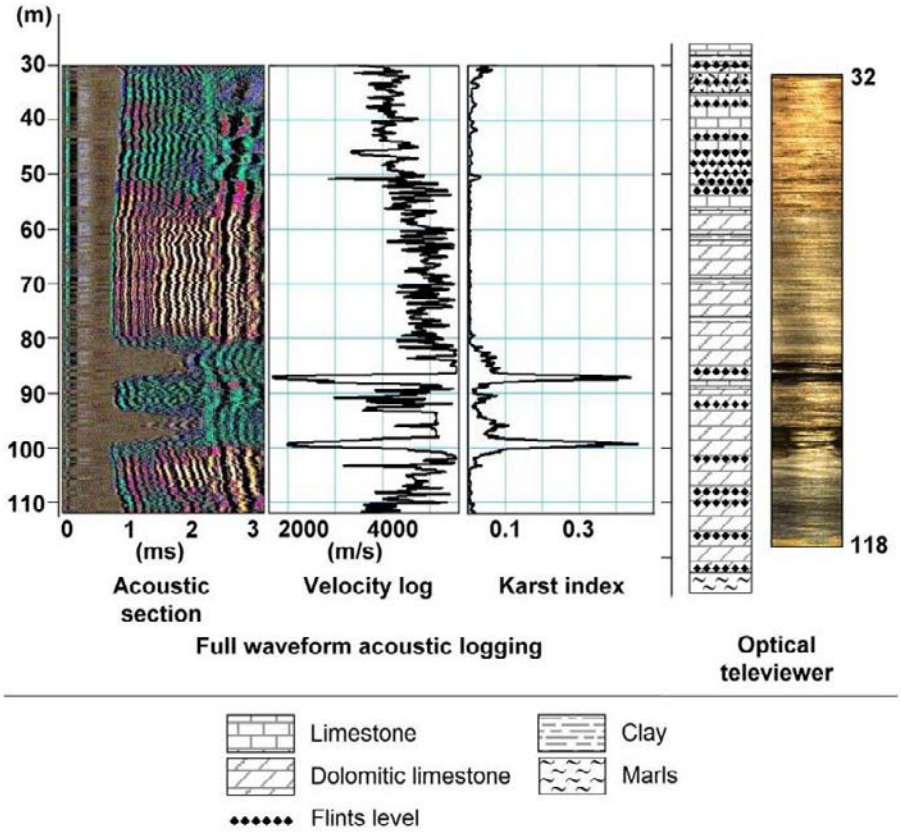

Figure 11 *Comparison of acoustic and optical wall imaging methods in borehole M20. From left to right: acoustic section, velocity log, karst index log, geological log, and optical wall imagery (OPTV).*

The uppermost porous horizon corresponds to bioturbated Bathonian limestones with bivalve assemblages, attributed to the "Assise à silextite" formation (flint band formation). This level covers the "banc à Ctenostreon," which marks the base of the Bathonian. This level is difficult to interpret using optical imagery, as most boreholes are cased down to 35 m depth. Only boreholes MP4, M17 and M22 reveal a more porous interval around 35 m. The intermediate porous interval, observed between 85 and 87 m depth, corresponds to the first dolomitized interval within the Oolitic Formation. It is characterized by centimetric vugs and coincides with the top of the "Bioclastic and Pelleted Formation," underlying the D7bis discontinuity. The coalescence of vugs may account for the formation of meter-scale cavities occasionally observed in optical televiewer images. The lowermost porous horizon is associated with the D6 discontinuity and corresponds to the Lower dolomitized zone.

For further details about seismic and acoustic methods, refer to Chapter 5 (Mari, 2026).

Stratigraphy versus borehole electrical methods

This stratigraphic framework has not yet been thoroughly correlated with borehole geophysical logging data, particularly natural gamma-ray (NGR) and resistivity logs (single point, short normal, and long normal). The main limitation lies in the difficulty of aligning the detailed stratigraphic interpretation with NGR signals, which generally provide low resolution in carbonate settings, and to a lesser extent, with short normal resistivity responses.

As illustrated in Figure 12, a comparison between the C1 core log and the M1 geophysical log—the two boreholes exhibiting the least karstification—demonstrates this discrepancy. In the C1 borehole, discontinuities D7 to D9 are clearly identified and supported by core observations. However, in borehole M1, the gamma-ray curve differs significantly, and only the D8bis discontinuity can be reliably identified, primarily due to the clay-rich nature of the erosional surface, which produces a clear GRN peak.

In contrast, resistivity logs provide more coherent results. For example, the D8bis discontinuity corresponds to a high-resistivity peak exceeding 3500 ohm·m, while the "Assise à terriers" Formation is characterized by a general increase in resistivity. A distinct peak around 3000 ohm·m is associated with the D7 discontinuity. These more consistent resistivity trends offer better stratigraphic correlation, although they remain locally disturbed.

The difficulty in log interpretation is partly attributed to karstic features filled with younger sediments, such as Cenomanian clays, which can significantly alter geophysical signatures (Bassil et al., 2016).

The first conductive horizon is identified on borehole M4, between 50.05 and 53.15 m depth, where a sequence of vertically stacked cavities up to 1 m in height is observed both on the OPTV log and on the long normal resistivity log (Fig. 13a). This karstified interval corresponds to a bioturbated interval that is also recognized in boreholes M09, M10, and M14. The second conductive zone, between 83 and 89 m depth, is attributed to the upper dolomitized interval. In borehole M11, a prominent cavity is located between the D7bis hardground and an overlying clay-rich horizon. This dolomitized zone, clearly delineated by low resistivity values (Fig. 13b), is consistently observed in boreholes M7, M8, and M20 (Fig. 11) and corresponds to dolomitization within the Oolitic formation.

In borehole M20, adjacent to M01, another cavity is detected from 96.4 to 102.2 m depth by acoustic data (Fig. 11). This feature lies above the D6bis discontinuity, which caps a sequence of well-preserved centimetric bioturbated strata.

Based on a long normal resistivity log, the most pronounced porous interval is the upper dolomitized zone, situated below the D7bis hardground that defines the top of the Oolitic Formation. A secondary conductive zone, above the D7 discontinuity, occurs within the Oolitic and Oncolitic formations of the *Concavum* Biozone (Aalenian) and is correlated with the middle-dolomitized zone, bounded at its base by the D7 discontinuity.

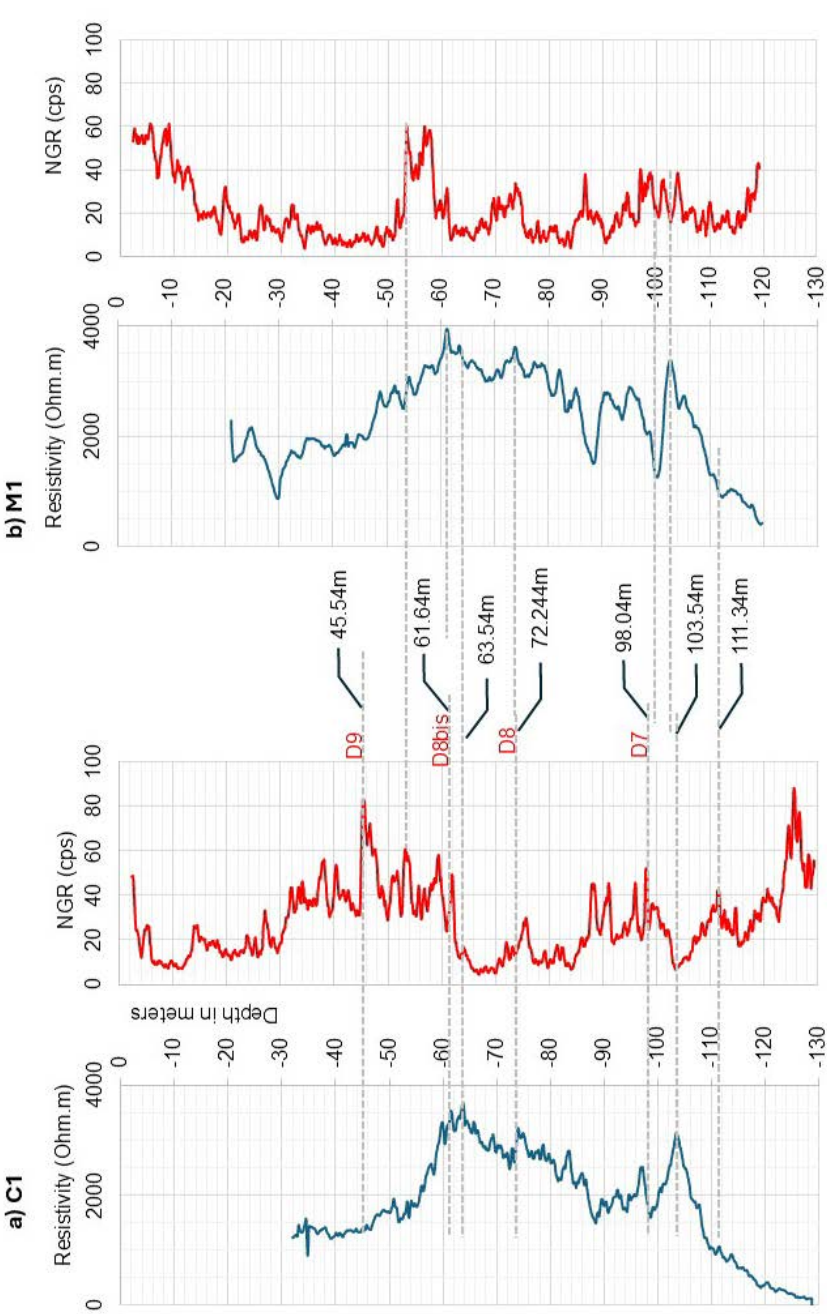

Figure 12 *Comparison of C1 and M01 logs.*

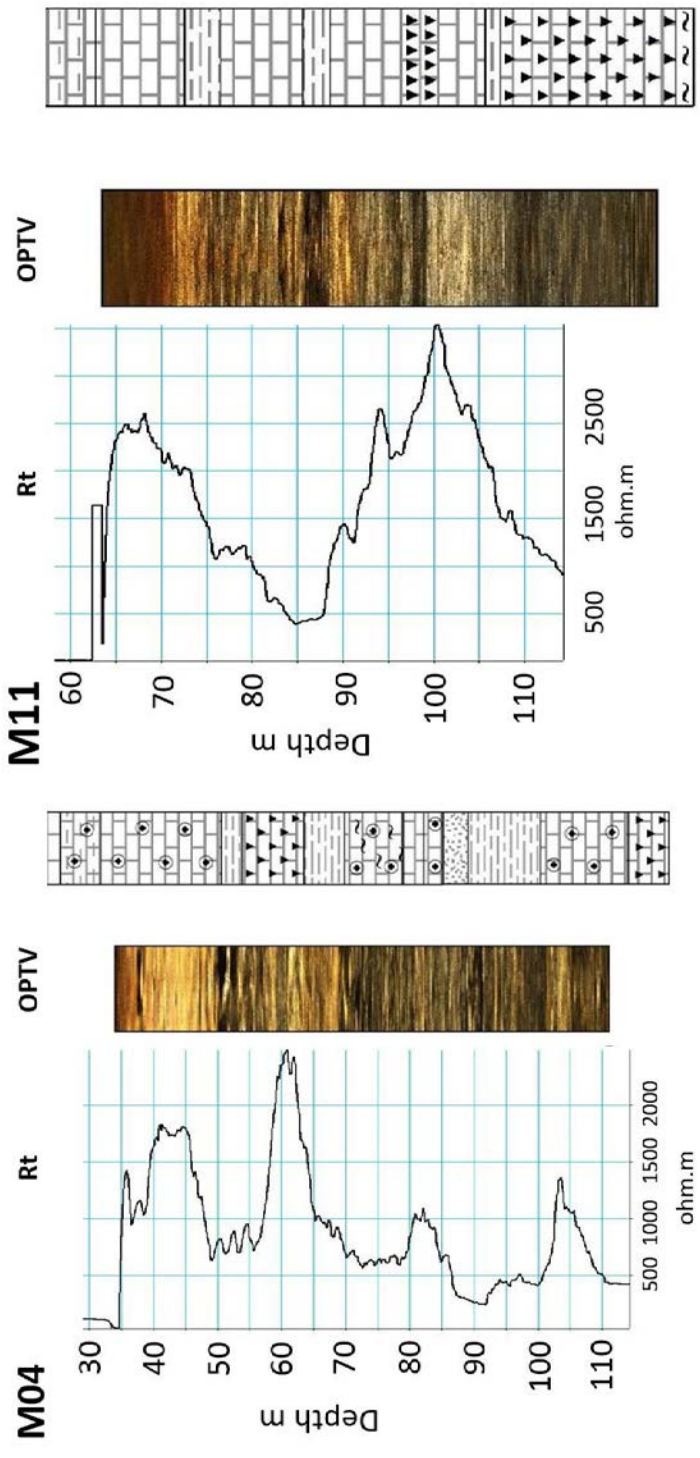

Figure 13 *Comparison of resistivity (Rt) logs and optical televiewer (OPTV) images in boreholes M04 (a) and M11 (b).*

Additionally, a marked resistivity contrast observed at ~110 m depth across all boreholes is likely associated with the D6 discontinuity and the laminated marl-limestone succession of the Opalinum Biozone (Aalenian).

In addition to conventional electrical logging, borehole electrical tests using electrical panels (Moreau et al., 2026) were conducted on the HES. Preliminary results indicate that the electrical panel sections correlate well with OPTV logs, long normal resistivity logs, and acoustic data (Mari, 2026). Electrical resistivity panels have proven to be effective in detecting individual karst conduits within the Dogger Limestone.

Stratigraphy and hydrogeological data

To complement geophysical data, flowmeter logging was conducted in selected boreholes (Audouin et al., 2008; Bodin et al., 2022; Boulais et al., 2026). These measurements aim to determine whether the porous intervals are hydraulically transmissive and capable of sustaining significant groundwater flow rates (>10 m^3/h). The goal is to assess the relationship between observed vugs and cavities and the development of an active karst system with ongoing groundwater circulation.

Audouin et al. (2008) identified an upper karstic level developed within granular limestones interbedded with cherty layers in the upper Bajocian, at a depth of approximately 50 m. This horizon is correlated with a bioturbated level situated beneath a chert bed within the *Parkinsoni* Biozone. An intermediate transmissive zone corresponds to the upper dolomitized interval of the Oolitic Formation, just below the D7bis discontinuity (at ~85 m). The lowermost productive zone, at a depth of ~110–115 m, is associated with the D6 discontinuity.

Recent hydrogeological investigations conducted by the University of Poitiers have identified productive intervals that reveal complex and spatially variable flow dynamics. Productive horizons were detected at depths of 62–65 m (MP06, M21), 72–75 m (M2, M11, M16), 80–85 m (M12, M20, M22), and 90–91 m (M11). These transmissive zones correspond to major stratigraphic discontinuities observed in boreholes, even in the absence of significant karst features (D8bis, D8, D7bis, and Upper Dolomitized Zone).

Radial convergent tracer tests further demonstrated vertical fluxes in boreholes originating from horizons at 110 m (Lower dolomitized zone), 85 m (D7bis), and 65 m (D8bis).

Flowmeter data indicate that transmissive horizons vary between boreholes, suggesting lateral discontinuity of the porous intervals and pointing to a compartmentalized aquifer structure.

Conclusion

Data acquired from various geophysical methods show a high degree of consistency and provide a coherent framework for the spatial distribution of karstic horizons identified at the Hydrogeological Experimental Site (HES) of Poitiers (France).

Importantly, fracture density alone does not account for the localization of karst features. All authors concur in describing sub-horizontal karstic levels, highlighting the predominant control of stratigraphy over structural factors. The main sedimentological controls on karst development are stratigraphic discontinuities, as described by Gabilly et al. (1985), and porous formations composed of oolitic grainstone limestones.

A synthesis of borehole optical logs (OPTV) enables the identification of distinct limestone units forming the Poitou Threshold. Through this correlation, the main karstic horizons within the supra-Toarcian aquifer are interpreted as follows:

The karst horizon at a depth of ~50 m corresponds to a bioturbated interval of the *Parkinsoni* Biozone. These beds were previously described by Benvel (1978, p. 35).

The karstic level between depths of 72 and 75 m, identified through crossflow logging, is associated with the D8 discontinuity.

The most prominent karstic horizon occurs between depths of 82 and 85 m. It lies within the Oolitic Formation. Beneath the D7bis discontinuity, the upper dolomitized zone is highly permeable.

The karstic zone observed between depths of 97 and 100 m is correlated with the D7 discontinuity. The D7 discontinuity is the upper limit of the middle-dolomitized zone contains open geodes.

The 110-115 m depth horizon is marked by D6 discontinuity and the contact with the Marl limestone lamination formation of the *Opalinum* zone. The Lower dolomitized zone began just below the D6 discontinuity.

The three dolomitized zones seem to appear under the discontinuities. The Upper one is probably related to the black clay layer, which supports pyrite and organic matter. The middle and lower zones contain centimetric microcavernes. These voids are probably the remains of fully dissolved calcite geodes.

Additional isolated cavities have been observed outside of these main discontinuities; however, they appear discontinuous and spatially limited. In the unsaturated zone, some cavities may develop along fractures in the chalky Callovian limestone, but their hydraulic connection to the main karstic horizons remains unproven. The 35 m depth horizon seems to be correlated with a bioturbated interval in the Bathonian limestone.

References

Audouin O., Bodin J., Porel G., Bourbiaux, B. (2008). Flowpath structure in a limestone aquifer: multi-borehole logging investigations at the hydrogeological experimental site of Poitiers, France. *Hydrogeology Journal*, 16 (5): 939-950. https://doi.org/10.1007/s10040-008-0275-4

Bassil J., Naveau A., Fontaine C., Grasset L., Bodin J., Porel G., Razack M., Kazpard V., Popescu S.-M. (2016). Investigation of the nature and origin of the geological matrices rich in selenium within the hydrogeological experimental site of Poitiers, France. *Comptes Rendus Geoscience*, 348 (8): 598-608. https://doi.org/10.1016/j.crte.2016.08.004

Benvel B. (1978). Étude stratigraphique, sédimentologique et structurale du Jurassique dans les vallées du Clain et de la Boivre en amont de Poitiers [Stratigraphic, sedimentological and structural study of the Jurassic in the Clain and Boivre valleys upstream from Poitiers]. Ph.D. thesis (Vol. I). Poitiers University, France.

Boulais A., Geairon H., Gaillard T. (2026). "Hydrogeological flow logging and dye tracer tests", Chapter 7 in *A new concept of karst development based on hydrogeology and geophysics*, EDP Science. https://doi.org/10.1051/978-2-7598-3934-6.c007

Bourbiaux B., Callot J.-P., Doligez B., Fleury M., Gaumet F., Guiton M., Lenormand R., Mari J.-L., Pourpak H. (2007). Multi-scale characterization of an heterogeneous aquifer through the integration of geological, geophysical and flow data: a case study. *Oil and Gas Science and Technology (IFP)*, 62: 347-373. https://doi.org/10.2516/ogst:2007029

Bodin J., Porel G., Nauleau B., Paquet D. (2022). Delineation of discrete conduit networks in karst aquifers via combined analysis of tracer tests and geophysical data. *Hydrology and Earth System Sciences*, 26 (6): 1713-1726. https://doi.org/10.5194/hess-26-1713-2022

Branger P., Gaillard T., Geairon H. (2026). "Stratigraphy of the Middle Jurassic", Chapter 2 in *A new concept of karst development based on hydrogeology and geophysics*, EDP Science. https://doi.org/10.1051/978-2-7598-3934-6.c002

Delay F., Mari J.-L., Porel G., Chabaux F., Ackerer P. (2022). Is subsurface geophysics as seismic and acoustic investigations a rescue to groundwater flow inversion? *Comptes Rendus Geoscience*, Part of Special Issue: Geo-hydrological data & models, https://doi.org/10.5802/crgeos.157

Gabilly J. (1978). *Itinéraire 12a : le versant Parisien in Guides géologiques régionaux : Poitou Charentes Vendée* [Itinerary 12a: the Parisian slope in geological guide of Poitou Charentes Vendée], with the collaboration of Brillanceau A., Cariou E., Ducloux J., Dupuis J., Hantzpergue P., Moreau P., Santallier P., Ters M., (éd. 1st edition), Masson.

Gabilly J., Cariou E., Hantzpergue P. (1985). Les grandes discontinuités du Jurassique : témoins d'évènements eustatiques, biologiques et sédimentaires [The large stratigraphic discontinuities at Jurassic time, witnesses of eustatic, biologic and sedimentary occurrences]. *Bulletin de la Société Géologique de France*, I(3): 391-401. https://doi.org/10.2113/gssgfbull.I.3.391

Gaillard T., Moreau M., Mari J.-L. (2024). Seismic and stratigraphic characterization of karstogenic horizons in a sequence of carbonate deposits: Example of the Dogger limestones of the Poitou threshold. Journées Scientifiques AGAP Qualité 2024, Poitiers, France, Edited by Asfirane, F.; Mari, J.-L.; *E3S Web of Conferences*, 504, 05005. https://doi.org/10.1051/e3sconf/202450405005

Gaillard T., Branger P. (2024). Le Jurassique moyen du seuil du Poitou [Middle Jurassic of the Poitou threshold] in *Le karst du seuil du Poitou : Approche stratigraphique et rôle de la tectonique*. Livret Guide de l'excursion du CFH sur le seuil du Poitou, 29 au 31 mars 2024.

Gaumet F., Guitton M., Callot J.-P. (2004). Hétérogénéité sédimentaire et fracturation dans le Jurassique du Site Expérimental Hydrogéologique de Poitiers [Sedimentary heterogeneity and fracturing in the Jurassic of the Hydrogeological Experimental Site of Poitiers]. Unpublished report.

Mari J.-L., Porel G. (2008). 3D Seismic Imaging of a Near-Surface Heterogeneous Aquifer: A Case Study. *Oil & Gas Science and Technology (IFP)*, 63(2): 179-201. https://doi.org/10.2516/ogst:2007077

Mari J.-L., Porel G., Bourbiaux B. (2009). From 3D Seismic to 3D Reservoir Deterministic Model Thanks to Logging Data: the Case Study of a Near Surface Heterogeneous Aquifer. *Oil & Gas Science and Technology (IFP)*, 64(2): 119-131. https://doi.org/10.2516/ogst/2008049

Mari J.-L., Porel G., Delay F. (2020). Contribution of Full Wave Acoustic Logging to the Detection and Prediction of Karstic Bodies. *Water*, 12(4): 948. https://doi.org/10.3390/w12040948

Mari J.-L., Porel G. (2024). The hydrogeological experimental site of Poitiers: Hydrogeological versus geophysical investigations, Journees Scientifiques AGAP Qualité 2024, *E3S Web of Conferences*, 504, 05003. https://doi.org/10.1051/e3sconf/202450405003

Mari J.-L. (2026). "Geophysical methods", Chapter 5 in *A new concept of karst development based on hydrogeology and geophysics*, EDP Sciences. https://doi.org/10.1051/978-2-7598-3934-6.c005

Moreau M., Brunel P., Mari J.-L. (2026). "Borehole electrical panels: an experiment", Chapter 6 *in A new concept of karst development based on hydrogeology and geophysics*, EDP Sciences. https://doi.org/10.1051/978-2-7598-3934-6.c006

Mourier J.-P. (1983). Le versant parisien du seuil du Poitou de l'Hettangien au Bathonien. Stratigraphie, sédimentologie, caractères paléontologiques, paleogéographie [The Parisian slope of the Poitou sill from the Hettangian to the Bathonian. Stratigraphy, sedimentology, paleontological features, paleogeography]. PhD thesis. Poitiers University, France.

Mourier J.-P., Gabilly J., Platel J.-P. (1986). Carte géologique de la France au 1/50000 : Notice explicative de la feuille de Poitiers [geological map of France at 1/50000 scale: Notice of Poitiers]. BRGM ed.

9

The Deffend hydrogeological model

T. Gaillard

Hydrogeological knowledge before Hydrogeological Experimental Site (HES) of Poitiers

Historical groundwater flow model of the Poitou Threshold

The hydrogeology of the Poitou Threshold has been studied since the 19th century, beginning with the work of Longuemar (1856). This author proposed a conceptual model of groundwater flow based on vertical fracture networks that drain groundwater toward valley-bottom springs located at the contact with the Toarcian marls. This hydrogeological model was later adopted and used by academics (Welsch, 1912), as well as by public service practitioners and engineering consultants for the location of boreholes and the interpretation of dye tracer tests. Observing the presence of water at the base of numerous quarries, Welsch expanded Longuemar's model by introducing the concept of "quarry water", corresponding to a continuous groundwater table within the limestones of the Supra-Toarcian Aquifer. Figure 1 presents the historical hydrogeological models of Longuemar and Welsch. It is worth noting, however, that Longuemar had described perched springs in cliffs,

© EDP Sciences, 2026
DOI: https://doi.org/10.1051/978-2-7598-3934-6.c009

which his model does not adequately explain. Welsch's model envisions dry valleys as preferential drainage axes for groundwater flowing toward springs located at the contact with Toarcian marls or with alluvial deposits (Welsch, 1912). This model, therefore, implies that springs should emerge at the outlets of dry valleys; however, in practice, springs are also found outside valley axes.

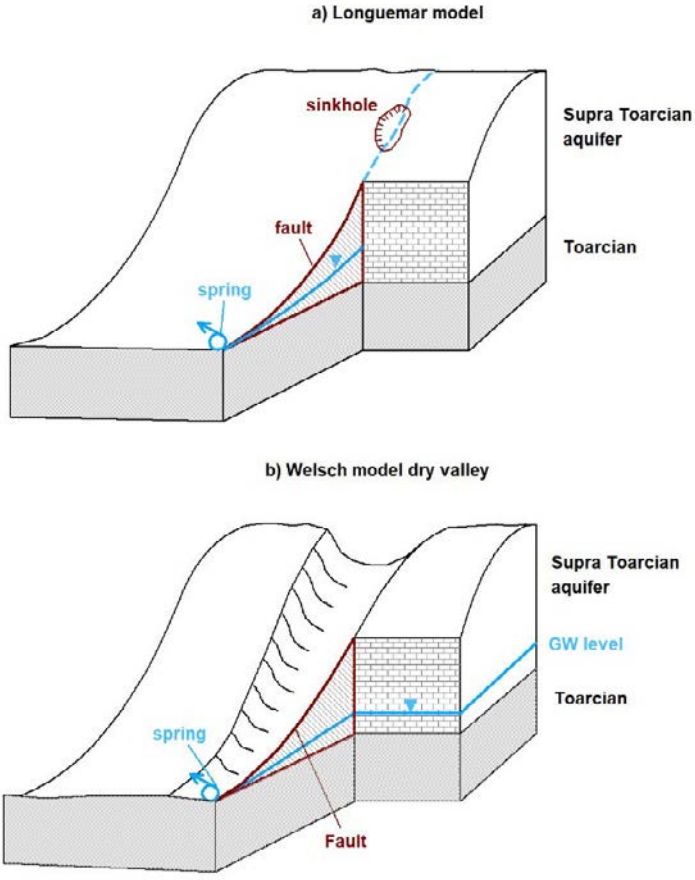

Figure 1 *Historical conceptual models of groundwater flow on the Poitou Threshold; (a) Longuemar's model (1856), (b) Longuemar's model modified by Welsch (1912).*

Another feature is that the Poitou Threshold is not particularly favourable to the karstification of Jurassic limestones. Hydraulic gradients are low due to the relatively low elevation of the plateaus, around 130 to 150 meters above sea level (m asl) around Poitiers, with riverbeds around 70 to 60 m asl. The plateaus are overlain either by red clays resulting from limestone weathering or by Plio-Pleistocene clayey-sandy sediments that inhibit infiltration. Poor descriptions of drilling cuttings and the lack of geophysical logging have further hindered understanding of the positioning of karst conduits. When a borehole encountered a sudden inflow of water, it was often attributed by

drillers and hydrogeologists to the presence of a “fault”. The facture model proposed by Longuemar and Welsch therefore seemed to be confirmed until the research on the Hydrogeological Experimental Site (HES) of the Poitiers University.

The Poitiers HES groundwater model

By the 1970s, the stratigraphy of the Middle Jurassic formations in the Poitou Threshold was already well established, and research conducted at the University of Poitiers helped bridge a century-long gap in paleontological investigations of the Poitou carbonate platform. However, it was not until the establishment of the Hydrogeological Experimental Site (HES) near Poitiers that new data on the karst systems of the Poitou Threshold became available.

Initial results demonstrated that the geometry of karst levels within the saturated zone is predominantly horizontal rather than vertical (Mari and Porel, 2008; Mari et al., 2009). Moreover, these horizontal karst levels are not randomly distributed but are strongly constrained by stratigraphy (Gaillard, Moreau, and Mari, 2024). Testing and experiments conducted at the HES established a direct link between stratigraphy and hydrogeology, leading to a substantial revision of earlier theories regarding the spatial organization of karst horizons in the Poitou Threshold.

The hydrogeological model developed from HES investigations is based on the superposition of several karst horizons within the Supra-Toarcian Aquifer. Borehole Optical Televiewer (OPTV) logs reveal that fractures predominantly affect the unsaturated zone and are less frequent in the saturated zone. Groundwater flow occurs mainly through karstified levels that show very little fracturing. The caves visible in cliff outcrops are relic features of these ancient karst systems (Gaillard et al., 2024; Gaillard, 2026). Current groundwater flow is partly routed toward overflow springs discharging into valleys, and partly beneath the valleys of the Clain and Vienne rivers. Figure 2 presents a block diagram of this conceptual model, referred to as the Deffend model

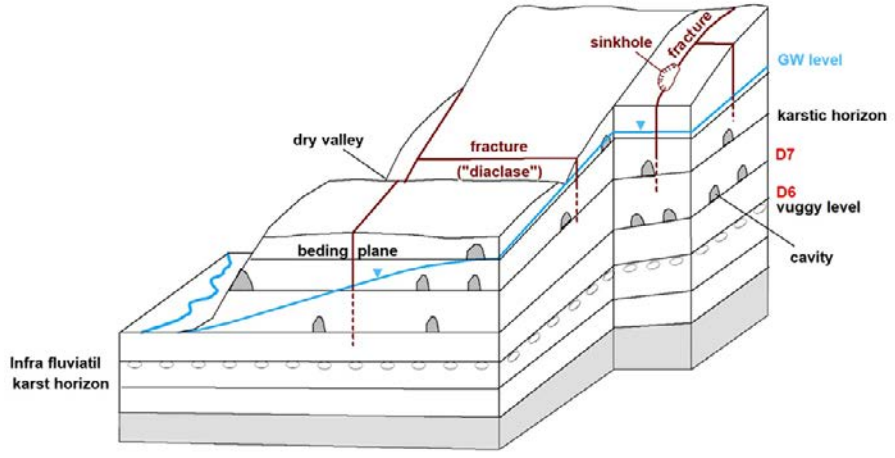

Figure 2 *The Deffend model.*

after the site name. In this model, fractures near the surface play a role in distributing groundwater recharge, while water in the saturated zone flows predominantly along horizontal karst horizons. For example, discontinuities D6 and D7 of Gabilly et al. (1985) correspond to two main karstic horizons. Each horizon acts as a drain for water percolating through the overlying limestone sequence. Some of these karst levels are not intersected by rivers (infra-fluvial karst horizons), and the relationship between such levels and modern river systems remains to be clarified.

Karst dating

The age of the Poitou Threshold karst has also been the subject of divergent theories. Gabilly et al. (1978, p. 19) correlated the three levels of caves around Poitiers with phases of valley downcutting of the Clain and Vienne rivers during the Quaternary, particularly during the Middle Pleistocene to the Riis glacial stage, the Mindel, and the Würm glacial stages. However, the infilling of some cavities by black clays and glauconitic sands dated from Cenomanian had long been recognized within the Middle Jurassic limestones (Cariou and Mathieu, 1959; Mathieu, 1960; Alvarez, 1980; Legendre, 1984). On the HES, palynological analyses of clays trapped within karstic conduits below the *Parkinsoni* biozone (Upper Bajocian) yielded ages ranging from the Cenomanian to the Santonian (Bassil, 2014). Recently, Valentin et al. (2021) discovered abundant and diverse fossil assemblages ranging from the Albian to the Cenomanian in cross-stratified deposits infilling a Bajocian paleokarst near Persac, on the east of the Poitou Threshold. However, Cenomanian formations do not outcrop on the Poitou Threshold itself. These examples demonstrate that karst horizons are older than the Cenomanian transgression (Tab. 1). These karst systems trapped marine sediments of Cretaceous age before their complete erosion on the Poitou Threshold (Fig. 3).

Table 1 *Location of Cretaceous sediment trapped in karst on the Poitou Threshold.*

Location	X Longitude	Y Latitude	Reference
Chardonchamp	0.3488°	46.6269°	Alvarez, 1980 (p. 93)
Persac	0.6985°	46.3577°	Valentin, 2021
Vouneuil-sous-Biard	0.261°	46.6035°	Mathieu, 1960
Poitiers SEH	0.4062°	46.5522°	Bassil, 2014
Lavoux	0.5248°	46.5964°	Cariou, Mathieu, 1959
Luzay	-0.1965°	46.9205°	Legendre, 1984 (p. 50)
Moulins, Smarves	0.3482°	46.5314°	Mathieu, 1960

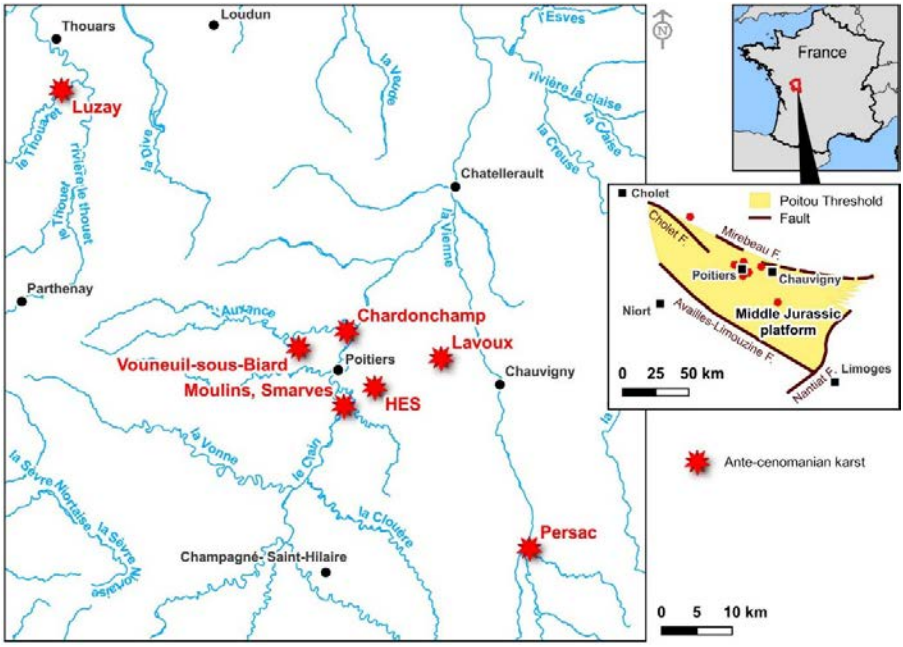

Figure 3 *Location of evidence of ante-Cenomanian karsts.*

Thus, between the Cenomanian transgression and the reactivation of karst associated with Quaternary valley downcutting, several million years of karst evolution remain to be reconstructed.

The absence of Albian and even Purbeckian sediments on the Poitou Threshold led some authors to conclude that the platform remained fully emergent during the Lower Cretaceous (Gabilly et al., 1978, p. 17; Alvarez, 1980, p. 86; Mourier et al., 1986). An initial phase of karstification is thus theoretically conceivable. This long-lasting subaerial exposure would therefore correspond to an ancient karstification episode, at least partially predating the Cenomanian. The absence of Lower Cretaceous sediments implies that the Poitou threshold uplifted by at least 100 m, simply assuming that the sea has risen in accordance with the Hardenbol sea level chart (1998). This tectonic phase could correspond to the beginning of the Atlantic north opening during the Tithonian stage (Dercourt et al., 1993).

The Cenomanian transgression subsequently deposited black clays, followed by glauconitic green sands over part of the Poitou Threshold. These formations, now largely eroded, extended southwards as far as the area around Poitiers (Mathieu, 1960) within a context of high stand sea level (Hardenbol et al., 1998). The discovery by Valentin et al. (2021) confirms that this marine transgression covered the entire Poitou Threshold and filled the karst from the surface (Fig. 3).

The red clays overlying the Bajocian and Bathonian limestones were interpreted as the result of weathering of the limestones from the late upper Cretaceous to

the Eocene (Gabilly et al., 1978, p. 19). From the Eocene onward, the plateau was once again overlain by continental deposits coming from the Massif Central mountains. A fluvial network draining westward gave rise to the so-called Ypresis River, named after its Ypresian age, determined at its mouth on the Atlantic coast (Godard et al., 1994). The overlying lacustrine limestones, though poorly dated — except at Fonliasmes (Mazerolles commune), where a Bartonian age was determined (Brunet and Gabilly, 1981), also contributed to covering the Jurassic karst. The Poitou Threshold was then entirely covered by the argillaceous-sandy complex of the Bornais Formation during the Plio-Pleistocene, lying between the Thouars-Mirebeau and Champagné-Saint-Hilaire fault zones.

Assuming that the downcutting of the valleys eroded the Bornais formation, the onset of plateau erosion likely corresponds to the lowering of sea level during the Günz glacial period (1.2 to 0.7 My BP). The corresponding fluvial terraces (Fv on the French geologic map) are clearly visible only north of the Threshold, around Châtellerault city, and may correspond to the Günz/Mindel interglacial (Bourgueil et al., 1976). The high terraces of the Vienne and Clain valleys (Fw) are mainly Middle Pleistocene in age. Their formation occurred in the context of a rising base level associated with the Mindel-Riss interglacial (421–395 ky).

The karst systems of the Passelourdin and Lussac-les-Châteaux sites are each located at elevations below those of the Fw terraces (Gaillard et al., 2024). In both cases, these cavities are altitudinally above the Fx terraces, which are dated to the Saalian (>110 ky BP) through the presence of Acheulean-Levallois and Mousterian industries, as well as faunal remains of *Elephas primigenius* and *Rhinoceros tricorhinus* (Facon, 1955; Voinchet et al., 2020). The reactivation of karst is therefore constrained between these two alluvial deposition events, i.e., between 421 and 110 ky BP. This karstic morphology extends beneath the entire Poitou Threshold plateau.

A significant issue remains, however: at the HES site, the karstified levels are clearly controlled by the Middle Jurassic stratigraphy, with no connection to the Clain valley downcutting or the terrace altimetry. The elevation of lower karst levels is below the current riverbed elevation of the Clain (Poitiers HES) and the Vienne (Civaux nuclear power plant area in Gaillard et al., 2024). These rivers could not have exported carbonates from below these levels.

Syngenetic karstification hypothesis

Karst systems located beneath river valleys cannot be explained by Quaternary valley downcutting. Furthermore, late-stage karstification of a carbonate massif requires the export of calcium and bicarbonate ions. Such export via drainage pathways is difficult for deep groundwater located below the current riverbeds. Syngenetic karstification therefore, remains a plausible hypothesis (Jennings, 1968; Grimes, 2006). Such karstification processes, associated with discontinuities, have been described in the

Bajocian and Bathonian formations of the Grands Causses in France (Charcosset et al., 2000) and in the Betic Cordillera in Spain (Molina et al., 1999). These discontinuities are defined by some authors as inception horizons (Filipponi et al., 2010) and play a key role in controlling karst development (Bosák, 2008).

On the Poitou Threshold, deposits ranging from the Aalenian to the Bathonian are primarily controlled by eustatic variations (Branger, 1989; Gonnin et al., 1992). Each depositional sequence is bounded by discontinuities characterized by the absence of one or several ammonite zones (Gabilly, 1962; Gabilly and Cariou, 1974; Gabilly et al., 1985; Branger, 1989). The model that best explains sedimentation on the Poitou Threshold platform is the Catch-up/Keep-up model (Emery, 1996). The Emery Catch-up / Keep-up model describes the response of carbonate platforms and reefs to relative sea-level rise. In the keep-up mode, the vertical accretion rate of the platform equals or exceeds the rate of sea-level rise, allowing the carbonate surface to remain close to sea level continuously. In the catch-up mode, carbonate growth is initially too slow to match rapid sea-level rise, leading to partial drowning. A third outcome, often referred to as the give-up mode, occurs when carbonate accumulation cannot compensate for accommodation creation, resulting in permanent drowning of the platform. Emery's Catch-up / Keep-up model can be directly related to the systems tracts of sequence stratigraphy in carbonate platforms. Keep-up platforms, where carbonate production matches relative sea-level rise, are expressed as aggradational successions typical of the transgressive systems tract (TST) or the highstand systems tract (HST). In contrast, keep-up platforms, which drown permanently, correspond to low systems tract (LST) or major sequence boundaries, often overlain by condensed pelagic deposits or siliciclastics.

In each depositional sequence, a lowstand systems tract formed along the edges of the platform, either on the outer platform or in basins bordering the threshold. On the platform itself, limited accommodation space prevented the development of lowstand systems tracts. The low accommodation was expressed by early lithification, the presence of benthic faunas, bioturbation, and abrasion by intertidal currents. During this low sea level phase, the limestones were dolomitized by continental freshwater or rainwater according to the Coastal Mixing Zone Dolomite theory (Humphrey and Quinn, 1989) or the reflux model (Patterson and Kinsman, 1982).

During transgression, when the sea level rose, the platform was drowned, and pelagic facies were deposited. Along the platform margin, these are represented by marly–calcareous condensed beds, forming thin strata enriched in ammonites and belemnites, which typify drowning intervals within the carbonate succession. Then, a highstand systems tract developed across the platform, characterized by increased carbonate production, consistent with the hypertrophic late sequence model of Gabilly and Cariou (1974). Concurrently, slope deposits thinned as carbonate accumulation declined in deeper, light-limited environments. The resulting highstand wedge subsequently served as a substrate for benthic colonization during the following sea-level fall.

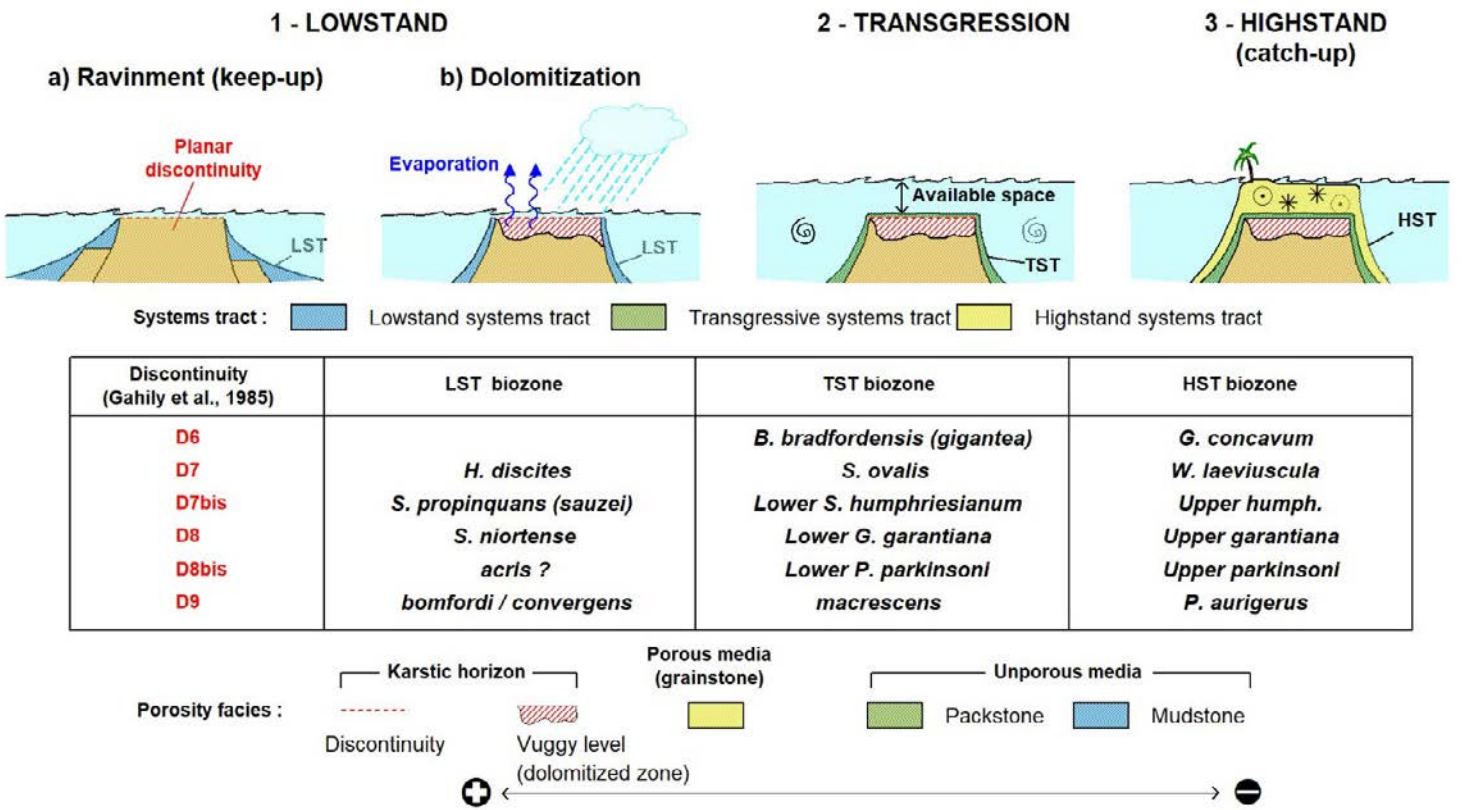

Discontinuity (Gahily et al., 1985)	LST biozone	TST biozone	HST biozone
D6		*B. bradfordensis (gigantea)*	*G. concavum*
D7	*H. discites*	*S. ovalis*	*W. laeviuscula*
D7bis	*S. propinquans (sauzei)*	*Lower S. humphriesianum*	*Upper humph.*
D8	*S. niortense*	*Lower G. garantiana*	*Upper garantiana*
D8bis	*acris ?*	*Lower P. parkinsoni*	*Upper parkinsoni*
D9	*bomfordi / convergens*	*macrescens*	*P. aurigerus*

Figure 4 *Stratigraphic control of aquifer porosity.*

On the Poitou Threshold, the catch-up/keep-up model recurred several times during the Middle Jurassic. The main discontinuities identified by Gabilly et al. (1985) correspond to phases of low sea level. Figure 4 shows a synthetic diagram of the systems tract during a transgression-regression cycle. A table shows the correspondence with ammonite zones, and porous bodies are represented by dolomitized strata with vuggy levels and discontinuities.

At the outcrop scale, the genetic units corresponding to lowstand and highstand deposits repeat this pattern. This model also makes it possible to suggest a sequence of diagenetic events affecting the limestones during deposition. During sea-level falls, dolomitization found favourable conditions due to the evaporation of marine waters trapped within the sediments around isolated shoals, combined with meteoric water input across the platform, promoting the precipitation of calcium and sulphates (Morda et al., 2012). The advance of the dolomitization front within the limestones would then be controlled by the freshwater/saltwater interface. This process could repeat with each cycle and would be particularly intense in the eastern part of the Poitou threshold, where the Montmorillon dolomite is located.

Within this framework, the depositional sequences that influenced the porosity of the supra-Toarcian limestone aquifer are as follows:

(i) at the end of highstand, when sedimentation has filled the available accommodation space, the platform is subjected to intense currents that scour the limestones and formed a more or less cemented sub-horizontal discontinuities, expressed as a bioturbated hardgrounds (Gabilly, 1962). These discontinuities, sometimes underlined by remnants of palaeosols, are conducive to the formation of highly porous hollow bedding planes;

(ii) during the lowstand, for example, the *discites* horizon (corresponding to the lowstand of sequence Bj1 of Gonnin et al., 1992), per descensum dolomitization occurred (Mourier, 1983). The limestone becomes more porous and forms vacuoles and vuggy levels, probably due to the dissolution of calcite geodes into the *laeviuscula* limestone;

(iii) the transgressive system tract is formed by thin strata, rich in pelagic fauna, but with relatively low porosity;

(iv) the highstand system tract is made up of metric strata, often oolitic and rich in crinoid debris, which can form a porous aquifer (grainstone facies).

In this schema, the absence of the *niortense/subfurcatum* zone could be related to a relative uplift of the Poitou threshold. Karstification associated with the D8 (and D8bis) discontinuity could be explained by this depositional gap, accompanied by intense bioturbation that enhanced subsequent dissolution (Figure 4).

The emersion event at the end of the *Parkinsoni* zone (*Bomfordi* subzone), identified by ostracod-bearing clays in the Vienne valley (Mourier and Almeras, 1986), is associated with the deposition of black clays in submerged areas and karstification marked by red clays observed in boreholes from the HES site (Gaillard, 2026).

Conclusion

Geophysical (Mari and Porel, 2008, 2009; Delay et al, 2022; Mari, 2026), hydrogeological investigations (Audouin et al., 2008; Bodin et al, 2022; Boulais et al., 2026), and borehole logging conducted at the Poitiers HES site have completely renewed the understanding of the supra-Toarcian aquifer.

The first scientific contribution is the demonstration that the productive horizons within the Middle Jurassic limestones (from Aalenian to Bathonian) are sub-horizontal. Fracturing, which was previously invoked as the main factor controlling the spatial distribution of transmissivity and porosity within the limestones, is in fact restricted to the upper part of the aquifer, particularly within the unsaturated zone. Below a certain depth, within the Bajocian limestones at the HES, horizontal structures form distinct superimposed karstic levels.

The second contribution is the demonstration that these levels are not randomly distributed. Stratigraphic analysis of borehole sections has shown that discontinuities associated with marine lowstands are well correlated with ravinement of the depositional surface, combined with dolomitization (Gaillard, 2026). The correlation between stratigraphy and the depths of karstic levels is a major scientific contribution.

The resulting hydrogeological model explains the formation of syngenetic karstic horizons within the context of a non-rimmed carbonate shelf. These levels were subsequently reactivated throughout geological time. The karst is thus highly polyphasic, evolving from an initial pre-Cenomanian stage to the Quaternary, with the downcutting of fluvial valleys that actually drain the Poitou Threshold. This model explains the presence of Cretaceous sediments within the Bajocian or Callovian limestones. Similarly, the presence of karstic levels beneath present-day riverbeds' elevation is consistent with the theory of syngenetic karstification at the top of the highstand systems tract.

References

Alvarez P. (1980). L'Oxfordien, le Cénomanien et le Turonien au NW de Poitiers (Vienne): stratigraphie, sédimentologie, cartographie et hydrogéologie [The Oxfordian, Cenomanian and Turonian to the NW of Poitiers (Vienne): stratigraphy, sedimentology, mapping and hydrogeology]. Ph.D. thesis, University of Poitiers, France.

Audouin O., Bodin J., Porel G., Bourbiaux, B. (2008). Flowpath structure in a limestone aquifer: multi-borehole logging investigations at the hydrogeological experimental site of Poitiers, France. *Hydrogeology Journal*, 16: 939–950. https://doi.org/10.1007/s10040-008-0275-4

Bassil J. (2014). Origine et processus de libération du sélénium dans l'aquifère carbonaté du Site Expérimental Hydrogéologique de Poitiers [Origin and release process of selenium in the carbonate aquifer of the Poitiers Hydrogeological Experimental Site]. Ph.D. thesis, University of Poitiers, France.

Bodin J., Porel G., Nauleau B., Paquet D. (2022). Delineation of discrete conduit networks in karst aquifers via combined analysis of tracer tests and geophysical data. *Hydrology and Earth System Sciences*, 26(6): 1713–1726. https://doi.org/10.5194/hess-26-1713-2022

Bosák P. (2008). Karst processes and time [Procesy krasowe a czas]. *Geologos*, 14(1): 19-36.

Bourgueil B., Cariou E., Moreau P., Ducloux J., Teissier J.-L. (1976). Carte géologique de la France au 1/50000 : feuille de Vouneuil-sur-Vienne [1:50,000 geological map of France: Vouneuil-sur-Vienne sheet], n° 567. BRGM ed.

Boulais A., Geairon H., Gaillard T. (2026). "Hydrogeological flow logging and dye tracer tests", Chapter 7 in *A new concept of karst development based on hydrogeology and geophysics*, EDP Science. https://doi.org/10.1051/978-2-7598-3934-6.c007

Branger P. (1989). La marge Nord-Aquitaine et le seuil du Poitou au Bajocien : stratigraphie séquentielle, évolution biosédimentaire et paléogéographie [The North Aquitaine margin and the Poitou sill in the Bajocian: sequence stratigraphy, biosedimentary evolution and palaeogeography]. Ph.D. thesis, University of Poitiers, France.

Brunet M., Gabilly J. (1981). Découverte d'une faune de vertérés bartoniens dans le Tertiaire continental du seuil du Poitou [Discovery of a Bartonian vertebrate fauna in the continental Tertiary of the Poitou sill]. *Bulletin de la Société Géologique de France*, XXIII(1): 95-100. https://doi.org/10.2113/gssgfbull.S7-XXIII.1.95

Cariou E., Mathieu G. (1959). Les phénomènes de silicifications ou meuliérisation dans les assises jurassiques des environs de Poitiers [Silicification phenomena in the Jurassic strata around Poitiers]. *Norois* (24): 406-408.

Charcosset P., Combes P.-J., Peybernès B., Ciszak R., Lopez L. (2000). Pedogenic and Karstic Features at the Boundaries of Bathonian Depositional Sequences in the Grands Causses Area (Southern France): Stratigraphic Implications. *Journal of Sedimentary Research*, 70(1): 255-264. https://doi.org/10.1306/2DC4090F-0E47-11D7-8643000102C1865D

Delay F., Mari J.-L., Porel G., Chabaux F., Ackerer P. (2022). Is subsurface geophysics as seismic and acoustic investigations a rescue to groundwater flow inversion? *Comptes Rendus Geoscience*, Part of Special Issue: Geo-hydrological data & models, https://doi.org/10.5802/crgeos.157

Dercourt J., Gaetani M., Vrielynck B., Barrier E., Biju-Duval B., Brunet M.F., Cadet J.P., Crasquin S., Sandulescu M. (1993). Atlas Peri-Tethys, Palaeogeographical maps. CCGM/CGMW, Paris: 24 maps and explanatory notes: I–XX; 1–269.

Emery D. (1996). Carbonate systems. in Sequence Stratigraphy edited by Emery D. and Myers K., Blackwell Science Ltd: 211-237.

Facon R. (1955). Les données poitevines pour la chronologie de la période froide [Data from Poitou for the chronology of the cold period]. *Bulletin de la Société Préhistorique de France*, 52(3/4): 219-222.

Filipponi M., Jeannin P.-Y., Tacher L. (2010). Understanding cave genesis along favourable bedding planes. The role of the primary rock permeability. *Zeitschrift für Geomorphologie*, Supplementary Issues, 54(2): 91-114. https://doi.org/10.1127/0372-8854/2010/0054S2-0006

Gabilly J. (1962). Les variations de sédimentations du Lias et du Jurassique en relation avec le seuil du Poitou [Variations in Lias and Jurassic sedimentation in relation to the Poitou Threshold]. 87e Congres des Societes Savantes : colloques sur les seuils en géologie, (pp. 679-699). Poitiers.

Gabilly J., Brillanceau A., Cariou E., Ducloux J., Dupuis J., Hantzpergue P., Moreau P., Santallier P., Ters M. (1978). Guides géologiques régionaux : Poitou Charentes Vendée [Regional geological guide: Poitou Charentes Vendée]. Masson, 1st edition.

Gabilly J., Cariou E. (1974). Groupe français d'études du Jurassique : Journée d'études et excursion en Poitou 14-15-16 et 17 octobre 1974. Field guide. Poitiers University.

Gabilly J., Cariou E., Hantzpergue P. (1985). Les grandes discontinuités du Jurassique : témoins d'évènements eustatiques, biologiques et sédimentaires [Jurassic main stratigraphic discontinuities, witnesses of eustatic, biologic and sedimentary occurrences]. *Bulletin de la Société Géologique de France*, I(3): 391-401. https://doi.org/10.2113/gssgfbull.I.3.391

Gaillard T., Bouilly P., Boulais A., Branger P., Debrabant F., Garcia G., Geairon H., Lalbat F., Moreau C. F., Moreau M., Mrani Z., Poncet D., Porel G., Ricaud A., Sibileau L. (2024). Le karst du seuil du Poitou : Approche stratigraphique et rôle de la tectonique. Livret Guide de l'excursion du CFH sur le seuil du Poitou [Stratigraphic approach and the role of tectonics. Field trip for the CFH excursion on the Poitou Threshold], 29 au 31 mars 2024. Comité français d'Hydrogéologie.

Gaillard T, Moreau M., Mari J.-L. (2024). Seismic and stratigraphic characterization of karstogenic horizons in a sequence of carbonate deposits: Example of the Dogger limestones of the Poitou threshold. *E3S Web of Conferences*, 504, Journées Scientifiques AGAP Qualité 2024, Poitiers, France, 26 au 28 mars 2024. https://doi.org/10.1051/e3sconf/202450405005

Gaillard T. (2026). "Hydrostratigraphic study of the Hydrogeological Experimental Site of Poitiers (France)", Chapter 8 in *A new concept of karst development based on hydrogeology and geophysics*, EDP Science. https://doi.org/10.1051/978-2-7598-3934-6.c008

Godard G., Chevalier M., Bouton P., Mouroux B. (1994). Un fleuve yprésien du Berry à la Vendée, témoin de l'évolution paléogéographique et tectonique du Centre-Ouest de la France au Cénozoïque [A Ypresian river from Berry to the Vendée, a witness to the paleogeographic and tectonic evolution of Central-Western France in the Cenozoic Era]. *Géologie de la France* (4) : 35-56.

Gonnin C., Cariou E., Branger P. (1992). Les facteurs de contrôle de la sédimentation au début du Jurassique moyen sur le seuil du Poitou et ses abords. *Compte Rendu de l'Académie des Sciences*, 135(II): 853-859.

Grimes K.G. (2006). Syngenetic Karst in Australia: a review. *Helictite*, 39(2): 27-38.

Hardenbol J., Thierry J., Farley M.B., Jacquin T., De Gracianski P.-C.V. (1998). Mesozoic and Cenozoic Sequence Chronostratigraphic Framework of European Basins. SEPM Special Publication n° 60.

Humphrey J.D., Quinn T.M. (1989). Coastal Mixing Zone Dolomite, Forward Modeling, and Massive Dolomitization of Platform-Margin Carbonates. *Journal of Sedimentary Petrology*, 59(3): 438-454. https://doi.org/10.1306/212F8FBC-2B24-11D7-8648000102C1865D

Jennings J.N. (1968). Syngenetic Karst in Australia. In P.W. Williams and J.N. Jennings [eds] Contributions to the Study of Karst, Research School of Pacific Studies, Australian National University. Department of Geography Publication G/5: 41-110.

Longuemar (Le Touzé de) A. (1856). Études sur la circulation naturelle des eaux superficielles et souterraines dans le département de la Vienne [Studies on the natural circulation of surface and ground water in the Vienne department]. Journal de la Vienne. Poitiers.

Legendre L. (1984). Les transgressions mézozoïques sur le promontoire oriental du massif vendéen [Mesozoic transgressions on the eastern promontory of the Vendean Massif]. Ph.D. thesis, University of Poitiers, France.

Mari J.-L., Porel G. (2008). 3D Seismic Imaging of a Near-Surface Heterogeneous Aquifer: A Case Study. *Oil & Gas Science and Technology (IFP)*, 63(2): 179-201. https://doi.org/10.2516/ogst:2007077

Mari J.-L., Porel G., Bourbiaux B. (2009). From 3D Seismic to 3D Reservoir Deterministic Model Thanks to Logging Data: the Case Study of a Near Surface Heterogeneous Aquifer. *Oil & Gas Science and Technology (IFP)*, 64(2): 119-131. https://doi.org/10.2516/ogst/2008049

Mari J.-L. (2026). "Geophysical methods", Chapter 5 in *A new concept of karst development based on hydrogeology and geophysics*, EDP Science. https://doi.org/10.1051/978-2-7598-3934-6.c005

Mathieu G. (1960). Pénétration des sédiments du Cénomanien dans le karst jurassique du Poitou [Penetration of Cenomanian sediments into the Jurassic karst of Poitou]. *Compte Rendu de l'Académie des Sciences*, 251(5): 755-757.

Molina J.M, Ruiz-Ortiz P.A, Vera J.A (1999). A review of polyphase karstification in extensional tectonic regimes: Jurassic and Cretaceous examples, Betic Cordillera, southern Spain. *Sedimentary Geology*, 1-2: 71-84. https://doi.org/10.1016/s0037-0738(99)00089-5

Morda S., Ketzer J., De Ros L. (2012). Linking diagenesis to sequence stratigraphy: an integrated tool for understanding and predicting reservoir quality distribution. In I. A. sedimentologists (Éd.), Linking diagenesis to sequence stratigraphy: 1-36. Wiley.

Mourier J.-P. (1983). Le versant Parisien du seuil du Poitou de l'Hettangien au Bathonien. Stratigraphie, sédimentologie, caractères paléontologiques, paleogéographie [The Parisian slope of the Poitou sill from the Hettangian to the Bathonian. Stratigraphy, sedimentology, paleontological features, paleogeography]. Ph.D. thesis, Poitiers University, France.

Mourier J.-P., Almeras Y. (1986). Les faunes de brachiopodes et de passage du Bajocien au Bathonien dans le sud-ouest du bassin parisien (France) [Brachiopod faunas and the Bajocian-Bathonian transition in the south-western Paris Basin (France)]. *GEOBIOS*, 19(6): 689-704. https://doi.org/10.1016/S0016-6995(86)80104-8

Mourier J.-P., Gabilly J., Platel J.-P. (1986). Notice explicative de la feuille Poitiers au 1/50000 [1:50,000 geological map of France: Poitiers sheet], n° 589, BRGM Ed.

Patterson R.J., Kinsman D.J.J. (1982) Formation of Diagenetic Dolomite in Coastal Sabkha along Arabian (Persian) Gulf. *AAPG Bulletin*, 66: 28-43.

Valentin X., Amiot R., Boura A. A, Cavin L., Martin-Closas C., Gobé J.-F., Godefroit P., Gomez B., Daviero-Gomez V., Martin J., Otero O., Pereda Suberbiola X., Sorrel P., Texier C., Vullo R., Garcia G. (2021). The fossil locality of Persac (Vienne, France): a unique window on a 100 million years old continental ecosystem. 27^{e} Réunion des sciences de la Terre (RST 2021), Nov 2021, Lyon, France.

Voinchet P., Airvaux J., Hérisson D., Beauval C., Antoine P., Despriée J., Bahain J.-J. (2020). Datation ESR des alluvions du Clain à Saint-Georges-Lès-Baillargeaux (Vienne) – Implications géologiques et archéologiques [ESR dating of the Clain alluvium at Saint-Georges-Lès-Baillargeaux (Vienne) – Geological and archaeological implications]. 12^{e} Colloque international « Quaternaire » Q12, Feb 2020, Paris-Aubervilliers, France.

Welsch J. (1912). Hydrologie souterraine du Poitou calcaire [Underground hydrology of the Poitou limestone region]. *Spelunca*, IX(69).

Conclusion

J.-L. Mari and T. Gaillard

Geophysical and hydrogeological investigations are essential for aquifer characterization. Drawing on their extensive experience in geophysics applied to the oil and gas sector — as well as in geotechnical and hydrogeological studies — the authors demonstrate how conventional seismic methods, typically used in exploration and reservoir imaging, can be effectively adapted for hydrogeological investigations, particularly in karstified geological formations.

The Hydrogeological Experimental Site (HES) of Poitiers, developed for long-term monitoring and experimentation on water and mass transfer processes, has been extensively studied using both hydrogeological and geophysical methods. This book presents an overview of the various field experiments conducted at the site and highlights their respective contributions to the understanding of the karstified Dogger limestone (identical to the supra-Toarcian aquifer) of the Poitou threshold.

A 3D seismic survey was designed to acquire a volumetric image with broad horizontal coverage. Structural interpretation revealed a nearly horizontal stratigraphy with a gentle westward dip of approximately one degree, indicating the absence of significant vertical tectonic displacements. In addition to the 3D seismic survey, the HES was also analyzed using pseudo three-dimensional (3-D) Electrical Resistivity Tomography.

The 3D seismic volume was then transformed into a pseudo-velocity model using acoustic velocity logs for calibration, and subsequently into a pseudo-porosity model. This model revealed three high-porosity, and presumably water-bearing, layers at depths of 35–40 m, 85–87 m, and 110–115 m — interpreted as karstic horizons. These horizons were confirmed through acoustic logging and borehole

© EDP Sciences, 2026
DOI: https://doi.org/10.1051/978-2-7598-3934-6.c905

wall imaging using an Optical Televiewer (OPTV). A specific acoustic attribute, K-index, was developed to identify karstic bodies. However, due to the seismic data's lower vertical resolution (on the order of meters) compared to that of logging tools (centimetric to decimetric), some karstic features were detected only by borehole logs.

The authors show that 3D seismic imaging enables the construction of a large-scale structural model that can highlight potential karstic zones. These must then be validated through high-resolution borehole investigations, such as full waveform acoustic and OPTV logging. By correlating karstic features with the stratigraphic framework, the discontinuities that control karst formation can be identified, leading to a new karstification model constrained by stratigraphy.

At the HES site, the authors demonstrate that karstic horizons in the Dogger limestone are closely associated with stratigraphic discontinuities and early diagenesis. Sedimentation hiatuses, precisely constrained by the absence of specific ammonite zones, together with the emersion of the Poitou Threshold carbonate platform, are interpreted as the primary controls on these levels, through the promotion of hardground formation and subsequent dolomitization. The aquifer is thus composed of multiple productive layers that may be hydraulically connected through faults in the vadose zone and joint systems in the saturated zone. Typically, boreholes are drilled to intersect all karstic levels, which results in mixing waters of varying pressure and chemical composition. These wells are particularly vulnerable to surface pollution, posing a risk of contamination to deeper karst systems. Therefore, a detailed lithological and paleontological description of each borehole is essential to assess the role of stratigraphy in water inflow distribution. Well logging should be systematically performed prior to completion and equipment installation, using techniques such as flowmeter, gamma-ray, OPTV, and other geophysical tools to accurately locate karstic horizons.

The karstification model proposed for the Poitou threshold has practical implications. Once a large-scale structural model and karstic levels have been identified, two key recommendations emerge:

1. acquire optical televiewer data from all available boreholes to refine stratigraphic interpretations and accurately locate karst features;
2. consider individually screening each karstic level during borehole completion. This approach allows for a better assessment of groundwater quality and vulnerability and supports the long-term management of deep karst resources as protected reserves.

The field experiments at the HES site support a multi-objective strategy for mapping karst conduit networks, based on the following key methods:

- identification of water-producing zones in each borehole. This involves logging techniques such as long normal resistivity, temperature, electrical conductivity, and flowmeter logging — the latter being particularly effective in detecting active flow zones. High-resolution borehole imaging via OPTV enables identification, localization, and sizing of fractures, vugs, and karst conduits.

Full waveform acoustic logs provide mechanical parameters (e.g., P-wave velocity) and are used in seismic inversion to define karst detection indices. Vertical Seismic Profiling (VSP) supports time-to-depth conversion and can indicate karst features through Stoneley wave analysis;

- 3D imaging of the aquifer reservoir. In karstified limestone aquifers, seismic methods are recommended to identify major karstic levels. The processed 3D seismic volume is converted into depth, then into a pseudo-velocity model constrained by acoustic logs, and finally into a pseudo-porosity model after calibration with borehole data;
- hydraulic tests. Cross-hole pumping tests are used to detect flow paths. High hydraulic diffusivity observed in slug tests aids in building connectivity maps. At the HES site, such tests differentiate wells that are hydraulically connected to the karst network from those that are not;
- tracer tests. Tracer breakthrough curves help define the number and nature of distinct flow paths between injection and observation points. These dye tracer tests also highlight the role of boreholes in the mixing of karstic levels by identifying ascending or descending hydraulic gradients within each borehole;
- combined geophysical and hydrogeological analysis. The integration of these data sets enables the detection of water-producing zones and the delineation of probable karst conduit networks.

Beyond the detailed case study of the Dogger limestone at the Poitou threshold, the authors offer a robust methodology for seismic and stratigraphic characterization that can be applied to other hydrogeological contexts and reservoir studies.

Acknowledgements

J.-L. Mari and T. Gaillard

The authors wish to express their sincere gratitude to the following individuals and institutions.

- **Gilles Porel** (University of Poitiers, France) for facilitating exchanges between researchers involved in various projects on fractured aquifers, and for generously sharing all data collected at the Hydrogeological Experimental Site (HES).

- **Benoît Nauleau** and **Denis Paquet** (University of Poitiers) for their invaluable support during field experiments and their dedicated assistance with data collection.

- **Patrick Meynier** (IFP Energies nouvelles) for his support in acquiring seismic data, and **Pierre Gaudiani** (Association Pédagogique et Expérimentale du Cher) for his contribution to acoustic data acquisition.

- **Patrizio Torrese** (University of Pavia, Italy) for his valuable and insightful contribution to the characterization of the HES using 3D electrical tomography.

Special thanks are extended to the researchers who contributed to the writing of the book: **Patrick Branger** (paleontologist), **Hélène Geairon**, **Mickaël Moreau**, **Adrien Boulais** (hydrogeologists, CPGF Horizon), and **Patrick Brunel** (geophysicist, Loggic).

© EDP Sciences, 2026
DOI: https://doi.org/10.1051/978-2-7598-3934-6.c906

Warm thanks to **Valérie Monange** (graphic designer, CPGF Horizon) for her invaluable support and assistance in creating the figures.

The authors are also grateful to **Frédérick Delay** (University of Strasbourg) and **Jacques Bodin** (University of Poitiers) for their insightful discussions.

Finally, special thanks to **Michel Hayet** (President, AGAP - Qualité) for his encouragement and support during the preparation of the manuscript.

PROfile

A new concept of karst development based on hydrogeology and geophysics

Thierry Gaillard and Jean-Luc Mari

Geophysical and hydrogeological investigations are essential for the characterization of aquifers. Drawing on their extensive experience in geophysics applied to the oil and gas industry, as well as in geotechnical and hydrogeological studies, the authors demonstrate how conventional seismic methods—commonly used in exploration and reservoir imaging—can be adapted to hydrogeological investigations, particularly in karstified geological formations. The Dogger limestone of the Poitou Threshold serves as a compelling case study.

This book offers a practical guide on how hydrogeology and geophysics contribute to developing robust regional groundwater flow models. It showcases how an integrated, multidisciplinary geoscientific approach—combining geophysical, hydrogeological, and stratigraphic analyses—can significantly enhance conceptual models of groundwater flow in fractured and karstified media.

The book begins with a geological overview of the Poitou Threshold and provides a detailed synthesis of the Middle Jurassic limestone stratigraphy, establishing the broader regional geodynamic context. It then focuses on the area's hydrogeology, before presenting the Hydrogeological Experimental Site (HES). Subsequent chapters explore the geophysical and hydrogeological methods employed, emphasizing how a Multiphysics approach can delineate karstic horizons' geometry.

The book highlights the importance of high-resolution stratigraphic analysis—through core sampling and optical televiewer (OPTV) imaging from open-hole drilling—in mapping the distribution of karstic zones and refining flow models.

More than just a methodological reference, this work encapsulates over two decades of research at the HES. It offers valuable insights into the sustainable management of drinking water resources, stressing the critical role of borehole stratigraphy and well completion design. The collaboration between scientists and engineers presented here exemplifies how applied geophysics can support hydrogeologists, water resource managers, and policymakers in addressing challenges such as groundwater scarcity and contamination.

In addition to the detailed case study of the Dogger limestone, the authors provide a replicable framework for seismic and stratigraphic characterization applicable to a wide range of hydrogeological and reservoir studies. As such, this book serves as both a reference and a teaching tool, ideal for academic courses and professional development programs.

978-2-7598-3934-6

9 782759 839346

edp sciences
www.edpsciences.org

Books of the PROfile collection are intended for the transmission of professional knowledge in different disciplines. They are written by recognized experts in their fields and contribute to the training and information of professionals.